Conference Proceedings of the Society for Experimental Mechanics Series

Zhu Mao *Editor*

Model Validation and Uncertainty Quantification, Volume 3

Proceedings of the 39th IMAC, A Conference and Exposition on Structural Dynamics 2021

Springer

Conference Proceedings of the Society for Experimental Mechanics Series

Series Editor

Kristin B. Zimmerman
Society for Experimental Mechanics, Inc.,
Bethel, CT, USA

The Conference Proceedings of the Society for Experimental Mechanics Series presents early findings and case studies from a wide range of fundamental and applied work across the broad range of fields that comprise Experimental Mechanics. Series volumes follow the principle tracks or focus topics featured in each of the Society's two annual conferences: IMAC, A Conference and Exposition on Structural Dynamics, and the Society's Annual Conference & Exposition and will address critical areas of interest to researchers and design engineers working in all areas of Structural Dynamics, Solid Mechanics and Materials Research.

More information about this series at http://www.springer.com/series/8922

Zhu Mao
Editor

Model Validation and Uncertainty Quantification, Volume 3

Proceedings of the 39th IMAC, A Conference and Exposition on Structural Dynamics 2021

Springer

Editor
Zhu Mao
Department of Mechanical Engineering
University of Massachusetts
Lowell, MA, USA

ISSN 2191-5644 ISSN 2191-5652 (electronic)
Conference Proceedings of the Society for Experimental Mechanics Series
ISBN 978-3-030-77347-2 ISBN 978-3-030-77348-9 (eBook)
https://doi.org/10.1007/978-3-030-77348-9

This Springer imprint is published by the registered company Springer Nature Switzerland AG
The registered company address is: Gewerbestrasse 11, 6330 Cham, Switzerland

Preface

Model Validation and Uncertainty Quantification represents one of nine volumes of technical papers presented at the 39th IMAC, A Conference and Exposition on Structural Dynamics, organized by the Society for Experimental Mechanics, and held between February 8 and 11, 2021. The full proceedings also include volumes on nonlinear structures and systems; dynamics of civil structures; dynamic substructures; special topics in structural dynamics and experimental techniques; rotating machinery, optical methods, and scanning ldv methods; sensors and instrumentation, aircraft/aerospace, energy harvesting, and dynamic environments testing; topics in modal analysis and parameter identification; and data science in engineering.

Each collection presents early findings from experimental and computational investigations on an important area within structural dynamics. Model validation and uncertainty quantification (MVUQ) is one of these areas.

Modeling and simulation are routinely implemented to predict the behavior of complex dynamical systems. These tools powerfully unite theoretical foundations, numerical models, and experimental data, which include associated uncertainties and errors. The field of MVUQ research entails the development of methods and metrics to test model prediction accuracy and robustness while considering all relevant sources of uncertainties and errors through systematic comparisons against experimental observations.

The organizers would like to thank the authors, presenters, session organizers, and session chairs for their participation in this track.

Lowell, MA, USA — Zhu Mao

Contents

Effect of Inspection Errors in Optimal Maintenance Decisions for Deteriorating Quoin Blocks in Miter Gates

Manuel A. Vega, Zhen Hu, and Michael D. Todd

Abstract Condition-based maintenance (CBM) is a modern maintenance approach that combines data-driven reliability models and information from a condition monitoring process (e.g., inspections and continuous monitoring). Maintenance schedules are predicted based on the results from diagnosis and prognosis. Due to aging, the US Army Corps of Engineers (USACE) has equipped some of its navigation infrastructure with sensors to allow continuous monitoring. Miter gates are one of the most important such structural assets because of their economic impact on navigation corridors. Miter gates prognosis and maintenance schedule capabilities can be improved when a discrete-state deterioration model based on inspection data is used. One of the sources of inspection data available for miter gates is the operational condition assessment (OCA) discrete ratings. However, these discrete ratings are highly abstracted, assigned at variable frequencies, and very prone to human error and to misinterpretations due to inspection protocols. In miter gates, OCA ratings are available for deteriorating components such as quoin blocks. Over time, contact between these quoin blocks deteriorates, ultimately leading to failure, which can be generally avoided with timely maintenance schedules. To overcome these issues, this paper proposes a structural health-monitoring-based CBM framework that accounts for different levels of human observation errors in the inspection data. This proposed framework shows (1) how to use physics-informed (e.g., finite element) simulations to perform damage diagnosis in miter gates and (2) how to account for human observation errors to improve prognosis and maintenance schedule capabilities for deteriorating components (e.g., quoin blocks) in miter gates.

Keywords Miter gates · Uncertainty quantification · Model updating · Prognosis and health management

1 Introduction

Miter gates are hydraulic steel structures that are considered the most common type of lock gate. The purpose of miter gates is to allow the passage of ships, boats, and watercraft between various water elevation levels in navigation routes systems in rivers. In the United States, the US Army Corps of Engineers (USACE) maintains and operates 236 locks at 191 sites [1]. Closure of a lock due to maintenance or repairs can cost up to $3 million per day to the US economy [2]. More than half of these structural assets, including miter gates, have surpassed their 50-year economic design life [3]. To help in prioritizing maintenance and repairs, operational condition assessment (OCA) ratings have been performed by USACE inspectors via visual inspections [4]. However, the OCA ratings are highly abstracted and are assigned at a varying frequency, which ranges from yearly to occurring to a maximum of every 5 years. Recently, many miter gates have been equipped with structural health monitoring (SHM) systems that can collect strain measurement data in real time [5]. These continuous monitoring systems aim to provide insight regarding deteriorating gates. A framework that integrates visual inspections accounting for human discrepancies and SHM for damage diagnosis and prognosis has been developed and presented in this work.

M. A. Vega · M. D. Todd (✉)
Department of Structural Engineering, University of California San Diego, La Jolla, CA, USA
e-mail: mdtodd@eng.ucsd.edu

Z. Hu
Department of Industrial and Manufacturing Systems Engineering, University of Michigan-Dearborn, Dearborn, MI, USA

Z. Mao (ed.), *Model Validation and Uncertainty Quantification, Volume 3*, Conference Proceedings of the Society for Experimental Mechanics Series, https://doi.org/10.1007/978-3-030-77348-9_1

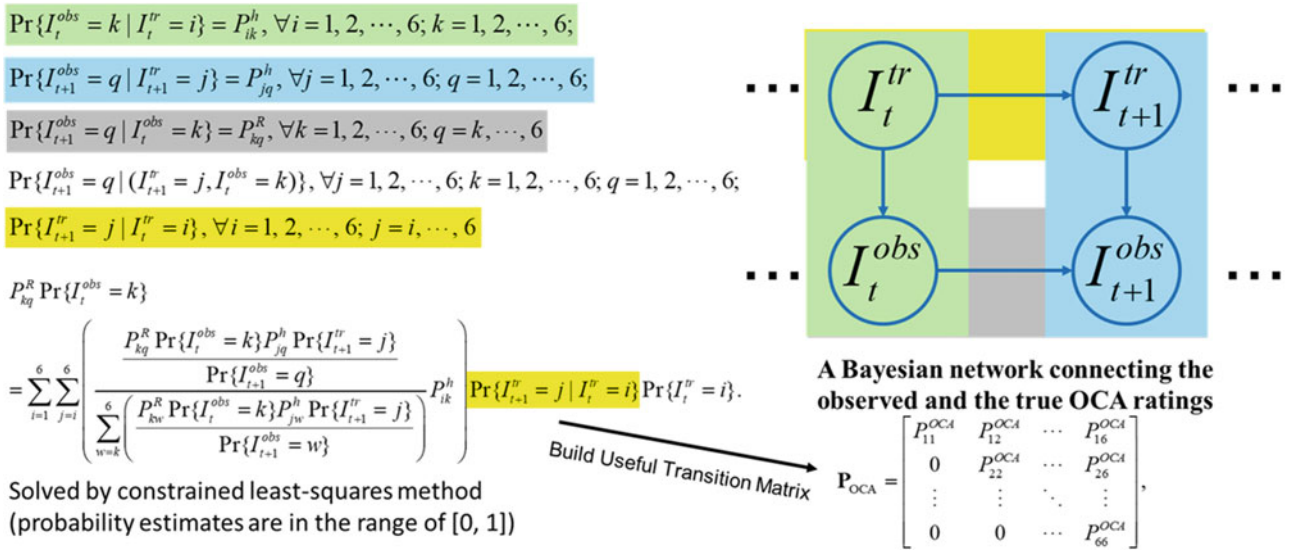

Fig. 1 Mapping between reported OCA transition matrix to compensated/true OCA transition matrix

2 Reported OCA Transition Matrix to True OCA Transition Matrix

Based on a large historical OCA database, the number of times that a component transitioned from one rating category to another (as determined by engineering expert elicitation) over a given inspection time step can be determined to generate the rating transition matrix. The transition matrix $\mathbf{P}$ (see Eq. (1)) is defined as a square matrix with nonnegative values that represents how some process "transitions" from one state to the next. In this application, an inspected state at time t, $I_{i,\,t}$ (with $i = 1 \ldots 6$, corresponding to the six-letter ratings specified above), will transition to inspected state at time $t + 1$, $I_{j,\,t+1}$, $j = 1...6$, according to

$$\mathbf{P}_{\text{Report}} = P\left(\mathbf{I}_{t+1}^{\text{obs}} \middle| \mathbf{I}_t^{\text{obs}}\right) = \begin{bmatrix} P\left(A_{t+1}^R \middle| A_t^R\right) & \cdots & P\left(\text{CF}_{t+1}^R \middle| A_t^R\right) \\ \vdots & \ddots & \vdots \\ P\left(A_{t+1}^R \middle| \text{CF}_t^R\right) & \cdots & P\left(\text{CF}_{t+1}^R \middle| \text{CF}_t^R\right) \end{bmatrix}, \tag{1}$$

In order to map the reported OCA rating transition matrix to the underlying "true" OCA transition matrix, the underlying true OCA rating is defined at time t as I_t^{tr} and that at $t + 1$ as I_{t+1}^{tr}, the reported OCA rating from field engineers at time t as I_t^{obs} and that at time $t + 1$ as shown in Fig. 1.

As shown in Fig. 1, to map $\mathbf{P}_{\text{Report}}$ to $\mathbf{P}_{\text{OCA}}$, the human observation error matrix needs to be obtained/estimated as follows:

$$\mathbf{P}_{\text{human}} = \begin{bmatrix} P_{11}^h & P_{12}^h & \cdots & P_{16}^h \\ P_{21}^h & P_{22}^h & \cdots & P_{26}^h \\ \vdots & \vdots & \ddots & \vdots \\ P_{61}^h & P_{62}^h & \cdots & P_{66}^h \end{bmatrix} \underset{\rightarrow}{\text{Assume}} \begin{bmatrix} 1 & 0 & 0 & 0 & 0 & 0 \\ 0.04 & 0.96 & 0 & 0 & 0 & 0 \\ 0 & 0.40 & 0.60 & 0 & 0 & 0 \\ 0 & 0.03 & 0.17 & 0.80 & 0 & 0 \\ 0 & 0 & 0 & 0.03 & 0.97 & 0 \\ 0 & 0 & 0 & 0 & 0.03 & 0.97 \end{bmatrix}, \tag{2}$$

in which $P_{ik}^h = \Pr\left\{I_t^{\text{obs}} = k | I_t^{\text{tr}} = i\right\}$ is the probability that the reported OCA rating is k, given that the true OCA rating is i. Now, the assumed $\mathbf{P}_{\text{human}}$ represents the behavior of an inspector that regularly tends to assess a structural component to be in a better condition than reality.

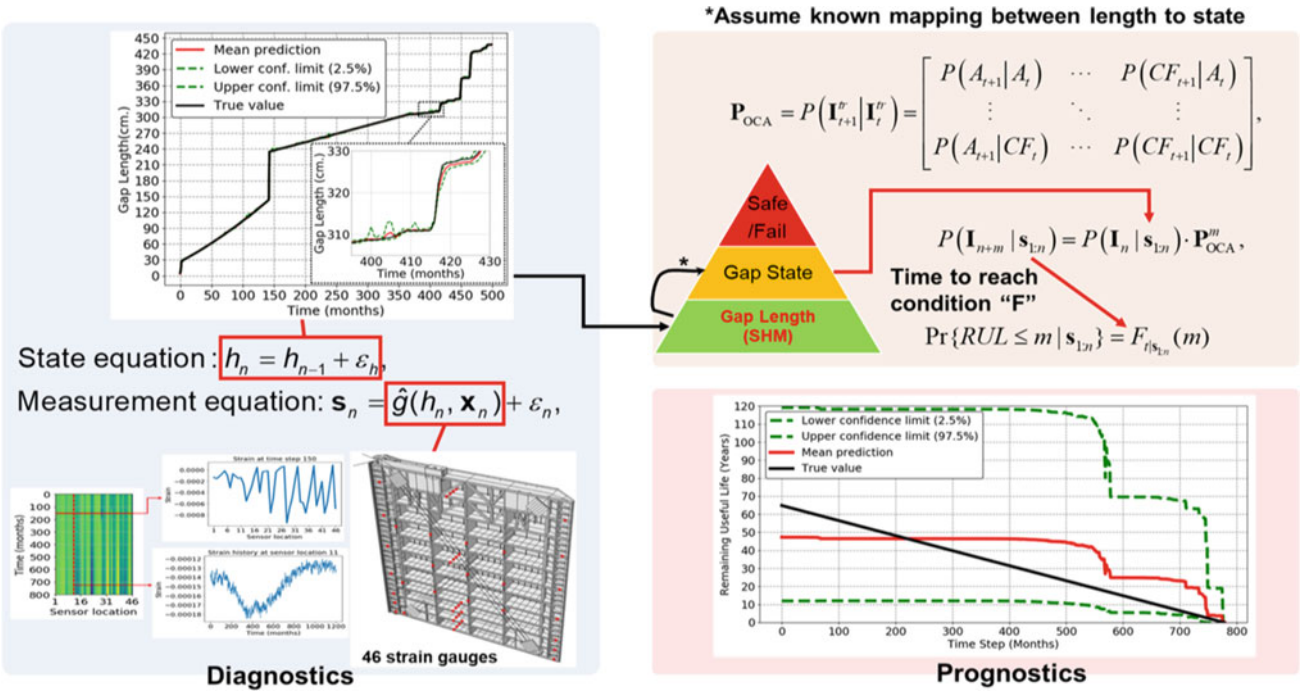

Fig. 2 Diagnosis and prognosis of gap lengths in miter gates using compensated OCA ratings and SHM systems

3 Framework and Results

As shown in this Fig. 2, the proposed framework first estimates the damage state (i.e., gap length) using online SHM data using sequential updating. After that, the estimated gap length is mapped from its continuous state to its corresponding gap (OCA rating) state. The current state at time "n" with the true OCA transition matrix is used to estimate the rating state at time "$n + m$," which can be used to estimate the probability of failure and the remaining useful life at this time step, as denoted in Fig. 2. This framework is categorized as a hybrid approach because it uses a physics-based (FE) model for diagnosis and a data-driven model (the transition matrix) for prognosis.

4 Conclusion

This work proposed a new hybrid CBM approach that integrates high-fidelity FE-model-based SHM with inspection-data-based transition matrix for an effective diagnosis or prognosis, which includes the quantification of the effects of uncertainty in OCA ratings. Results capture correctly the true gap length and the true remaining useful life of the quoin blocks, assuming its only deterioration mechanism is the formation of a bearing gap.

Acknowledgments This research was supported by the US Army Corps of Engineers through the US Army Engineer Research and Development Center Research Cooperative Agreement W912HZ-17-2-0024. The support is gratefully acknowledged.

References

1. U.S. Army Corps of Engineers Headquarters, "Navigation," 2018. [Online]. Available: http://www.usace.army.mil/Missions/CivilWorks/Navigation.aspx. Accessed 1 Aug 2018
2. Eick, B.A., et al.: Automated damage detection in miter gates of navigation locks. Struct. Control Health Monit. **25**(1), 1–18 (2018)
3. Foltz, S.D.: Investigation of Mechanical Breakdowns Leading to Lock Closures, Champaign, U.S. Army Engineer Research and Development Center, Construction Engineering Research Laboratory (2017)

4. Przybyla, J.: Best Practices in Asset Management, Alexandria, U.S. Army Engineer Research and Development Center, Institute for Water Resources (2013)
5. U.S. Army Corps of Engineers Headquarters, “SMART GATE,” 2007. [Online]. Available: https://www.erdc.usace.army.mil/Media/Fact-Sheets/Fact-Sheet-Article-View/Article/476668/smart-gate/. Accessed 1 Aug 2018

Model Uncertainty Quantification and Updating of a Boundary Condition Model of a Miter Gate Using Strain Measurements

Chen Jiang, Manuel A. Vega, Michael D. Todd, and Zhen Hu

Abstract This paper presents a model uncertainty quantification and updating approach for a boundary condition model of a miter gate. A boundary condition model is used as the forward model to predict the boundary load condition of a miter gate for a given gap length. The boundary force prediction is then employed as inputs to a strain analysis model that predicts the strain response of the gate. Due to model simplifications, the boundary condition model may not accurately represent the true physics. By following the Kennedy and O'Hagan (KOH) framework under a Bayesian scheme, this paper corrects the unobservable boundary condition model using the strain measurements by simultaneously estimating the gap length and quantifying the model uncertainty. Results show that the proposed approach can effectively estimate the unknown gap length and improve the prediction of both the boundary condition model and the strain response model.

Keywords Miter gates · Boundary condition model · Model calibration · Uncertainty quantification · Model updating

1 Introduction

The US Army Corps of Engineers (USACE) maintains 236 miter gates at 191 sites [1]. One of the most common failures of the miter gates is the deterioration of quoin blocks due to the rolling contact between the supporting wall and miter gate, leading to the loss of contact, i.e., gap. An unexpected closure of miter gates will happen when a high-stress area where boundary force exceeds the limit states emerges as the gap length increases. Early gap prediction is required before the gap length becomes too large to maintain the normal operation of miter gates. Even though models have been developed to predict the boundary forces along quoin blocks by using a contact model or by simplifying the contact as a pin boundary condition, these models may not accurately predict the boundary load condition due to model assumptions and simplifications. In addition, the unknown gap length of the quoin block further complicates the boundary load condition analysis. In this work, we are going to implement Bayesian calibration to identify the gap length and correct the boundary condition model. Since true boundary force is distributed and unobservable, we construct a multilevel model for miter gates and use strain measurements for Bayesian calibration.

2 Multilevel Simulation Models

A high-fidelity ABAQUS finite element simulation model was developed for stress analysis and boundary contact analysis, as shown in Fig. 1 [2], in which the distributed boundary forces at normal and tangential directions can be respectively obtained for a given gap length. Based on the finite element model, a reduced-order model of strain analysis was developed for the prediction of strain gauges using the static condensation method [3] with the distributed boundary force as input. Even though both the boundary contact analysis model and the strain analysis model share the same finite element model, the analyses are performed in a multilevel manner. As shown in Fig. 2, the boundary condition model, $g_{\mathrm{BC}}^{\mathrm{m}}$, is called the

C. Jiang · Z. Hu (✉)
Department of Industrial and Manufacturing Systems Engineering, University of Michigan-Dearborn, Dearborn, MI, USA
e-mail: zhennhu@umich.edu

M. A. Vega · M. D. Todd
Department of Structural Engineering, University of California San Diego, La Jolla, CA, USA

Z. Mao (ed.), *Model Validation and Uncertainty Quantification, Volume 3*, Conference Proceedings of the Society for Experimental Mechanics Series, https://doi.org/10.1007/978-3-030-77348-9_2

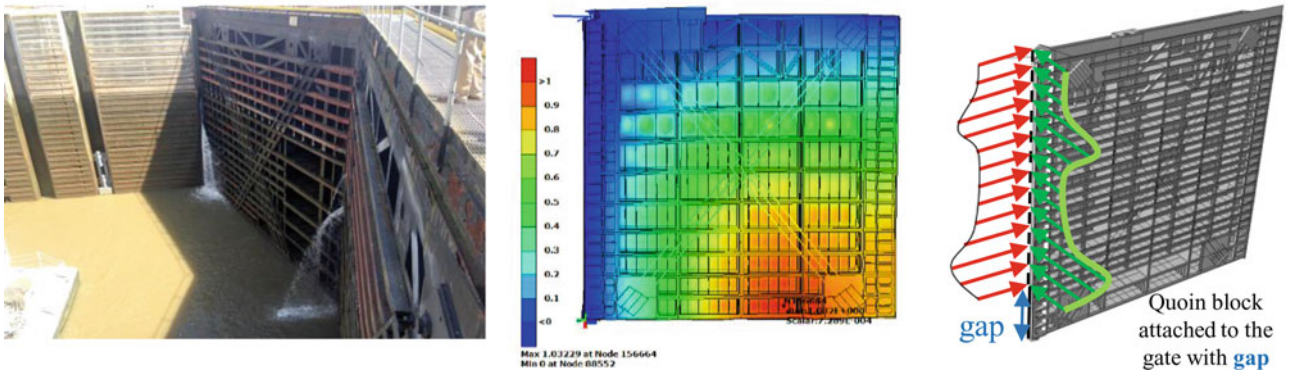

Fig. 1 Miter gate and finite element model (left: miter gate, middle: stress analysis, right: contact force analysis)

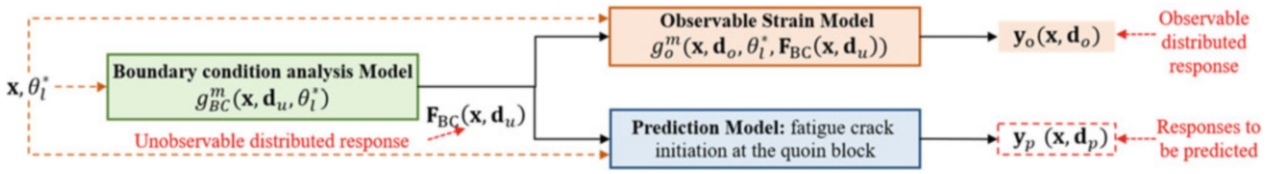

Fig. 2 Multilevel analysis model of miter gate

unobservable model since the distributed boundary force $\mathbf{F}_{\mathrm{BC}}(\mathbf{x}, \mathbf{d}_{\mathrm{u}})$ is unobservable, whereas the strain analysis model, $g_{\mathrm{o}}^{\mathrm{m}}$, is called the observable model because the strain gauge data $\mathbf{y}_{\mathrm{o}}(\mathbf{x}, \mathbf{d}_{\mathrm{o}})$ can be measured. Furthermore, the unobservable distributed boundary force may be one of the inputs of the prediction model, such as the fatigue analysis model. In Fig. 2, $\mathbf{x}$ pertains to the upstream and downstream water levels governing the hydrostatic load on the gates and θ_{l}^* is the unknown true gap length since gap is underwater in practice. On the other hand, $\mathbf{d}_{\mathrm{u}}$, $\mathbf{d}_{\mathrm{o}}$, and $\mathbf{d}_{\mathrm{p}}$ are respectively the spatial coordinates in the different model responses.

3 Modularized Bayesian Calibration of the Multilevel Model

The underlying true unobservable boundary force can be modeled by

$$\mathbf{F}_{\mathrm{BC}}^{\mathrm{true}}(\mathbf{x}, \mathbf{d}_{\mathrm{u}}) = \begin{cases} \rho g_{\mathrm{BC}}^{\mathrm{m}}\left(\mathbf{x}, \mathbf{d}_{\mathrm{u}}, \theta_{\mathrm{l}}^*\right) + \boldsymbol{\delta}_{\mathrm{BC}}(\mathbf{x}, \mathbf{d}_{\mathrm{u}}), & \text{if } \mathbf{d}_{\mathrm{u}} \geq \theta_{\mathrm{l}}^* \\ 0, & \text{otherwise} \end{cases}, \tag{1}$$

where N_{u} is the number of spatial coordinates; $\mathbf{d}_{\mathrm{u}}$, $\boldsymbol{\delta}_{\mathrm{BC}}(\mathbf{x}, \mathbf{d}_{\mathrm{u}})$ represent the model discrepancy of $g_{\mathrm{BC}}^{\mathrm{m}}$ due to the model assumptions or simplifications; and ρ is an unknown regression coefficient. Since unobservable distributed response $\mathbf{F}_{\mathrm{BC}}^{\mathrm{true}}(\mathbf{x}, \mathbf{d}_{\mathrm{u}}) \in \mathbb{R}^{2N_{\mathrm{u}} \times 1}$ cannot be obtained in practice to calibrate $g_{\mathrm{BC}}^{\mathrm{m}}$, we employed the strain measurements given below:

$$\mathbf{y}_{\mathrm{o}}^{\mathrm{e}}(\mathbf{x}, \mathbf{d}_{\mathrm{o}}) = \mathbf{y}_{\mathrm{o}}^{\mathrm{true}}(\mathbf{x}, \mathbf{d}_{\mathrm{o}}) + \boldsymbol{\varepsilon}(\mathbf{d}_{\mathrm{o}}) = g_{\mathrm{o}}^{\mathrm{m}}\left(\mathbf{x}, \ \mathbf{d}_{\mathrm{o}}, \ \theta_{\mathrm{l}}^*, \ \mathbf{F}_{\mathrm{BC}}^{\mathrm{true}}(\mathbf{x}, \mathbf{d}_{\mathrm{u}})\right) + \boldsymbol{\varepsilon}(\mathbf{d}_{\mathrm{o}}), \tag{2}$$

where $\boldsymbol{\varepsilon}(\mathbf{d}_{\mathrm{o}}) = \left[\varepsilon\left(\mathbf{d}_{\mathrm{o},1}\right), \ldots, \varepsilon\left(\mathbf{d}_{\mathrm{o},N_{\mathrm{o}}}\right)\right]^{\mathrm{T}}$ are the measurement errors of strain data $\left\{\mathbf{x}^{\mathrm{e}}, \mathbf{y}_{\mathrm{o}}^{\mathrm{e}}\right\}$ and N_{o} is the number of $\mathbf{d}_{\mathrm{o}}$.

The modularized Bayesian scheme [4, 5] is adopted. In Module 1, a reduced-order model is constructed for $g_{\mathrm{BC}}^{\mathrm{m}}$ and $g_{\mathrm{o}}^{\mathrm{m}}$ using the Lagrange multiplier method and static condensation method, respectively [3]. Module 2 estimates $\hat{\rho}$ and constructs the surrogate model $\hat{\boldsymbol{\delta}}_{\mathrm{BC}}(\mathbf{x}, \mathbf{d}_{\mathrm{u}}, \ \boldsymbol{\omega}^*)$ based on the strain observations $\left\{\mathbf{x}^{\mathrm{e}}, \mathbf{y}_{\mathrm{o}}^{\mathrm{e}}\right\}$, where $\boldsymbol{\omega}^*$ is the hyper-parameters of the constructed discrepancy surrogate model. Module 3 updates the posterior distribution of θ_{l} (i.e. $f_{\theta|\mathbf{y}}\left(\theta_{\mathrm{l}}|\mathbf{y}_{\mathrm{o}}^{\mathrm{e}}, \ \mathbf{x}^{\mathrm{e}}, \ \boldsymbol{\omega}^*, \rho^*\right)$) through the Bayesian inference scheme. In Module 4, the distributed boundary force after calibration and correction is predicted as

$$\hat{\mathbf{F}}_{\mathrm{BC}}\left(\mathbf{x}, \mathbf{d}_{\mathrm{u}}\right) \mid \mathbf{y}_{\mathrm{o}}^{\mathrm{e}}, \quad \mathbf{x}^{\mathrm{e}}, \quad \boldsymbol{\omega}^{*}, \rho^{*}=\int_{\theta_{\mathrm{l}}} \rho^{*} g_{\mathrm{BC}}\left(\mathbf{x}, \mathbf{d}_{\mathrm{u}}, \theta_{\mathrm{l}}\right) f_{\theta \mid \mathbf{y}}\left(\theta_{\mathrm{l}} \mid \mathbf{y}_{\mathrm{o}}^{\mathrm{e}}, \quad \mathbf{x}^{\mathrm{e}}, \quad \boldsymbol{\omega}^{*}, \rho^{*}\right) d \theta_{\mathrm{l}} + \hat{\boldsymbol{\delta}}_{\mathrm{BC}}\left(\mathbf{x}, \mathbf{d}_{\mathrm{u}}, \quad \boldsymbol{\omega}^{*}\right) \in \mathbb{R}^{2 N_{\mathrm{u}} \times 1}, \tag{3}$$

and the corrected strain response prediction is obtained in a similar manner to Eq. (3).

4 Results

For the purpose of demonstrating and verifying the proposed method, we assume the boundary force discrepancy functions as

$$\boldsymbol{\delta}_{\mathrm{N}}\left(\mathbf{x}, \mathbf{d}_{\mathrm{u}}\right)=3\left(x_{\mathrm{up}}-x_{\mathrm{down}}\right)\left[\left(762-\mathbf{d}_{\mathrm{u}}\right) / 1200\right]^{3}, \quad \text{if } \mathbf{d}_{\mathrm{u}} \geq \theta_{\mathrm{l}}^{*}, \tag{4}$$

$$\boldsymbol{\delta}_{\mathrm{T}}\left(\mathbf{x}, \mathbf{d}_{\mathrm{u}}\right)=\left[\left(x_{\mathrm{up}}-x_{\mathrm{down}}\right) / 100\right]^{2} \sin \left(\mathbf{d}_{\mathrm{u}} / 240\right), \quad \text{if } \mathbf{d}_{\mathrm{u}} \geq \theta_{\mathrm{l}}^{*}, \tag{5}$$

where both $\boldsymbol{\delta}_{\mathrm{N}}(\mathbf{x}, \mathbf{d}_{\mathrm{u}})$ and $\boldsymbol{\delta}_{\mathrm{T}}(\mathbf{x}, \mathbf{d}_{\mathrm{u}})$ will equal to zero if $\mathbf{d}_{\mathrm{u}} < \theta_{\mathrm{l}}^{*}$, $\boldsymbol{\delta}_{\mathrm{N}}(\mathbf{x}, \mathbf{d}_{\mathrm{u}})$ and $\boldsymbol{\delta}_{\mathrm{T}}(\mathbf{x}, \mathbf{d}_{\mathrm{u}})$ are the discrepancy of normal and tangential boundary force, respectively. The formula $\mathbf{x} = [x_{\mathrm{up}}, x_{\mathrm{down}}]$ denotes the upstream and downstream water levels varying over [24, 744] inches; $\mathbf{d}_{\mathrm{u}}$ denotes the height coordinates along the quoin block, whose height is equal to 762 inches (i.e., $\mathbf{d}_{\mathrm{u}} \in [0, 762]$), θ_{l}^{*} represents the true gap length, which is assumed to be 150 inches for illustration. Building upon the boundary condition model, assumed discrepancy functions, and gap length, 500 strain data are synthesized by Eq. (2) with $\rho = 0.8$, and each group of data has seven strain responses collected through the strain gauges in Fig. 1. The standard deviation of strain measurement error is assumed to be $\sigma_{\varepsilon} = 1$. After that, θ_{l}^{*}, $\boldsymbol{\delta}_{\mathrm{N}}(\mathbf{x}, \mathbf{d}_{\mathrm{u}})$, $\boldsymbol{\delta}_{\mathrm{T}}(\mathbf{x}, \mathbf{d}_{\mathrm{u}})$, and ρ are assumed to be unknown while performing Bayesian calibration. A noninformative uniform distribution θ_{l}~Unif(135, 165) inches is assumed to be the prior distribution of θ_{l}.

The regression coefficient is estimated to be 0.83, and the maximum a posterior estimation of θ_{l} is equal to 149 inches, which is very close to the assumed true θ_{l}^{*}. Figure 3 shows the normal force prediction after correction. Figure 3a and 3b respectively compare the normal force discrepancy and total normal force prediction at a certain water level (upstream level: 426 inches, downstream level: 120 inches). Figure 3c shows an error surface by fixing the downstream water level at 120 inches. The results show that Bayesian calibration improves the prediction accuracy of the boundary force analysis model. Moreover, Fig. 4 depicts the comparison of strain response prediction errors at the seven sensor locations of 50 different input settings by respectively fixing downstream and upstream levels. It indicates that the prediction accuracy of the observable strain model can also be improved dramatically after the calibration and correction of the unobservable boundary condition model.

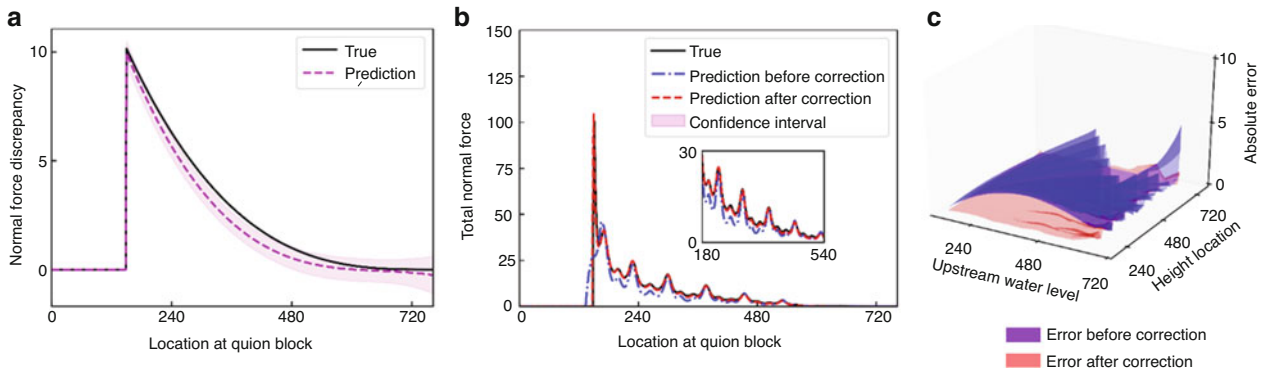

Fig. 3 Normal force prediction after correction: (**a**) normal force discrepancy reconstruction and (**b**) total normal force prediction at a certain water level, as well as (**c**) normal force prediction errors by fixing downstream water level at 120 inches

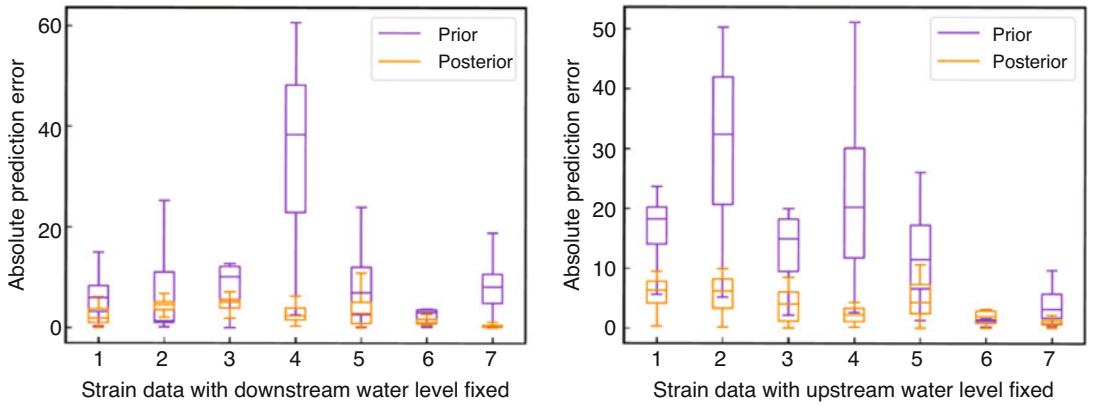

Fig. 4 Prediction errors of seven strain responses with downstream water level or upstream water level fixed

5 Conclusions

This work proposed a modularized Bayesian calibration method for the multilevel simulation model of miter gates, where the observable strain measurements are employed to tackle the challenge of correcting the unobservable model with a distributed boundary force response. Results show that the prediction accuracies of both unobservable and observable models are improved.

Acknowledgments This research was supported by the US Army Corps of Engineers through the US Army Engineer Research and Development Center Research Cooperative Agreement W912HZ-17-2-0024. The support is gratefully acknowledged.

References

1. U.S. Army Corps of Engineers Headquarters: Navigation. https://www.usace.army.mil/Missions/Civil-Works/Navigation/
2. Eick, B.A., Treece, Z.R., Spencer, B.F., Smith, M.D., Sweeney, S.C., Alexander, Q.G., Foltz, S.D.: Automated damage detection in miter gates of navigation locks. Struct. Control. Health Monit. **25**(1), e2053 (2018)
3. Parno, M., O'Connor, D.T., Smith, M.: High dimensional inference for the structural health monitoring of lock gates. arXiv preprint arXiv: 1812.05529 (2018)
4. Kennedy, M.C., O'Hagan, A.: Bayesian calibration of computer models. J. R. Stat. Soc. Ser. B Stat. Methodol. **63**, 425–464 (2001)
5. Jiang, C., Hu, Z., Liu, Y., Mourelatos, Z.P., Gorsich, D., Jayakumar, P.: A sequential calibration and validation framework for model uncertainty quantification and reduction. Comput. Methods Appl. Mech. Eng. **368**, 113172 (2020)

Fusion of Test and Analysis: Artemis I Booster to Mobile Launcher Interface Validation

Joel W. Sills, Arya Majed, and Edwin E. Henkel

Abstract The National Aeronautics and Space Administration (NASA) is in the midst of bold and exciting next steps in human exploration and spaceflight. The designs of the new Space Launch System (SLS), the Orion spacecraft, and the Exploration Ground Systems (EGS) for vehicle processing and launch are essentially complete, and there has been significant progress in the manufacturing and assembly of specific hardware for the Artemis I and Artemis II missions. Equally as important, the program level and integrated system-level testing and analyses are also well underway to support integrated verification, validation, and Certificate of Flight Readiness (CoFR) for Artemis I. Testing and analysis are key to addressing technical challenges faced by the Artemis missions. Building block approaches are required that provide the right balance between component, element, and/or system-level testing that satisfies verification and validation objectives where uncertainties are quantified and minimized. Artemis I is a system of systems that requires a fusion of test and analysis that adeptly characterizes critical interfaces between major program elements. An example of this fusion involves characterizing the interface between the SLS booster and the Mobile Launcher (ML) Vertical Support Post (VSP) interfaces. Proper characterization of this interface represents a number of challenges, beginning with the fact that it is a mating of ground support structure in the form of a civil structure to flight hardware. Both sides of the interface are built to different construction standards but are governed by interface requirements to ensure compatibility when mated. From past program experience, the flexibility at the booster to the ML interface is critical in developing accurate prelaunch stacking and cryogenic preloads, squat loads, and pad separation release of preloads and squat loads. This same premise holds for Artemis I. To describe the asymmetric characteristics at this interface, careful consideration of static forces due to gravity loading with the commensurate effects resulting from ML VSP leveling, spacing, and shimming during booster stacking and associated geometric nonlinear forces due to booster lateral displacements are necessary for inclusion in pretest assessments. This paper will look at these issues for the upcoming booster pull test, in which two boosters will be installed on the ML and one of these boosters will undergo static lateral loading, followed afterward by dynamic excitation into resonance and free decay. This paper evaluates the booster to the ML interface by characterizing the flexibility between the booster aft skirt and the ML VSP. Furthermore, this paper methodically evaluates the effect of the following on the test outcome: gravitational effects on the booster and ML; the effects of VSP leveling, spacing, and shimming under gravitational loading during booster stacking; the effect of geometric nonlinear follower force due to center of gravity (CG) offset as the booster is laterally displaced; and the system coupling between the booster under test, ML, and the second booster. Simulated results for a static load pull and dynamic excitation provide insight into the differences in prediction vs measured response with and without the inclusion of the abovementioned boundary condition and geometric nonlinear effects.

Keywords Artemis · Booster · Booster pull · Building block approach · Certificate of Flight Readiness · Exploration Ground Systems · Free decay · Interface flexibility · Mobile Launcher · Gravitational effects · Geometric nonlinear forces · Orion · Space Launch System · Static loading · Vehicle Support Post · Verification and validation

J. W. Sills (✉)
NASA Johnson Space Center, Houston, TX, USA

A. Majed · E. E. Henkel
Applied Structural Dynamics, Houston, TX, USA

Z. Mao (ed.), *Model Validation and Uncertainty Quantification, Volume 3*, Conference Proceedings of the Society for Experimental Mechanics Series, https://doi.org/10.1007/978-3-030-77348-9_3

1 Introduction

The booster pull test discussed herein evolved from a continuous reevaluation of the Artemis I dynamic building block test program. The original building block included a partial stack modal test (PSMT) that included the booster systems and the SLS core stage (CS); however, that test was removed from consideration. The PSMT served as a precursor to the integrated modal test (IMT), which sought to gather system response data of the integrated SLS system mounted to the ML at eight VSPs. With the removal of the PSMT, it was still recognized that characterization of the booster to the ML interface was critical to informing the analytical models. This realization gave rise to the booster pull test to provide needed information prior to the IMT. The IMT represents a convergence of civil structure, in the form of the ML, and aerospace structure, in the form of the SLS system, with the ML serving as the test fixture for the IMT. This system of system tests represents a new paradigm in testing and departs from the more traditional modal testing where you minimize any interactions between the test fixture and the article under test.

For this effort, a smart dynamic test approach to testing is required. The following definition formulated by Dr. David Ewins and Dr. Michael Hale states that a smart dynamic test is one that utilizes analytical models to take full account of the influence of fixtures and vibration generation devices on the dynamic response of the test structure to ensure that in-service dynamic conditions are accurately replicated in a controlled laboratory setting. Given that this testing involves flight hardware and comes late in the ground system flow, a methodical process that embraces the smart dynamic test definition provides the basis for determining the amount of success one will have in understanding the dynamic characteristics of the system. To that end, the process pursued first seeks to characterize the interface flexibility between the booster aft skirt and the ML VSP. This is critical to understanding the influence of each side of the interface on the coupled system. The next steps are to methodically evaluate the effect of the following on the test outcome: (1) the effects of gravity (1-g) acting on both the booster and ML and (2) the effects that booster stacking has on the system. Each booster is comprised of multiple segments, and these segments are assembled onto the ML with the need for level, space, and shim to meet tolerance requirements. These effects are captured using a Deformed Geometry Synthesis (DGS) approach [1, 2]. DGS determines induced preloads by modeling components in their deformed geometry states and then enforcing compatibility by closing the resulting "deadbands." The next step is to determine the geometric nonlinear follower force effects resulting from CG offset as the booster is pulled to a maximum load. Further, system coupling between the booster under test, ML, and the second booster is explored when subjected to dynamic transient inputs. Lastly, an assessment is made of the sufficiency of test measurements to correlate finite element models (FEMs) for the booster aft skirt, VSPs, and ML haunches, as well as a determination of the booster cantilever bending mode.

2 Booster Pull Test Overview

The main objective of the booster pull test is to obtain lateral deflections (i.e., displacements) in two orthogonal directions. This will be accomplished by applying applied loads near the top of the booster and recording deflection data at five separate distributed locations along the length of the booster. Figure 1 provides an illustration of the test configuration, along with a definition of ML VSP locations. The rationale for collecting data in two orthogonal directions is that the interface between the booster and the ML is asymmetric. As a result of this geometric feature, one has a strong axis and a weak axis to measure coupling stiffness. An attempt will also be made to record strain from strain gauges located on each VSP. Figure 2 shows the location of the strain gauges for each VSP. Seven separate loads in increasing load amplitude up to 15,000 lbs (i.e., 15 kip) will be applied by pulling at the lowest level first and incrementing to each subsequent higher pull load until reaching the highest pull load, pausing for at least 30 seconds at each pull level to capture a steady-state measurement. Upon reaching the highest pull load, the pull schedule will be executed in reverse order. The schedule will be completed three times for both Y-direction and Z-direction pull configurations.

The ML underwent a modal survey inside the Vehicle Assembly Building (VAB), which was completed on June 27, 2019 [4, 5]. This test did not include any provision for mass loading the ML VSP interfaces. As a result, this critical interface requires further verification and validation. Test data obtained during the booster pull test will be used to validate the stiffness of the ML haunch, VSP, and booster aft skirt region of the stacked ML/SLS system. Dynamic models will be updated as required based on the findings. The testing objectives also include a booster push test, which is synonymous with a sine dwell test, followed by a free decay. The intent of this test is to characterize the booster cantilever bending mode and obtain 10 minutes of frequency and damping data from the decay on the booster.

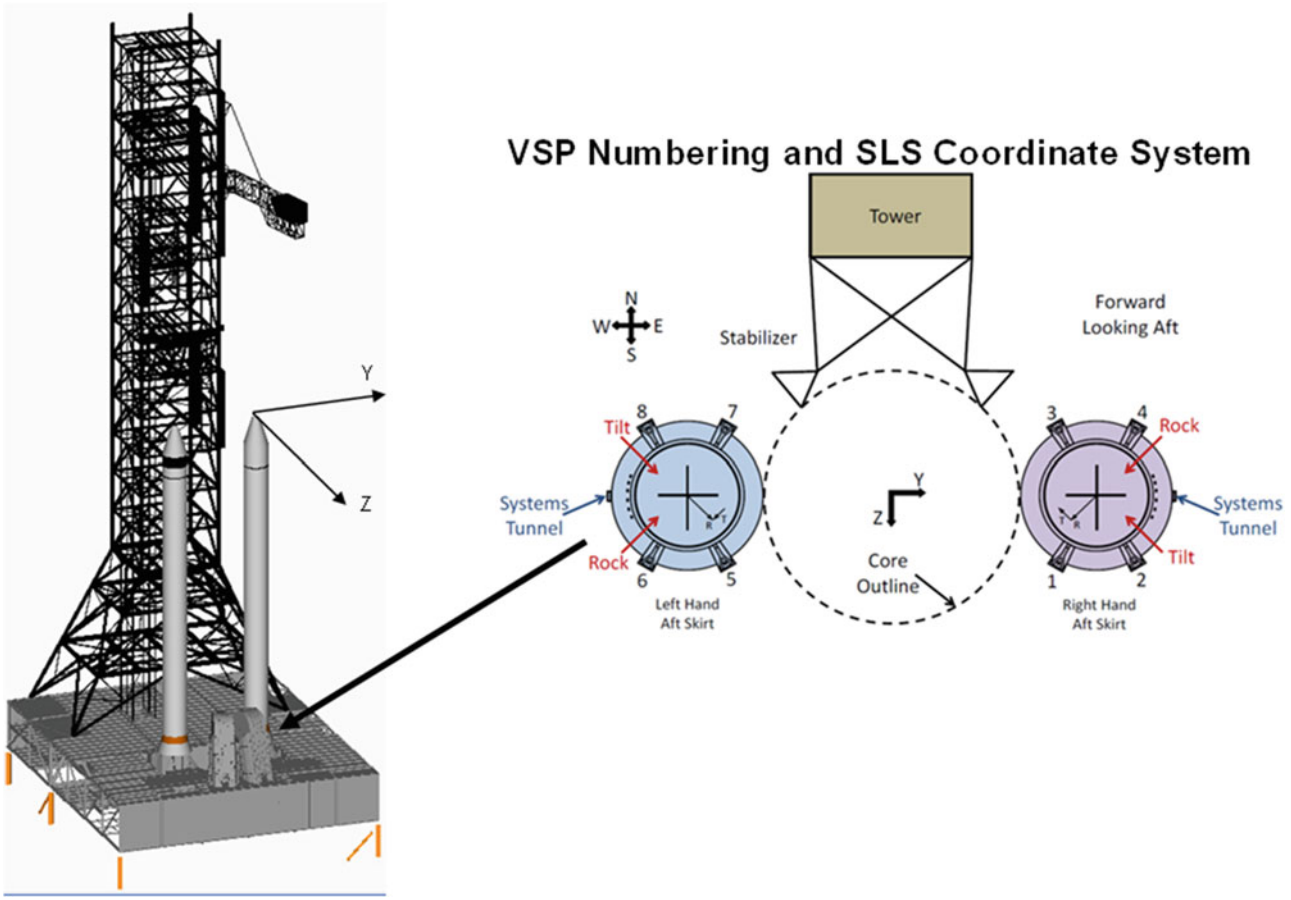

Fig. 1 Booster pull test setup and ML VSP definition

3 Historical Perspective

A booster pull test is not a new test or idea as there have been many instances of booster testing used to validate the fundamental bending modes. For NASA, a similar test occurred in 1979 [3] using an inert booster mounted to the Shuttle-era Mobile Launcher Platform (MLP). The necessity for this test was driven by concerns regarding Shuttle umbilical capabilities. The objectives for this test were to measure stiffness and determine the frequency of the first pitch-bending mode of the combined booster and MLP. In this test, five different loads up to 10,000 lbs were applied in one lateral direction only to capture data. The instrumentation used to capture the data included accelerometers, optical measurements, and potentiometers. These are shown in Fig. 3.

Results from this proved to be important as it indicated that the actual hardware was on the order 10% stiffer than the FEM predictions. Posttest, it was determined that for this case, the cantilevered mode structural stiffness characteristics were more sensitive to the booster stiffness rather than the MLP stiffness.

Fast-forwarding to the Constellation program and starting with the vintage of the Ares I Reusable Solid Rocket Motor (RSRMV) finite element model (FEM), a decision was made to use the Shuttle vintage aft skirt model. This aft skirt best matched the stiffness data obtained from the 1979 Step-Relaxation Test performed on the booster/MLP assembly. The SLS aft skirt is directly derived from the Ares I RSRMV aft skirt.

4 Understanding Booster AFT Skirt to ML VSP Interface Flexibility

Since the past serves as a great mentor and teacher, the first step into understanding the envisioned test is to determine if the findings from the 1979 testing still hold. Sensitivity analyses serve to inform what flexibility exists between the ML side of

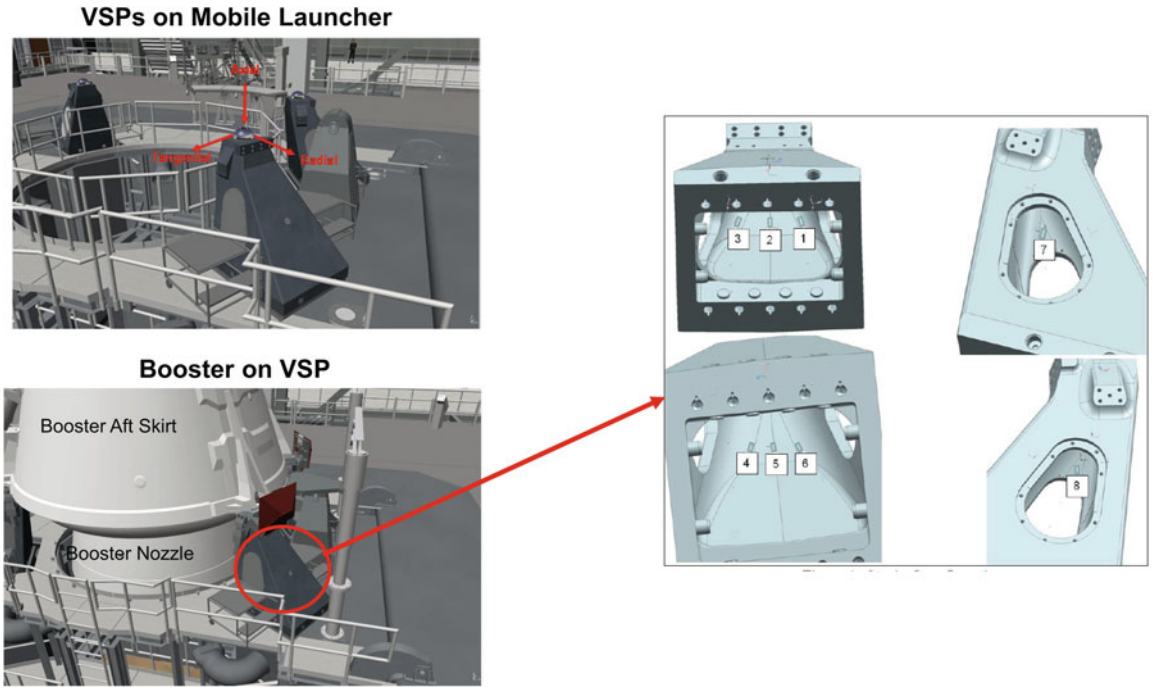

Fig. 2 Location of VSPs on ML and relative to the booster and location of strain gauges

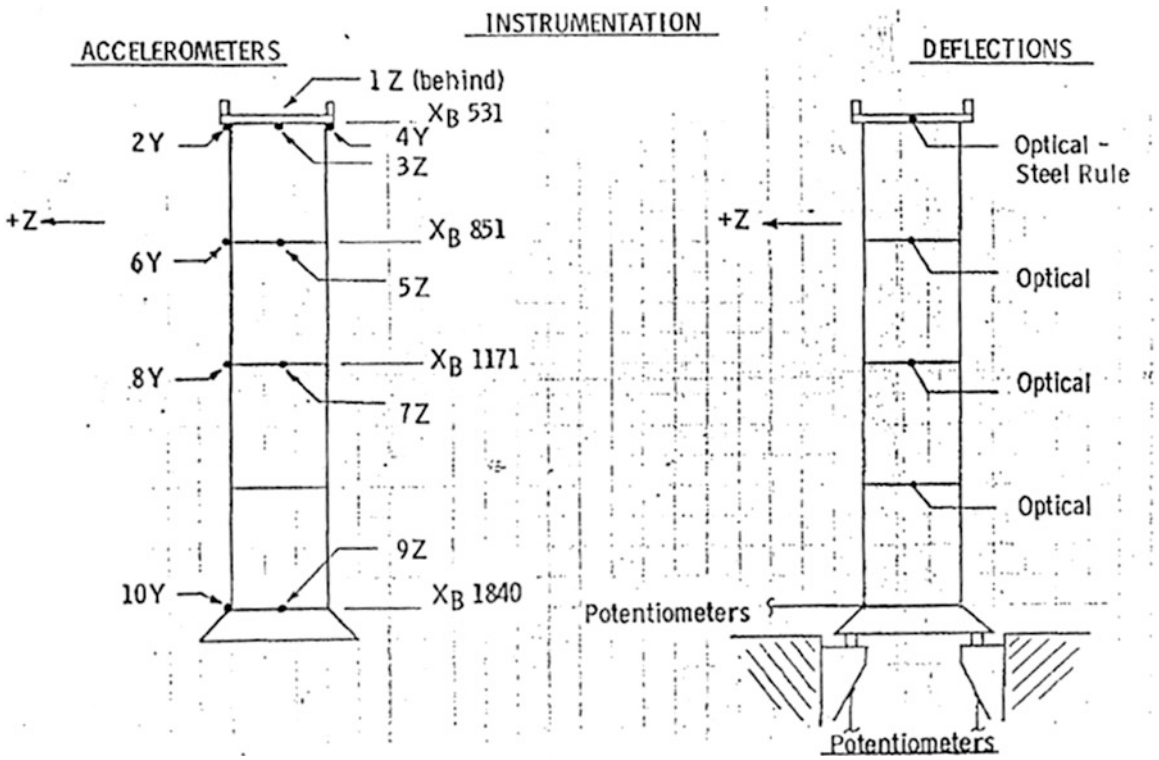

Fig. 3 Circa 1979 Booster Pull Test Instrumentation Suite

the interfaces and the booster aft skirts. For this effort, one extracts the VSP flexibility matrix with a size of 24 × 24 (e.g., eight VSP locations × 3 translational degrees of freedom (DoFs) per location) using the ML VSP numbering (see Fig.~1). Each flexibility matrix column (i) is a displacement vector, corresponding to DoFs 1 through 24, due to the unit force acting at DoF (i). All calculations are relative to the ground supports upholding the ML. An excerpt of the full matrix for the right-

	1X	1Y	1Z	1RX	1RY	1RZ	2X	2Y	2Z	2RX	2RY	2RZ
1X	-245.05%	13930.55%	-1469.56%	1843.57%	2483.40%	7128.98%	248.81%	2141.09%	1709.29%	-57908.35%	-2295.66%	-9620.91%
1Y	13930.55%	-224.27%	11891.38%	6.01%	-2874.36%	977.57%	-3972.16%	-279.41%	13523.91%	436.13%	-34169.13%	10278.68%
1Z	-1469.56%	11891.38%	-322.46%	424.82%	1059.33%	-2942.02%	1479.88%	-2446.51%	214.60%	-10591.55%	-2077.51%	29144.56%
1RX	1843.57%	6.01%	424.82%	-1130.03%	-2961.60%	-3269.43%	156677.11%	433.58%	-9065.71%	43589.37%	-191300.68%	-169949.89%
1RY	2483.40%	-2874.36%	1059.33%	-2961.60%	-864.98%	63493.25%	-2161.41%	28699.79%	-1949.31%	85107.84%	8699.77%	-272595.18%
1RZ	7128.98%	977.57%	-2942.02%	-3269.43%	63493.25%	-656.50%	-18108.86%	10502.65%	-37416.20%	-303483.63%	59940.91%	-17329.36%
2X	248.81%	-3972.16%	1479.88%	156677.11%	-2161.41%	-18108.86%	-252.82%	-2085.42%	-1442.71%	1552.29%	2443.17%	5884.50%
2Y	2141.09%	-279.41%	-2446.51%	433.58%	28699.79%	10502.65%	-2085.42%	-223.25%	2502.61%	3.85%	-2573.20%	975.41%
2Z	1709.29%	13523.91%	214.60%	-9065.71%	-1949.31%	-37416.20%	-1442.71%	2502.61%	-318.42%	310.76%	1060.88%	-2607.87%
2RX	-57908.35%	436.13%	-10591.55%	43589.37%	85107.84%	-303483.63%	1552.29%	3.85%	310.76%	-1127.43%	-3029.08%	-3284.82%
2RY	-2295.66%	-34169.13%	-2077.51%	-191300.68%	8699.77%	59940.91%	2443.17%	-2573.20%	1060.88%	-3029.08%	-859.33%	38859.44%
2RZ	-9620.91%	10278.68%	29144.56%	-169949.89%	-272595.18%	-17329.36%	5884.50%	975.41%	-2607.87%	-3284.82%	38859.44%	-658.53%

Fig. 4 Excerpt of booster aft skirt to ML VSP interface flexibilities ratios

	1X	1Y	1Z	1RX	1RY	1RZ	2X	2Y	2Z	2RX	2RY
1X	-11.79%	-12.10%	-12.23%	-13.71%	-10.00%	-10.05%	-9.77%	-11.76%	-13.07%	-11.41%	-13.75%
1Y	-12.10%	-10.85%	-13.42%	52.35%	-11.24%	-6.48%	-11.00%	-11.32%	-12.14%	31.17%	-12.31%
1Z	-12.23%	-13.42%	-12.34%	215.71%	-8.99%	-11.44%	-13.79%	-12.82%	-18.84%	-10.97%	-26.54%
1RX	-13.71%	52.35%	215.71%	-18.23%	-19.67%	-20.17%	-12.36%	29.64%	-11.84%	-13.11%	-10.58%
1RY	-10.00%	-11.24%	-8.99%	-19.67%	-4.85%	-3.51%	-11.74%	-14.08%	-20.06%	-10.87%	-12.39%
1RZ	-10.05%	-6.48%	-11.44%	-20.17%	-3.51%	-5.86%	-10.54%	-13.43%	-12.14%	-10.98%	-10.02%
2X	-9.77%	-11.00%	-13.79%	-12.36%	-11.74%	-10.54%	-11.13%	-11.54%	-11.87%	-40.82%	-8.83%
2Y	-11.76%	-11.32%	-12.82%	29.64%	-14.08%	-13.43%	-11.54%	-10.79%	-12.98%	50.14%	-10.24%
2Z	-13.07%	-12.14%	-18.84%	-11.84%	-20.06%	-12.14%	-11.87%	-12.98%	-12.29%	133.50%	-8.48%
2RX	-11.41%	31.17%	-10.97%	-13.11%	-10.87%	-10.98%	-40.82%	50.14%	133.50%	-18.00%	-15.52%
2RY	-13.75%	-12.31%	-26.54%	-10.58%	-12.39%	-10.02%	-8.83%	-10.24%	-8.48%	-15.52%	-4.08%
2RZ	-11.28%	-13.17%	-12.95%	-11.97%	-11.29%	-11.11%	-9.50%	-6.43%	-11.02%	-21.04%	-3.21%

Fig. 5 Excerpt of booster aft skirt interface flexibilities due to aft skirt element promotion

hand booster is shown in Fig. 4. What is shown in Fig. 4 is the ratio of booster aft skirt to ML VSP interface flexibilities with negative values indicating that the aft skirt side stiffness is less than the ML interface stiffness at the VSP interface. This exercise is confirming of the conclusions from the 1979 testing. This is an important result as it indicates that an accurate capture of aft skirt flexibilities during the pull test is critical to updating the booster aft skirt region of the stacked ML/SLS system. This in turn is important as this interface has an impact on stacking preloads and SLS/ML liftoff separation.

Further sensitivity studies pursued an examination of the aft skirt modeling to understand the local stiffness effects. It is well known that the booster/VSP interface flexibilities derive primarily from the membrane action of plate elements. The aft skirt model consists of NASTRAN CQUAD4 elements that have been correlated to test data. Upon closer inspection, the aft skirt mesh appears too coarse for accurate interface flexibility finite element method (FEM) predictions. CQUAD4 membrane stiffness derives from linear displacement field approximation (i.e., constant strain). To determine the element member membrane displacement field sensitivity, the CQUAD4 elements were promoted to CQUAD8 elements. This has the effect of promoting the plate element membrane displacement fields from linear to parabolic. A comparison of the booster aft skirt VSP flexibilities between the CQUAD4 and CQUAD8 modeling is shown in Fig. 5. Note that Fig. 5 is an excerpt similar to Fig. 4 and shows two of the VSP flexibility results. The conclusion from this exercise is that the booster aft skirt interface flexibilities show considerable sensitivity to modeled membrane displacement field approximation.

5 Understanding Booster to ML Coupling

As we begin to understand the boundary conditions and the stiffness relationship between the booster and the ML, we turn next to understanding the interactions between the two structures when coupled together. To start this process, the boosters are coupled to the ML in the exact physical manner in which they are stacked for flight. To facilitate this exercise, the Deformed Geometry Synthesis (DGS) technique [2] is invoked. The DGS is a specialized procedure in modal synthesis where components are coupled in their deformed geometry states by enforcing compatibility at the interfaces using a process that

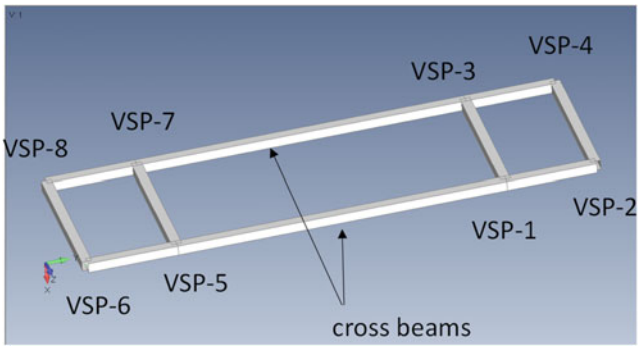

Fig. 6 IATT FEM

Table 1 ML/IATT interface forces with no VSP leveling and spacing

VSP	RIATT	VSP	LIATT
1	−2057.90	5	−1721.09
	34398.98		−31673.17
	93583.70		94989.98
2	2001.02	6	1777.96
	71295.62		−70116.92
	95796.21		96480.91
3	−204.11	7	−875.44
	11223.19		−12856.48
	−96251.65		−94423.23
4	320.13	8	759.42
	58189.01		−60460.21
	−92504.41		−97671.52
All forces in lbs	SUM	X	0.00
		Y	0.00
		Z	0.00

quasi-statically closes the resulting deadbands to lock in the preloads. The DGS allows a closer inspection of the effects due to the gravitational effects on the booster and ML and the effects of VSP leveling, spacing, and shimming under gravitational loading during booster stacking. This in turn provides necessary insight into how each of these effects contributes to the expected test outcome.

As a first step, an Interface Alignment Testing Tool (IATT) FEM (Fig. 6) verified the VSP leveling and spacing processes using DGS. The IATT is a stiff beam structure that is built to the undeformed geometry (i.e., zero G) of the VSPs with two crossbeams for checking the leveling and spacing between the starboard (i.e., right) and port (i.e., left) sides. Coupling the IATT to the ML and turning on the gravity (i.e., 1G) on the ML will only result in a set of redundant interface forces between the two structures. If the ML VSPs are leveled and spaced under 1G, then no interface forces should be reacted between the ML and IATT. To illustrate this verification, one computes the ML/IATT interface forces at the eight VSPs with no leveling and spacing in 1G deformed geometry. Table 1 shows that with no VSP leveling and shimming, large redundant forces are reacted at each VSP and the VSP loads sum to zero in each direction. Next, one computes the ML/IATT interface forces at the eight VSPs with leveling and spacing in 1G deformed geometry. Table 2 contains the results, and one observes that with VSP leveling and shimming, the ML/IATT interface forces are numerical zeros. This verifies the DGS numerical implementation for VSP leveling and spacing.

As the boosters are stacked on the ML, they undergo leveling and spacing updates to assure that the boosters are in the proper orientation and location on the ML and for Core Stage mating. Table 3 shows the VSP interface forces as a percentage of overall weight when VSP leveling and spacing is or is not considered. Table 3 further delineates the individual difference in interface force at each VSP interface degree of freedom when VSP leveling and spacing is or is not considered. Negative values indicate an increase in load due to VSP leveling and spacing. Differences range as much as 14%, which is not insignificant.

A similar exercise looked at the effects of shimming (X shim) in the booster longitudinal direction. Shimming is a pitch and yaw procedure, much like leveling and spacing, to allow for correct positioning to mate the boosters with the Core Stage. It is intended to be a small rigid body rotation shimming and does not introduce any additional inertial loads. It is done

Table 2 ML/IATT interface forces with VSP leveling and spacing

VSP	RIATT	VSP	LIATT
1	−1.1401E-05	5	$8.4913E-06$
	6.7847E-04		$9.5027E-05$
	9.4231E-05		$6.3166E-05$
2	8.3728E-06	6	$-5.4628E-06$
	−3.9222E-04		$-3.9177E-04$
	9.9758E-05		$4.5312E-05$
3	1.0383E-05	7	$-1.2757E-05$
	−1.0396E-03		$2.9178E-04$
	−8.9273E-05		$-4.9359E-05$
4	−6.7802E-06	8	$9.1548E-06$
	1.3865E-03		$-6.2816E-04$
	−1.0949E-04		$-5.4346E-05$
All forces in lbs	SUM	X	$9.0000E-10$
		Y	$2.7000E-08$
		Z	$-1.0000E-09$

in a way not to introduce any redundant loading as well. Thus, there should be no change to the interface forces from this process, and this was confirmed. However, one does expect small changes in displacement along the length of the booster as a result of shimming. Figure 7 shows displacement plots for both boosters in the two lateral directions with and without the shims. As expected, one sees changes in displacement with increasing delta displacement as one moves up to the top of the booster. The displacements in Fig. 7 include 1G acting on the ML, 1G acting on the boosters, ML VSP leveling and spacing, and ML VSP X-shim effects. The orange dots along the abscissa provide an approximate spatial reference for where planned displacement measurements will be made during the pull tests.

The next exercise evaluated the effects of the center of gravity (CG) offset due to the lateral pull. Figure 8 illustrates the effect of when the CG offset, a geometric nonlinear effect that increases the lateral displacements and overturning moments at the booster base, is considered. The data shown in Fig. 8 constitute the "initial deformed state" of the system prior to pull loads. The actual pull test will measure delta strains and displacements from this initial deformed geometry state.

From an evaluation of these exercises, it is clear that the 1G acting on the ML, the 1G acting on the boosters, ML VSP leveling and spacing, ML VSP X-shim effects, and CG offset effects must be considered in preparing for the booster pull test and subsequent dynamic test. If they are casually dismissed, the chances of a successful test and subsequent model updating effort diminish.

6 Simulating the Booster Pull Test

As discussed in the booster pull test overview, an applied load of 15,000 lbs will be applied at the top of the booster in the two lateral directions. For the purpose of this paper, the maximum load application and the resulting observation are discussed. Loads are applied to the right-hand side booster (Fig. 1) in the $+Y$ and $+Z$ directions. It is noted that the geometric nonlinear CG offset effects caused by the lateral pull increase the ML/booster aft skirt VSP loads by 7–10%. Booster tip displacements are increased by 10–15% (Fig. 9). The static nonlinear analysis in Fig. 9 includes 1G on the ML, 1G on the boosters, ML VSP leveling and spacing, ML VSP X-shims (toe-in), and lateral pull loads. Results are shown with and without CG offset effects. The encircled areas indicate increased flexibility in the booster aft skirt region.

The encircled areas in Fig. 9 show where the stiffness begins to change, indicating increased flexibility in the booster in this area and then changes again in the aft skirt range. This indicates multiple stiffness changes along the booster length.

7 Booster Dynamic Excitation

The booster testing provides an interesting challenge as each booster is coupled individually to four VSPs separated by a distance apart. As already noted in this paper, the ML interface is stiffer than the booster aft skirt based on analytical data and anecdotal data from 1979. To further understand if one can ideally separate one booster from another in a dynamic test,

Table 3 Effect of VSP leveling and spacing on ML/booster interface forces (IFFs)

No VSP leveling/spacing			
VSP	Right booster	VSP	Left booster
1	11.97%	5	12.25%
	−1.68%		1.75%
	4.96%		5.06%
2	1305%	6	12.78%
	1.93%		−1.87%
	5.43%		5.31%
3	13.02%	7	12.75%
	−1.96%		1.89%
	−5.40%		−5.27%
4	11.96%	8	12.23%
	1.70%		−1.77%
	−4.98%		−5.10%

Sum	X	100%
	Y	0%
	Z	0%

With VSP leveling/spacing			
VSP	Right booster	VSP	Left booster
1	12.19%	5	12.32%
	−1.19%	1.95%	
	4.61%	4.66%	
2	12.83%	6	12.70%
	2.07%	−2.04%	
	4.94%	4.88%	
3	12.81%	7	12.67%
	−2.07%	2.04%	
	−4.88%	−4.80%	
4	12.17%	8	12.31%
	1.91%	−1.95%	
	−4.68%	−4.73%	

SUM	X	100%
	Y	0%
	Z	0%

Difference			
VSP	R_Booster	VSP	L_Booster
1	−1.77%	5	−0.64%
	−14.11%	−11.50%	
	7.06%	8.05%	
2	1.62%	6	0.61%
	−6.98%	−8.95%	
	8.88%	8.13%	
3	1.63%	7	0.61%
	−5.70%	−7.65%	
	9.73%	8.85%	
4	−1.77%	8	−0.64%
	−12.53%	−10.08%	
	6.14%	7.30%	

analyses were performed to evaluate the coupling effects. The plan for the actual test is to push on the booster to excite the first cantilevered mode in each lateral direction. For analysis purposes and this study, the booster was displaced at 4 inches in each of the lateral directions and displacements measured along the length of the booster. The displacement magnitude is arbitrary and is sufficient enough to excite the first bending mode of the booster. Figure 10 shows the results from the *Z*-direction displacement. Displacements include 1G acting on the ML, 1G acting on the boosters, ML VSP leveling and spacing, ML

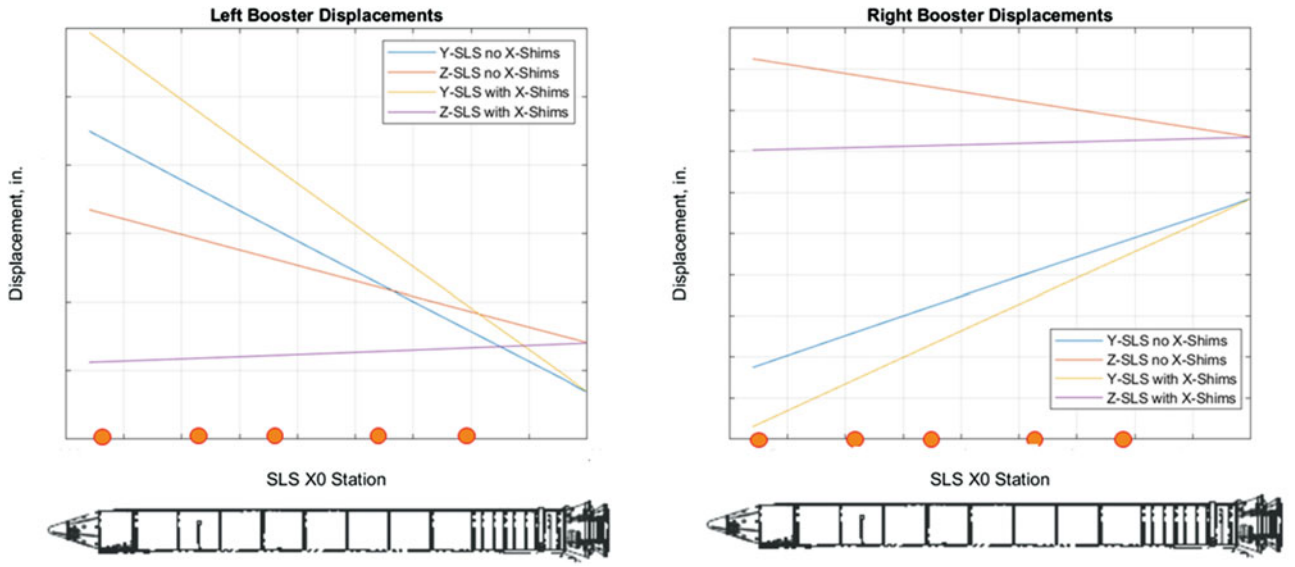

Fig. 7 Effect of VSP X-shims on booster displacements

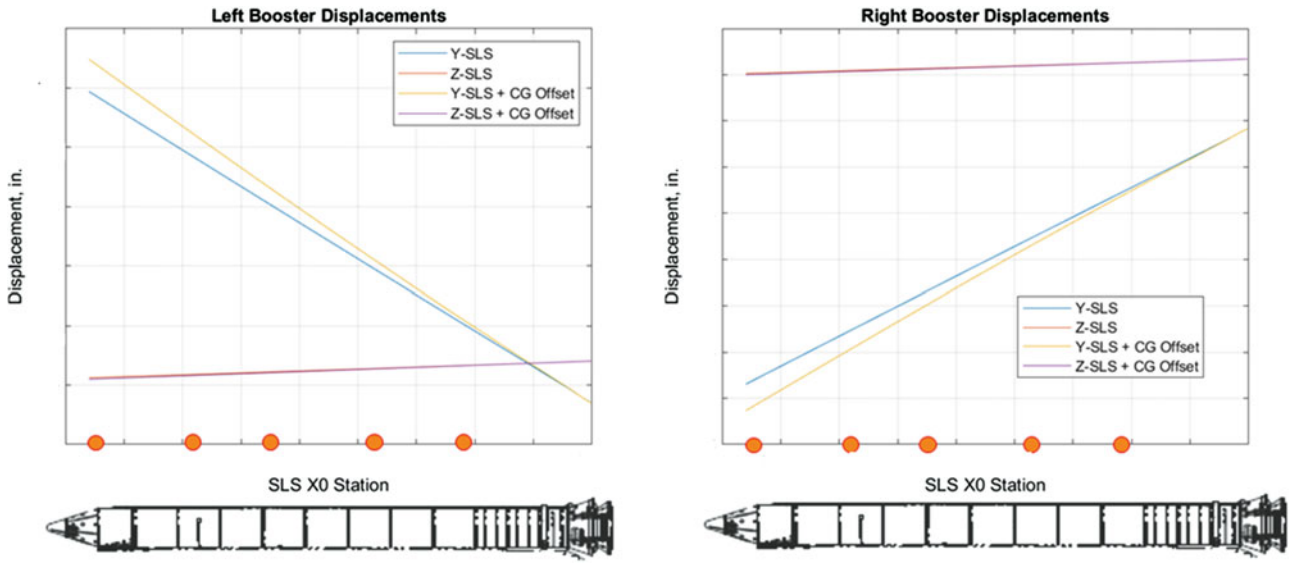

Fig. 8 Effect of CG offset on booster displacements

VSP X-shim effects, 1G offset, and lateral enforced displacement. The results show that the left booster responds out of phase as the right-hand booster responds. While the first inclination is to classify the response as a beat frequency, the response is more indicative of a sympathetic vibration. A sympathetic vibration is a harmonic phenomenon wherein a formerly passive vibratory body (in this case the left booster) responds to external vibrations to which it has a harmonic likeness. The motion is transferred through the ML base through the VSP/haunches from one body to the next. This result clearly illustrates that one cannot treat an individual booster as a singular entity and highlights the need to instrument the left booster to monitor its response.

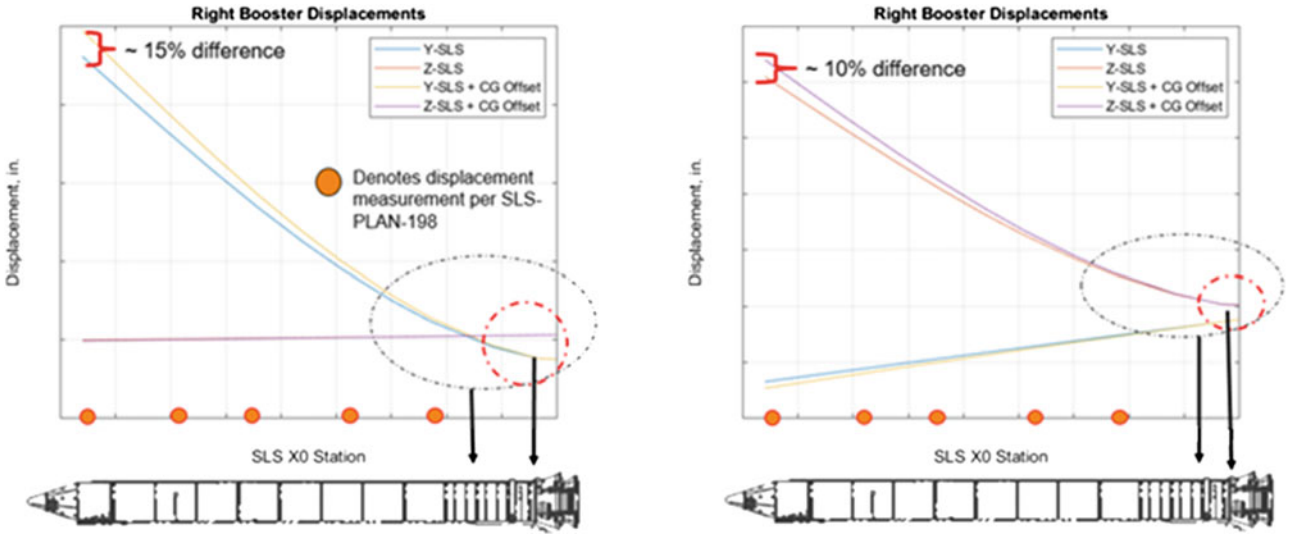

Fig. 9 Booster displacements under a 15-kip load

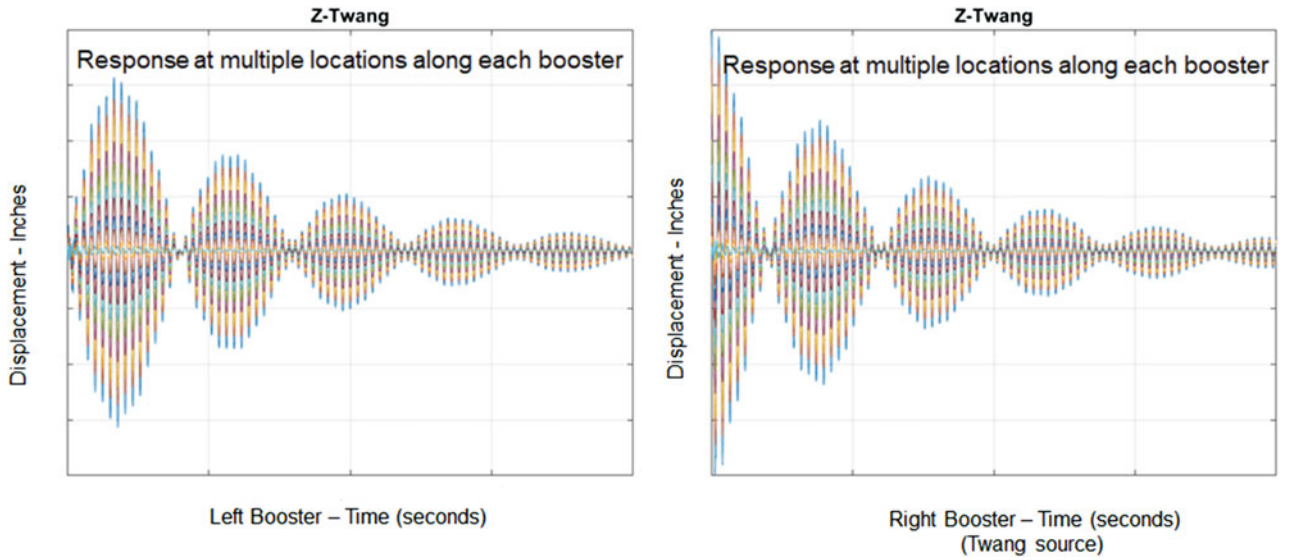

Fig. 10 Booster displacement results from a 4-inch+ Z-SLS twang on right booster

Looking at the *Y*-direction excitation displacements due to the same magnitude input, one sees a very different response. This is due in part to the differences in the symmetry between axes at the ML VSP to the booster aft skirt interface. Figure 11 shows the results from the *Y*-direction displacement. Displacements include 1G acting on the ML, 1G acting on the boosters, ML VSP leveling and spacing, ML VSP X-shim effects, 1G offset, and lateral enforced displacement. Each time history vibrates about its respective "X-shim + CG off-set" datum and will eventually settle at that value with simulation carried for a longer duration. It is interesting to note how the left booster responds as the right-hand booster response decays in Fig. 11. This result, while different from the Z-axis response, clearly illustrates that one cannot treat an individual booster as a singular entity and highlights the need to instrument the left booster to monitor its response.

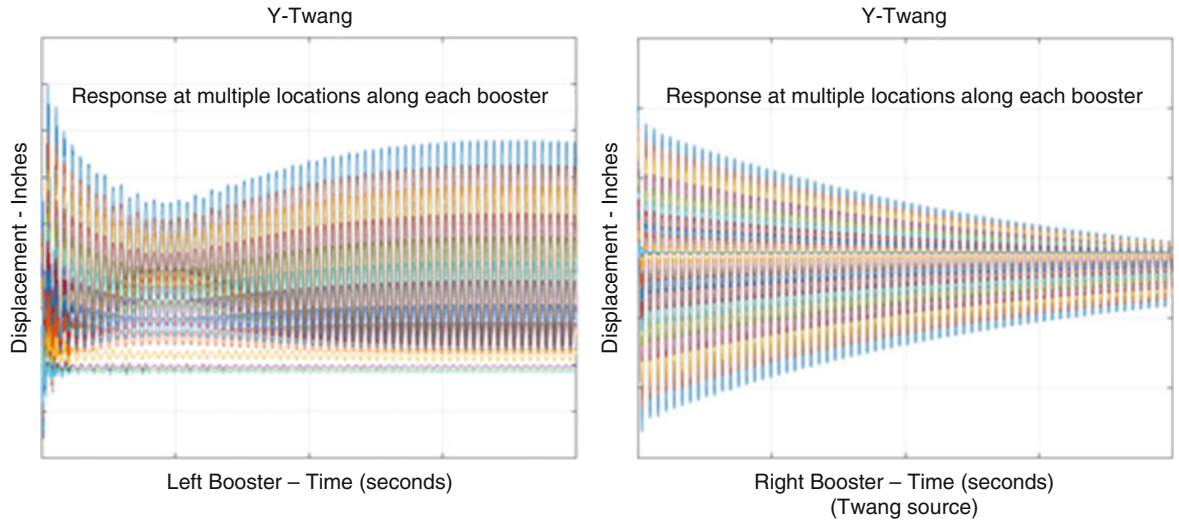

Fig. 11 Booster displacement results from a 4-inch+ Y-SLS twang on right booster

8 Conclusion

The subject pretest analysis demonstrates that accurate capture of the booster aft skirt flexibilities is critical to updating the booster FEM aft skirt region of the stacked ML/SLS system. This is in lieu of the fact that it is shown that the ML/VSP interface stiffness is significantly greater than the booster/VSP interface stiffness in accordance with the latest generation of models. Furthermore, the coupled ML/booster FEM centerline displacements clearly show an increased curvature as the booster aft skirt region is approached. In fact, accurate modeling of the booster aft skirt determines that these interface flexibility coefficients have a strong influence on stacking/cryogenic preloads, booster squat loads, and the release of strain energy in the SLS pad separation, commonly known as liftoff "twang." It was also found that the geometric nonlinear CG offset effects as the booster is pulled laterally to the maximum load must be included in the simulations to properly establish testing requirements. Errors in the interface forces can be between 7% and 10% and tip displacements 10% and 15% if these CG offset forces are not considered. It was also found that the dynamic excitation of a single booster results in sympathetic vibrations of the other booster since the two boosters that are attached to the ML haunches form a coupled dynamic system and cannot be handled as decoupled components.

Several recommendations that flow from this work consist of (1) considering additional instrumentation to capture booster aft skirt flexibility, booster/VSP interface flexibility, and the displacements of both boosters and the ML tower; (2) including the geometric nonlinear CG offset forces in pretest and posttest correlations; and (3) utilizing the initial booster deformed geometry (i.e., displacements, including the 1G on ML and boosters, ML VSP leveling and spacing, ML VSP X-shims (toe-in), and 1G offset geometric nonlinear forces) as the reference configuration for pretest, test execution, and posttest analyses. This requires obtaining displacement measurements of the boosters after stacking is complete and before the test starts to establish the initial deformed geometry state.

In closing, this study is very much aligned with the smart dynamic test philosophy by implementing analytical models to take full account of the influence of fixtures (i.e., the Mobile Launcher in this case) and vibration generation devices on the dynamic response of the test structure to ensure that in-service dynamic conditions are accurately replicated in a controlled laboratory setting. Given that this testing involves flight hardware and comes late in the ground system flow, this case study provides a methodical process that embraces the smart dynamic test definition and provides a basis for determining the amount of success one will have in understanding the dynamic characteristics of the system.

References

1. Sills, J., Majed, A., Henkel, E.: Independent verification of SLS block 1 pre-launch, liftoff, and ascent gust methodology and loads, Part 1: prelaunch stacking analysis, NASA TM-2018-220073, NESC-RP-16-01128, 1 Mar 2018
2. Sills, J., Majed, A., Henkel, E.: A deformed geometry synthesis technique for determining stacking and cryogenically induced preloads for the space launch system. In: Proceedings of the 38th International Modal Analysis Conference, February 2019
3. Deyulia, J.F.: Step-relaxation ("Twang") test of SRB/MLP, Rockwell International Memorandum SSP-204-79-036, 18 April 1979
4. Akers, J.; Sills, J.: Space launch system mobile launcher modal pretest analysis. In: Proceedings of the 39th International Modal Analysis Conference, 2020
5. Stasiunas, E., Parks, R., Sontag, B., Chandler, D.: Modal test of the NASA mobile launcher at Kennedy Space Center. In: Proceedings of the 39th International Modal Analysis Conference, 2020

Quantifying the Benefits of Structural Health Monitoring Using Value of Information and Decision Risk Modeling

Mayank Chadha, Zhen Hu, and Michael D. Todd

Abstract The primary objective of the structural health monitoring (SHM) system is to continuously oversee and assess the state of the structure and evaluate its integrity at any time based on the appropriate analysis of in situ measured data. Therefore, among other things, an SHM system is an information-gathering mechanism. Gathering the information that is representative of the structural state and correctly analyzing the data help us better understand the state of the structure and mitigate possible losses by taking appropriate actions. However, the design, installation, maintenance, research, and development of an SHM system is an expensive endeavor. Therefore, agreeing to pay for new information is rationally justified if the reduction in the expected losses by new information is more than the intrinsic cost of the information-acquiring mechanism. We investigate the economic advantage of installing an SHM system for damage detection as well as risk and life-cycle management by using the value of information analysis. Among many possible choices of SHM system designs, preposterior decision analysis can be used to pick the most feasible design that can be installed on the structure. We demonstrate the framework on a miter gate application.

Keywords Value of information · Decision theory · Structural health monitoring · Uncertainty quantification · Miter gate

1 Introduction

As is the case with an experiment, a structural health monitoring (SHM) system is an information-gathering mechanism. The design, installation, maintenance, and operation of an information-gathering system (like an SHM system) are economically expensive. Therefore, it is reasonable to question the value of the acquired information in terms of the monetary benefits it yields as a consequence of decision-making (like performing maintenance) over the lifespan of the structure. Along the lines of the discussion by Howard [1], the SHM system is desirable only if the benefit obtained using the acquired information outweighs the cost of installing the SHM system. Hence, the value of SHM essentially depends on its design. In this paper, we briefly lay the theoretical framework to evaluate the value of information (VoI) (refer to [2, 3]) for decision-making at a given time instance.

The miter gate structure with a strain gauge network is considered as a demonstration case where the degree of damage is defined by the continuous state parameter, i.e., the gap length of the miter gate, quantifying the gap degradation [4]. The gap degradation is defined by a large loss of contact between the gate and the wall quoin block. To evaluate the VoI, we first discuss the decision-making framework. Finally, we present a VoI-focused application example for selecting an appropriate/optimal information-gathering system from the available set of choices using preposterior decision analysis.

M. Chadha · M. D. Todd (✉)
Department of Structural Engineering, University of California San Diego, La Jolla, CA, USA
e-mail: mdtodd@eng.ucsd.edu

Z. Hu
Department of Industrial and Manufacturing Systems Engineering, University of Michigan-Dearborn, Dearborn, MI, USA

Z. Mao (ed.), *Model Validation and Uncertainty Quantification, Volume 3*, Conference Proceedings of the Society for Experimental Mechanics Series, https://doi.org/10.1007/978-3-030-77348-9_4

2 Miter Gate and Decision-Making Framework

Consider that an SHM based decision-making problem (like choosing a maintenance action) that depends on the state parameter (gap length) defined by the random variable Θ, such that $\theta \in \Omega_\Theta = [\theta_{\min} = 0, \theta_{\max} = 180 \text{ in}]$ (see Fig. 1) is a realization of Θ and $f_\Theta(\theta)$, is the prior distribution of the state parameter. Let θ_{true} represent the true gap length value. Consider a binary decision space $\Omega_D = \{d_0, d_1\}$, such that:

$$\begin{aligned} d_0 &: \text{ Label/rating indicating that the gate is undamaged with an excellent operational capacity} \\ d_1 &: \text{ Label/rating indicating that the gate is damaged and is not safely operational} \end{aligned} \tag{1}$$

Let M_0 and M_1 represent the actions associated with the labels d_0 and d_1, respectively. That is, if the structure is labeled/rated as d_i, then we perform the maintenance M_i, such that:

$$\begin{aligned} M_0 &: \text{ Do nothing} \\ M_1 &: \text{ Shutdown, inspect, and repair or replace if required based on the inspection results} \end{aligned} \tag{2}$$

Choosing either M_0 or M_1 will have an associated consequence cost depending on what the true state of damage is. For instance, choosing M_0 for a newly constructed gate (with the true gap length value being zero or small) is an optimal decision. On the other hand, the same maintenance action M_0 can lead to catastrophic consequences when the true value of gap length is close to $\theta_{\max}$ (implying a heavily damaged gate). Similarly, choosing M_1 for a pristine gate is unnecessary, while it may be an optimal decision when the gate is approaching critical failure (with a larger value of true gap length). Therefore, to consider the economical consequence of deciding a maintenance action (or equivalently choosing the state label), the organization needs to estimate the cost of performing maintenance for all the possible true degrees of damage defined by the state parameter gap length θ_{true}. The organization estimates this cost based on a detailed cost analysis of past maintenance data and/or their current maintenance policies. For the sake of demonstration problem, we assume a linear cost function $L(d_i, \theta_{\text{true}}) : \Omega_D \times \Omega_\Theta \longrightarrow \mathbb{R}$ for decision d_i, such that:

$$\begin{aligned} L\left(d_0, \theta_{\text{true}}\right) &= \left(\frac{L(d_0,\theta_{\max}) - L(d_0,\theta_{\min})}{\theta_{\max} - \theta_{\min}}\right)\theta_{\text{true}} + L\left(d_0, \theta_{\min}\right); \\ L\left(d_1, \theta_{\text{true}}\right) &= \left(\frac{L(d_1,\theta_{\max}) - L(d_1,\theta_{\min})}{\theta_{\max} - \theta_{\min}}\right)\theta_{\text{true}} + L\left(d_1, \theta_{\min}\right). \end{aligned} \tag{3}$$

In the equation above, the extreme costs $L(d_i, \theta_{\max})$ and $L(d_i, \theta_{\min})$ are assumed to be known and fixed by the organization. The base cost functions $L(d_i, \theta_{\text{true}})$ are defined by the organization. Although the base cost is assumed to be linear in this paper, it can bear any form (step function, piecewise function, quadratic, etc.). In most cases, these costs are estimated based on the available data and are approximate.

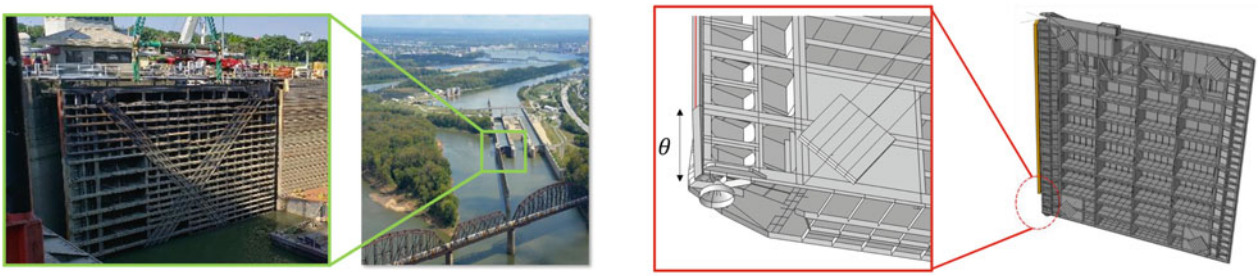

Fig 1a: Locks and miter gate

Fig 1b: Physics-based model of the miter-gate and gap

Fig. 1 Miter gate and the submerged gap. (**a**) Locks and miter gate. (**b**) Physics-based model of the miter gate and gap

When no new information is available, the gap length is described using its prior distribution $f_\Theta(\theta)$. The expected loss $\Psi_{\text{prior}}(d_i)$ for the decision d_i and the optimal decision $d_{\text{prior}} \in \Omega_{\text{D}}$ are given by:

$$\Psi_{\text{prior}}(d_i) = E_\Theta [L(d_i, \theta)];$$

$$d_{\text{prior}} = \text{argmin}_{d_i} \left(\Psi_{\text{prior}}(d_i)\right). \tag{4}$$

We now consider a scenario where additional information is available. For the sake of argument, we assume that the new information is obtained by a mechanism z (for example, an SHM system). Let Ω_{X_z} represent the continuous measurement (or additional information) space, such that $x_z \in \Omega_{X_z}$. Let X_z denote the random variable representing the new/additional measurement/information obtained by the mechanism z. Installing the information-gathering system incurs an intrinsic cost $C(z)$. With the availability of additional information, we define our *Bayes conditional risk* R_z and obtain the optimal decision d_z as:

$$R_z(d_i; x_z) = E_{\Theta|X_z} [L(d_i, \theta) + C(z)];$$

$$d_z(x_z) = \text{argmin}_{d_i} (R_z(d_i; x_z)). \tag{5}$$

3 Preposterior Decision Analysis and Expected Value of Information

Let Ω_z represent the space of all the possible information-acquiring mechanisms or systems (synchronously called experiments from here on), such that $\Omega_z = \{z_0, z_1, \ldots, z_m\}$. Here, z_0 represents the null case of carrying no experiment. Let X_{z_i} represent the random variable denoting the outcome/measurement of the data obtained by carrying out the experiment z_i, such that $x_{z_i} \in \Omega_{X_{z_i}}$. Let $C(z_i)$ represent the intrinsic cost of conducting the experiment z_i, with $C(z_0) = 0$. However, our goal for the preposterior analysis is to decide if the experiment and which experiment must be performed such that the new information obtained adds to the value of decision-making. Since the experiment is actually not carried out, all the possible outcomes must be considered. For that, the quantity that interests us is the expected value of the *minimum Bayes conditional risk* $R_{z_i}\left(d_j; x_{z_i}\right)$ averaged over all the possible outcomes $x_{z_i} \in \Omega_{X_{z_i}}$. It is defined by the average Bayes risk $\Psi_{\text{avg}}(z_i)$,for an experiment z_i is then obtained as:

$$\Psi_{\text{avg}}(z_i) = E_{X_{z_i}} \left[R_{z_i}\left(d_j; x_{z_i}\right)\right] \tag{6}$$

The *Expected Value of Information* for making a decision (at a given time) is defined as:

$$\text{EVoI}(z_i) = E_{X_{z_i}} \left[R_{z_i}\left(d_{z_i}\left(x_{z_i}\right); x_{z_i}\right) - \Psi_{\text{prior}}\left(d_{\text{prior}}\right)\right] = \Psi_{\text{avg}}(z_i) - \Psi_{\text{prior}}\left(d_{\text{prior}}\right) = -C_{\text{save}}(z_i) + C(z_i). \tag{7}$$

Here, $C_{\text{save}}(z_i)$ represents the monetary savings as a consequence of using the SHM system to make decisions. Therefore, performing an experiment/inspection to gain new information is advantageous if and only if the cost of the experiment $C(z_i)$ is less than the reduction in losses $C_{\text{save}}(z_i) \geq C(z_i)$.

4 A Simple Example of Preposterior Decision Analysis

To demonstrate a simple example of VoI analysis applicable to the miter gate problem, we consider one instance of decision-making (not the life-cycle cost analysis). Consider $\Omega_Z = \{z_0, z_1, z_2\}$, such that z_0: no data acquisition, z_1: send the diver to measure the gap length, and z_2: dewater the gate and measure the exact gap length. Assume $C(z_1) = \$0.02$ million and $C(z_2) = \$0.2$ million. We assume the prior distribution of the gap length as $f_\Theta(\theta) = \phi\left(\frac{\theta-75}{20}\right)$. We also assume that the gap length measured by the diver has some noise modeled by Gaussian noise of zero mean and a standard deviation of 3 inches

Table 1 Information-gathering mechanisms and their expected value of information

Strategy	$C(z_i)$	$\Psi_{\text{avg}}(z_i)$	EVoI(z_i)	$C_{\text{save}}(z_i)$
z_0	0	0.254	0	0
z_1	0.020	0.135	−0.119	0.139
z_2	0.200	0.223	−0.031	0.231

leading to the likelihood $f_{X_{z_1}|\Theta}\left(x_{z_1}|\theta\right) = \phi\left(\frac{x_{z_1}-\theta}{3}\right)$. Since z_2 is a perfect experiment (leading to the exact value of the state parameter), we have $f_{X_{z_2}|\Theta}\left(x_{z_2}|\theta\right) = \delta\left(x_{z_2} - \theta\right)$. For the given three inspection strategies, Table 1 represents the expected costs and the value of experimentation/inspection EVoI(z_i). Table 1 clearly indicates that performing both the experiments z_1 and z_2 will be beneficial because $C_{\text{save}}(z_i) \geq C(z_i)$ or EVoI(z_i) < 0. However, although dewatering yields a higher net saving $C_{\text{save}}(z_2) > C_{\text{save}}(z_1)$, sending the diver in for taking measurement yields the best risk-adjusted reward.

5 Conclusion and Ongoing Investigation

In this brief paper, we have broadly discussed the framework to quantify the benefit of obtaining additional information/data about the system. Our ongoing investigations are targeted on two fronts. Firstly, when it comes to maintenance decisions guided by the organization's maintenance policies or collective experience, in the real-world scenario inspection engineers are authorized to execute those decisions. These decisions are subjected to the engineer's experience and their thought processes assumed commensurate with the broader policies or guidance provided by the organization. Therefore, the maintenance decisions may have slightly different cost consequences, as defined by the base cost function. We are currently investigating incorporating human behavioral subjectivity into decision-making. Secondly, the framework discussed here can be extended to analyze the value of information acquired through an SHM system throughout the life cycle of the structure by considering decision-making at different time steps. Over the lifecycle of the miter gate, the state evolves from *pristine condition* (defined by 0 gap length value) to *approaching critical failure* (defined by the gap length being unacceptably high as $\theta_{\max}$). The efforts to analyze VoI for a lifecycle cost analysis for the miter gate problem are currently underway.

References

1. Howard, R.A.: Information value theory. IEEE Trans. Syst. Sci. Cybern. **2**(1), 22–26 (1966)
2. Thons, S.: On the value of monitoring information for the structural integrity and risk management. Comput. Aided Civ. Inf. Eng. **33**(1), 79–94 (2018)
3. Konakli, K., Faber, M.H.: Value of information analysis in structural safety. In: Vulnerability, Uncertainty, and Risk: Quantification, Mitigation, and Management, pp. 1605–1614 (2014)
4. Foltz, S.D.: Investigation of Mechanical Breakdowns Leading to Lock Closures. ERDC-CERL Champaign, United States (2017)

Error Localization Examples: Looking for a Needle in a Haystack

Lucas G. Horta, Mercedes C. Reaves, and Clay W. Fulcher

Abstract Finite element models (FEM) are routinely developed and used during fabrication of high dollar-value hardware. NASA, as part of the pre-flight certification of launch vehicles, routinely conducts vibration and static tests to calibrate models used for flight-risk assessments. During model calibration, certain areas of the model are modified, using engineering judgment and sensitivity analysis, to match the test results. Unfortunately, tools to identify problem areas in the FEM using test data directly are scarce and infrequently applied. Over the years, error localization algorithms have been proposed with very limited success. Recently, the Analytical Dynamics Model Improvement (ADMI) algorithm, which computes closed-form mass and stiffness corrections to match the test data exactly, has been shown to be an effective Error Localization Algorithm (ELA). The paper discusses three examples where ELA is used with simulated test data to locate problem areas. To gain confidence in the approach, the exact answer is shown along with ELA results. Results show that ELA is able to identify general problem areas consistent with known problem areas. In all examples, the ELA identified area is larger than the exact problem area. Nonetheless, with proper optimization tools, calibration results using the ELA identified areas provide excellent results.

Keywords Error localization · Modal test · Model calibration

1 Introduction

NASA and the aerospace industry routinely use Finite Element Models (FEM) to conduct analyses for risk assessments and flight readiness reviews. During the development of such models, contributions from many different areas are brought together to develop FEM, which are later validated and verified through carefully crafted tests. Because inputs from many engineers are integrated into the model at various stages of the hardware development, the task of model calibration, as defined in Refs. [1–4], often requires model developers to correct model deficiencies. Unfortunately, there is no universally accepted approach to identify problem areas in the FEM, which is particularly difficult with high-dimensional models. Often, analysts must correct model deficiencies with very little information about model flaws. Model adequacy is judged using established calibration metrics. For dynamic problems, calibration metrics are expressed in terms of frequency errors between test and analysis, cross-orthogonality errors [5], and frequency response principal values [6]. To reconcile the model with test, the standard approach relies on engineering judgment, calibration metrics, sensitivity analysis, and energy analysis to decide what areas of the model to correct. Although these tools provide information about what is important in the model, this information is not necessarily related to problem areas in the model. Conventional metrics show the effects of model flaws as opposed to the causes. On the other hand, Error Localization Algorithms (ELA) are tools, which guided by test data provide recommendations for model corrections. Hence, this is the focus of our work.

Although several ELA approaches have been proposed over the years, no particular approach has been adopted in commercial tools. Work here expands on the work in [7], which uses the Analytical Dynamics Model Improvements (ADMI) approach developed in [8]. The ADMI algorithm computes in closed-form, explicit mass, and stiffness corrections to match

L. G. Horta (✉) · M. C. Reaves
NASA Langley Research Center, Hampton, VA, USA
e-mail: lucas.g.horta@nasa.gov; mercedes.c.reaves@nasa.gov

C. W. Fulcher
Jacobs Engineering, NASA Marshall Space Flight Center, Huntsville, AL, USA
e-mail: clay.w.fulcher@nasa.gov

Z. Mao (ed.), *Model Validation and Uncertainty Quantification, Volume 3*, Conference Proceedings of the Society for Experimental Mechanics Series, https://doi.org/10.1007/978-3-030-77348-9_5

test frequencies and mode shapes with analysis. Admittedly, many factors affect and even hinder our ability to compute model corrections. For example, the number of sensors, the number of modes, the quality of the measured data, and more importantly the fidelity of the nominal model are all extremely important factors. Nonetheless, under ideal conditions, ADMI can compute both mass and stiffness corrections exactly to reconcile model with test. Even under less than ideal conditions, ADMI can still provide model corrections, which can then be used to identify problem areas. The process of using ADMI results to connect to elements in the FEM is effectively the ELA process.

To gain confidence in the ability of the ELA process to identify problem areas, our work here presents three analytical examples: (1) a cantilever beam, (2) a tube, and (3) an isogrid panel. All three examples had their FEM perturbed to create simulated test data for use in the study. Degrees-of-freedoms (DOFs) affected by mass and stiffness corrections are mapped to elements, which are subsequently mapped to model properties. Results from applying ELA to each example are compared visually to known problem areas. Quantitatively, results are compared in terms of orthogonality values and frequency errors. Before showing the examples, a brief discussion of the model calibration process is presented.

2 Model Calibration Process

The model calibration process used with all examples starts with determining model areas in need of correction using the measured frequencies and mode shapes. Calibration starts with a reduced mass and stiffness from the nominal FEM, referred here as the Test Analysis Model (TAM). Because DOFs in the TAM connect the test data to potential problem areas in the model, TAM matrices should be as large as computationally possible to reduced loss of accuracy in the mass matrix. More importantly, TAM matrices are the basis from which corrections to the mass and stiffness are computed. DOFs or nodes affected by the corrections are mapped to FEM elements and subsequently to element properties. This process has been automated for FEM data decks generated using MSC Nastran [9] format.

Exact mass and stiffness corrections computed using ELA are difficult to implement through the physical FEM properties. Instead, corrections must be approximated using optimization tools. To implement corrections, the FEM is partitioned into zones according to the required changes. Specifically, the FEM bulk file is altered to have elements and properties renumbered according to zones. Once renumbered, any commercial model update tool can be used to conduct parameter updates. In our implementation, the MATLAB [10] optimization toolbox is used.

With the FEM bulk file altered, the next step is to solve for parameter values using optimization. The optimization strategy seeks to determine model parameters to reconcile the measured frequencies and modes shapes with the analysis. To accommodate both metrics, i.e., frequency and mode shapes, the objective function is defined in terms of a 2-norm

$$J = \left\| w_1 \Delta\lambda^T \gamma^T \gamma \Delta\lambda \; w_2 tr(AA^T) \right\|_2 \tag{1}$$

The first scalar term in the objective function corresponds to the eigenvalue error defined as $\Delta\lambda^T = \left[\omega_1^2 - \mu_1^2 \; \omega_2^2 - \mu_2^2 \ldots \omega_n^2 - \mu_n^2\right]$, where ω_i are the predicted frequencies, μ_i are the measured frequencies, n is the total number of frequencies being reconciled, γ is a weighting vector for the individual frequencies, and w_1 is a user-prescribed scalar to adjust the objective function scaling. To apply Eq. 1, test and analysis frequencies must be paired first using orthogonality. Pairing links a test mode to an analysis mode when the cross-orthogonality value is above a user-prescribed threshold.

The second scalar term in Eq. 1 is the orthogonality error computed using the trace $tr(AA^T)$,where $A = \Phi^T M \Psi - I$. This calculation includes the measured modes shapes Φ, the analysis mode shapes Ψ, a reduced mass matrix M, an identity matrix I, and an arbitrary user-prescribed scalar w_2 to adjust the objective function scaling. Close-form expressions for the gradient have been developed and used.

3 Error Localization Examples

To understand the capabilities and limitations of ELA, it is best to use examples where problem areas are known. For this purpose, three examples are discussed where FEM alterations are implemented to create simulated test data. Data in terms of frequencies and mode shapes from the altered models are used to identify problem areas. Because the altered locations are known, results from ELA are easily verified qualitatively.

3.1 Cantilever Beam

Our first example is a beam, shown in Fig. 1, with translations constrained at both ends and no longitudinal rotations. Ten bar elements with rectangular cross-sections are used to construct the model. Heretofore, the term test data is used to refer to simulated mode shapes and frequencies from a perturbed FEM. Test shapes contain displacements at 9 locations in the lateral (y) and vertical (z) directions. In this example, the perturbed FEM has the cross-section height, in the area labeled Mod 1, changed from 0.125 to 0.150, and the width in the area of Mod 2 reduced from 1.0 to 0.8 inches.

Starting with TAM matrices sized 27 × 27, six test modes are used with ELA to compute mass and stiffness changes to match the test data. ELA results in Fig. 2a, show the sorted mass changes and Fig. 2b shows the sorted stiffness changes a function of the number of degrees of freedom changed. In here, the number of degrees of freedom refers to the number of changes as a function of diagonal elements in ΔM and ΔK to produce the necessary change. After reviewing the mass changes, it should be apparent that only four DOFs show the largest change. However, stiffness changes include many more DOFs.

When computing ELA corrections, the ability to correct a model depends on many factors. It is critical that TAM mode shapes span the vector space of the measured modes. Cross-orthogonality (CO) results (i.e. triple product $\Phi^T M \Psi$) between test data (ordinate) and the corrected model (abscissa), shown in Fig. 3, are a way to verify the adequacy of the ELA solution. CO values of 1 are shown in black. Note that the first six modes are matched exactly, as evident when comparing test and corrected model frequencies. A corrected ELA model is simply the TAM model with corrections, i.e.,$M + \Delta M$ and $K + \Delta K$. These matrices are not necessarily realizable through the FEM parameters. FEM parameter changes to approximate the corrected ELA solution must be implemented using numerical optimization.

Implementation of model changes begins by linking DOFs identified by ELA to elements and properties in the FEM. Figure 4 shows such a link among the FEM elements and locations in need of corrections. Six bar elements, marked using different colors, must be repaired based on ELA corrections. With elements identified, users must still choose among a large number of parameters for calibration. Table 1 lists 16 parameters for the repaired area, comprised of 4 parameters per bar element.

To set up the optimization problem, weights for the first six test modes are prescribed as $\gamma^T = \left[{}^{10}/_{\mu_1^2} \; {}^{10}/_{\mu_2^2} \; {}^{10}/_{\mu_3^2} \; {}^{1}/_{\mu_4^2} \; {}^{1}/_{\mu_5^2} \; {}^{1}/_{\mu_6^2} \right]$ and the objective function weights are set to $w_1 = 10$ and $w_2 = 10$. Parameter sensitivities are computed using Solution 200 in MSC Nastran [9] while mode shape derivatives are computed using Nelson's

Fig. 1 Beam model

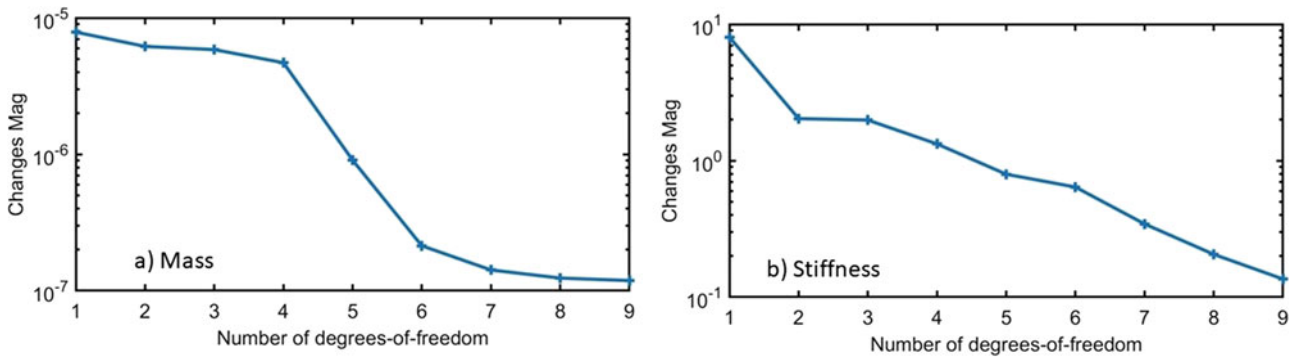

Fig. 2 Error localization computed changes for (**a**) mass and (**b**) stiffness

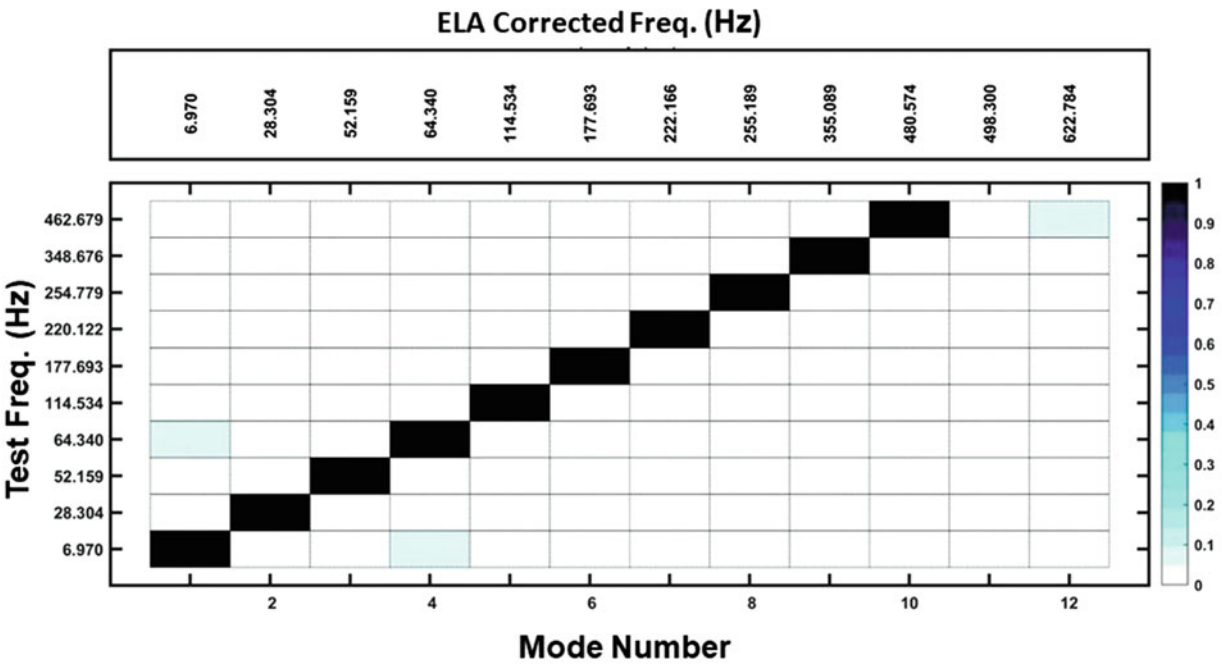

Fig. 3 Cross-orthogonality between test and ELA corrected model

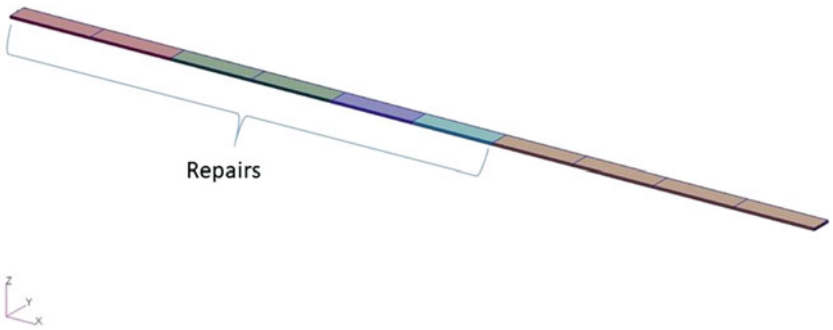

Fig. 4 Beam repair areas identified using ELA

Method [11]. A gradient-based optimization algorithm is linked to MSC Solution 200 for optimization. After 148 iterations, the optimizer found the solution listed in Table 1 under $Cal.\ Value$. Of the 16 parameters, only 7 show appreciable changes within four significant digits. Table 2 compares frequencies for the perturbed, nominal, and calibrated model. Note that frequency errors for the calibrated model are all within 0.64%. In addition, Cross-orthogonality (CO) results are compared in Fig. 5; test (ordinate) versus nominal (abscissa) is shown in Fig. 5a and test versus calibrated model is shown in Fig. 5b; off-diagonal values are all within 5% for the calibrated model. A good rule-of-thumb is to have CO diagonal values near 1 and off-diagonal values less than 5%. Finally, because geometrical parameters are adjusted, it is worth noting that the total mass after calibration increased from 0.5008 lbs to 0.5010 lbs. If one needs to maintain a fixed mass, mass can be included as an additional constraint.

3.2 Cantilever Tube

The second example shown in Fig. 6 is a cantilever tube 36 inches long with diameter of 2 inches, modeled with 1589 grid points and 768 CQUAD elements. For this study optimal sensor placement, conducted as part of the pretest analysis, selected 209 locations; marked with green arrows in Fig. 6. Optimal sensor placement is extremely important to ensure that modes are distinguishable from each other. Table 3 lists the first 8 frequencies of the perturbed, nominal, and calibrated models.

Table 1 Beam calibration parameters

Par no.	Zone ID	Units	Nominal value	Label	Cal. value
1	555001	in^2	0.1250	A	0.1179
2	1110001	in^2	0.1250	A	0.1248
3	1665001	in^2	0.1250	A	0.1250
4	2220001	in^2	0.1250	A	0.1435
5	555001	in^3	0.0002	I1	0.0002
6	1110001	in^3	0.0002	I1	0.0002
7	1665001	in^3	0.0002	I1	0.0002
8	2220001	in^3	0.0002	I1	0.0002
9	555001	in^3	0.0104	I2	0.0083
10	1110001	in^3	0.0104	I2	0.0104
11	1665001	in^3	0.0104	I2	0.0083
12	2220001	in^3	0.0104	I2	0.0083
13	555001	in^3	0.0006	J	0.0006
14	1110001	in^3	0.0006	J	0.0006
15	1665001	in^3	0.0006	J	0.0006
16	2220001	in^3	0.0006	J	0.0006

Table 2 Beam frequencies for nominal, perturbed, and calibrated model

Par. no.	Pert. freq. (Hz)	Nom. freq. (Hz)	Nom. freq. error (%)	Cal. freq. (Hz)	Cal. freq. error (%)
1	6.97	6.967	−0.04	6.976	0.09
2	28.304	27.867	−1.54	28.249	−0.19
3	52.159	55.666	6.72	52.194	0.07
4	64.340	62.730	−2.50	63.930	−0.64
5	114.534	111.630	−2.54	114.077	−0.40
6	177.693	174.807	−1.62	178.04	0.20

The perturbed FEM is created by altering the region indicated with magenta arrows in Fig. 6. Eight test modes, from the perturbed model, are used to locate errors using ELA. After applying ELA, results produced mass corrections as shown in Fig. 7a and stiffness corrections as shown in Fig. 7b. The ordinate in Fig. 7a and b shows the magnitude of diagonal elements in ΔM and ΔK, respectively, sorted in descending order as a function of number of DOFs. Note that mass corrections are very small, with the largest changes between 6.86×10^{-9} and 1.8×10^{-9}, encompassing only 33 DOFs. In contrast, stiffness corrections are significant and affect a large number of DOFs.

Because mass corrections are small, model repairs map only stiffness DOFs identified by ELA onto elements in the FEM. Figure 8 shows ELA element mapping using color shading. Superimposed onto the tube in yellow is the perturbed area. Note that the known perturbed area is within the stiffness changes recommended by ELA. As mentioned earlier, ELA corrections are not linked to physical parameters in the FEM. In order to connect ELA corrections to physical parameters, the FEM must be partitioned and elements renumbered according to ELA. Because of the large number of model changes required, the process is automated and the partitioned FEM along with renumbered properties are created and stored in a separate file. In this example, the partitioned FEM contains 123 zones, as shown in Fig. 8. To adjust stiffness values in the zones, the modulus is used in the optimization process to reconcile the model with test.

Ideally, one would like to change physical parameters to match the computed ELA corrections exactly. Unfortunately, this problem is very difficult and can only be approximated using numerical optimization. In this example, the optimization starts by prescribing test frequencies weights $\gamma^T = 10\left[1/\mu_1^2\ 1/\mu_2^2 \cdots 1/\mu_8^2\right]$ and objective function weights as $w_1 = 1$ and $w_2 = 0.1$. As with the first example, a gradient-based optimization algorithm is used to reconcile model with test. After 48 iterations, the optimizer converged and the calibrated model frequencies are shown in Table 3 under Cal-1, frequency errors less than 0.2%.

At this point, it is educational to compare calibration solutions when using ELA versus a standard approach where zoning is based on engineering judgment and sensitivity. For that purpose, the tube model is also calibrated using standard zoning and ATA Engineering Attune Software [12] and [13]. Frequencies, when using the calibrated parameters and standard zoning are shown in Table 3 under Cal-2. Note that frequency matching is excellent with errors under 1%. When comparing frequencies between calibrated models, it is not apparent that the actual stiffness changes with each approach are drastically different. A way to examine these two calibrated models is to compare the actual stiffness changes produced by each solution. Figure 9a

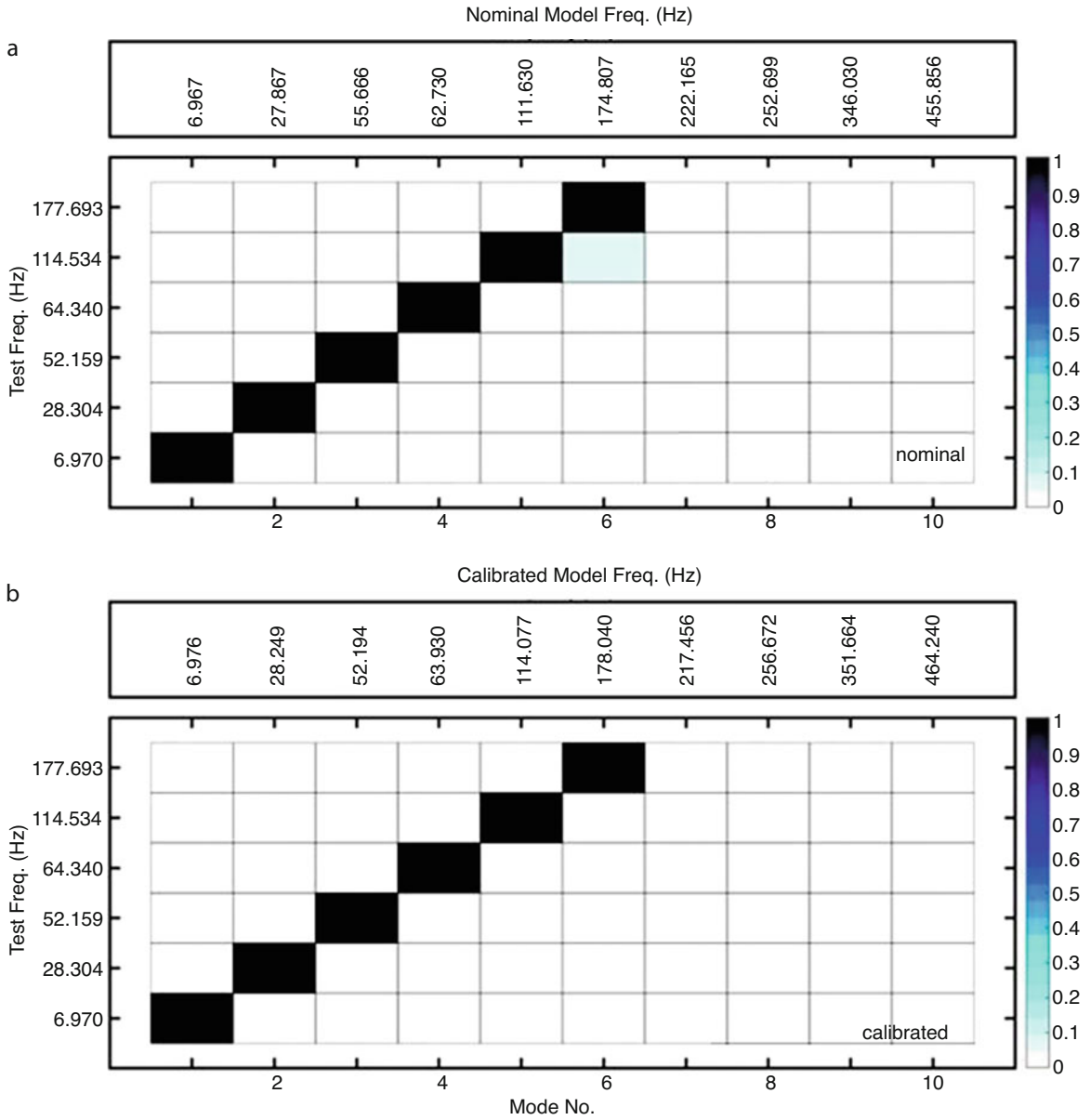

Fig. 5 Cross-orthogonality for: (**a**) test versus nominal, (**b**) test versus calibrated

shows contour plots of Cal-1 stiffness changes when using ELA zoning (front-view top, back-view at the bottom), and Fig. 9b shows Cal-2 stiffness changes when using the standard zoning approach. Clearly, not only the stiffness changes are dramatically different but also the affected regions. More importantly, ELA changes are concentrated near the known problem area, whereas the standard approach produced changes over the entire tube.

Figure 10a shows CO results for test (ordinate) versus Cal-1 (abscissa), whereas Fig. 10b shows test versus Cal-2. CO off-diagonal values for Cal-1 are all within 5% for the calibrated model, whereas for Cal-2 some values are about 10%. High Cal-2 CO errors after calibration with Attune simply indicate that the solution has not converged and additional iterations are needed.

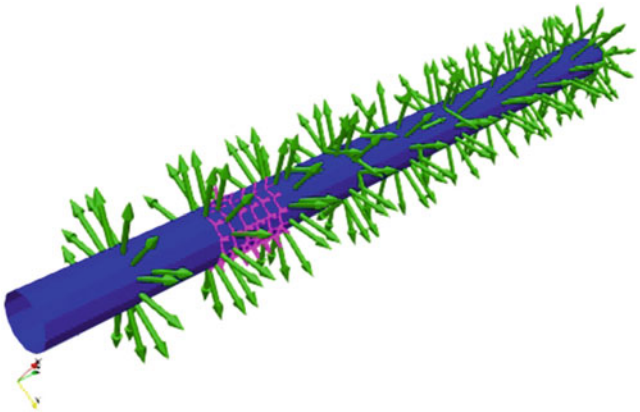

Fig. 6 Tube sketch with sensor placement (green arrows) and damaged area (magenta arrows)

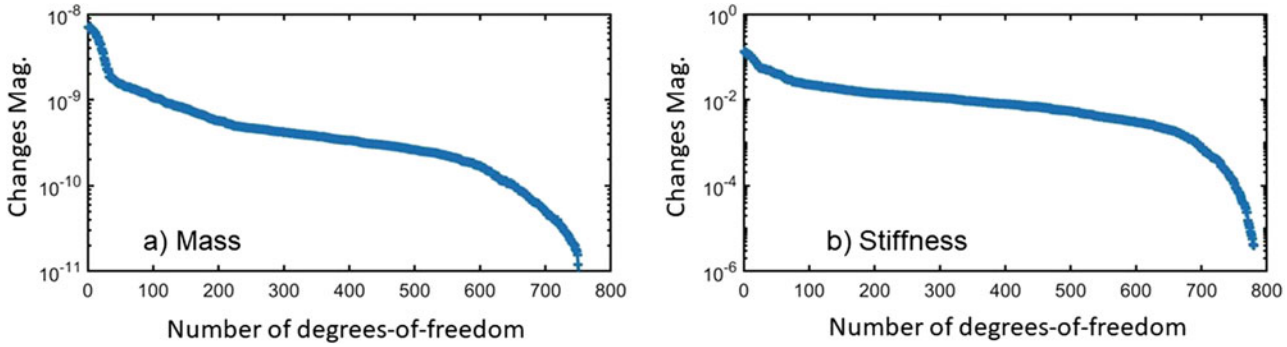

Fig. 7 Error localization computed changes for (**a**) mass and (**b**) stiffness

Table 3 Tube frequencies for perturbed, nominal, and calibrated models

Mode no.	Pert. freq. (Hz)	Nom. freq. (Hz)	Nom. freq. error (%)	Cal-1 freq. (Hz)	Cal-1 error (%)	Cal-2 freq. (Hz)	Cal-2 error (%)
1	53.8	54.4	1.0	53.8	−0.1	53.7	−0.3
2	58.6	61.1	4.1	58.7	0.2	59.1	0.8
3	334.0	332.6	−0.4	333.2	−0.2	334.5	0.1
4	368.6	367.1	−0.4	367.8	−0.2	366.7	−0.5
5	527.6	529.0	0.3	527.9	0.1	532.8	1.0
6	536.8	538.5	0.3	537.1	0.0	535.0	−0.3
7	543.1	546.9	0.7	543.6	0.1	543.7	0.1
8	551.5	555.8	0.8	551.9	0.1	547.2	−0.8

3.3 Isogrid Panel

The third example discussed here is motivated by a study conducted at NASA Langley to evaluate the adequacy of using equivalent panel properties, derived from static approximations, to model the dynamic behavior of isogrid panels. Figure 11 shows on the left a picture of a rectangular isogrid panel 8 × 14 1/8 × 3/32 inches weighting 1.35lbf. For small panels, modeling the complex pattern of the ribs is not difficult, but for large panels, the computational complexity is often large. In 1973, the McDonald Douglas Astronautics Company under contract for NASA [14] developed a computational handbook with formulas to estimate the equivalent properties for isogrid designs to approximate their static behavior. On the right of Fig. 11 is a sketch of the FEM, hereafter referred to as the Panel Equivalent Model (PaEM), developed using equivalent isogrid properties. As before, simulated test data are created by perturbing the FEM. Specifically, the perturbed FEM has an edge added along the border. For ELA evaluation, test data are collected at the 23 locations shown with arrows in Fig. 11.

Although the panel geometry is relatively simple, the panel itself has a slight curvature, which makes the modeling effort somewhat more difficult. The PaEM, modeled with MSC Nastran while suspended from soft strings, has 496 nodes (2976 DOFs) and 450 CQUAD4 elements. Panel layers (i.e., skin and ribs) are modeled using composite laminate theory with

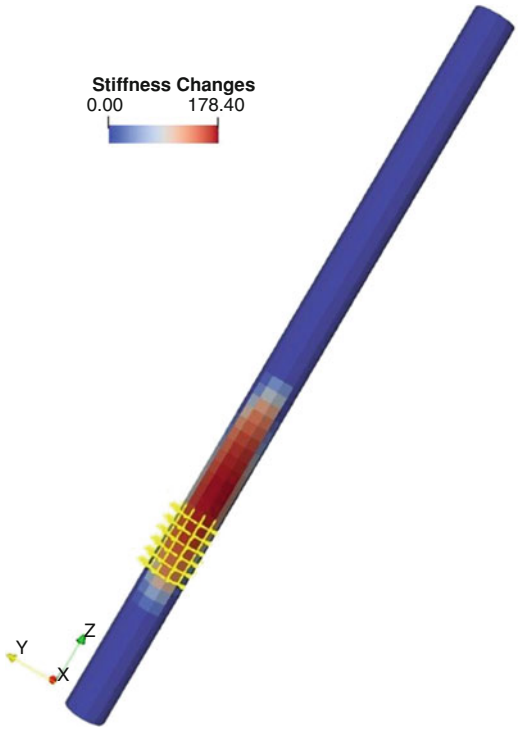

Fig. 8 Mapping of ELA stiffness corrections onto elements in the FEM

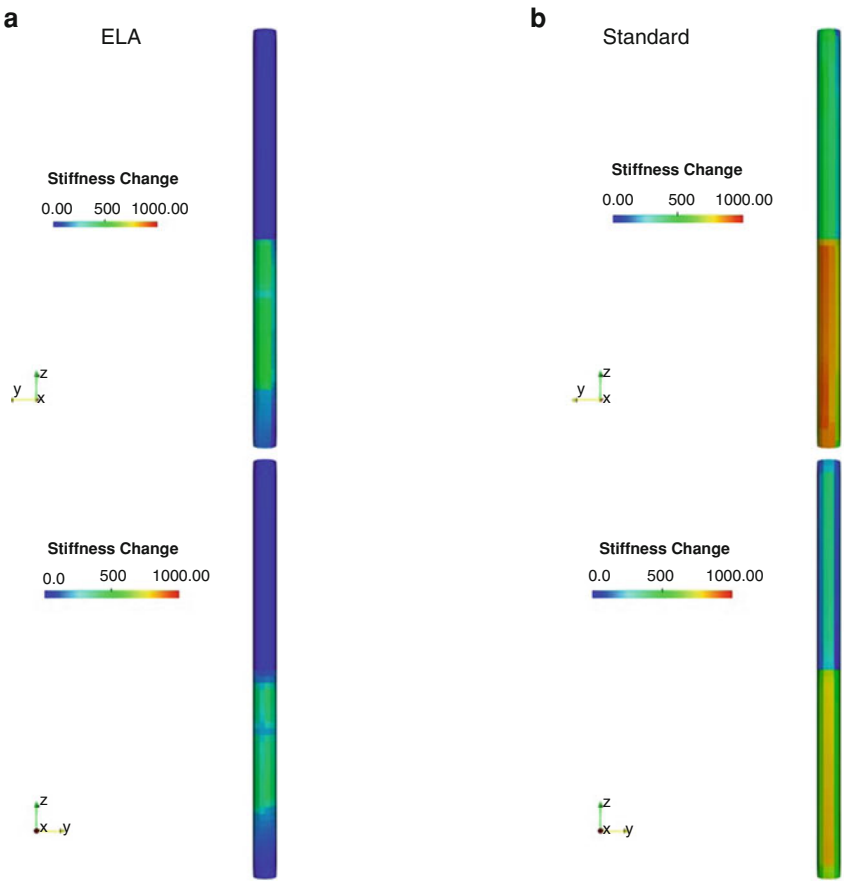

Fig. 9 Calibrated model changes using: (**a**) ELA zoning, and (**b**) standard sensitivity information

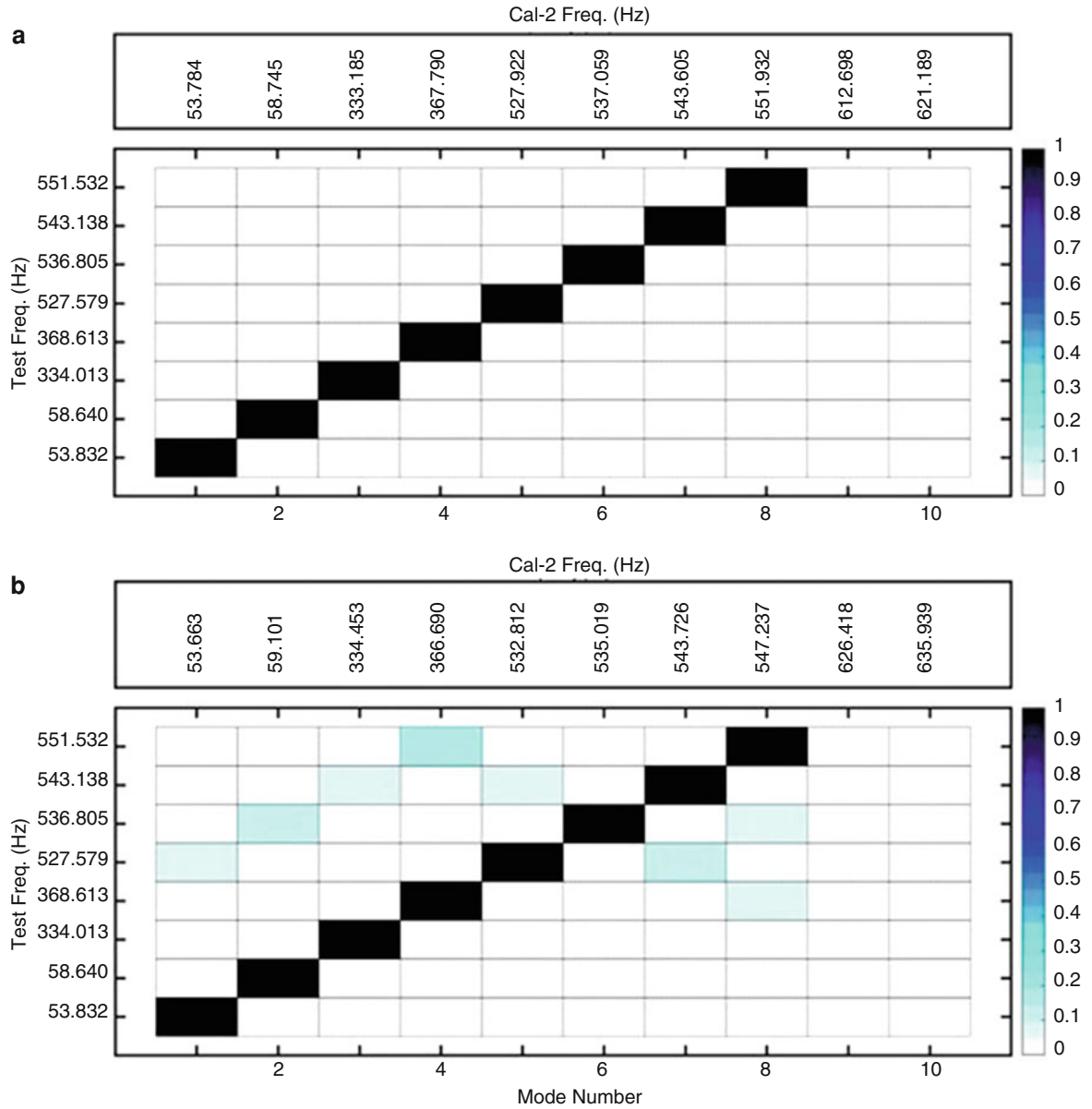

Fig. 10 Tube cross-orthogonality of calibrated model when using (**a**) ELA zoning and (**b**) standard zoning

isotropic properties for the skin and isogrid properties for the rib, properties computed using the isogrid design formulas [14]. Table 4 lists the first 6 modal frequencies excluding low frequency pendulum modes.

To implement the ELA, a TAM model for the PaEM is created with 1488 DOFs. TAM pendulum modes are shifted outside the frequency range of interest in this study. The first 6 test modes, all perturbed modes, are used in ELA to compute mass and stiffness corrections that reconcile the test frequencies and mode shapes with the analysis. Figure 12 shows mass and stiffness corrections, sorted in descending order, as a function of the number of DOFs. Of importance is the relative magnitude of the necessary changes to correct the model. If the magnitudes are large, this can be a reflection of either bad test data, inadequacy of sensor placement, or a poorly constructed model. Linking of the affected DOFs (or nodes) to elements in the FEM is what provides users with a more intuitive picture of problem areas. Figure 13 shows a contour plot of ELA stiffness changes needed to reconcile the model. Also shown is the FEM perturbed area marked with green arrows. Note that most of the perturbed area overlaps the ELA corrections but not all. The number of sensors and number of modes have a significant impact on our ability to identify problem areas, and in this example, only 23 sensors and 6 modes are used.

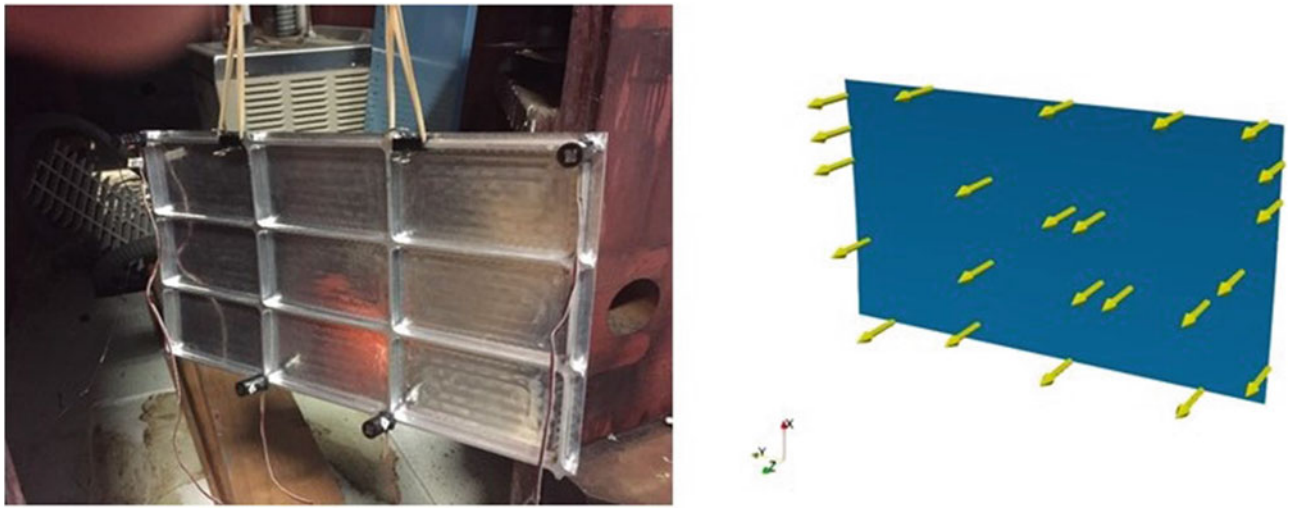

Fig. 11 Isogrid panel (left) and FEM sensor placement (right)

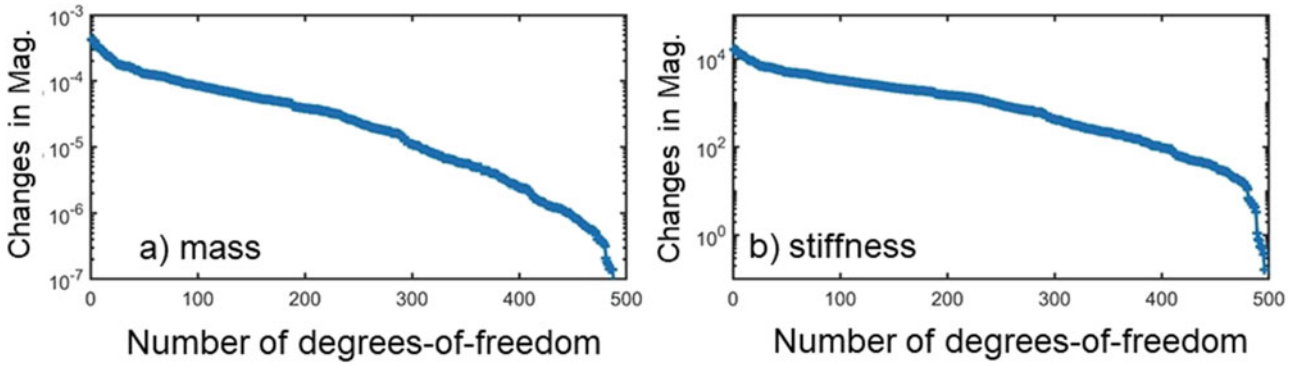

Fig. 12 Sorted ELA corrections to repair 6 modes of the nominal model for (**a**) mass, and (**b**) stiffness as a function of the number of degrees of freedom

Table 4 Panel equivalent model frequencies

Mode no.	Pert. freq. (Hz)	Nom. freq. (Hz)	Nom. freq. error (%)	Cal. freq. (Hz)	Cal. error (%)
1	114.5	107.7	−5.94	115.2	0.61
2	378.2	359.2	−5.02	382.5	1.14
3	437.8	392.5	−10.35	434.9	−0.66
4	792.0	767.8	−3.06	798.0	0.76
5	881.3	795.7	−9.71	874.7	−0.75
6	992.0	953.9	−3.84	994.8	0.28

A more difficult task is to map ELA corrections to physical parameters. For this, the FEM is partitioned into 123 zones. After extracting parameters for the 123 zones, the material modulus is optimized to reconcile the model with test.

To begin the optimization process, test frequencies weights are set to $\gamma^T = \left[1/\mu_1^2\ 1/\mu_2^2 \cdots 1/\mu_6^2\right]$ and the objective function weights are $w_1 = 100$ and $w_2 = 1$. As before, a gradient-based optimization algorithm is used to reconcile the model with test. After 40 iterations, the optimizer converged and the calibrated model frequencies, shown in Table 4 under calibrated model, show that frequency errors have been reduced to less than 1.2%. Moreover, actual stiffness changes with the calibrated model are shown in Fig. 14. In this problem, only the modulus of the material has been changed and therefore the system mass is constant. Clearly, the optimization process is intended to reproduce the stiffness changes shown in Fig. 13. To seek a closer solution, users can select other parameters within the 123 zones (like thickness, moments of inertia, etc.) for optimization. Nonetheless, in spite of the obvious differences between ELA and the calibrated model stiffness, frequencies errors are relatively small.

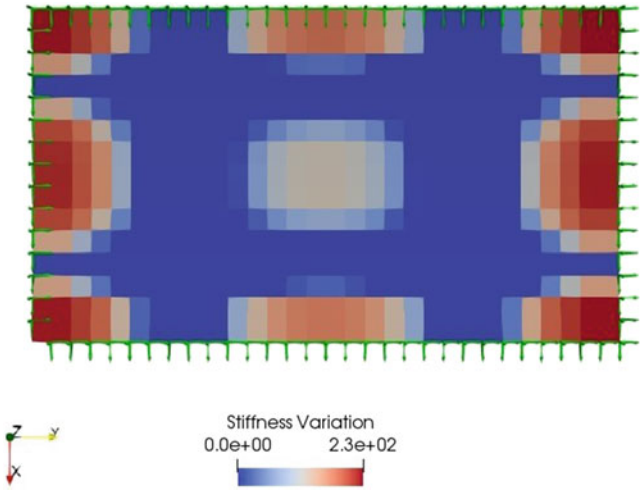

Fig. 13 Computed stiffness corrections using ELA; green arrows correspond to the known perturbations

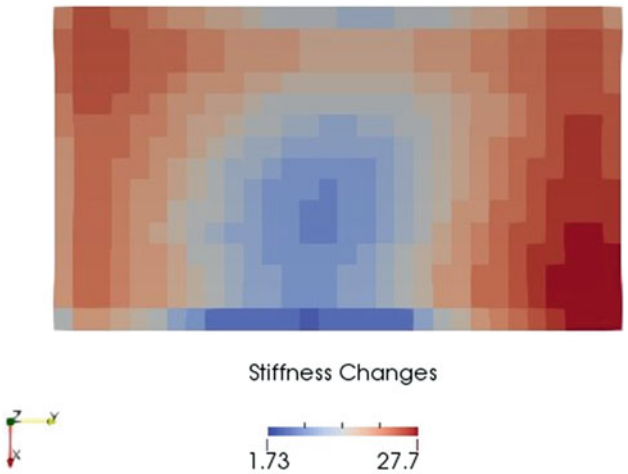

Fig. 14 Stiffness changes when using calibrated parameters

Finally, results for the CO are shown in Fig. 15. As before, color shading correspond to CO values between 0 and 1. Standard practices often recommend CO off-diagonal values be less than 5%. Figure 15a shows that off-diagonal values for the nominal and calibrated models are less than 30%. Improvements from calibration are primarily associated with the frequencies and mode 6 alignment. Large errors in the CO off-diagonal are mainly due to a small sensor count.

As should be evident by these three example problems, the ELA method is able to identify problem areas in the model when provided with adequate test mode shapes and frequencies. Nonetheless, readers are reminded that there are many factors that affect our ability to determine problem areas in the FEM. For example, poorly planned tests, improper sensor placement, missing modes, and inadequate FEM models are among the most critical. Until now, users have never been able to use test data directly to identify problem areas in the model. From the perspective of a user, finding model flaws is like finding a needle in a haystack.

4 Conclusions

The objective of this paper is to discuss the application of an Error Localization Algorithm (ELA) to identify problem areas in a Finite Element Model using modal test data. Three examples are presented to demonstrate the ability of the ELA approach to identify repair areas in the model. ELA determines numerical mass and stiffness corrections, which point to problem areas in the model. Although ELA corrections are not linked directly to parameter changes, the link is established using numerical

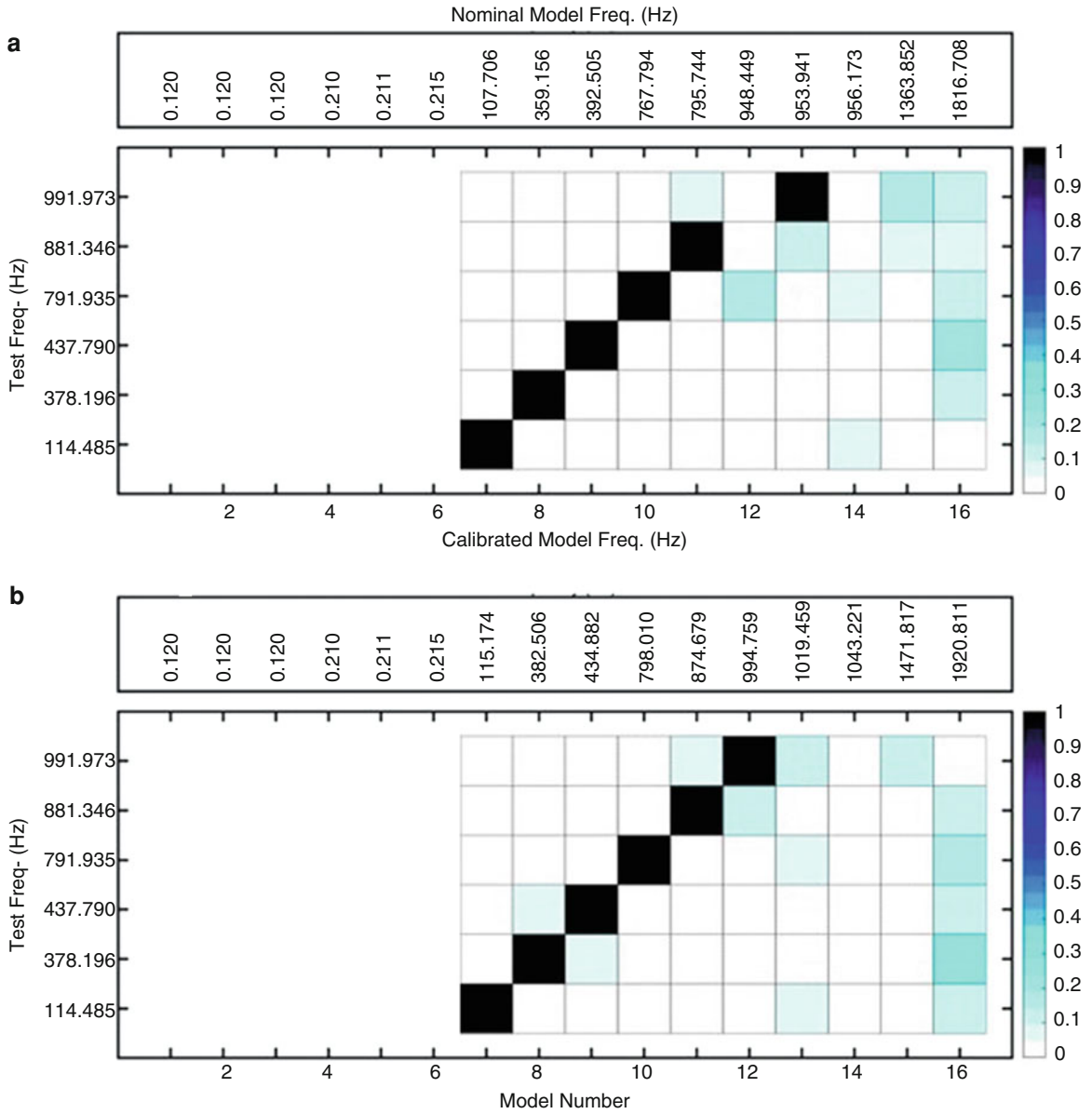

Fig. 15 Cross-orthogonality between (**a**) test versus nominal model, and (**b**) test versus calibrated model

optimization. The paper shows that ELA is able to identify general problem areas consistent with known problems. More importantly, using the identified areas, models are reconciled successfully. In general, the identified areas are larger than the exact answer.

Results from comparing stiffness changes using ELA versus a standard approach revealed that although model calibration, in terms of mode and frequency matching, is certainly possible with more heuristic approaches, changes in the stiffness between the two approaches can be drastically different. Without the benefit of knowing what areas to correct, the only option is to adjust everything because commercial model update tools rely exclusively on sensitivity to implement model changes. ELA can now provide a new capability to better localize update areas.

References

1. Friswell, M.I, Mottershead, J.E.: Finite Element Model Updating in Structural Dynamics. Copyright Kluwer Academic Publisher, Amsterdam (1995). Reprinted 1996, ISBN 0-7923-3431-0
2. Maia, N.M.M, Silva, J.M.M, He, J., Lieven, N.A.J, Lin, R.M., Skingle, G.W., To, W.-M., Urgueira, A.P.V.: Theoretical and Experimental Modal Analysis. Research Studies Press, Boston (1997). ISBN 0-471-97067-0
3. Anonymous: AIAA Guide for the Verification and Validation of Computational Fluid Dynamics Simulations. AIAA, G-077-1998 (1998)
4. Anonymous: Guide for Verification and Validation in Computational Solid Mechanics. ASME, Verification and Validation 10-2006 (2006)
5. Blelloch, P.A., Vold, H.: Orthogonality of large models - What's the Problem. In: Proceedings of the 23rd International Modal Analysis Conference (IMAC) (2005)
6. Horta, L.G., Reaves, M.C., Buehrle, R.D., Templeton, J.D., Lazor, D.R, Gaspar, J.L., Parks, R.A., Bartolotta, P.A.: Finite element model calibration for ares I-X flight vehicle. J. Eng. Mech. (2011). https://doi.org/10.1001/s11340-010-9456-x
7. Horta, L.G., Reaves, M.C.: An implementation of error localization algorithms for model calibration of dynamical systems. SN Appl. Sci. **2**, 1027 (2020). https://doi.org/10.1007/s42452-020-2744-x
8. Wei, F-S.: Analytical dynamic model improvement using vibration test data. AIAA J. **28**, 175–177 (1990)
9. Anonymous: MSC Nastran multidisciplinary structural analysis. The MacNeal-Schwendler Corporation, https://www.msc.software.com (2019)
10. Anonymous: MATLAB R-2018B, Copyright 1994-2019, The Mathworks Inc. http://www.mathworks.com (2018)
11. Nelson, R.B.: Simplified calculation of eigenvector derivatives. AIAA J. **14**(9), 1201–1205 (1976)
12. IMAT: http://www.ata-e.com/software/imat
13. ATTUNE: http://www.ata-e.com/software/attune
14. Anonymous: Isogrid Design Handbook. Prepared by McDonnel Douglas Astronautics Company, MDC-G4295A, Contract NAS 8-28619 (1973). Revised April 2004

WaveImage Bridges the Gap Between Measurement and Simulation. An Application Example of How to Create a Modal Digital Twin Using FE Model Updating

Mario Koddenbrock, Jan Heimann, Daniel Herfert, Johannes Pehe, and Lisa Wargulski

Abstract In this paper, a best-practice example of a digital twin is presented. For this purpose, the authors choose a test model of a machine frame with a rotating motor to simulate a situation from an industrial context. During the manufacturing process, this type of frame undergoes excitation from the imbalance forces of a single-speed drive. In order to avoid a failure of a structure when operating conditions change, it is important to be able to simulate the impact accurately. This accurate simulation requires an adequate digital twin. In this context, a good digital twin is one that reproduces the modal characteristics of the structure properly.

In this paper, the modal parameters of the machine frame are determined by experimental modal analysis. Afterward, model updating is performed to approximate the simulated modal parameters to the ones obtained from the real structure experiment. The full process is executed using the software WaveImage, which provides an easy-to-use modular kit for experimental modal analysis, finite element analysis, and finite element model updating.

Keywords Finite element simulation · Experimental modal analysis · Digital twin · Model updating

Nomenclature

K	Stiffness matrix
M	Mass matrix
K_0	Initial stiffness matrix
M_0	Initial mass matrix
K	Stiffness matrix
M	Mass matrix
α	Scalar stiffness optimization factor
β	Scalar mass optimization factor
n	Number of experimentally measured modes
$\phi_i i.$	Experimentally calculated eigenvector
$\psi_i i.$	Simulatively calculated eigenvector
$\lambda_i i.$	Experimentally calculated eigenvalue
$\mu_i i.$	Simulatively calculated eigenvalue
a	Scalar weighting of the eigenvalue deviation
b	Scalar weighting of the eigenvector deviation

M. Koddenbrock · J. Heimann · D. Herfert (✉)
Society for the Advancement of Applied Computer Science, Berlin, Germany
e-mail: herfert@gfai.de

J. Pehe
gfai tech GmbH, Berlin, Germany

L. Wargulski
GFaI e.V., Berlin, Germany

Z. Mao (ed.), *Model Validation and Uncertainty Quantification, Volume 3*, Conference Proceedings of the Society for Experimental Mechanics Series, https://doi.org/10.1007/978-3-030-77348-9_6

1 Introduction

Awareness of the necessity and usefulness of an adequate digital twin has spread more and more in the field of structural dynamics in recent years. With the integration of the digital twin creation process into the software WaveImage (gfai tech GmbH), access to this technology has become substantially facilitated. This means that a digital twin model can now be created in a short amount of time and with very little expert knowledge, without having to cut back on important details.

The key parameters that the digital twin must reproduce are the eigenfrequencies and mode shapes. These can be determined by means of a classical experimental modal analysis (EMA) [1]. However, it is essential that the planning, measurement, and mode extraction are accurately done in order to minimize uncertainties on the experimental investigation side.

Once we have successfully extracted the modal parameters of a structure, the finite element model updating component of WaveImage offers a multidimensional optimization of several material parameters. In practice, these parameters are often unknown or incorrect, so that the modal parameters of the simulated results deviate from the actual behavior of the structure. By generating a digital twin, the material parameters of the simulation are perfectly adapted to the modal parameters of the real structure. Thus, external forces, fixations, or constructional modifications can be easily and adequately tested before realization. All we need is a geometry of the structure in STL or OBJ format. Rotation, scaling, and translation according to the coordinates of the measurement can be calculated and aligned in the software by selecting a few reference points.

2 Theory

The implementation of the model updating component in the WaveImage (gfai tech GmbH) software is based on a work by Dong and Wang [2]. Its approach works with a formulation of differences in the modal properties. The optimization problem is formulated by minimizing the differences between measured and simulated eigenvalues and eigenvectors of the dynamic system. Therefore, the optimization variables α and β are introduced, which change the system matrices of the stiffness K and the mass M of the linear structure until the differences in the modal properties between simulation and experiment are minimized. The optimization variables α and β correspond to material parameters such as Young's modulus and mass density. The variables are scaled and indicate the percentage relative value change from the initial value. The matrices K and M can be formulated as a function of the optimization variables (α, β) as follows:

$$K(\alpha) = K_0 + \alpha \cdot K_\alpha$$

$$M(\beta) = M_0 + \beta \cdot M_{\beta.}$$

K_0 and M_0 describe the determined system matrices of the simulation before the model updating. K_α and M_β are constant input matrices of the parameters to be updated, assigned according to the optimization variable. For each i between 0 and n, the simulated eigenvalues (μ_i) and eigenvectors (ψ_i) are obtained as a solution to the eigenvalue problem

$$(K(\alpha) - \mu \cdot M(\beta)) * \psi_i = 0.$$

In addition, the experimentally determined eigenvalues λ_i and eigenvectors ϕ_i are extracted from the measured data using classical modal analysis.

The correlation rate between experimental and simulated modes must take into account the deviation of the natural frequencies as well as the mode shapes. For this purpose, a combination of the Modal Assurance Criterion (MAC) and a frequency difference is chosen as the minimization function to be optimized. Here, MAC is defined as the scalar product between the normalized eigenvectors [2]:

$$\mathrm{MAC}(\phi, \psi) := \frac{\left(\phi^T * \psi\right)^2}{\left(\phi^T * \phi\right)\left(\psi^T * \psi\right)}$$

With ϕ and ψ as eigenvectors, the MAC value is always between 0 and 1. This defines the minimization function as

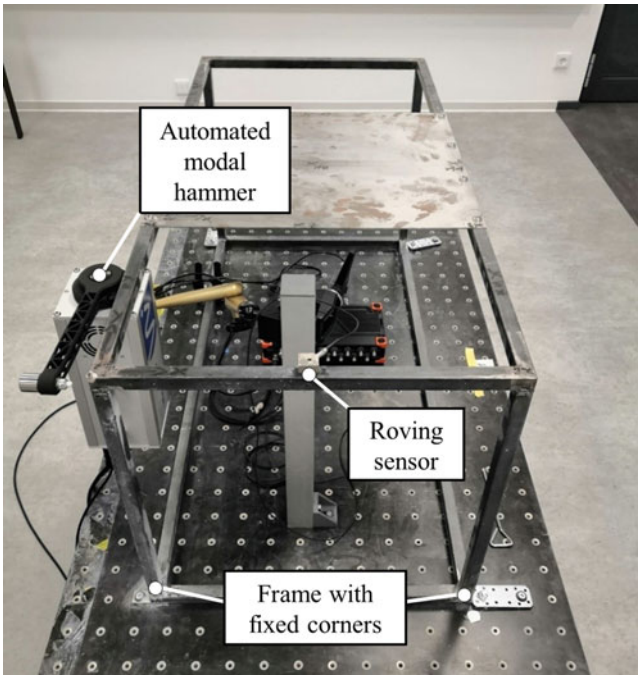

Fig. 1 Setup for the experimental modal analysis on the steel frame. With a roving-sensor approach, the system response was measured using a triaxial accelerometer at 19 discrete points distributed over the surface. Therefore, the system was excited by an automated modal hammer (WaveHit^{MAX}, gfai tech GmbH) providing a constant and high force amplitude to introduce sufficient energy into the frame

$$\delta := \sum_{i=1,\ldots,n} \underbrace{\left(a \cdot \frac{\lambda_i - \mu_i}{\lambda_i}\right)^2}_{\text{Frequency error}} + \underbrace{\left(b \cdot \frac{1 - \sqrt{\text{MAC}\,(\phi_i, \psi_i)}}{\sqrt{\text{MAC}\,(\phi_i, \psi_i)}}\right)^2}_{\text{Mode shape error}}$$

3 Measurement Setup

The vibration response of a steel frame to a selective force excitation was investigated to conduct the experimental modal analysis. The steel frame consists of rectangular 20 × 20 mm solid profiles. It measures 500 × 500 × 1000 mm with fully welded joints. On top, a 500 × 400 × 2 mm steel plate is screwed for mounting. The outer bottom corners of the frame were fixed to a vibration-isolated laboratory table. Thus, fixed boundary conditions can be assumed for these four-corner points. To determine the system response at different discrete measurement points distributed on the object, the roving sensor method was chosen. Therefore, the steel frame was excited by an automated modal hammer (WaveHit^{MAX}, gfai tech GmbH) on a fixed position; see Fig. 1. This modal hammer offers the advantage of automated repetitions of single-hit excitation with a defined and constant force amplitude. Equipped with a force sensor (PCB type 208C03), a plastic tip, and an additional mass of 60 g, a repeatable excitation of 2 kN has been achieved in order to obtain the best signal-to-noise ratio at all measurement points. The response of the steel frame into all three directions (*X, Y, Z*) to the impact excitation was measured with a triaxial accelerometer (MMF KS943B.100) roving from point to point to repeat the measurement sequence for every single point. To achieve a sufficient energy impact in every single direction, the modal hammer was repositioned to excite in the appropriate direction, and the measurements were repeated. Nineteen measurement points distributed equidistantly over the whole top surface of the frame were taken into account.

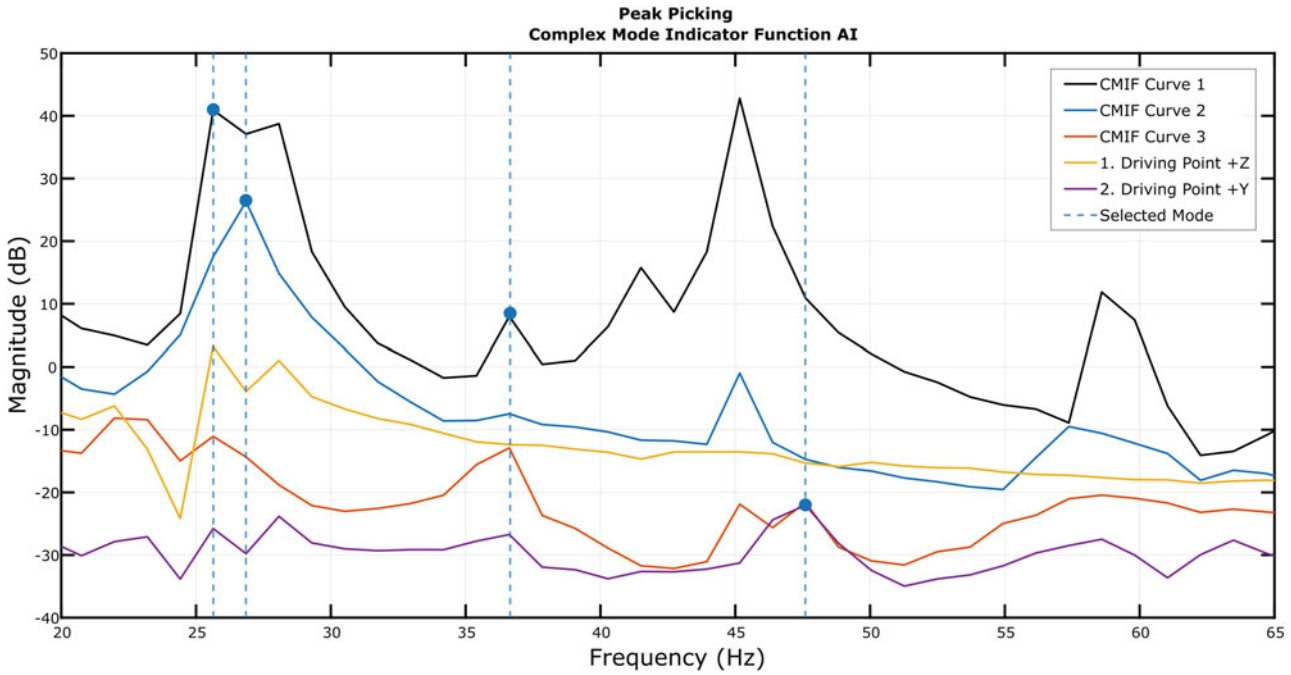

Fig. 2 Peak picking on the first three CMIF curves, together with the first two driving points

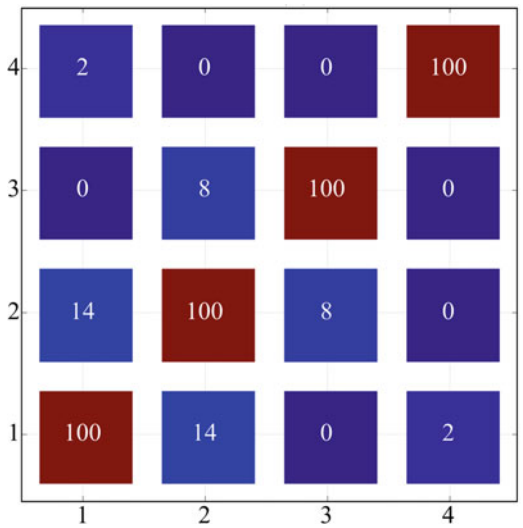

Fig. 3 Modal Assurance Criterion (MAC) matrix of the four measured modes

4 Analysis

At the beginning of the creation of a digital twin, the modal behavior of the structure must be extracted from the measured data. For this purpose, we used the experimental modal analysis of the software WaveImage (gfai tech GmbH) to extract the eigenfrequencies and mode shapes using the CMIF-AI [3] algorithm. We concentrated on the frequency range between 20 and 60 Hz because we want to use a rotating machine with up to 3600 revolutions per minute on the frame.

In Fig. 2, you can see the peak picking on the first three complex mode indication function (CMIF) [4] curves, together with the first two driving points. Furthermore, the frequency lines of the four identified modes are shown. The point indicates the curve on which the peak picking was performed to extract this mode. In Fig. 3, you can see the Modal Assurance Criterion (MAC) matrix of the four selected modes, and Figs. 4, 5, 6, and 7 show the mode shapes.

The MAC matrix is used to validate the independence of the detected modes. In our case, the MAC matrix only shows a small dependence of the first two shear modes of 14%. This indicates that the measurement was performed correctly.

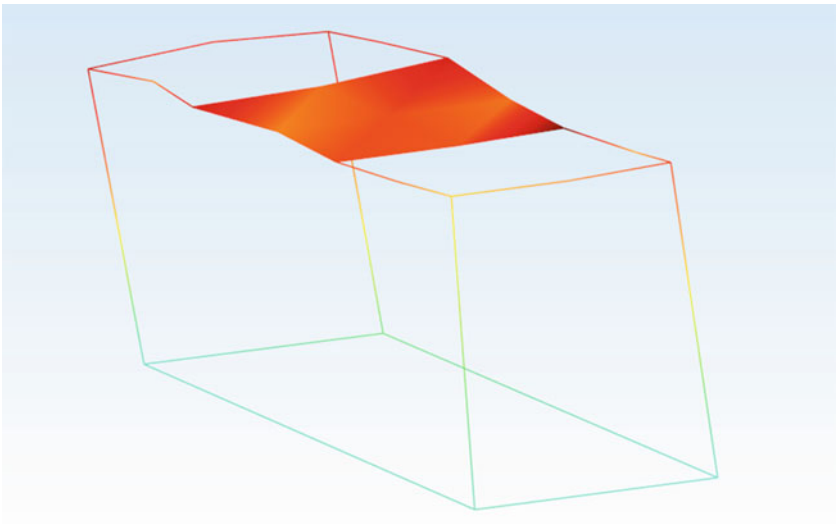

Fig. 4 EMA mode 1: shearing mode in *X* direction at 26 Hz

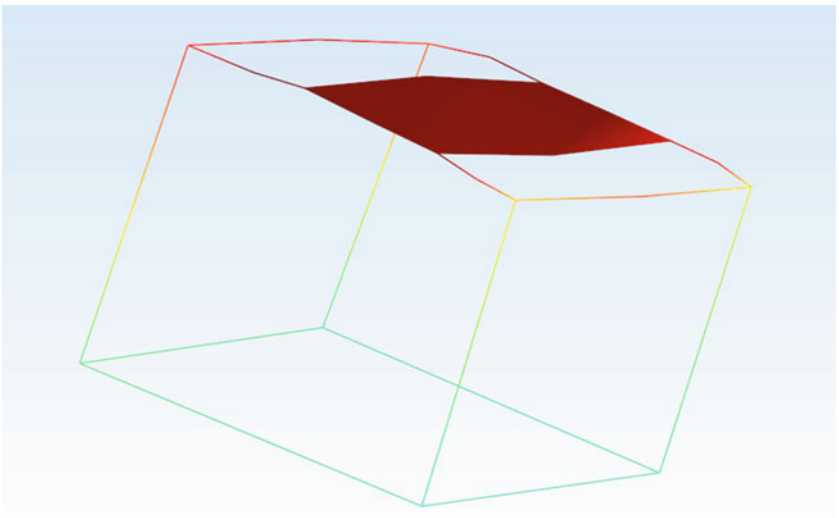

Fig. 5 EMA mode 2: shearing mode in *Y* direction at 27 Hz

For the simulation, we only need the geometry of the examined structure. This is often already available during the design phase of a machine or other structures. In the finite element component of WaveImage (gfai tech GmbH), the required mesh can then be generated automatically.

In this paper, a mesh with 18,425 nodes is used. The only boundary condition was a fixation of the stands, as it was done for the measured frame. The element size of the tetrahedral mesh ranged from 1.4 mm to 1.9 mm in diameter. The material is initially set to unalloyed, common structural steel of type S235JR with the following material parameters [5]:

$$\text{Mass density} = 7800 \ \frac{\text{kg}}{\text{m}^3}$$

$$\text{Young}'\text{s modulus} = 210 \text{ GPa}$$

$$\text{Poisson}'\text{s ratio} = 0.3$$

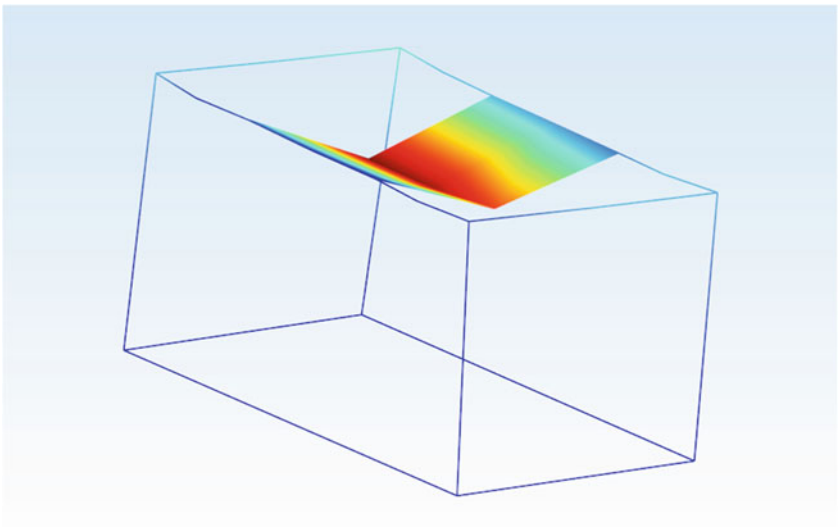

Fig. 6 EMA mode 3: bending mode at 37 Hz

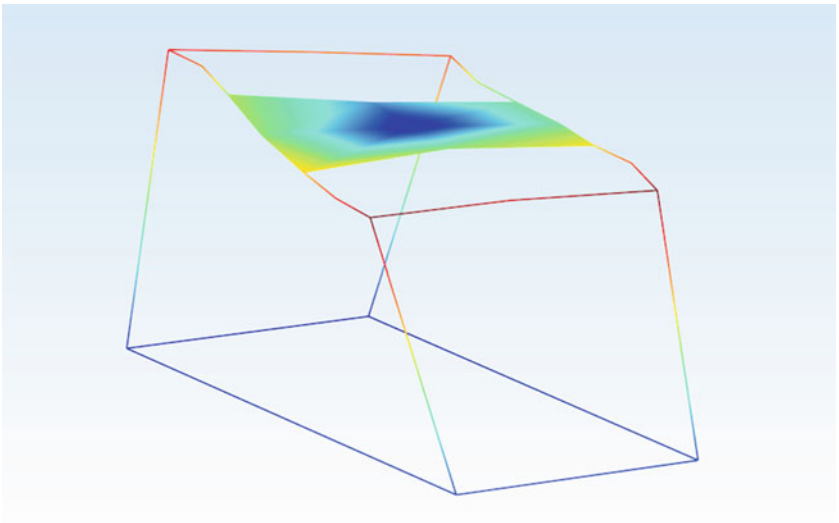

Fig. 7 EMA mode 4: rotation mode at 48 Hz

Table 1 EMA and FEA frequencies compared with their absolute difference and relative deviation before any optimization

EMA frequency	FEA frequency	Difference	Deviation
26 Hz	34 Hz	8 Hz	30%
27 Hz	36 Hz	9 Hz	33%
37 Hz	50 Hz	13 Hz	35%
48 Hz	53 Hz	5 Hz	10%

In the initial finite element simulation, the same four modes as in the measurement can be found. However, the frequencies still have a deviation up to 35% (Table 1, Figs. 8, 9, 10, and 11).

A problem when comparing mode shapes between measurement and simulation can be a different orientation of the coordinate systems. WaveImage (gfai tech GmbH) offers a semi-automatic solution to this problem, which only requires a selection of a few reference points by the user. In Fig. 12, the two geometries from the simulation and the measurement are placed one upon the other. A tolerance for the identification of the points can be set manually. In our example, a tolerance of 11 mm was sufficient to assign all nodes of the measurement to the corresponding nodes of the simulation.

With this assignment of the geometries, the MAC values between the simulated and the measured modes can now be calculated (Fig. 13). If the MAC values are not distinct, there may be problems with the identification of the modes. In

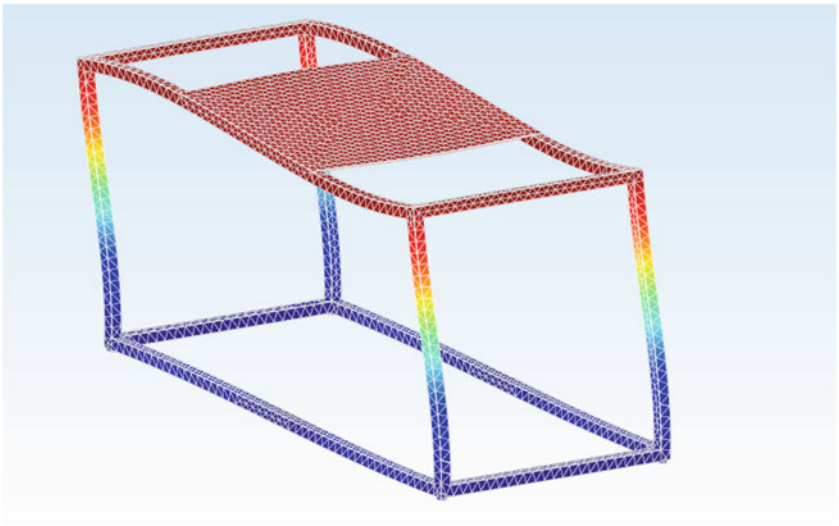

Fig. 8 FEA mode 1: shearing mode in *X* direction at 34 Hz

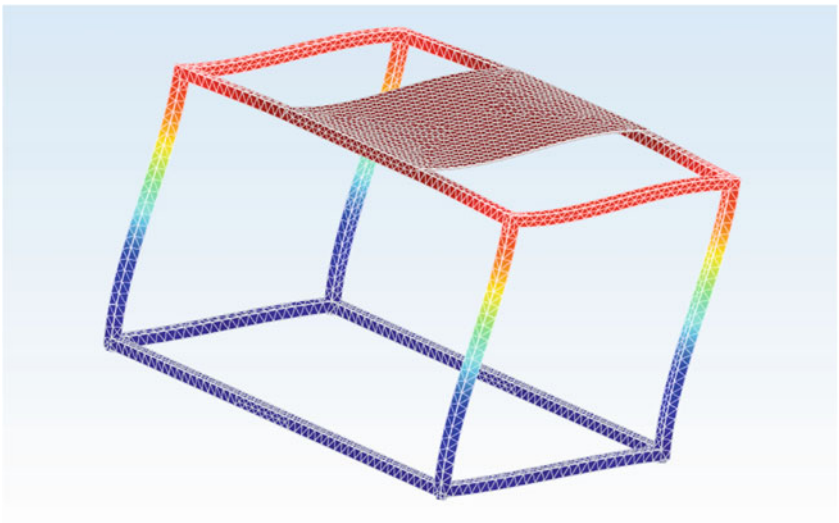

Fig. 9 FEA mode 2: shearing mode in *Y* direction at 36 Hz

the worst case, two modes are identified and their frequencies are compared, which do not belong together. A manual user assignment can help in this case.

In our example, the MAC matrix between the measured and simulated modes (Fig. 13) is very clear. So the model updating can automatically identify and assign the modes. In order to minimize the frequency deviation, simultaneous optimization of the material parameters mass density and Young's modulus is performed in this paper. Due to the nonlinearity of the minimization space, several starting points are chosen from which the iterative optimizer starts.

These starting points are shown in Fig. 14 with the respective value of the minimization function at the end of the iteration.

This chart shows an optimum at a mass density of 7800 kg/m^3 and a Young's modulus of 130 GPa. After the optimization, we get the following frequencies in the simulation and thus a significantly lower deviation from the measured frequencies (maximum 12%) (Table 2).

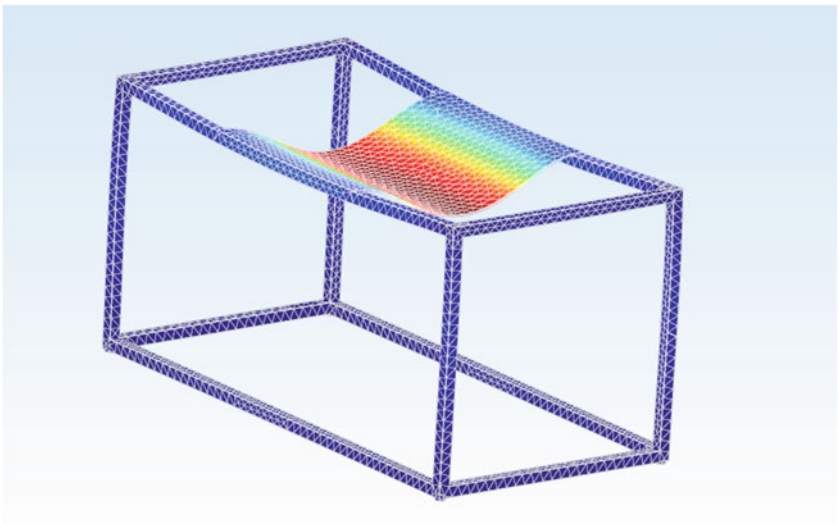

Fig. 10 FEA mode 3: bending mode at 50 Hz

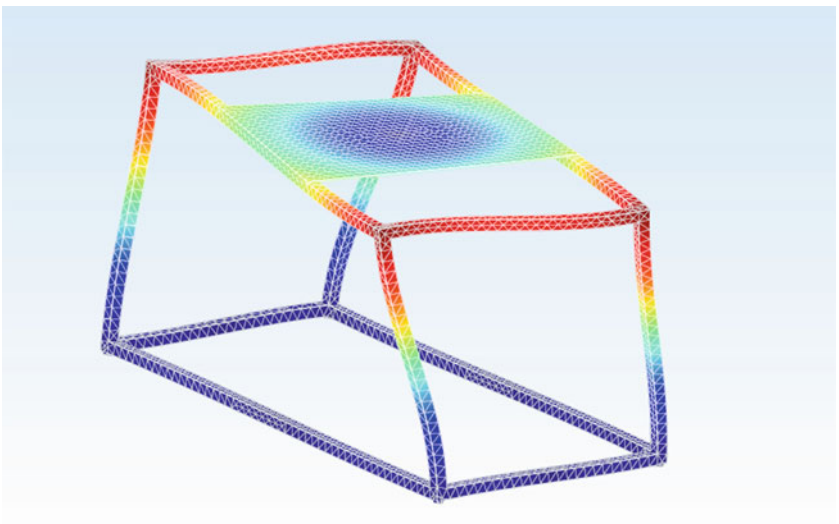

Fig. 11 FEA mode 4: rotation mode at 53 Hz

5 Conclusion

By using the model updating process, we have adjusted our finite element model to the modal parameters of the real structure. The model now serves as a digital twin for future simulations, for example, in a transient analysis under varying loads or to simulate constructional changes in order to shift resonance frequencies out of the excitation range. In this example, we see that the optimization of the modal properties of the structure leads to material parameters that are no longer fully consistent with the actual material. This is acceptable since the digital twin is designed to reproduce the modal properties of the structure.

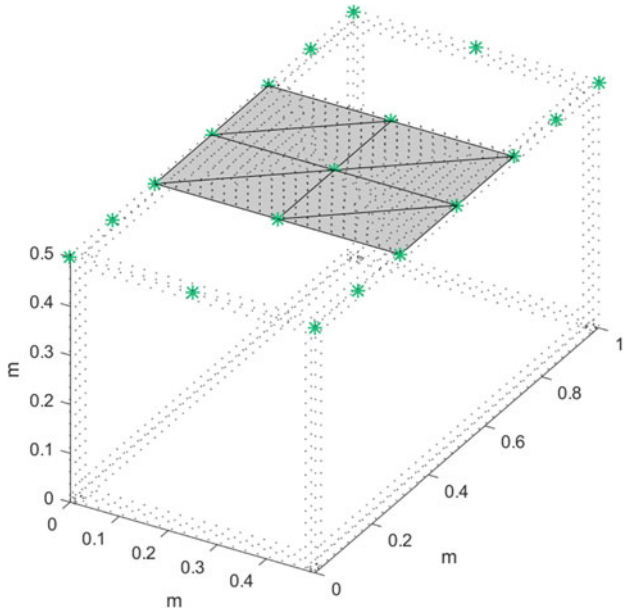

Fig. 12 All 19 nodes of the measurement (green) are assigned to the nodes of the simulation (black)

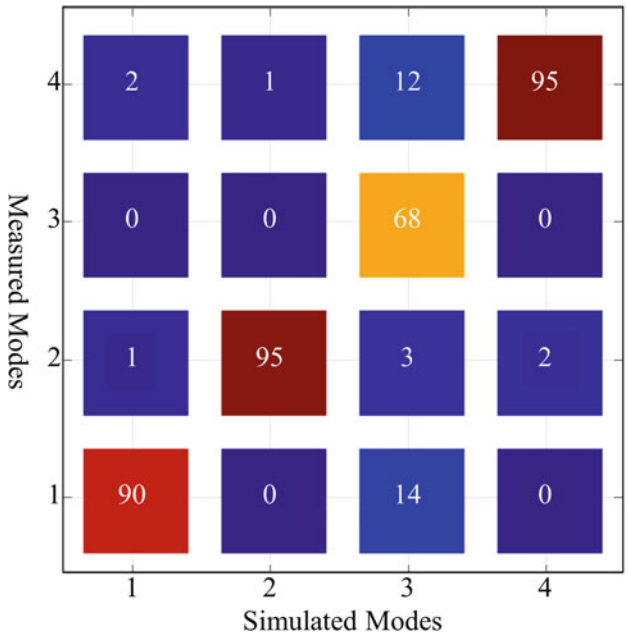

Fig. 13 Modal Assurance Criterion (MAC) matrix of the four measured and the four simulated modes

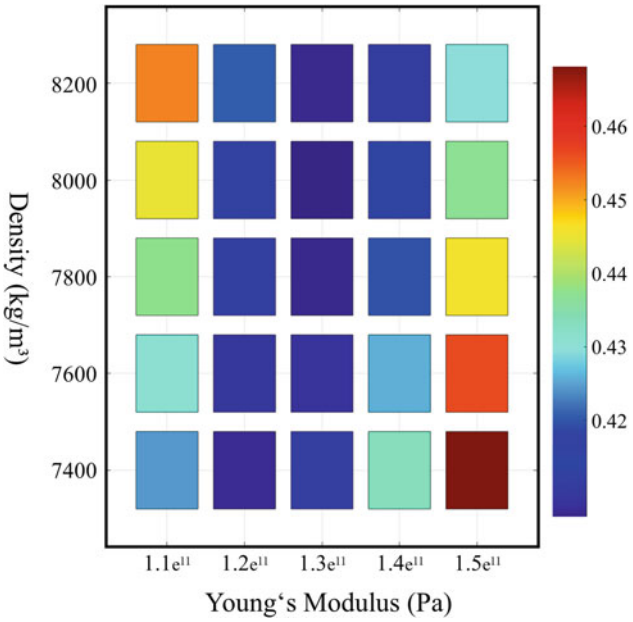

Fig. 14 Minimization function values depending on the two optimization parameters mass density and Young's modulus

Table 2 EMA and FEA frequencies compared with their absolute difference and relative deviation after the optimization

EMA frequency	FEA frequency	Difference	Deviation
26 Hz	27 Hz	1 Hz	4%
27 Hz	28 Hz	1 Hz	4%
37 Hz	37 Hz	0 Hz	0%
48 Hz	42 Hz	6 Hz	12%

References

1. Leurs, W.; Deblauwe, F.; Lembregts, F.: Modal Parameter Estimation Based on Complex Mode Indicator Functions, 1993
2. Dong, X.; Wang, Y.: Formulation and Optimization Algorithm Comparison for the FE Model Updating of Large-Scale Structures, 2018
3. Gollnick, M., Herfert, D., Heimann, J.: 9. Automatic modal parameter identification with methods of artificial intelligence. In: Topics in Modal Analysis & Testing, vol. 8. Springer International Publishing (2021)
4. Allemang, R.; Brown, D.: A Complete Review of the Complex Mode Indicator Function (CMIF) with Applications (2006)
5. Ovako Material data sheet S235JR: https://steelnavigator.ovako.com/steel-grades/s235/pdf?variantIDs=701

Virtual Sensing for Wind Turbine Blade Full Field Response Estimation in Operational Modal Analysis

Silvia Vettori, Emilio Di Lorenzo, Bart Peeters, and Eleni Chatzi

Abstract The inaccessibility of wind turbine components after their installation and the stochastic nature of the excitation they are subjected to, render their dynamic behavior challenging for investigation. Wind turbine blade manufacturers are required to carry out extensive test campaigns on each single blade individually prior to proceeding with commercialization. Static and fatigue tests are usually performed on prototypes in order to ensure that each blade can stand extreme loads, even after being subjected to high cyclic loading. The same instrumentation used for static and fatigue tests can be adopted for performing Operational Modal Analysis with the purpose of identifying the blade modal parameters, which can help analyzing failure modes and system stability problems. Measurements performed during tests are usually acquired at accessible locations and with a limited number of sensors due to their high cost. This work focuses on providing alternatives to costly and impractical physical measurements on wind turbine blades by combining information from cost-effective simulated models and more realistic test data through the so-called Virtual Sensing techniques, e.g., Kalman-type filters and Modal Expansion methods.

Keywords Wind turbine blades · Operational modal analysis · Virtual sensing · Dynamic tests · Response estimation

1 Introduction

Throughout the life cycle of a wind turbine, its blades are constantly exposed to irregular loading. The integrity of such blades is usually ensured performing extensive test campaigns including not only static and fatigue tests, but also dynamic tests aimed at identifying modal parameters and failure modes. Dynamic tests normally include shaker or hammer tests with the blade in free-free or clamped-free boundary conditions, and the so-called pull and release tests. Output-only measurements acquired during pull and release tests should give information about the full field response of the blade. The discrete nature of standard sensors, the instrumentation cost, and the inaccessibility of some locations on the structure often limit the possibility of retrieving the system response in a spatially continuous manner. Virtual Sensing (VS) techniques such as Kalman-type filters [1], can be therefore adopted for predicting the operational responses of the tested blade at locations where physical sensors could not be positioned [2, 3]. Moreover, joint input-state estimation techniques can be used for estimating unknown inputs applied to the system. This work adopts the Augmented Kalman Filter (AKF) [4] for joint input-state-response estimation of a 14.3 m long research blade during pull and release tests. The blade, manufactured by Olsen Wings, has been designed, tested, and extensively studied [5] by the DTU Wind Energy department in the framework of the project "BLATIGUE: Fast and efficient fatigue test of large wind turbine blades." The estimation results, i.e., the predicted input and strain responses at unmeasured locations during pull and release tests on the research blade in clamped-free boundary conditions are hereby proposed.

S. Vettori (✉)
Siemens Digital Industries Software, Leuven, Belgium

Institute of Structural Engineering, Zürich, Switzerland

E. Di Lorenzo · B. Peeters
Siemens Digital Industries Software, Leuven, Belgium
e-mail: emilio.dilorenzo@siemens.com; bart.peeters@siemens.com

E. Chatzi
Institute of Structural Engineering, Zürich, Switzerland
e-mail: chatzi@ibk.baug.ethz.ch

Z. Mao (ed.), *Model Validation and Uncertainty Quantification, Volume 3*, Conference Proceedings of the Society for Experimental Mechanics Series, https://doi.org/10.1007/978-3-030-77348-9_7

2 Pull and Release Tests for Wind Turbine Blades Operational Modal Analysis

The object of this work concerns a 14.3 m long research blade made of glass fiber reinforced plastics. The blade was designed by DTU Wind Energy and manufactured by Olsen Wings in the framework of the "BLATIGUE" project. The DTU Wind Energy department has kindly provided the FE model of the blade required for the present work, along with the experimental data on the tests this work refers to.

As shown in Fig. 1 (left), during the herein considered pull and release test, the blade was clamped to a rigid steel-reinforced concrete block through the circular interface plate in a flapwise configuration. The test consisted in pulling the blade downward by making use of a bungee applied at a distance of 13.1 m from the clamping. Once the blade tip reached the desired displacement, it was released. The blade was instrumented via 76 strain gauges distributed on 12 sections along its length and all measuring in the length direction of the blade. Figure 1 (right) shows the sensor locations along the blade.

The FE model has been developed in MSC Nastran and afterwards exported in Simcenter 3D, where it was validated using modal parameters obtained from hammer tests performed on the blade in clamped-free conditions, i.e., the same boundary conditions adopted during the pull and release test.

3 Response-Input Estimation During Pull and Release Tests on the Research Blade

The AKF has been applied in this work in order to simultaneously retrieve the full field strain response of the blade and the applied input profile during the pull and release test herein taken into account. For employing the AKF for VS purposes, a Reduced Order Model (ROM) of the blade has been built, following the procedure described in [6–8]. The ROM reduction basis has been created including the first ten normal modes (frequency range of interest: 0–43 Hz) and one residual attachment mode related to the unknown force to be estimated.

In order to prove the algorithm validity, only a selected set of sensors among the 76 strain responses acquired during tests has been used as observations set for the AKF. The remaining responses have been predicted using the AKF and then compared to the corresponding acquired time histories to evaluate the estimation performance. Figure 2 (left) reports "measured" and " unmeasured" sensor locations according to the adopted configuration, i.e., blade instrumented at a limited number of sections.

Uncertainties on both the observations and the system model need to be taken into account when employing the AKF, i.e., when a Bayesian statistical framework is foreseen. In particular, the measurement noise covariance has been computed from the available static measurements in order to assume a physically reasonable value. The process noise covariances related to the input and the states instead have been respectively assumed to be equal to 10^8 and 10^1.

Figure 2 (right) shows the comparison between the actual force profile adopted during the previously mentioned pull and release test and the input profile estimated via the AKF. Although the predicted input shows an offset with respect to the actual null force after the blade release, it correctly detects the time instant when the force drops to zero. Moreover, it approximately matches the actual value of the static force adopted to pull the blade during the test.

Response estimation results are reported in Fig. 3 for the three locations pointed out in Fig. 2 (left). Plots included in Fig. 3 compare the estimated time histories not only to the measured ones, but also to the responses obtained by performing a forward simulation of the blade ROM when the actual input is applied. The reported results show that employing the AKF for response estimation allows to correct the model error throughout the entire time history, including the initial static frame.

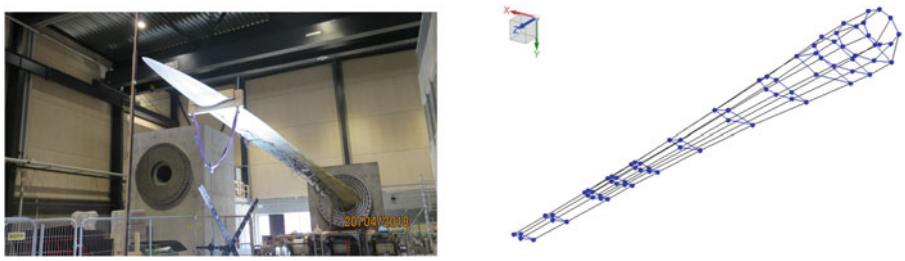

Fig. 1 Wind turbine blade setup during the pull and release test (left). Test geometry (right)

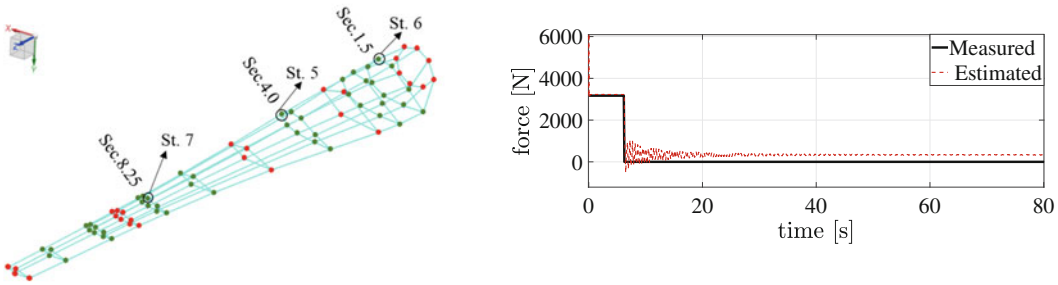

Fig. 2 "Measured" (red) and "unmeasured" (green) locations (left). Input "measured" (black) and estimated (red) time histories (right)

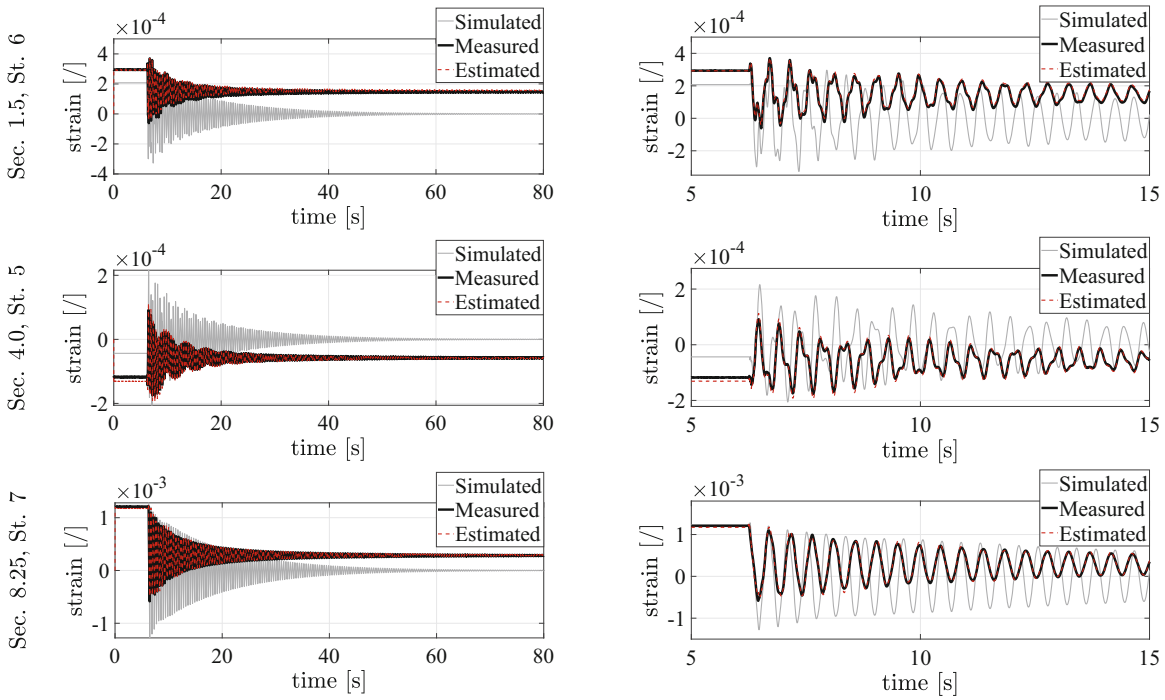

Fig. 3 Time histories (left) and detailed time histories (right) of strain responses at strain gauges St.6 (Sec1.5), St.5 (Sec4.0), St.7 (Sec8.25)

4 Conclusions

The use of the AKF for joint input-state estimation during the so-called pull and release tests on a wind turbine blade has been proposed in this paper. The blade object of this work is a 14.3 m long research blade designed by DTU Wind Energy and manufactured by Olsen Wings. Output-only measurements were carried out on the blade during the mentioned pull and release test and the strain response was acquired at 76 locations. The blade was subjected to initial downward pull and subsequent release after the desired tip displacement was reached. For this work, a set of measured responses has been used as observations for the AKF implementation with the purpose of estimating the "unmeasured" quantities, i.e., the remaining strain responses and the applied input. It has been demonstrated that the AKF can furnish an accurate response prediction. Although the predicted input profile shows a non-zero mean value after the blade release, it is able to match the actual input step profile. Moreover, the time instant when the blade is released is also correctly identified. Possible future investigations will consist in studying the influence of the adopted physical sensing configurations on the virtual predictions delivered via use of Kalman-type filters (AKF, DKF...) for joint input-state estimation.

Acknowledgments The authors gratefully acknowledge the European Commission for its support of the Marie Sklodowska Curie program through the ITN DyVirt project (GA 764547).

The authors would like to extend their gratitude to the DTU Wind Energy department for providing the blade FE model and relevant experimental data, developed in the framework of the project "BLATIGUE: Fast and efficient fatigue test of large wind turbine blades," supported by the Danish Energy Agency through the Energy Technology Development and Demonstration Program (EUDP), Grant No. 64016-0023.

The authors would like to also acknowledge the project "RELIABLADE: Improving Blade Reliability through Application of Digital Twins over Entire Life Cycle," supported by the Danish Energy Agency through the Energy Technology Development and Demonstration Program (EUDP), Grant No. 64018-0068, the support of which is greatly appreciated.

References

1. Azam, S.E., Chatzi, E., Papadimitriou, C., Smyth, A.: Experimental validation of the Kalman-type filters for online and real-time state and input estimation. J. Vib. Control **23**(15), 2494–2519 (2017)
2. Dertimanis, V.K., Chatzi, E.N., Azam, S.E., Papadimitriou, C.: Input-state-parameter estimation of structural systems from limited output information. Mech. Syst. Sig. Process. **126**, 711–746 (2019)
3. Papadimitriou, C., Fritzen, C.-P., Kraemer, P., Ntotsios, E.: Fatigue predictions in entire body of metallic structures from a limited number of vibration sensors using kalman filtering. Struct. Control Health Monit. **18**(5), 554–573 (2011)
4. Lourens, E., Reynders, E., De Roeck, G., Degrande, G., Lombaert, G.: An augmented kalman filter for force identification in structural dynamics. Mech. Syst. Sig. Process. **27**, 446–460 (2012)
5. Luczak, M.M., Peeters, B., Manzato, S., Di Lorenzo, E., Reck-Nielsen, K., Berring, P., Haselbach, P.U., Branner, K.: Research sized wind turbine blade modal tests: comparison of the impact excitation with shaker excitation. J. Phys. Conf. Ser. **1102**, 012022 (2018)
6. Craig Jr, R.R.: A Review of Time-Domain and Frequency-Domain Component Mode Synthesis Method (1985) https://ntrs.nasa.gov/citations/19860042139
7. Vettori, S., Di Lorenzo, E., Peeters, B., Chatzi, E.: A virtual sensing approach to operational modal analysis of wind turbine blades. In: Proceedings of ISMA2020 International Conference on Noise and Vibration Engineering, Leuven, Belgium (2020)
8. Vettori, S., Di Lorenzo, E., Cumbo, R., Musella, U., Tamarozzi, T., Peeters, B., Chatzi, E.: Kalman-based virtual sensing for improvement of service response replication in environmental tests. In: Model Validation and Uncertainty Quantification, vol. 3, pp. 93–106. Springer, Berlin (2020)

Dynamics of a Nonlinear Oscillator: Dependencies on Extrinsic Conditions and Model Form Uncertainty

Thomas P. Roberts, Scott A. Ouellette, and Adam J. Wachtor

Abstract Closed-cell polymer foams are commonly employed as support structures to absorb shock and vibration in mechanical systems. Engineering analysts responsible for system designs that incorporate these closed-cell foams have a need to understand the effect that extrinsic environmental conditions have on the dynamic response of the mass supported by the foams. Environmental conditions such as preload, forcing energy, and forcing frequency, along with inherent model form uncertainty, have the potential to drive such a system into nonlinear, and sometimes chaotic, behavior. A suite of studies utilizing finite element (FE) analysis and numerical simulations of a material meta-model was used to perform a parametric study on the extrinsic forcing conditions to understand such effects on the nonlinear system dynamics. A simple two-dimensional (2D) plane strain FE model of a mass supported on both sides by foam was used to perform two tasks—to implicitly determine stress states from precompression in the foam and to explicitly solve for the system's response when subject to a dynamic input. Using prior knowledge of uncertain quantities in the model and ranges of possible environmental conditions, parameter sets of extrinsic conditions were used as inputs to the models to obtain the time-domain responses of the suspended mass. The corresponding frequency domain characteristics of the suspended mass were used in conjunction with the input parameter distributions to form conclusions about the influence of variation in each parameter on the natural frequency of the system. Considering the results from the extrinsic property sensitivity analysis, the models were perturbed from linear, harmonic oscillation to showing signs of nonlinear motion. Small changes in extrinsic conditions while oscillating near the system's nonlinear stiffness regime are hypothesized to cause sudden changes in a holistic response. This work aims to discuss the effects of model form uncertainty and the effects of changing the extrinsic conditions in an inherently nonlinear dynamic system.

Keywords Model uncertainty · Non-linear vibration · Sensitivity analysis · Parametric modeling · Closed-cell foam

1 Introduction

Hyperelastic material models are a special class of materials that respond elastically to large compressive or tensile deformations [1]. Rubber-like materials are a common application for hyperelastic constitutive modeling techniques. These materials can exhibit complicated behaviors that extend well beyond the linear elastic theory, such as large deformations, plastic and viscoelastic properties, and stress softening (Mullins effect) [2]. Starting with a constitutive model form, Ogden or neo-Hookean for example, experimental data are used to fit constitutive model parameters, and thus a hyperelastic material model is born. The downside to constitutive models, however, is that they rely on a fitting process. A consequence of such a process is the lack of physics involved in using the model outside of its calibration range [3]. Thus, it should be obvious that the typical hyperelastic material models have shortcomings, and this work utilizes a material model that aims to overcome such issues. At the heart of this work is the verification and uncertainty quantification of a physics-based porous foam material model, CHIPFoam. The CHIPFoam material model developed by Lewis [4] was created to improve upon the

T. P. Roberts (✉)
Department of Mechanical Engineering, University of Utah, Salt Lake City, UT, USA

Los Alamos National Laboratory, Los Alamos, NM, USA
e-mail: tproberts@lanl.gov

S. A. Ouellette · A. J. Wachtor
Los Alamos National Laboratory, Los Alamos, NM, USA

Z. Mao (ed.), *Model Validation and Uncertainty Quantification, Volume 3*, Conference Proceedings of the Society for Experimental Mechanics Series, https://doi.org/10.1007/978-3-030-77348-9_8

hyperelastic modeling techniques that are commercially available in finite element codes, such as the ABAQUS UHYPER subroutine. The CHIPFoam model consists of four components—small deformation for capturing a buckling behavior in the foam, incompressible considerations for describing stiffening at large deformations, matrix compressibility to allow for a consistent response at large compressive strains, and an optional term to model the effects of gas compression in the cells of the foam [4]. CHIPFoam is designed to model the behavior of closed-cell polymer foams under large compressive loads. It is much more common for hyperelastic materials to be tested and fit to tensile loading data [3, 5, 6]. This work tests the CHIPFoam model in a purely compression regime with large values of compressive strain up to 48%.

The CHIPFoam model contains nine total parameters, some independent, some state-dependent, and others dependent on state and independent parameters. The nature of these parameters points to global sensitivity analysis methods rather than local as global methods can be used in large parameter spaces where coupling between parameters is of possible concern [7]. With any model, the exact value of any parameter is only known within some uncertainty. This is referred to as manufacturing process uncertainty. Ultimately, analysts want to know the variability in the solution to their model, given the uncertainty in each parameter in the model. By modeling the uncertainty of model parameters as a random set of variables, statistical sampling measures can be used to sample a parameter space and generate a sensitivity index for model inputs [8]. In this work, Latin hypercube sampling (LHS) is used to generate a suite of parameter sets that are used to evaluate finite element models. The results from these models are used for a variety of purposes—performing a sensitivity analysis on the CHIPFoam material model and simulating full responses of systems with closed-cell foam components.

The sensitivity of the model to parameter uncertainty will be evaluated based on the outputs of the suite of parameterized finite element models. Simple partial derivative-based methods, such as that proposed in ref [9], can be used for systems of multiple dependent inputs; however, this work uses a polynomial chaos expansion method within the Dakota toolbox, a previously developed statistical data analysis tool from the Sandia National Laboratory [10]. Using the parameter sets from the LHS process, models will be evaluated, and the resulting system responses will be recorded and processed for specific metrics. To gain insight into parameter sensitivity at more than just a single value of foam precompression, the polynomial chaos expansion method will be used, instead, at every value of displacement that is computed by the finite element models. With these techniques, a sensitivity index of all parameters that were considered will be generated as a function of the model's displacement regime.

In addition to studying the effects of material parameter uncertainty, this work quantifies the effects of uncertainties in the subsequent life cycle steps of the system—assembly conditions and environmental excitation. After manufacturing, closed-cell foams are typically assembled as vibration absorbers subject to preloading conditions. Ideally, the preloading process allows the dynamic response of the system to be easily targeted and adjusted; however, uncertainty in preloading conditions can hinder that advantage. Finally, uncertainty in the environmental excitation imposed on the system can result in unexpected dynamic behavior because of the complex mechanical response that is characteristic of closed-cell polymer foams. The coupling of material parameter uncertainty, preload uncertainty, and excitation uncertainty is hypothesized to result in large variation in frequency response and transitions to nonlinear vibration of an otherwise simple single degree of freedom (SDOF) oscillator.

2 Modeling

This work considers three forms of uncertainty to encompass the entire engineering life cycle of a closed-cell foam vibration absorber—manufacturing uncertainty, assembly condition uncertainty, and environmental excitation uncertainty. Each form of uncertainty is studied independently via three parametric studies, all of which are implemented using the 2D, plane strain finite element (FE) model shown in Fig. 1. The FE model consists of two instances of a closed-cell polymer foam; each instance of foam was assigned the CHIPFoam material model [4]. Suspended between the foam instances is a solid stainless steel mass. The choice of stainless steel as the suspended mass material is arbitrary as the material need only be rigid compared to the foam. The model is precompressed, or preloaded, via a displacement boundary condition at one end, and the other end is fixed. To help maintain the numerical stability of the CHIPFoam model, the long edges are constrained to prevent an outward projection of the foam. A dynamic excitation is applied as a nearly instantaneous initial velocity at the center of the suspended mass.

2.1 Manufacturing Process Uncertainty

Manufacturing process uncertainty is typically a result of uncertain control parameters involved in making the bulk material and in the forming of the meta-material. Closed-cell polymer foams are typically manufactured by forcing gas through the

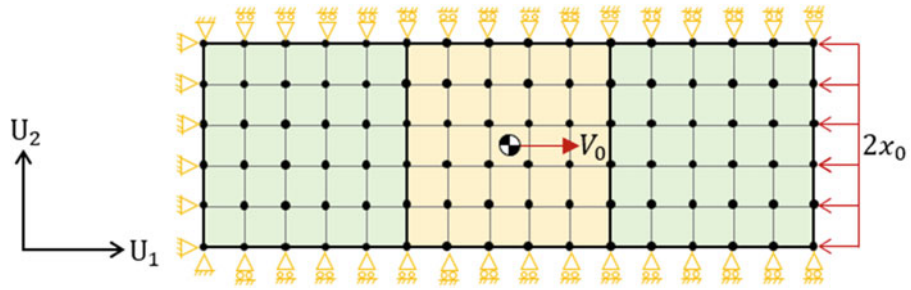

Fig. 1 Full system FE model schematic consisting of two instances of closed-cell foam (green, left and right) and a rigid suspended mass (yellow, center). The model is precompressed with a displacement boundary condition, x_0, and excited with an initial velocity applied to the suspended mass, V_0

Table 1 Sampling bounds and nominal values of material parameters for the manufacturing process parametric study

Parameter	Lower bound	Nominal value	Upper bound
Initial porosity (φ)	0.001	0.633	0.701
Bulk modulus [MPa] (K)	8.50	10.00	11.50
Neo-Hookean modulus [MPa] (C_{10})	0.0100	0.0148	0.0400
Nominal sample amount: 15			
Total simulations: 76 (75 parameterized, one nominal)			

A total of 76 FE simulations were generated using Latin hypercube sampling

heated bulk material [11]. Uncertainties in the mechanical properties of the bulk rubber and in the porosity that results from the gas-blowing process are represented in the CHIPFoam material model as bulk modulus K and initial porosity φ. An additional form of manufacturing process uncertainty that is considered in this parametric study is uncertainty in calibrated material model quantities, such as the neo-Hookean modulus C_{10}. Each of these three parameters encompasses relevant uncertainty in the manufacturing of the material and the utilization of the material model.

Latin hypercube sampling (LHS) is used to generate a suite of simulations for evaluating the FE model's dynamic response with respect to the changing parameters. A nominal value of 15 samples is drawn from a normal distribution of each of the three previously mentioned parameters. For each sample of the three model parameters, an additional two Null parameters are sampled. Since the Null parameters have no effect on the model, they will be used to set a threshold for parameter significance. The Null parameters are, essentially, setting a value for random noise in the simulation. Any noticeable effect from the Null parameters is an indication that the sensitivity analysis is not effectively representing the interactions between the physics of the model and the three selected parameters. A total of 76 parameter sets are generated; the nominal values and boundaries for the parameter distributions in this study are summarized in Table 1.

The two output quantities of this parametric study are the mechanical response of the material and a parameter sensitivity index for the material model. This study aims to illustrate the amount of variability in the material's mechanical response and the system's frequency response because of manufacturing process uncertainty. The parameter sensitivity index will indicate the extent to which small changes in material parameters affect the stiffness of the material. Polynomial chaos expansion (PCE) is used to assess the variance of the model with respect to the changing parameters, and the computation is done using tools within Dakota [10]. Polynomial chaos is chosen over other common variance analysis methods, such as analysis of variance (ANOVA), because PCE allows for a global, multiinput sensitivity analysis (SA) that also considers effects from dependent parameter coupling [12–14].

2.2 Assembly Condition Variability

The most significant source of uncertainty in the assembly process of a polymer foam vibration absorber is the precompression, or preload, of the foam sections. Polymer foams are designed to be preloaded to tailor the dynamic response of the object suspended between the foam sections. A typical force-displacement curve for the material is shown in Fig. 2, where x_0 is the equilibrium displacement of the suspended mass after preloading. After the application of precompression, each foam section (represented as a simple spring in Fig. 2) operates at a different equilibrium displacement, x_1' and x_2'. The stiffness of the foam is the displacement derivative of the curve and is represented by the red-dashed tangent lines in Fig. 2.

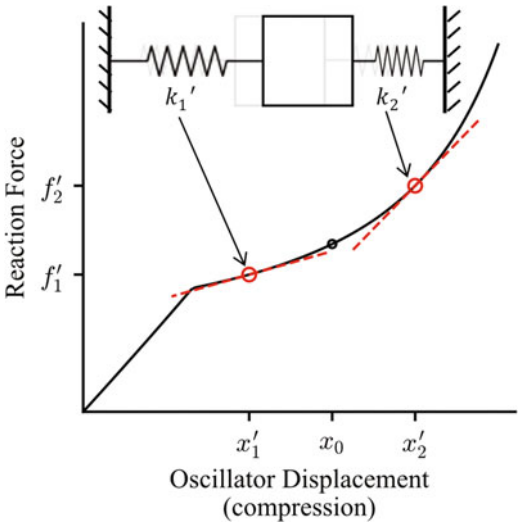

Fig. 2 Nonlinear stiffness schematic for a system consisting of a mass suspended by two pieces of closed-cell foam (shown as springs). Uncertainty in preloading conditions propagates to the static stress state, and therefore the stiffness, of each piece of foam

As the suspended mass vibrates, each piece of foam imposes a time- and displacement-varying restoring force on the mass. When uncertainty in the initial precompression of the model is present, this propagates to uncertainty in the restoring forces in the model and consequently uncertainty in the dynamic response of the suspended mass.

The effects of assembly condition uncertainty are quantified in a single-parameter study where the precompression value is varied to encompass the entire operating strain regime of the material. Other parameters, such as forcing conditions and material properties, are left constant for this parametric study.

2.3 Environmental Uncertainty

Uncertainty in the environment imposed on the system can accentuate the nonlinear behavior of the material, particularly because of strain-rate sensitivity and unexpected large amplitude oscillations. Strain-rate sensitivity is a property of the material where higher frequency oscillations cause the material to respond dynamically softer, i.e., a shift toward a lower resonant frequency, thus changing the stiffness-displacement response entirely. While this phenomenon is not directly addressed in this paper, the material model includes these effects in its formulation, and experiments have shown this behavior [15, 16]. Large amplitude oscillations can result from environmental excitations being higher than expected, and such oscillations can lead to drastic changes in the stiffness of the material. When the static stress state of the material is uncertain (due to assembly condition uncertainty), large deflections can cause the material to displace to unstable regimes of stiffness over time. This is qualitatively illustrated in Fig. 3. On the left, Fig. 3 depicts the typical force-displacement response of the material. Overlaid on the F-Δ curve are representations of how the system oscillates over the curve in time. Shown in green is a system that oscillates in the linear displacement regime and in blue a system that oscillates in a highly displacement-sensitive regime. On the right, Fig. 3 depicts the resulting time-varying stiffness of the foam for both linear- and displacement-sensitive systems.

It is important to note that the "linear" stiffness profile (shown in green) is not exactly linear as real data will rarely produce such behavior. However, the standard deviation in stiffness over time is less than 1%, and it can be considered linear compared to the displacement-sensitive stiffness profile. The displacement-sensitive stiffness profile (shown in blue) has a standard deviation in stiffness of 79.2%, and the stiffness experiences large fluctuations over time. When coupled with uncertainty in assembly conditions, unknown environmental conditions can drive a system from oscillating as expected (in the linear regime) detrimental dynamic behavior (in the displacement-sensitive regime) with only small changes in extrinsic properties.

The effects of environmental uncertainty are quantified in a single-parameter study where the magnitude of the shock velocity is varied to encompass all exceptions that allow the material model to maintain numerical stability. Other parameters, such as preload conditions and material properties, are left constant for this parametric study.

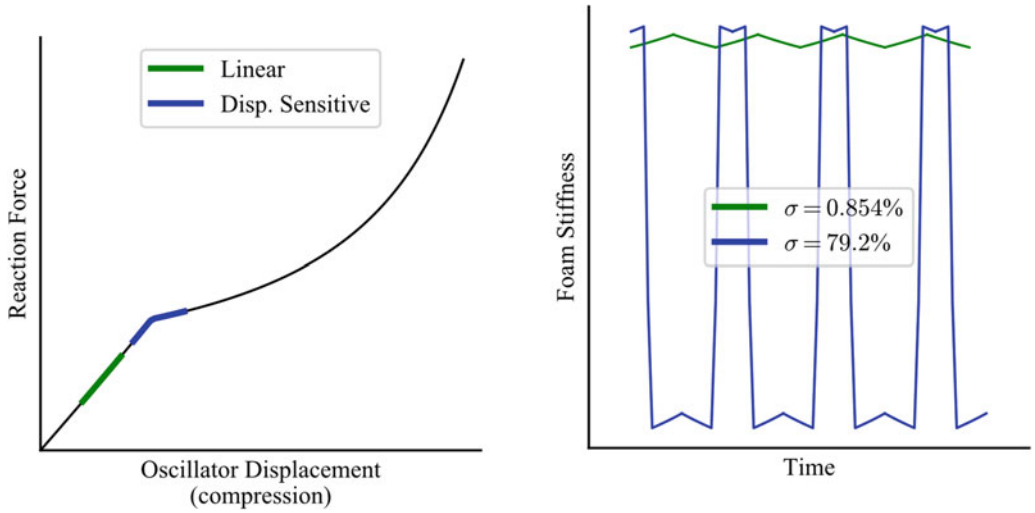

Fig. 3 Effect of environmental uncertainties on the stiffness of the material over time. Left: typical F-Δ response for closed-cell polymer foam with linear (green) and displacement-sensitive (blue) displacement regimes. As a system oscillates over these two displacement regimes, the stiffness over time can be dramatically influenced by uncertainty in preloading and environmental excitation

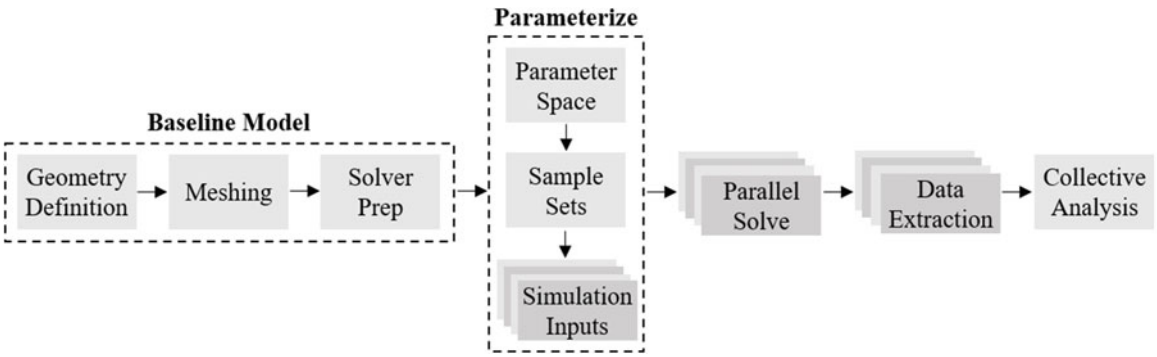

Fig. 4 Computational workflow for parametric studies. The baseline model is varied based on the parameter sampling distributions. Independent models can be solved, and data are extracted in parallel. Data are collectively analyzed with respect to the changing parameters

2.4 Computational Implementation

Each of the parametric studies starts with a baseline model with consistent geometry, meshing characteristics, and general preprocessing information. The material model, boundary conditions, and dynamic excitation take the same form in each parametric study. Sample sets are generated using a variety of strategies (LHS for multiple parameters, full factorial for single parameters), and the baseline model's preprocessing information is perturbated based on these parameter sets to fill the parameter space. The result is a suite of independent models that can be solved in parallel, and data are extracted in parallel to increase computational efficiency. The final step is to collectively analyze the data from all the models with respect to the varying parameters. Figure 4 illustrates this computational workflow.

3 Analysis

In this paper, uncertainty is represented as the variability in the mechanical response of the material and the frequency response of the suspended mass system. Manufacturing process uncertainty, assembly condition uncertainty, and environmental uncertainty are evaluated independently; no coupling of material parameter uncertainty, preload uncertainty, or excitation uncertainty is considered. A nominal model is defined with arbitrarily chosen precompression and shock excitation

values, and material parameters are chosen to represent a single sample of closed-cell polymer foam. It should be noted that the dynamic response of the system is expected to be dependent on all parameters simultaneously.

3.1 Material Parameter Uncertainty

The first output of the material model parametric study is the variability in the mechanical response of the foam as a result of uncertainty in material parameters; this is shown on the left in Fig. 5. In certain strain regimes, especially after the cell wall buckling phase, the restoring force from the foam is more than an order of magnitude different because of uncertain material parameters. A brief inspection of the parameter sets that cause this variation leads to a suspicion that the initial porosity drives the stiffness of the material. Qualitatively, the general shape of the force-displacement curves changes significantly with uncertainty in the material parameters. For example, the sharp transition from bending to buckling of the cell walls completely disappears as the material becomes less porous and more homogeneous, and the transition from elastic bending to cell wall buckling has a significant influence on the stiffness of the material over time.

The second output of the material model parametric study is the material parameter sensitivity index, which is shown on the right in Fig. 5. The sensitivity index supports the conclusions from the force-displacement results and physical intuition that suggest that porosity has the most influence on the material's stiffness. In addition, the sensitivity index provides insight pertaining to the functionality of the material model. The sensitivity index provides verification that the material model is working correctly as the strain-regime-dependent parameters (bulk modulus and neo-Hookean modulus) show significance only in the strain regimes they are designed to model. Furthermore, the Null parameters account for other parameters in the model that were not considered in the parametric study but might still have an effect on the model. The varying significance of the Null parameters suggests that some variation happening in the model cannot be captured by the variation in φ, K, and C_{10} alone.

As a result of significant changes in porosity, the natural frequency of the system is shown to be sensitive to uncertainties in the material model parameters. Figure 6 shows the frequency response at the upper and lower ends of the parameter space as well as the frequency response of the arbitrary nominal model. In this parameter space, the fundamental frequency of the system shows over 71% variation. As previously mentioned, the nominal model is chosen with arbitrary properties, so it is not of concern that the nominal model is biased toward one end of the parameter space.

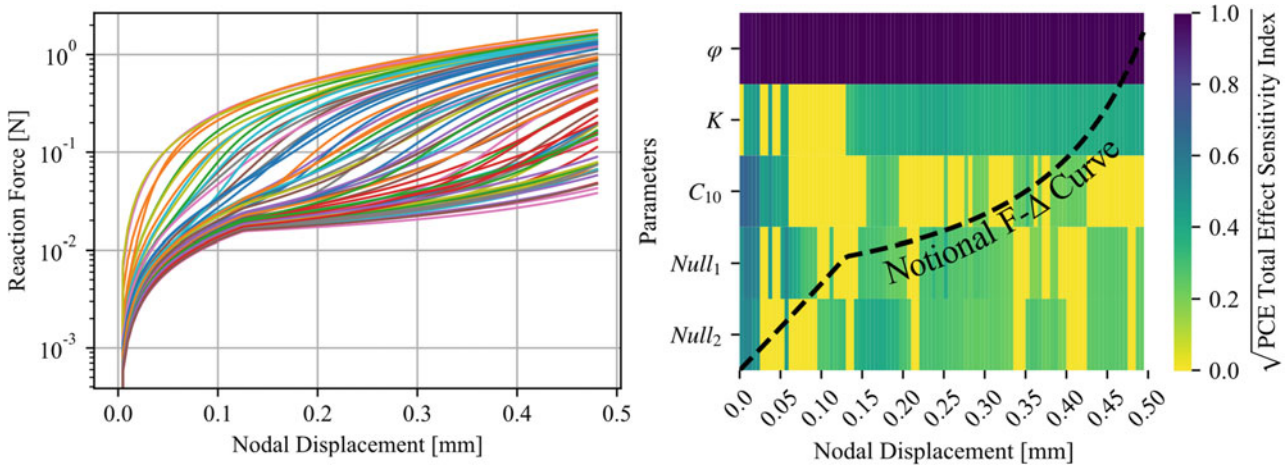

Fig. 5 Variation in mechanical properties and material parameter sensitivity index from the manufacturing process parametric study. Left: 76 force-displacement curves are the direct output of the material model parametric study. Right: material parameter sensitivity index that maps the influence of each parameter on the stiffness of the material to the operating strain of the material

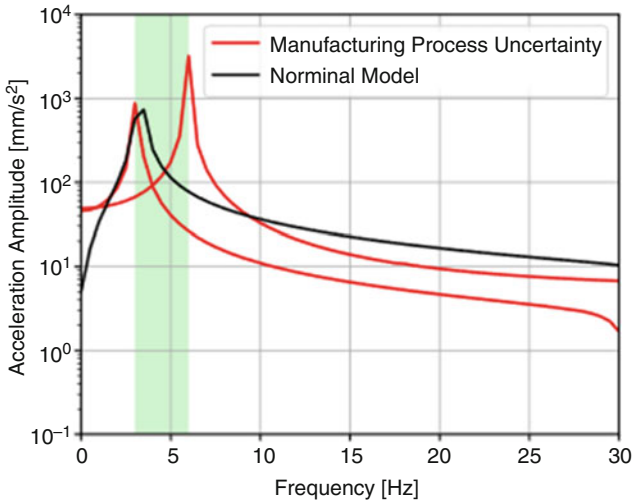

Fig. 6 Frequency response of the closed-cell foam and suspended mass FE model over the manufacturing process uncertainty parameter space. Manufacturing process uncertainty results in 71% variation in the fundamental frequency of the system

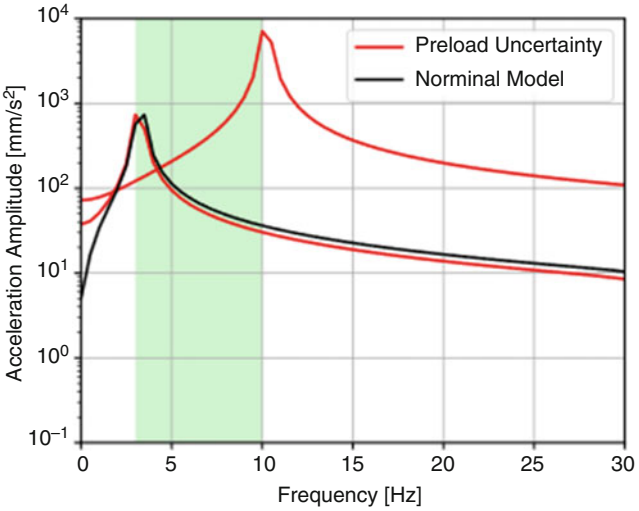

Fig. 7 Frequency response of the closed-cell foam and suspended mass FE model over the assembly condition uncertainty parameter space. Preload uncertainty results in 185% variation in the fundamental frequency of the system

3.2 Preload Uncertainty

In the parametric study for preload uncertainty, the material parameters and shock excitation are held constant. The nominal model is excited with relatively small excitation to keep the material model in a compressive state through all values of preload in the parameter space; this is a requirement based on the formulation of the numerical subroutine used to implement the material model. In addition, small excitations will result in small oscillations, so the effects of a time-varying stiffness of the material are not meant to be captured in this parametric study. Figure 7 shows the frequency response of the upper and lower ends of the parameter space. The variation in preload alone is enough to significantly change the stiffness of the foam, even though the foam is locally acting linearly (small displacements). This parameter space results in over 185% variation in the fundamental frequency of the system.

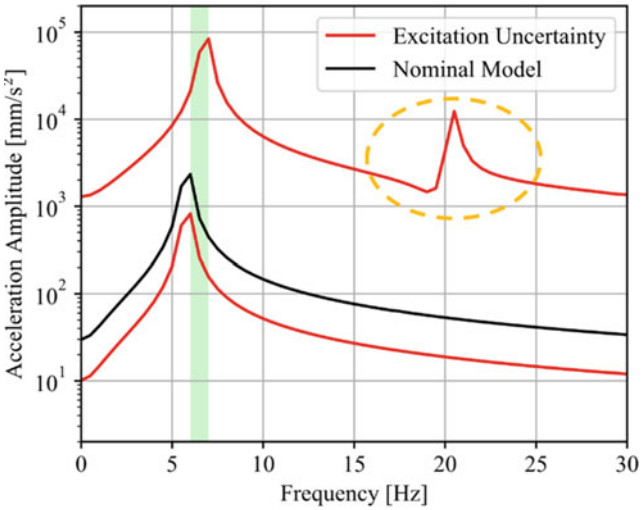

Fig. 8 Frequency response of the closed-cell foam and suspended mass FE model over the environmental uncertainty parameter space. Environmental excitation uncertainty results in a 16% variation in the fundamental frequency of the system. The upper end of the parameter space indicates a transition from linear, harmonic oscillation to nonlinear vibration because of extreme loading conditions

3.3 Excitation Uncertainty

For the excitation uncertainty parametric study, shock velocities are chosen to fill the parameter space with the extremes of the material model's capability while still maintaining a compressive state for numerical stability. To allow this, the preloading was still held constant but was increased compared to the other two parametric studies. Figure 8 shows the frequency response of the upper and lower ends of the parameter space where the result is a 16% variation in fundamental frequency. Though this variation is significantly less than that from the other two sources of uncertainty, Fig. 8 exhibits unique behavior as a result of the time-varying stiffness characteristics of the material.

A truly linear, SDOF oscillator will have only one resonance in its frequency response; however, the upper edge of this parameter space shows that extra peaks appear in the frequency response. In this case, the system is responding with multiple resonances at higher energies than the fundamental frequency, and the amplitude of the entire response is of comparable magnitude to the peak values at the other end of the parameter space. From a design perspective, this phenomenon is problematic as there are now multiple resonance frequencies to avoid within the systems' operating frequency range. In addition, this parametric study shows behavior at the boundaries of the parameter space, but it is of interest to know what parameter combinations cause such nonlinear behavior to occur.

4 Conclusion

In this paper, three sources of uncertainty were considered to analyze the effects of model form uncertainty throughout the entire engineering life cycle of closed-cell polymer foam vibration absorbers.

Manufacturing process uncertainty can significantly affect the features present in the mechanical response of the material. Foams are generally designed to be compressed to the plateau region of the F-Δ curve, but some combinations of material parameters cause that characteristic of the F-Δ curve to disappear entirely. It is not possible to test every piece of foam that is manufactured, so it is imperative to predict all possible outcomes that result from uncertainty in material parameters.

Assembly condition uncertainty has large effects on the stiffness of the material, even when small oscillations allow the material to act locally linear. In addition, the nonlinear nature of the material's stiffness causes each piece of foam to have different, time-varying stiffness that is sensitive to the equilibrium stress state. When coupled with uncertain levels of excitation, the material could bifurcate to strain regimes with unstable stiffness characteristics.

Environmental uncertainty that results in more extreme conditions than designed for can cause the amplitude and the frequency(s) of the system's response to shift significantly. In some cases, excitation becomes large enough that stiffness fluctuations cause a previously linear vibratory system to exhibit nonlinear characteristics.

Considerations for parametric modeling – model stability can be dependent on both physical and numerical constraints, and both need to be equally considered in parametric modeling. One of the main considerations when employing a computational model is numerical stability, which is independent of physical constraints. For example, the CHIPFoam model used in this work must always be in a compressive state. Otherwise, the model yields unstable and unphysical results. The problem may define a physical parameter space that exceeds the stability limits of the computational model (i.e., assumed excitation uncertainty has upper limits that exceed the capabilities of the model). In this case, an engineering analyst has two choices—tighten the threshold on physical uncertainties or improve the capabilities of the model.

Considerations for parametric modeling – bounding versus *explicit modeling*: the response of the system can yield a wide range of results with varying implications. In general, the three parametric studies discussed in this paper are cases of bounding studies. The results presented illustrate the system's response at the edges of the parameter space to determine total uncertainty and assess the effects of changing parameters. This is efficient as we postprocess and analyze fewer data sets, and this is a reasonable approach so long as the entire parameter space exhibits the same general characteristics. Bounding is problematic when there are significant changes to the architecture of the response within the parameter space. For example, the excitation uncertainty parametric study did not quantify the transition from a linear to a nonlinear vibration of the system. When only a single bounding metric (i.e., fundamental frequency) is considered, analysts risk overlooking other detrimental behaviors hidden within the parameter space.

Explicit modeling entails studying, in detail, the solution to every parameter set. This is expensive as a full-fidelity solution needs to be computed for all parameters. However, an explicit modeling strategy allows the advantages of bounding as well as identifying unexpected behavior within the parameter space.

Acknowledgments This work was funded under the auspices of the Advanced Engineering Analysis Group at Los Alamos National Laboratory (LANL, W-13) and done in collaboration with the LANL National Security Education Center – Engineering Institute (NSEC-EI).

The main author would like to express great thanks to his mentors, Dr. Scott Ouellette (LANL, W-13) and Dr. Adam Wachtor (LANL, NSEC-EI), for their professional guidance and the opportunity for this work. The authors would also like to recognize the following individuals of LANL's Advanced Engineering Analysis Group for their knowledge and assistance with computational resources: Dr. Kyle Brindley, Thomas Lebrun, Isaac Salazar, Brandon Stone, and Dr. Trevor Tippetts.

References

1. Bergström, J.: Elasticity/Hyperelasticity. In: Mechanics of Solid Polymers, pp. 209–307. Elsevier (2015)
2. Ali, A., Hosseini, M., Sahari, B.: A review of constitutive models for rubber-like materials. Am. J. Eng. Appl. Sci. **3**(1), 232–239 (2010)
3. Ogden, R.W., Saccomandi, G., Sgura, I.: Fitting hyperelastic models to experimental data. Comput. Mech. **34**, 484–502 (2004)
4. Lewis, M.: A robust, compressible, hyperelastic constitutive model for the mechanical response of foamed rubber. Tech. Mech. **36**(1–2), 88–101 (2015)
5. Khajehsaeid, H., Arghavani, J., Naghdabadi, R.: A hyperelastic constitutive model for rubber-like materials. Eur. J. Mech. A. Solids. **38**(1), 144–151 (2013)
6. Wu, Y., Wang, H., Li, A.: Parameter identification methods for hyperelastic and hyper-viscoelastic models. Appl. Sci. **6**(12), 386–399 (2016)
7. Ouisse, M., Ichchou, M., Chedly, S., Collet, M.: On the sensitivity analysis of porous material models. J. Sound Vib. **331**(1), 5292–5308 (2012)
8. Mckay, M.D., Beckman, R.J., Conover, W.J., and: A comparison of three methods for selecting values of input variables in the analysis of output from a computer code. Technometrics. **42**(1), 55–61 (1979)
9. Hajhashemkhani, M., Hematiyan, M.: Determination of material parameters of isotropic and anisotropic hyper-elastic materials using boundary measured data. J. Theor. Appl. Mech. **54**(4), 895–910 (2015)
10. Dakota: Explore and predict with confidence. National Technology and Engineering Solutions of Sandia, LLC., 2017. [Online]. Available: https://dakota.sandia.gov/content/getting-dakota-source-code. Accessed 12 Aug 2019
11. Altan, M.: Thermoplastic foams: processing, manufacturing, and characterization. IntechOpen. (2017). https://doi.org/10.5772/intechopen.71083
12. Sudret, B.: Global sensitivity analysis using polynomial chaos expansions. Reliab. Eng. Syst. Saf. **93**, 964–979 (2008)
13. Crestaux, T., Maitre, O.L., Martinez, J.: Polynomial chaos expansion for sensitivity analysis. Reliab. Eng. Syst. Saf. **94**, 1161–1172 (2009)
14. Ni, P., Xia, Y., Li, J., Hao, H.: Using polynomial chaos expansion for uncertainty and sensitivity analysis of bridge structures. Mech. Syst. Signal Process. **119**, 293–311 (2019)
15. Barnes, T.A., Ravi-Chandar, K., Kyriakides, S., Giatanaros, S.: Dynamic crushing of aluminum foams: part I - experiments. Int. J. Solids Struct. **51**, 1631–1645 (2014)
16. Linul, E., Marsavina, L., Kovacik, J., Sadowski, T.: Dynamic and quasi-static compression tests of closed-cell aluminum foams. Proc. Romanina Acad. Ser. A. **18**(4), 361–369 (2017)

Uncertainty Quantification and Effectiveness of Cantilevered Pipeline Conveying Fluid with Constraints

Timothy Alvis, Samantha Ceballes, Michael Ross, and Abdessattar Abdelkefi

Abstract Researchers have studied cantilevered pipelines conveying fluid for many decades for their practical applications and interesting dynamic behaviors. These applications can include oil pipelines and risers, mechanical pumps, and micro-/nanofluidic nanotubes, which can be used in drug delivery. Because the stability of these systems is so important to companies and industries, many researchers have investigated methods to improve their overall system stability. Some of the implemented methods include adding a mass to the tip of the pipe and motion-limiting constraints. The constraints introduce an impacting force that can produce interesting nonlinear chaotic behavior. The implementation of ideas and strategies that improve system stability leads to increasingly more complex systems with a greater number of input parameters. The cantilevered pipe conveying fluid itself already has many parameters to consider, including the flow speed, smoothness of the internal structure, size of the pipe, and position of motion-limiting constraints, to name a few. Additionally, each input parameter possesses its own uncertainty. The propagation of uncertainty in these parameters can significantly alter the dynamic response and stability of the proposed system. It is important for engineers to design the system with a firm understanding of how the system is going to behave and respond in the presence of these uncertainties. Therefore, it is necessary to employ uncertainty quantification methods. In this study, a sensitivity analysis is performed on a cantilevered pipeline conveying fluid with motion-limiting constraints to determine which parameters in the system are most dominant. By finding these dominant parameters, more uncertainty quantification methods can be employed to better understand the response of the system.

Keywords Uncertainty quantification · Nonlinear behavior · Fluid-structure interaction

1 Introduction

Researchers have been studying the cantilevered pipeline system conveying fluid and its highly nonlinear behavior for decades. This is because the system has a wide variety of practical applications, including mechanical pumps [1], pipelines and risers [2], and micro-/nanosystems that are often used in drug delivery applications [3]. The cantilever pipeline conveys fluid at varying flow speeds, and once the flow speed reaches a critical velocity, the pipeline begins to oscillate periodically and can eventually become chaotic. In an attempt to better control the system, many researchers have implemented different additions to the cantilevered pipeline systems. Some of these additions include a mass to the tip of the pipe and motion-limiting constraints. Many improvements have been observed by these additions, but research is still needed to fully understand how the uncertainties in the input affect the behavior of the system.

Understanding how a system behaves in all scenarios is one of the most important aspects engineers must study during the design process. This is particularly challenging because many of the parameters that can affect the system in any way are unknown to the engineers designing the system. Therefore, it is important that researchers study many different variations of parameters to ensure that the system will work for various combinations of input parameters. Some of these unknown parameters that engineers must research are different environmental factors like wind speeds and forces imparted by strong gusts of wind or how temperature shifts may affect the materials used to make the system. Other parameters come from the

T. Alvis (✉) · S. Ceballes · A. Abdelkefi
Department of Mechanical and Aerospace Engineering, New Mexico State University, Las Cruces, NM, USA
e-mail: tim48@nmsu.edu

M. Ross
Sandia National Laboratories, Albuqueurque, NM, USA

Z. Mao (ed.), *Model Validation and Uncertainty Quantification, Volume 3*, Conference Proceedings of the Society for Experimental Mechanics Series, https://doi.org/10.1007/978-3-030-77348-9_9

manufacturing of the system itself. The material properties alone can slightly change by the way the material was refined. Additionally, the machines cutting and drilling the different parts of the system are not completely accurate and can lead to the finished product being slightly different than it was designed to be. Although the differences caused by these inaccuracies are usually very close to the original design, these small differences in the input can have significant impacts on the output of the system. This work shows the modeling of a cantilevered pipeline system that conveys fluid and studies how uncertainty in several of the inputs affects at which flow speed the onset of instability occurs.

2 Modeling

The extended Hamilton's principle is employed to find the system's equations of motion following the work of Semler et al. [4]. Many assumptions are made that make the calculations easier, including that the fluid is incompressible, the pipeline is inextensible, and the pipeline diameter is small compared to the length, allowing for the use of the Euler-Bernoulli beam theory. Using Galerkin's method to discretize the equation of motion and following the work of Taylor et al. [5], the following reduced-order model is obtained:

$$\begin{aligned}\ddot{q}_i + \left[C_{ij} + u(Cu)_{ij}\right]\dot{q}_j + \left[K_{ij} + u^2(Ku)_{ij}\right]q_j + \left[M_{ijkl}\right]\dot{q}_j\dot{q}_k q_l \\ + \left[uN_{ijkl}\right]\dot{q}_j q_k q_l + \left[P_{ijkl} + u^2(Pu)_{ijkl}\right]q_j q_k q_l = 0\end{aligned} \tag{1}$$

Because this research only focuses on the onset of instability, the nonlinear terms can be disregarded due to the fact that an eigenvalue problem analysis is all that is required to find the critical flow speed. This is because the onset of instability occurs when the damping coefficient changes sign.

3 Analysis

This effort investigates how a uniform input distribution with ±5% uncertainty applied to the following five parameters: outer diameter (*OD*), inner diameter (*ID*), length (*L*), density (ρ), and modulus of elasticity (*E*), which can alter the system's output. Each parameter is varied at the same time by randomly selecting a value that is plus or minus a percent of the designed value. The output distribution for the onset speed of instability for this analysis is shown in Fig. 1.

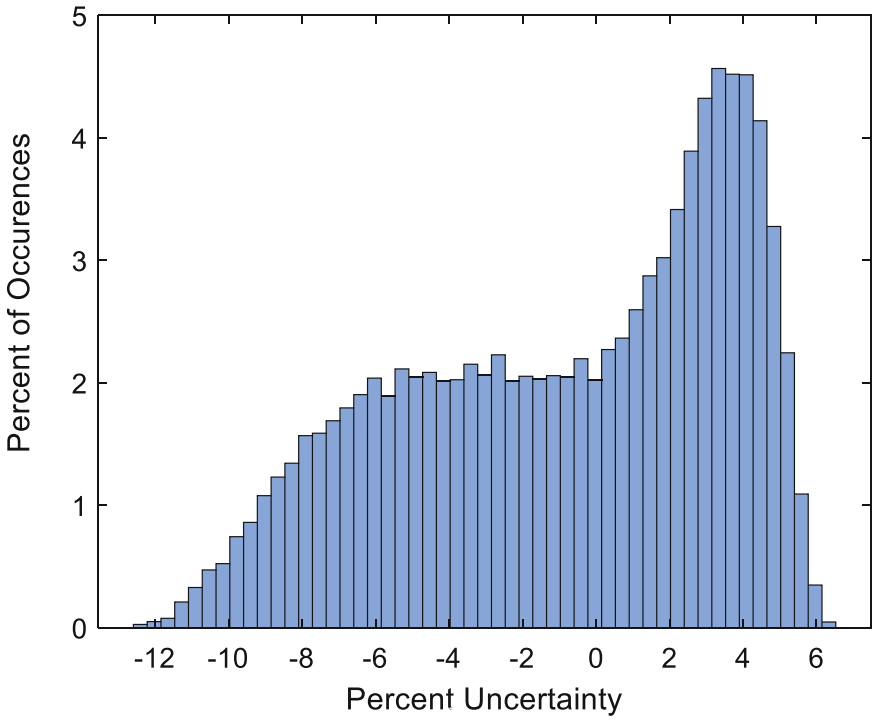

Fig. 1 Output distribution of onset speed of instability while varying five parameters

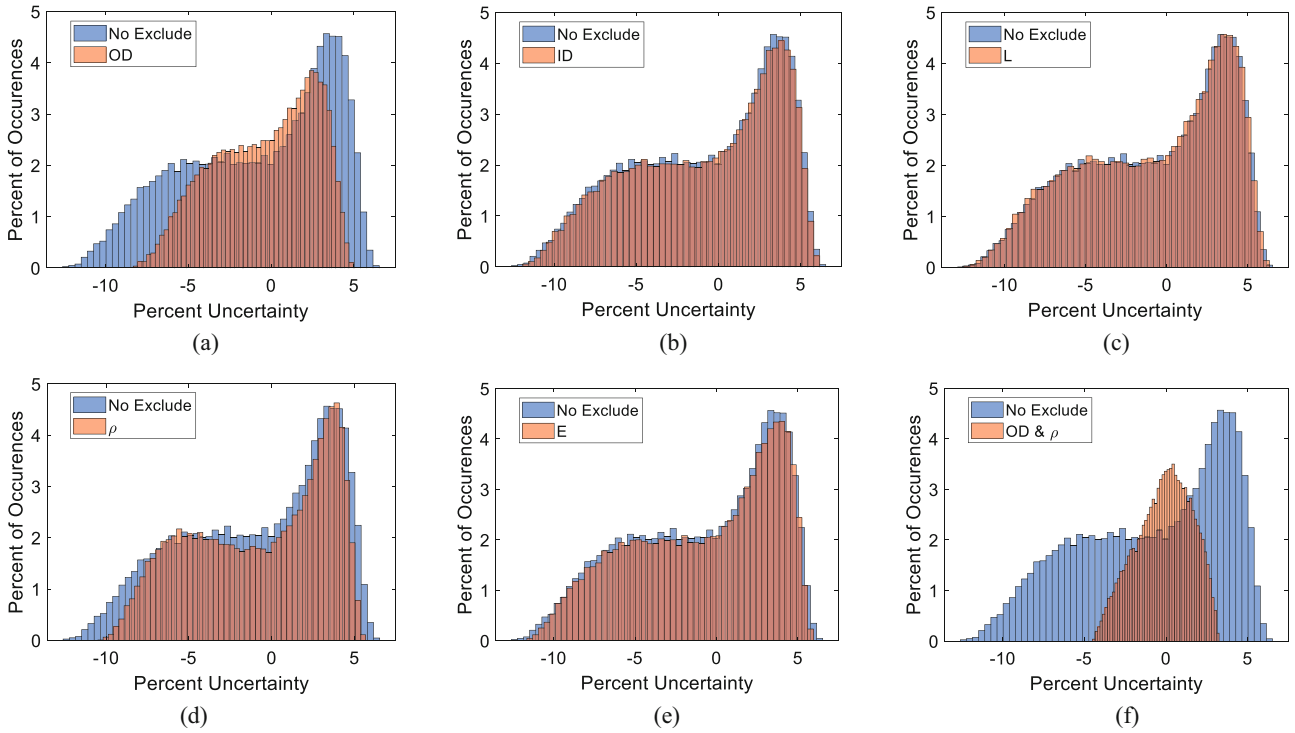

Fig. 2 Output distribution while varying four parameters and keeping one constant. The constant parameters in each graph are (**a**) outer diameter, (**b**) inner diameter, (**c**) length, (**d**) density, (**e**) modulus of elasticity, and (**f**) both outer diameter and density

Usually while performing an uncertainty quantification analysis, the output distribution is Gaussian around the designed output. This is preferable because the system behaves close to how it was designed even though there is some uncertainty introduced into it. It is clear to see by investigating Fig. 1, however, that this is not the case with this system. There is a wide range of uncertainty in the output, and there is a peak of outputs above the designed flow speed. This behavior is likely caused by the interaction between the parameters, and a nonlinear reaction from the parameters. To have the system behave as close to the designed case as possible, it is important to find which parameters are most impacting the system. Once the most influential parameters are determined, the designing engineers can find the best methods to decrease the uncertainty in those specific parameters to keep the output as close to the designed response as possible. To determine the most influential parameter, the same uncertainty analysis is run another five times where one parameter is kept at its original value while the other parameters are varied. The results are shown in Fig. 2. It is clear that the outer diameter and density are the most influential parameters. Keeping them constant results in obtaining output-dominant results near the ideal case, as shown in Fig. 2f.

4 Conclusions

For the system under investigation, it was determined that the most influential parameters are the outer diameter and density. This is clear because the other parameters show the same output distribution as when they are held constant. Because the density has a similar output distribution but lower range of uncertainty, it can be determined that the outer diameter is more influential than the density. It is important for designing engineers to keep the uncertainty in these two parameters as low as possible.

Acknowledgments Authors T. Alvis and A. Abdelkefi would like to thank Sandia National Laboratories for their funding of this project. Authors S. Ceballes and A. Abdelkefi would like to thank the National Science Foundation Graduate Research Fellowship Program for funding support. *Sandia National Laboratories is a multi-mission laboratory managed and operated by National Technology and Engineering Solutions of Sandia, LLC, a wholly owned subsidiary of Honeywell International Inc., for the U.S. Department of Energy's National Nuclear Security Administration under contract DE-NA0003525. SAND2020-13519 A.*

References

1. Askarian, A.R., Haddapour, H., Firouz-Abadi, R., Abtahi, H.: Nonlinear dynamics of extensible viscoelastic cantilevered pepes converying pulsatile flow with an end nozzle. Int. J. Non Linear Mech. **91**, 22–35 (2017)
2. Housner, G.W.: Bending vibrations of a pipe when liquid flows through it. J. Appl. Mech. **19**, 205–208 (1952)
3. Rinaldi, S., Prabhakar, S., Vengallator, S., Paidoussis, M.: Dynamics of microscale pipes containting internal fluid flow: damping, frequency shift, and stability. J. Sound Vib. **329**, 1081–1088 (2010)
4. Semler, C., Li, G.X., Paidoussis, M.P.: The non-linear equations of motion of pipes conveying fluid. J. Sound Vib. **169**(5), 577–599 (1994)
5. Taylor, G., Ceballes, S., Abdelkefi, A.: Insights on the point of contact analysis and characterization of constrained pipelines conveying fluid. Nonlinear Dyn. **93**, 1261–1275 (2018)

Playability of a 1734 Guarneri Cello: Info-Gap Robustness Analysis of Uncertainty

R. Viala, S. Le Conte, S. Vaiedelich, S. Cogan, and Y. Ben-Haim

Abstract Mechanical stresses due to strings are imposed on an instrument when it is played. Such stress can lead to long-term strains or damages. In the cultural heritage domain, this can prevent an instrument from being played if the risk of damage is too high. Most of the properties of such instrument are uncertain, such as mechanical parameters, relative humidity or already existing cracks. Model-based approaches dealing with deep uncertainties can be a very efficient approach for decision support. In this paper, an example is given with an antique cello, which exhibits damages, especially boreholes or galleries created by wood-eating insects. A model is created for static analysis to compute the stress field that will be used as a basis for the info-gap robustness analysis of the uncertainties and their impact on the sustainability of the instrument, considering defects, probabilistic distributions of elastic constants and Knightian uncertainties of yield stresses of wood.

Keywords Cultural heritage · Chordophones · Info-gap robustness analysis · Uncertainties · Wood mechanics · Decision support tool

1 Introduction

Substantial mechanical stresses are imposed on a musical instrument when it is played. These stresses can result in damage to the instrument, and the decision to allow the use of an instrument depends on assessing the potential for this damage. This decision is particularly difficult and important when dealing with a heritage instrument of great cultural value but of uncertain mechanical properties. Numerous mechanical properties are relevant, including environmental humidity and temperature. In addition, typical string instruments contain components made of maple, ebony, and spruce, and these types of wood have different and variable rigidity, density and elastic limits. Finally, the criterion for mechanical failure depends on mechanical properties, geometry, temperature and humidity, in a functional form that may be uncertain.

Models can be used to support decisions on playability. However, models – and the data and knowledge upon which they are based – are sometimes subject to deep uncertainty, as mentioned above. Deep uncertainty refers to situations involving substantial disparity between what is known and what needs to be known in order to support a responsible decision. Deep uncertainty is a nonprobabilistic state of ignorance about some important aspects of the decision. Under deep uncertainty, it is useful to assess the model-based decision for its robustness to ignorance, error or surprise. This will enhance the decision-maker's confidence that the outcome of the decision will be acceptable. In this paper, we develop a model as a basis to employ the info-gap decision theory [1] to evaluate robustness and support decision-making.

The study focuses on an antique cello, made by Pietro Guarneri in 1734 and kept at La cite de la Musique – Philharmonie de Paris. The cello exhibits numerous previously repaired cracks and a gallery made by wood-eating insects. As curators aim at bringing the cello to a playable state, the issue of the gallery has been raised as a potential weakness and cause of crack

R. Viala
Institut Technologique Européen des Métiers de la Musique, ITEMM, Le Mans, France

S. Le Conte · S. Vaiedelich
Musée de la musique Cité de la musique, Philharmonie de Paris, France

S. Cogan (✉)
FEMTO-ST Institute, Department of Applied Mechanics, University of Franche-Comté, Besançon, France
e-mail: scott.cogan@univ-fcomte.fr

Y. Ben-Haim
Yitzhak Moda'i Chair in Technology and Economics, Technion — Israel Institute of Technology, Haifa, Israel

Z. Mao (ed.), *Model Validation and Uncertainty Quantification, Volume 3*, Conference Proceedings of the Society for Experimental Mechanics Series, https://doi.org/10.1007/978-3-030-77348-9_10

ignition when the strings will be stretched. The application will be performed on a model of the cello, similar to the one presented in ref. [2]. The model of the cello is developed to evaluate the stress field subsequent to the tension of strings when they are tuned to be played. The Hill yield criterion [3] is used as an estimator of the potential damage near a defect due to wood-eating insects. The elastic constants of the back are modified, and the evolution of the Hill criterion is studied. This study is a starting point for info-gap decision-making under severe uncertainties.

2 Analysis

The robustness analysis is based on the Hill yield criterion. This mechanical feature is computed using the finite element method applied on the computer-aided design of the cello, shown in Fig. 1. The computer-aided design is made of 40 solids constructed to match the dimensions of the real cello, following steps close to the ones used by makers for real instruments. The study focuses on the existing defect due to wood insects that carve a gallery on the bottom left part of the back. The gallery is modelled as an application area of the Hill yield criterion. The gallery is simplified as a circular-shaped removal of material. The Hill yield criterion is based on stress field components and yield stresses of wood in different directions.

The cello is modelled as a mechanical system, under continuous linear orthotropic elastic hypotheses, where stress is associated with strain, as given in Eq. (1):

$$\begin{Bmatrix} \sigma_{11} \\ \sigma_{22} \\ \sigma_{33} \\ \sigma_{12} \\ \sigma_{23} \\ \sigma_{31} \end{Bmatrix} = [S]^{-1} \begin{Bmatrix} \varepsilon_{11} \\ \varepsilon_{22} \\ \varepsilon_{33} \\ \varepsilon_{12} \\ \varepsilon_{23} \\ \varepsilon_{31} \end{Bmatrix} \tag{1}$$

With S as the compliance matrix, given by Eq. (2):

$$[S] = \begin{bmatrix} S_{11} = \frac{1}{E_{11}} & S_{12} = -\frac{\nu_{12}}{E_{11}} & S_{13} = -\frac{\nu_{13}}{E_{11}} & & & \\ S_{21} = -\frac{\nu_{21}}{E_{22}} & S_{22} = \frac{1}{E_{22}} & S_{23} = -\frac{\nu_{23}}{E_{22}} & & 0 & \\ S_{31} = -\frac{\nu_{31}}{E_{33}} & S_{32} = -\frac{\nu_{32}}{E_{33}} & S_{33} = \frac{1}{E_{33}} & & & \\ & & & S_{44} = \frac{1}{G_{12}} & & \\ & 0 & & & S_{55} = \frac{1}{G_{23}} & \\ & & & & & S_{66} = \frac{1}{G_{31}} \end{bmatrix} \tag{2}$$

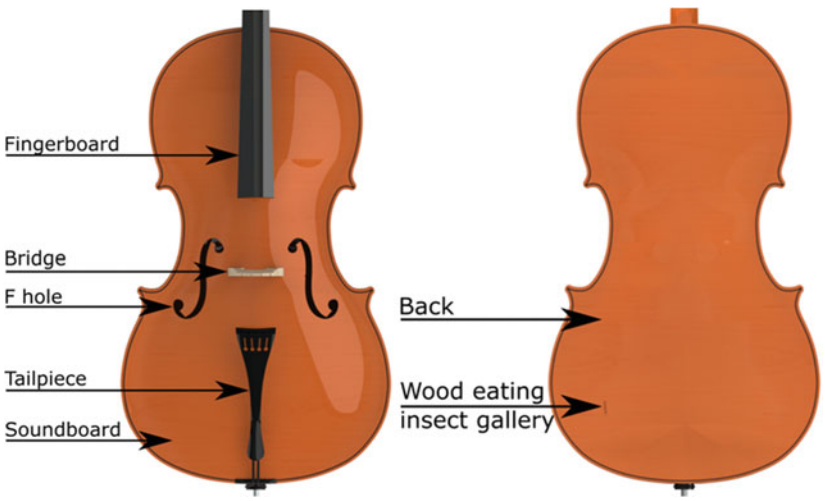

Fig. 1 Computer-aided design of the 1734 Pietro Guarneri cello. Left: top view, right back view

Table 1 Initial values of the elastic and physical constants, values from refs. [4–6]

	Species			
	Spruce	Maple	Ebony	Rosewood
E_L (MPa)	12,350	12,200	15,700	15,700
E_R (MPa)	955	1820	2500	2500
E_T (MPa)	655	1030	1570	1450
ν_{LR}	0.37	0.33	0.33	0.33
ν_{RT}	0.48	0.68	0.68	0.68
ν_{TL}	0.02	0.03	0.03	0.03
G_{LR} (MPa)	800	1370	1850	1610
G_{RT} (MPa)	44	430	650	610
G_{TL} (MPa)	770	1010	1370	1300
Specific gravity	0.44	0.64	1.09	0.78

Table 2 String tension and tuning frequency of the four strings of the cello, for a string length equal to 690 mm

	Strings			
	C	G	D	A
Frequency (Hz)	65.4	98	146.8	220
Tuning tension (N)	130	135	135	160

Where E_{ii} corresponds to Young's moduli of wood in ii direction, G_{ij} corresponds to shear moduli in ij plane, and ν_{ij} corresponds to Poisson's ratios in the ij plane. The initial values of the elastic constants are given in Table 1.

The stiffness matrix $[K]$ of the system is created using the finite element method based on the computer-aided design of the instrument. The static analysis is performed following Eq. (3):

$$[K]\{u\} = \{f\} \tag{3}$$

with $\{u\}$ as the translation displacement vector of n degrees of freedom and $\{f\}$ the vector of the forces applied on the system. The strain field $[\varepsilon]$ is based on the displacement results. The stress field $[\sigma]$ is then calculated following a linear elastic behaviour. The yield criterion, H, is given by the Hill criterion, for an orthotropic material, in Eq. (4):

$$H = E(\sigma_{22} - \sigma_{33})^2 + F(\sigma_{33} - \sigma_{11})^2 + G(\sigma_{11} - \sigma_{22})^2 + 2L\sigma_{23}^2 + 2M\sigma_{31}^2 + 2N\sigma_{12}^2 \tag{4}$$

with:

$$E = \frac{1}{2}\left[\frac{1}{(\sigma_2^y)^2} + \frac{1}{(\sigma_3^y)^2} - \frac{1}{(\sigma_1^y)^2}\right]; F = \frac{1}{2}\left[\frac{1}{(\sigma_3^y)^2} + \frac{1}{(\sigma_1^y)^2} - \frac{1}{(\sigma_2^y)^2}\right]; G = \frac{1}{2}\left[\frac{1}{(\sigma_1^y)^2} + \frac{1}{(\sigma_2^y)^2} - \frac{1}{(\sigma_3^y)^2}\right]$$

$$\begin{aligned} E &= \tfrac{1}{2}\left[\tfrac{1}{(\sigma_2^y)^2} + \tfrac{1}{(\sigma_3^y)^2} - \tfrac{1}{(\sigma_1^y)^2}\right]; F = \tfrac{1}{2}\left[\tfrac{1}{(\sigma_3^y)^2} + \tfrac{1}{(\sigma_1^y)^2} - \tfrac{1}{(\sigma_2^y)^2}\right]; G = \tfrac{1}{2}\left[\tfrac{1}{(\sigma_1^y)^2} + \tfrac{1}{(\sigma_2^y)^2} - \tfrac{1}{(\sigma_3^y)^2}\right] \\ L &= \tfrac{1}{2(\sigma_{23}^y)^2}; M = \tfrac{1}{2(\sigma_{31}^y)^2}; N = \tfrac{1}{2(\sigma_{12}^y)^{2.}} \end{aligned} \tag{5}$$

In Eqs. (4) and (5), σ_{ii} corresponds to the axial stress value in ii direction, σ_{ij} the shear stress value in ij plane, σ_{ii}^y the yield axial stress of maple wood in ii direction (whose values can differ between compression and tension), and σ_{ij}^y the yield shear stress of maple wood in ij plane. A value of H equal to 1 corresponds to the limit of elastic behaviour and the beginning of plastic behaviour. Under standard relative humidity (50%) and temperature (21 °C) values, resulting in moisture content between 8% and 12%, the plasticity of wood is reduced, and therefore reaching such values can result in cracks and irreversible strains. The string tension has been evaluated using a tension bench. For a given length (690 mm), the string was tuned and the corresponding tension has been measured, given in Table 2. The string tension is projected on the bridge, pegs, top and bottom saddle, and tailpiece button on the finite element model.

3 Results

The displacement in the Z direction due to the string tension is shown in Fig. 2. The displacement comprised between -0.8 and 1 mm is consistent with what is generally observed by makers, especially the elevation of the head and lowering of the fingerboard end when the strings are tuned.

The strain field is computed with initial values of elastic constants of wood, as shown in Fig. 3. It is interesting to observe that the strain field is consistent with the usual location of cracks and damages on real instruments, such as sound post cracks of the soundboard and back cracks, f holes, top and bottom heel cracks of the soundboard, and breaking of the neck and pegbox.

The Hill criterion is computed for discretised varying values of the longitudinal and radial Young's modulus of maple. The varying values of maple elastic constants are taken from ref. [7]. The Hill criterion increases for decreasing values of the radial modulus of maple, which is the most influential parameter. Therefore, it is possible to consider the probability density function of the values of radial and longitudinal moduli E_{L} and E_{R} of maple in order to match realistic variable values. The info-gap robustness analysis will therefore be computed with the Knightian uncertainty of each yield stress σ_{ij}^{y} value whose variability is still unknown. This approach will enable the info gap robustness analysis and provide robustness curves of the Hill yield criterion (Fig. 4).

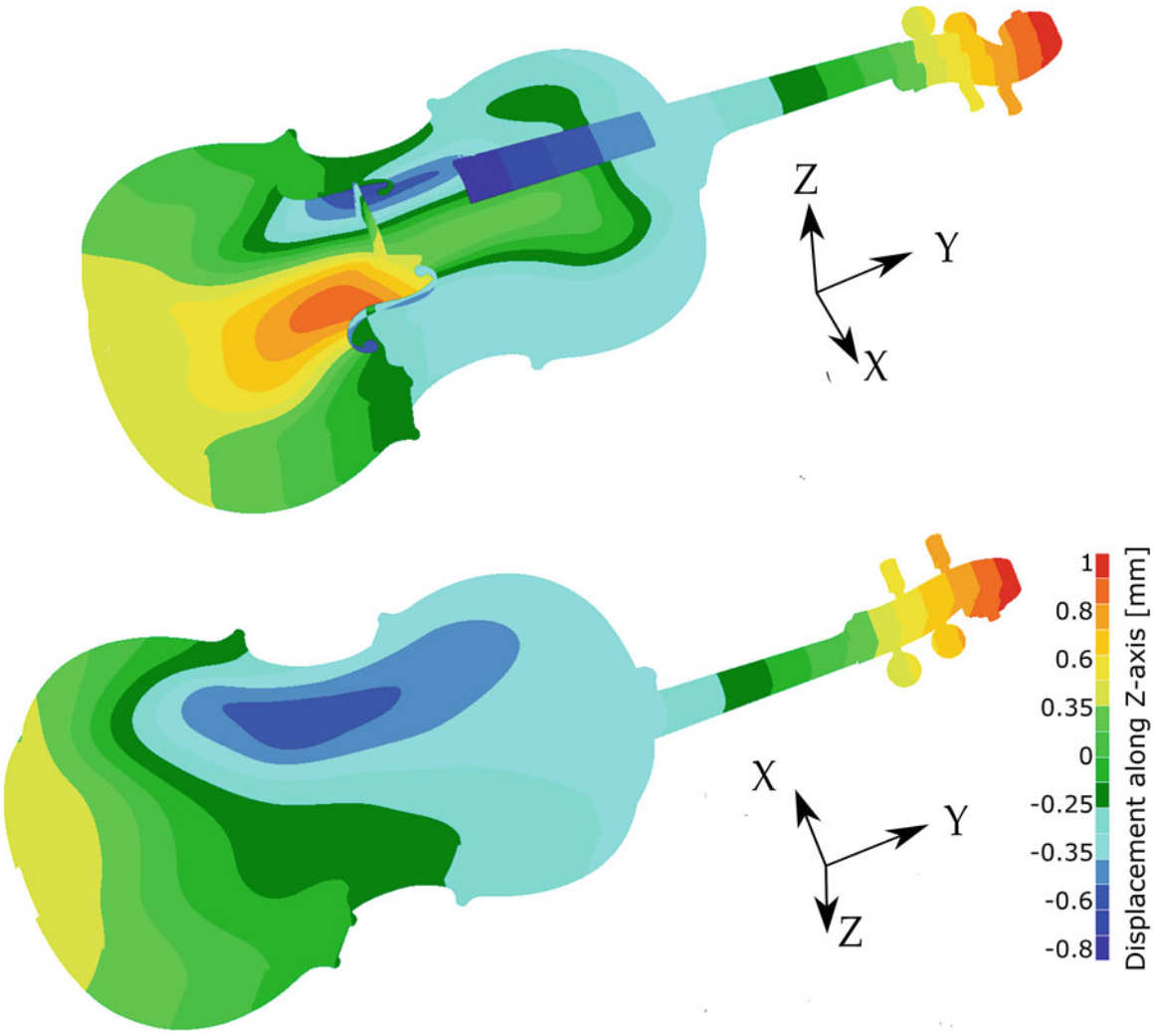

Fig. 2 Displacement (mm) along the Z axis subsequent to string tension

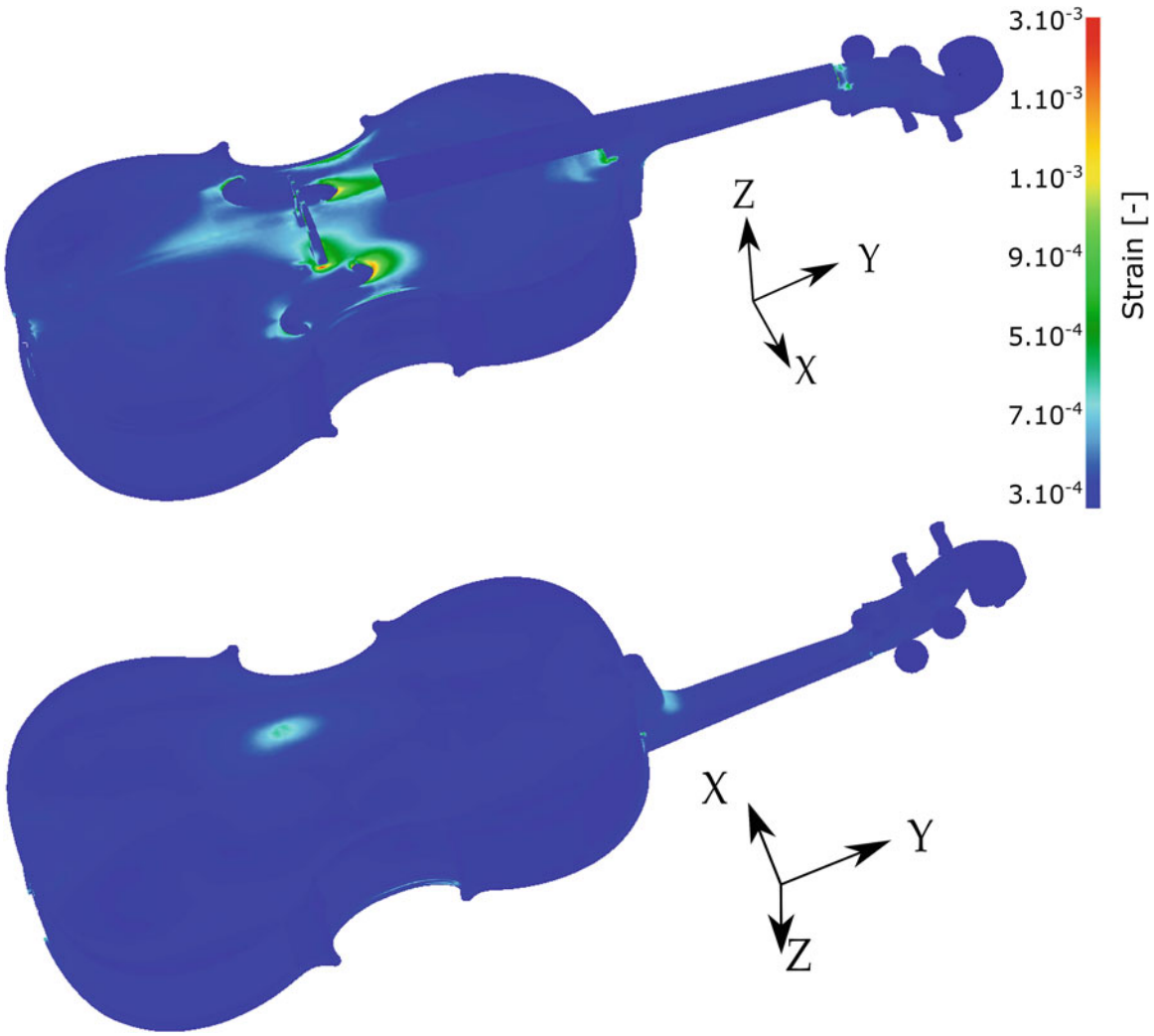

Fig. 3 Strain field in the cello due to strings tension, for initial values of wood

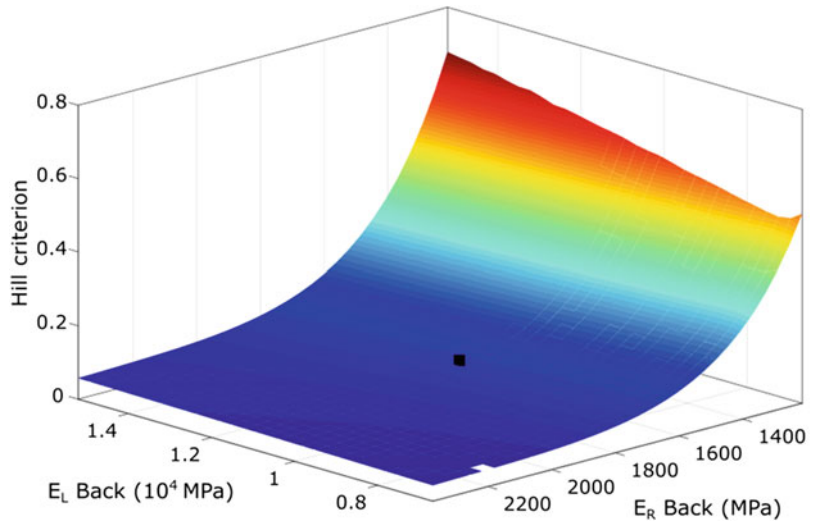

Fig. 4 Evolution of the Hill yield criterion at the back gallery for varying values of longitudinal and radial directions of young modulus of the back, made with maple

4 Conclusion

This paper aimed at proposing a methodology for cultural heritage conservation by performing an info-gap robustness analysis under severe uncertainties. As a first step, this study proposes an application case on an antique instrument. This study highlights the capacity of models to compute the stress field of a complex assembly and to observe realistic patterns of displacement, strain or stress fields when the strings are stretched on the instrument to match a modern tuning. The area corresponding to the wood-eating insect gallery has been studied, and the Hill yield criterion has been computed for multiple equi-probabilistic values of elastic constants. It was observed that the Hill yield criterion was mainly dependent on the radial modulus of maple wood used to make the back of the instrument. Therefore, the next step is to consider a probabilistic definition of the radial modulus of maple as well as the Knightian uncertainties on yield stress components of maple wood, leading to an info-gap robustness analysis, which will be the topic of a further study.

References

1. Ben-Haim, Y.: Info-Gap Decision Theory: Decisions under Severe Uncertainty, 2nd edn. Academic Press, London (2006)
2. Viala, R., Placet, V., Le Conte, S., Vaiedelich, S., Cogan, S.: Model-Based Decision Support Methods Applied to the Conservation of Musical. Application to an Antique Cello, Instruments (2019). https://doi.org/10.1007/978-3-319-74793-4
3. Hill, R.: A theory of the yielding and plastic flow of anisotropic metals. Proc. Roy. Soc. London. **193**, 281–297 (1948)
4. Guitard, D., El Amri, F.: Modèles Prévisionnels de Comportement Élastique Tridimensionnel Pour Les Bois Feuillus et Les Bois Résineux. Ann. Sci. For. **44**(3), 335–358 (1987)
5. Ross, R.J., Forest Products Laboratory: USDA Forest Service. 2010. In: Wood Handbook: Wood as an Engineering Material
6. Viala, R., Placet, V., Cogan, S.: Simultaneous non-destructive identification of multiple elastic and damping properties of spruce tonewood to improve grading. J. Cult. Herit. **42**, 108–116 (2020). https://doi.org/10.1016/j.culher.2019.09.004
7. Viala, R.: Towards a model-based decision support tool for stringed musical instrument making (Université Bourgogne Franche-comté). Retrieved from http://www.theses.fr/2018UBFCD002 (2018)

Uncertainty Quantification of Axially Loaded Beams with Boundary Condition Imperfections

A. Binder, M. Cheng-Guajardo, M. Vasquez, S. Ceballes, S. Zimmerman, and A. Abdelkefi

Abstract Manufacturing process errors and inaccurate readings of material properties in beam-based systems can result in uncertainties in the static and dynamic responses of the system. For this reason, this study focuses on the critical buckling loads, buckling mode shapes, and natural frequencies of the axially loaded beam by introducing uncertainties in the length, width, height, density, and Young's modulus. Ideal fixed boundary conditions are first considered, and the output uncertainties in the natural frequencies and critical buckling load are determined. Then flexibility in the beam's boundary conditions is introduced by modeling them with torsional springs, allowing for uncertainty in the boundary conditions to be studied. The results show that a 5% uncertainty in the input parameters may lead to 15% uncertainties in the system's outputs. The results also show the importance of accurately determining the input parameter properties and boundary conditions of the system in order to avoid any wrong estimation of the critical buckling load and natural frequencies of the system.

Keywords Axially loaded beams · Parameter uncertainty · Gaussian distribution · Critical buckling load · Sensitivity analysis

1 Introduction

Errors in manufacturing and inaccurate material property characterization are sources of input parameter uncertainties in systems that can propagate through the anticipated output [1, 2]. Manufacturers are typically expected to construct systems and report their material properties within a specified tolerance. The tolerance ranges can be represented as input uncertainties that will alter the linear and nonlinear dynamic response of the system. In the design of any system, acceptable tolerance ranges for part and material accuracies are included in the assembly of the system. In many cases, these tolerance ranges can cause very large effects on the expected dynamical response of the system. Variations in the length, width, height, density, and Young's modulus of a beam system are all possible sources of input uncertainties, which may result in uncertainties in the system's response, including critical buckling, natural frequencies, amplitudes, etc. When manufacturing error becomes large, catastrophic effects can become present in the system. When studying simple or complex systems, manufacturing tolerance ranges can be modeled as input parameter uncertainties and used in the modeling of the dynamic response. Utilizing a clamped-clamped beam, input parameter uncertainties can be modeled and tested for various ranges, and output uncertainty and sensitivity in the natural frequency, critical buckling loads, and buckling mode shapes can be studied.

Though many researchers have studied input parameter uncertainties, boundary conditions are often assumed as perfect in order to omit extensive modeling. Because boundary condition uncertainties can be very difficult to measure, they are often neglected in the uncertainty conditions, leaving them as idea clamped, free, or hinged boundaries. By modeling the boundary conditions as torsional springs [3], their uncertainties can be quantified. In this way, ideal clamped-clamped boundary conditions can be modeled as torsional springs with infinite stiffness and hinged-hinged as zero stiffness. Taking this modification into account, beam system response uncertainties can be accurately measured using varying input distribution

A. Binder, M. Cheng-Guajardo and M. Vasquez contributed equally with all other contributors.

A. Binder (✉) · M. Cheng-Guajardo · M. Vasquez · S. Ceballes · A. Abdelkefi
Department of Mechanical and Aerospace Engineering, New Mexico State University, Las Cruces, NM, USA

S. Zimmerman
Los Alamos National Laboratories, Los Alamos, NM, USA

Z. Mao (ed.), *Model Validation and Uncertainty Quantification, Volume 3*, Conference Proceedings of the Society for Experimental Mechanics Series, https://doi.org/10.1007/978-3-030-77348-9_11

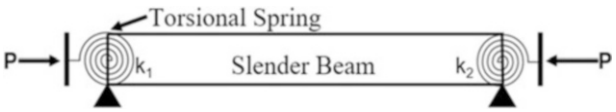

Fig. 1 Schematic of an axially loaded beam with torsional spring boundary conditions

models. Utilizing uniform and Gaussian distributions, different input uncertainty ranges are considered in geometric, material, and boundary conditions and compared to an ideal system.

2 System's Modeling

The system under consideration is a simple beam with flexible boundary conditions modeled as torsional springs, as shown in Fig. 1. The applied axial load is denoted by P. The beam is of length L with cross-sectional area A and second area moment of inertia I. Young's modulus of the beam is denoted by E, while density is represented by ρ. Lastly, the torsional springs at the left and right end are k_1 and k_2, respectively.

In order to derive the governing equations of motion and boundary conditions, the extended Hamilton principle and Euler-Bernoulli beam theory are considered. Additionally, the von Kármán strain-displacement relationship is used to account for mid-plane stretching of end-constrained beams. Using these, the equation of motion and boundary conditions are [3, 4]:

$$m\frac{\partial^2\hat{w}}{\partial\hat{t}^2}+\hat{P}\frac{\partial^2\hat{w}}{\partial\hat{x}^2}+EI\frac{\partial^4\hat{w}}{\partial\hat{x}^4}=\frac{EA}{2L}\frac{\partial^2\hat{w}}{\partial\hat{x}^2}\int_0^L\left(\frac{\partial\hat{w}}{\partial\hat{x}}\right)^2 d\hat{x} \tag{1}$$

$$\begin{cases}\hat{w}(0)=0\\ \hat{w}''(0)-k_1\hat{w}'(0)=0\\ \hat{w}(L)=0\\ \hat{w}''(L)+k_2\hat{w}'(L)=0\end{cases} \tag{2}$$

3 System's Sensitivity to Input Parameter Uncertainties

In Fig. 2, the static bifurcations diagrams are plotted for several configurations. In Fig. 2a, clamped-clamped boundary conditions are considered to focus only on the uncertainties in the beam geometry and material properties. In this case, all input parameters are varied by $\pm 5\%$ around a nominal configuration, shown in red. From this figure, it is concluded that varying the input parameters can alter both the critical buckling load and the displacement at the midspan of the beam by up to 20%. In Fig. 2b, c, an emphasis is placed on the imperfections in the boundary conditions rather than the geometric or material parameters. Leaving all other parameters constant at the ideal values, boundary conditions are varied up to 100%. This adjustment resulted in dynamic response uncertainties of up to 40%, with critical buckling loads ranging from 3 kN to 5 kN.

In the obtained results in Fig. 2, an extended parametric study was used to create an envelope of the output uncertainty around a nominal configuration. The natural frequencies of the system are studied next, as depicted in Fig. 3. Two different input distributions are considered for uncertainty quantification. Overall, it is shown that small uncertainties in the system geometry and material properties lead to large dynamic response uncertainties. Given a 5% uncertainty in the five geometric and material properties of the beam, the first bending mode frequency of up to 18% is obtained. There is an important characteristic that differentiates between the two output distributions. In Fig. 3a, uniform distribution for the input parameter is considered. In Fig. 3b, normal distribution is selected for the input parameters. In both cases, the bounds or tolerance for the geometric and material properties is the same. However, for the uniform case, the likelihood that all parameters have an uncertainty of $+5\%$ is the same as the probability of having input parameters equal to their ideal values. In the case of a normal input distribution, the input parameters are centered around the ideal configuration. For the normal distribution, the probability of selecting an input parameter with $+5\%$ uncertainty is much lower than selecting an input parameter equal

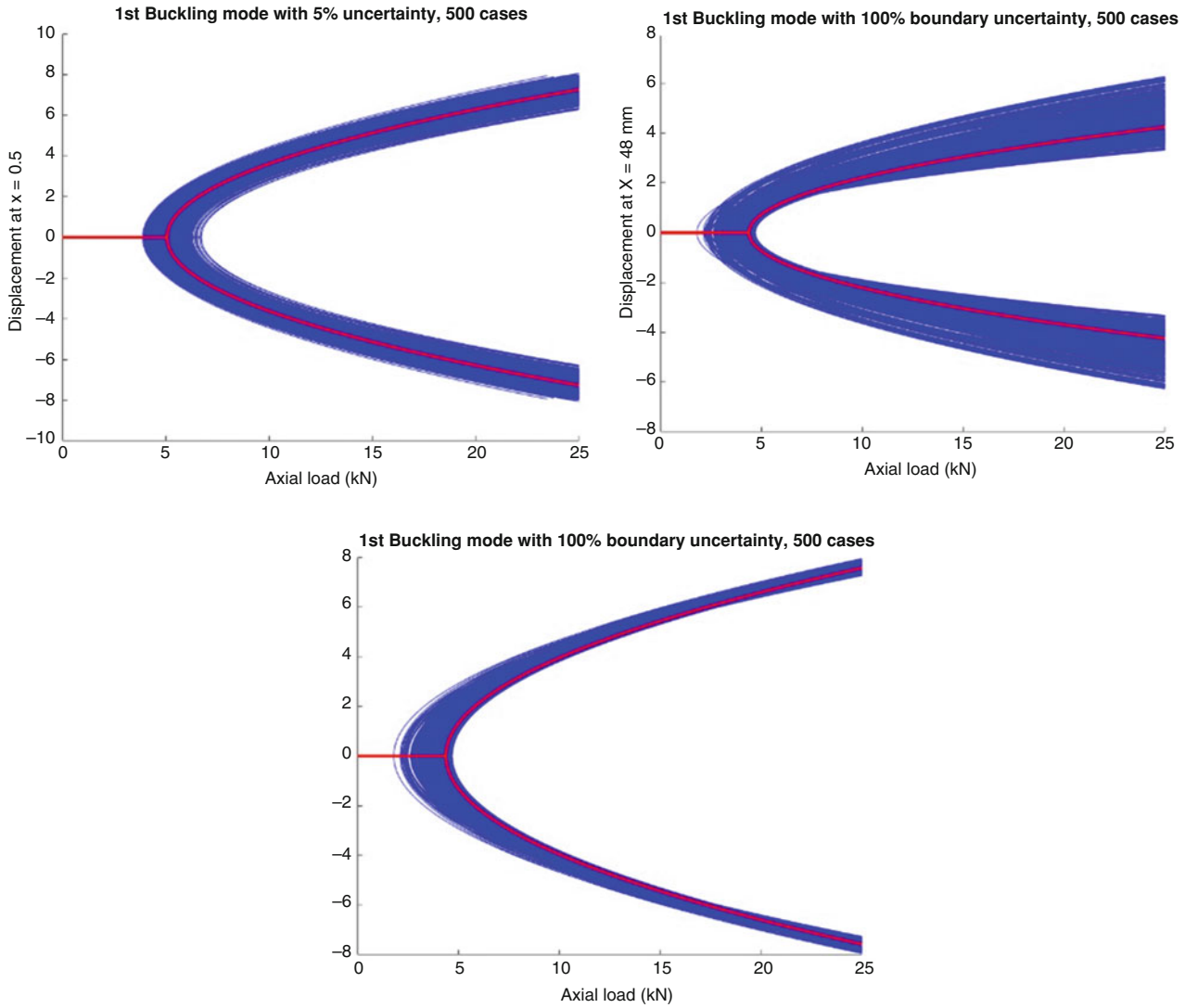

Fig. 2 (**a**) Buckling error analysis for a clamped-clamped case given a 5% input uncertainty and (**b**, **c**) 100% uncertainty in spring stiffness given nondimensionalized values of $k_1 = 24.5$ and $k_2 = 27$ at (**b**) 48 mm and (**c**) half-beam length

to the ideal value. Because of this, the shapes of the output distributions cannot be expected to be the same. For a uniform distribution, the output distribution is broader and is not well fit by normal distribution. The opposite is true for the normal input distribution. It should be noted that the system's natural frequency uncertainty may reach up to 15% with a 5% input parameter uncertainty.

4 Conclusions

This research focused on uncertainty quantification for an axially loaded beam with imperfect boundary conditions. The purpose of this was to demonstrate that small uncertainties in any of the system's inputs can lead to rather large uncertainties in the outputs. The uncertainties propagate and thus cause the output uncertainty to grow. It was shown that these uncertainties can lead to changes in the critical buckling loads and first natural frequency. It was also shown that different input distributions clearly do not lead to the same output distributions. Better characterization of these uncertainties in the boundary conditions and the beam's geometry and material properties will lead to more reliable and robust systems in the future.

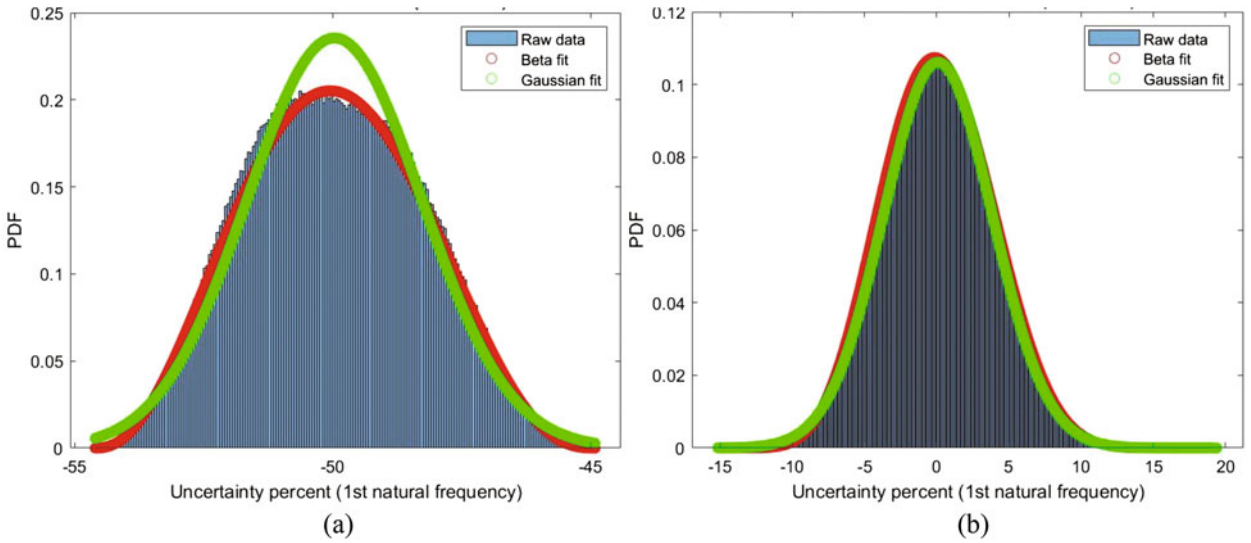

Fig. 3 First natural frequency error analysis given a 5% uncertainty in length, height, width, elastic modulus, and density for both (**a**) uniform and (**b**) Gaussian input distributions

Acknowledgements The authors would like to acknowledge the financial support from Los Alamos National Laboratory. Authors S. Ceballes and A. Abdelkefi would like to acknowledge the National Science Foundation Graduate Research Fellowship Program for funding support. Special thanks are given to Dr. Thomas Burton and Jonathan Ortiz for their fruitful discussions.

References

1. Kujawski, E.: Unintended Consequences of Performance Specifications for the Reliability of Military Weapon Systems, p. 40 (2009)
2. Siranosian, A.A., Schembri, P.E., Miller, N.A.: The Benchmark Extensible Tractable Testbed Engineering Resource (BETTER) (No. LA-UR-16-23828). Los Alamos National Lab. (LANL), Los Alamos (2016)
3. Abdelkefi, A., Yan, Z., Hajj, M.R.: Modeling and nonlinear analysis of piezoelectric energy harvesting from transverse galloping. Smart Mater. Struct. **22**, 025016 (2013)
4. Nayfeh, A.H., Emam, S.: Exact solution and stability of postbuckling configurations of beams. Nonlinear Dyn. **54**, 395–408 (2008)

Parameter Uncertainty Effects on the Buckling Characteristics of Cylindrical Structures in a Thermal Environment

M. Vasquez, A. Binder, M. Cheng-Guajardo, S. Ceballes, S. Zimmerman, and A. Abdelkefi

Abstract Material and geometric input parameter uncertainties and their effects on the static and dynamic responses of a cylindrical structure subject to thermal loading with clamped-clamped boundary conditions are studied. Different thermal loads acting as an induced axial force are considered, including uniform, linear, and nonlinear thermal distributions. Following the derivation of the governing equations of motion and boundary conditions, several methods for sensitivity analysis and uncertainty quantification are introduced. Then static and dynamic analyses are performed for different variations of the material and geometric parameters and thermal loads. Specifically, the critical buckling temperatures and prebuckling natural frequencies are discussed via sensitivity analysis methods, including the Morris method, correlation coefficients, parametric studies, and output distributions. Utilizing these methods allows for the determination of the most influential input parameters for the proposed system as well as the output uncertainties.

Keywords Sensitivity analysis · Uncertainty quantification · Thermal loading · Buckling analysis · Probability density function

1 Introduction

In recent years, there have been several studies that investigated beam structures in a thermal environment [1, 2]. These studies can be useful for different applications, such as rocket or weapon systems [3]. Though the geometry and thermal environment can be complex in nature, starting by considering these structures with a simple geometry is a necessary step [4]. In this field and others, uncertainty quantification and sensitivity analysis are being implemented to evaluate the characteristic behavior on the output responses of a system due to the uncertainty of the system's input parameters. As systems become more complex, there are typically more input parameters. With more input parameters, their uncertainties may propagate and lead to higher output uncertainty. Previous researchers have implemented uncertainty quantification and sensitivity analysis in many fields and applications, including dynamic milling models and building energy-model-based investigations [5, 6]. The application of sensitivity analysis and uncertainty quantification methods to dynamical systems, especially those including thermal effects, is limited. The goal of this study is to emphasize a specific geometry subject to clamped-clamped boundary conditions and thermal effects and understand the static and dynamic responses. Different sensitivity analysis methods are implemented to determine the effects of material parameters and geometric uncertainty on the critical buckling temperature and natural frequencies. Understanding which parameters are most influential toward the system's response should prove useful to other researchers.

M. Vasquez, A. Binder and M. Cheng-Guajardo contributed equally with all other contributors.

M. Vasquez (✉) · A. Binder · M. Cheng-Guajardo · S. Ceballes · A. Abdelkefi
Department of Mechanical & Aerospace Engineering, New Mexico State University, Las Cruces, NM, USA
e-mail: mattv7@nmsu.edu

S. Zimmerman
Los Alamos National Laboratory, Los Alamos, NM, USA

Z. Mao (ed.), *Model Validation and Uncertainty Quantification, Volume 3*, Conference Proceedings of the Society for Experimental Mechanics Series, https://doi.org/10.1007/978-3-030-77348-9_12

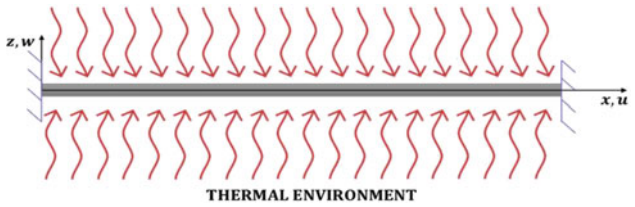

Fig. 1 Cylindrical structure with clamped-clamped boundary conditions

2 Thermal Load Representations and System's Modeling

A hollow cylinder of length L is considered, as shown in Fig. 1. The coefficient of thermal expansion is represented by α. The governing equations of motion are derived using Hamilton's principle and the Euler-Bernoulli beam theory. The von Kármán strain-displacement relationship is considered to account for mid-plane stretching nonlinearity. Three different types of thermal loads are considered, including a uniform, linear, and nonlinear temperature distribution. The difference between these thermal load representations and the ambient temperature is denoted by ΔT. The three cases of ΔT_{UTR}, ΔT_{LTR}, and ΔT_{NLTR} are expressed as [1]:

$$\Delta T_{\mathrm{UTR}} = T_{\mathrm{UTD}} - T_{\mathrm{ref}} \tag{1}$$

$$\Delta T_{\mathrm{LTD}} = -\left(T_{\mathrm{o}} - T_{\mathrm{i}}\right)\left(\frac{r_{\mathrm{o}} - r}{r_{\mathrm{o}} - r_{\mathrm{i}}}\right) + T_{\mathrm{o}} - T_{\mathrm{ref}} \tag{2}$$

$$\Delta T_{\mathrm{NLTD}} = \frac{\left(T_{\mathrm{o}} - T_{\mathrm{i}}\right)}{\ln\left(\frac{r_{\mathrm{o}}}{r_{\mathrm{i}}}\right)}\ln(r) - \frac{\left(T_{\mathrm{o}} - T_{\mathrm{i}}\right)}{2\ln\left(\frac{r_{\mathrm{o}}}{r_{\mathrm{i}}}\right)}\ln\left(r_{\mathrm{i}} r_{\mathrm{o}}\right) + \frac{\left(T_{\mathrm{o}} + T_{\mathrm{i}}\right)}{2} - T_{\mathrm{ref}} \tag{3}$$

where T_{i} and T_{o} are the inner and outer temperatures while r_{i} and r_{o} are the inner and outer radii. The reference temperature is T_{ref} and r is the change in length with respect to the wall thickness. Considering these different distributions, the final governing equation of motion can be expressed as [1, 4]:

$$EI\frac{\partial^4 w}{\partial x^4} + \rho A\frac{\partial^2 w}{\partial t^2} - \left(\frac{EA}{2L}\int_0^L \left(\frac{\partial w}{\partial x}\right)^2 dx - \int_A E\alpha\,\Delta T\, dA\right)\frac{\partial^2 w}{\partial x^2} = 0 \tag{4}$$

3 Results and Discussion

Statistical methods are used to model the uncertainty in the input parameters, including the cylinder length, the inner and outer radii, density, Young's modulus, and the coefficient of thermal expansion. The sampling method used for this study is the Monte-Carlo sampling method. In Fig. 2, a sensitivity analysis is performed to determine the critical buckling load for uniform and linear thermal loads. In Fig. 2a, an extended parametric study is performed around a set of nominal material and geometric parameters. Each input parameter is varied individually in the region at $\pm 5\%$ of its ideal configuration. The slopes in this figure demonstrate the trend of the input parameter and its strength. In Fig. 2b, the Morris method elementary effects [7] are shown. Finally, Fig. 2b shows the correlation coefficients for the uniform and linear thermal distribution. The correlation coefficient can be thought of as the covariance of the two variables divided by the product of their standard deviations. A correlation coefficient of $+1$ indicates a total positive linear correlation, -1 indicates a total negative linear correlation, and 0 indicates no linear correlation between the input and output. From all figures, it is first concluded that the

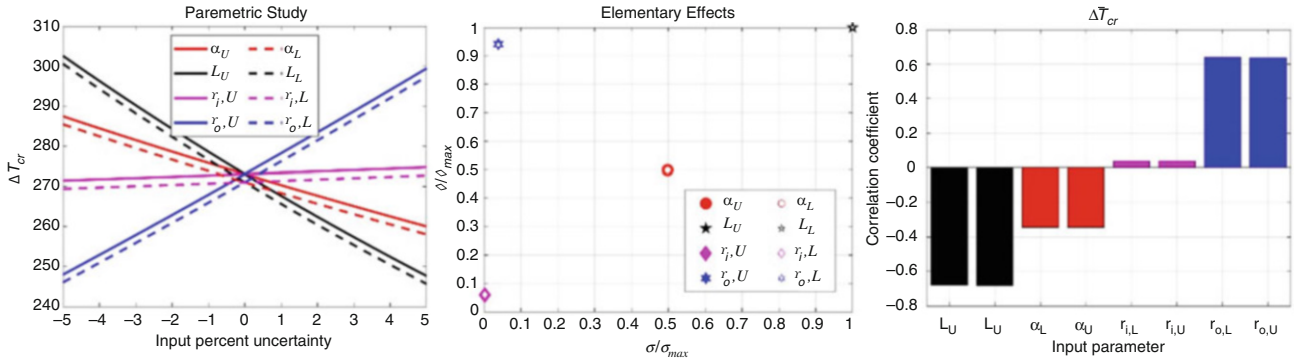

Fig. 2 Sensitivity analysis for the critical buckling temperature using (**a**) an extended parametric study, (**b**) the Morris method elementary effects, and (**c**) the correlation coefficients

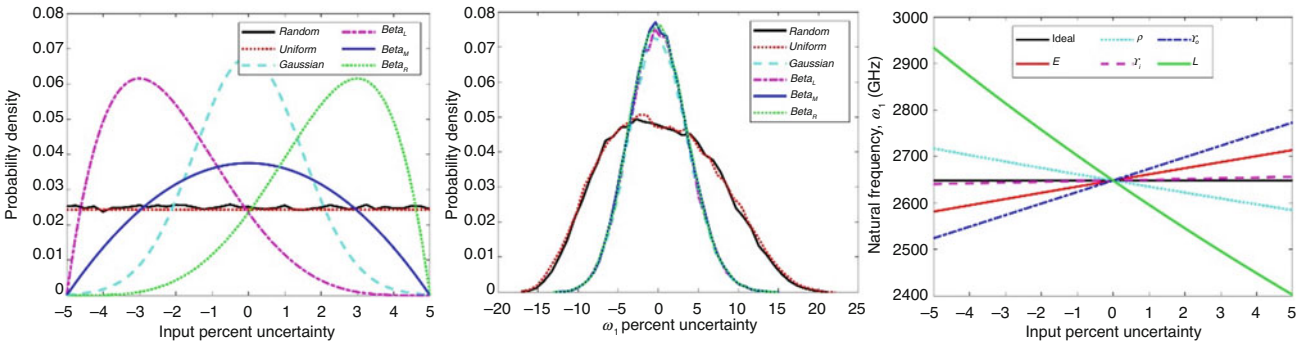

Fig. 3 Uncertainty quantification for the first natural frequency considering parameters with (**a**) input distributions leading to (**b**) output distributions and (**c**) extended parametric study to show the effects of input parameters

uniform thermal load representation overestimates the critical buckling load. Additionally, it is shown that the length of the cylinder is the most influential in altering this critical value, while the inner radius has nearly negligible effects.

In Fig. 3, uncertainty quantification is performed for the first natural frequency of the hollow cylinder. In this case, it is assumed that all of the parameters are altered by ±5%. The input distributions are shown in Fig. 3a, and the resulting natural frequency output distribution uncertainty is shown in Fig. 3b. There are several conclusions that can be drawn from these results. First, referring to the extended parametric study, it is shown that the length is the most influential in altering the natural frequency, while the inner radius is the least influential. From the input-output distributions, it is shown that the uniform and linear input distributions yield nearly identical output distributions and that the distribution is rather broad. For all other input distributions, the output distribution is nearly identical and narrow. Further, the output distributions show that varying the input parameters by ±5% causes the natural frequency to vary between approximately −17%and +22%.

4 Conclusions

In this effort, a cylindrical structure with clamped-clamped boundary conditions subject to thermal effects was evaluated. Different thermal loads were introduced showing the importance of developing reliable reduced-order models. Following the derivation of the governing equations, several sensitivity analyses and uncertainty quantification methods were applied to further investigate the critical buckling temperature for the uniform and linear thermal loads and the natural frequency for the unloaded case. These methods included an extended parametric study, the Morris method elementary effects, and the correlation coefficients. Different input uncertainty distributions were considered for uncertainty quantification of the natural frequency. Overall, it was shown that the length plays an important role in both the critical buckling temperature and natural frequency and that the input parameter uncertainties significantly propagate through the observed output for this system.

Acknowledgments The authors would like to acknowledge the financial support from Los Alamos National Laboratory. Authors S. Ceballes and A. Abdelkefi would like to acknowledge the National Science Foundation Graduate Research Fellowship Program for funding support. Special thanks are given to Dr. Thomas Burton and Jonathan Ortiz for their fruitful discussions.

References

1. Ghaffari, S.S., Ceballes, S., Abdelkefi, A.: Effects of thermal loads representations on the dynamics and characteristics of carbon nanotubes-based mass sensors. Smart Mater. Struct. **28**(7), 074003 (2019)
2. Kadhim, D.E., Jobair, H.K., Abdullah, O.I.: Analytical evaluation of temperature dependent thermal conductivity for solid and hollow cylinders subjected to a uniform heat generation. Int. J. Mech. Eng. Technol. **9**(10), 1095–1106 (2018)
3. Siranosian, A.A., Schembri, P.E., Miller, N.A.: The Benchmark Extensible Tractable Testbed Engineering Resource (BETTER) (No. LA-UR-16-23828). Los Alamos National Lab. (LANL), Los Alamos (2016)
4. Nayfeh, A.H., Emam, S.A.: Exact solution and stability of postbuckling configurations of beams. Nonlinear Dyn. **54**(4), 395–408 (2008)
5. Li, K., He, S., Liu, H., Mao, X., Li, B., Luo, B.: Bayesian uncertainty quantification and propagation for prediction of milling stability lobe. Mech. Syst. Signal Process. **138**, 10653 (2020)
6. Kristensen, M.H., Petersen, S.: Choosing the appropriate sensitivity analysis method for building energy model-based investigations. Energ. Buildings. **130**, 166–176 (2016)
7. Morris, M.D.: Factorial sampling plans for preliminary computational experiments. Technometrics. **33**(2), 161–174 (1991)

An Initial Concept for an Error-Based Digital Twin Framework for Dynamics Applications

Lara J. Edington, Nikolaos Dervilis, Paul Gardner, and David J. Wagg

Abstract This work introduces the beginnings of an error-based mathematical framework for digital twins, with the intention of providing an effective platform from which digital twins of engineering applications can be built. The framework assumes a digital twin to be some optimal combination of a physics- and data-based model and operates by weighting the contribution of each model depending on its relative mean square error compared to data measured from the physical system being twinned (the so-called physical twin). These weightings then provide a quantifiable measure of the ratio of physics- to data-based components in the resulting digital twin, and this offers a means of consistently comparing different digital twin models. The framework aims to improve the initial physics-based model of the system over time by updating it to the optimal model combination.

The initial framework is applied to a simulated Duffing oscillator, where the equivalent linear system is assumed as the physics-based model. The data-based model is learnt by identifying the system parameters from the measured system response with polynomial regression. The digital twin framework aims to detect the type of nonlinearity from the measured data (cubic in this case) and is successful in improving the physics-based model.

The framework is then extended to acceleration data recorded from the vibration response of a physical 3 degree-of-freedom structure, in order to analyse its performance in a real-world application. In this case, the assumed physics-based model uses estimated system parameters, and the data-based model is trained with a genetic algorithm to improve the accuracy of results. The digital twin framework improves the parameter estimations of the physics-based model.

It is anticipated that by developing this error-based framework and incorporating other aspects such as uncertainty analysis and optimisation, a unified method of implementing digital twins will be enabled for future research efforts.

Keywords Digital twin · Mathematical · Framework · Dynamics · Uncertainty

1 Introduction

Over recent years, the modern world has seen the initiation of a digital industrial revolution. A plethora of related concepts have emerged amidst this revolution, due to significant improvements in computing power, sensor technology, and data management. Such concepts include the digital twin, which is often described as a real time, virtual representation of some physical system/product that fuses high-fidelity computational models with data measured from the system/product. The digital twin aims to mirror and make accurate predictions of its physical system's behaviour for specific contexts of interest. The concept has received considerable attention from a range of disciplines since it was devised by Michael Grieves in 2002 [1], and interest in the concept continues to grow exponentially.

This fast-paced growth has resulted in a multitude of varying definitions of the concept, which have brought a lack of clarity and coherence. While there exist numerous examples of case-specific digital twin applications to engineering systems throughout the literature, see for example [2–8], and attempts at defining the concept [9, 10], there is no widely accepted framework to govern their implementation and, consequently, it is a challenge to consistently compare the performance of different digital twin models.

L. J. Edington (✉) · N. Dervilis · P. Gardner · D. J. Wagg
Dynamics Research Group, Department of Mechanical Engineering, University of Sheffield, Sheffield, UK
e-mail: ljedington1@sheffield.ac.uk; n.dervilis@sheffield.ac.uk; p.gardner@sheffield.ac.uk; david.wagg@sheffield.ac.uk

Z. Mao (ed.), *Model Validation and Uncertainty Quantification, Volume 3*, Conference Proceedings of the Society for Experimental Mechanics Series, https://doi.org/10.1007/978-3-030-77348-9_13

This paper introduces the beginnings of an error-based mathematical framework in the hope of providing a clearly defined and consistent way by which to evaluate the performance of digital twins of dynamic systems. The framework is based on the central idea that a digital twin model can be produced as some evolving optimal combination of a physics-based model (PBM), which models all known (or assumed) physics of the system to be twinned, and a data-based model (DBM), trained using data measured from the system. The advantages of combining both PBMs and data-based techniques are well-recognised, and this approach is used in multiple digital twin applications [2, 3, 9, 11].

It is anticipated that, in developing such a mathematical framework, the aforementioned issues will begin to be addressed.

2 An Error-Based Mathematical Framework

2.1 Initial Framework

The initial framework was developed from an equation provided by Kennedy and O'Hagan [12], which describes the relationship between a true process and a computer model of that process, and is given as follows:

$$z_i = \zeta(\mathbf{x}_i) + e_i = \rho\eta(\mathbf{x}_i, \boldsymbol{\theta}) + \delta(\mathbf{x}_i) + e_i, \tag{1}$$

where z_i denotes the ith of N recorded observations of the true process ζ, given inputs $\mathbf{x}_i$ with observation error (or noise) e_i. Here η is a computer model of the true process, with parameters $\boldsymbol{\theta}$ and model discrepancy of δ, and ρ is a yet-to-be-determined regression parameter.

This equation was modified to apply to a digital twin model, η_{DT}, with parameters $\boldsymbol{\theta}_{DT}$ and discrepancy $\delta_{DT,i}$ (considered as a residual error and not functional) at observation i. In this context, the physical system would be represented by ζ and data measured from that system by z_i. The digital twin model was taken as a weighted combination of a PBM, η_1, and a DBM, η_2, as follows:

$$z_i = \eta_{DT}(\mathbf{x}_i, \boldsymbol{\theta}_{DT}) + \delta_{DT,i} + e_i \tag{2}$$

$$= \rho[\eta_1(\mathbf{x}_{1,i}, \boldsymbol{\theta}_1) + \delta_{1,i}] + (1-\rho)[\eta_2(\mathbf{x}_{2,i}, \boldsymbol{\theta}_2) + \delta_{2,i}] + e_i, \tag{3}$$

where the PBM (resp. DBM) has parameters $\boldsymbol{\theta}_1$ (resp. $\boldsymbol{\theta}_2$) and discrepancy $\delta_{1,i}$ (resp. $\delta_{2,i}$) from the physical system and $\mathbf{x}_{1,i}, \mathbf{x}_{2,i} \subseteq \mathbf{x}_i$. The parameter $\rho \in [0, 1]$ in Eq. (3) is defined to weight the contributions of each model to the digital twin. By tuning ρ, the digital twin can be more or less influenced by one model over the other. This parameter would then provide a measure of the composition of the digital twin in terms of the ratio between the physics- and data-based components, so may be thought of as the *physics-to-data model ratio* of the digital twin.

The value of the physics-to-data model ratio should be optimised to produce the best digital twin model from the available PBM and DBM. With this in mind, the weight was based on the relative discrepancies of the two models. If the PBM was a worse reflection than the DBM of the physical system, it would be weighted to provide a smaller contribution to the digital twin. This is represented for the ith observation only as

$$\frac{\rho}{1-\rho} = \frac{\delta_{2,i}}{\delta_{1,i}}. \tag{4}$$

However, rather than take only one observation into account, this should be generalised to apply to all N observations measured from the physical twin. To do this, the root mean square discrepancy was used to provide an averaged measure over all observations while penalising larger model discrepancies, and ensuring positive and negative values would not cancel each other out:

$$\frac{\rho}{1-\rho} = \frac{\sqrt{\frac{1}{N}\sum_{i=1}^{N}\delta_{2,i}^2}}{\sqrt{\frac{1}{N}\sum_{i=1}^{N}\delta_{1,i}^2}} = \sqrt{\frac{\sum_{i=1}^{N}\delta_{2,i}^2}{\sum_{i=1}^{N}\delta_{1,i}^2}}. \tag{5}$$

From Eq. (1), this can be written in terms of the observations, model outputs, and observation error as

$$\frac{\rho}{1-\rho} = \sqrt{\frac{\sum_{i=1}^{N}(\mathbf{z}_i - \eta_2(\mathbf{x}_{2,i}, \boldsymbol{\theta}_2) - e_i)^2}{\sum_{i=1}^{N}(\mathbf{z}_i - \eta_1(\mathbf{x}_{1,i}, \boldsymbol{\theta}_1) - e_i)^2}}, \tag{6}$$

which, if the observation error is assumed to be small, can be approximated as

$$\frac{\rho}{1-\rho} \approx \sqrt{\frac{\sum_{i=1}^{N}(\mathbf{z}_i - \eta_2(\mathbf{x}_{2,i}, \boldsymbol{\theta}_2))^2}{\sum_{i=1}^{N}(\mathbf{z}_i - \eta_1(\mathbf{x}_{1,i}, \boldsymbol{\theta}_1))^2}} = \sqrt{\frac{J_2}{J_1}}, \tag{7}$$

where $J_{1,2} = \frac{1}{N}\sum_{i=1}^{N}(\mathbf{z}_i - \eta_{1,2}(\mathbf{x}_{1,2,i}, \boldsymbol{\theta}_{1,2}))^2$ are the mean square error (MSE) values of the PBM and DBM respectively, compared to the data.

Defining the value $\beta = \sqrt{\frac{J_1}{J_2}}$ gives a simple approximation for ρ as

$$\rho \approx \frac{1}{\beta + 1} \tag{8}$$

and it is this value of the physics-to-data model ratio that is assumed throughout the applications of the framework in this paper. As it may be thought of as a proportion of relative trust in the two models, the ratio may be used to determine the parameters $\boldsymbol{\theta}_{DT}$ of a digital twin model given the parameters $\boldsymbol{\theta}_p$ and $\boldsymbol{\theta}_d$ of the PBM and DBM respectively as:

$$\boldsymbol{\theta}_{DT} = \rho\boldsymbol{\theta}_p + (1-\rho)\boldsymbol{\theta}_d. \tag{9}$$

2.2 Parameter Updating Procedure

This approach to determining the digital twin parameters made two assumptions, namely that the optimal combination of PBM & DBM responses would also give the optimal combination of their parameters, and that the parameter errors of the two models could compensate for one another, given $\rho \in [0, 1]$ (i.e. if the parameters of one consistently over-estimated those of the physical system, and the parameters of the other consistently under-estimated). However, initial trials showed this was often not the case, and either the PBM or DBM response would have a smaller error than the resulting digital twin response.

To address this caveat, an automatic parameter updating procedure was implemented. If the MSE of either the PBM or DBM was less than that of the digital twin model, then the model ratio would update to a value of 1 or 0, respectively. These conditions can be summarised as

$$\rho = \begin{cases} \frac{1}{\beta+1}, & \text{if } J_{DT} < J_1 \text{ and } J_{DT} < J_2 \\ 0, & \text{if } J_{DT} < J_1 \text{ and } J_{DT} > J_2 \\ 1, & \text{if } J_{DT} > J_1 \text{ and } J_{DT} < J_2, \end{cases} \tag{10}$$

where J_{DT} is the MSE of the originally determined digital twin model. In essence, this original digital twin model provides a third option in addition to the PBM and DBM. The framework simply chooses the model option with the minimum MSE.

2.3 Temporal Evolution

The ability to update in (at least near-) real time is a defining characteristic of a digital twin that distinguishes it from a general computational model. For this reason, the framework was developed to incorporate temporal evolution.

To approximate a continuously updating digital twin, the time history of the data measured from the system would be split into sections (batches), and the implementation of the framework would become iterative. A new DBM is trained for each data section, which is compared to a PBM over the corresponding time period to produce multiple model ratios and digital twin models. The PBM for each time period is taken as the digital twin model of the previous period, so is updated

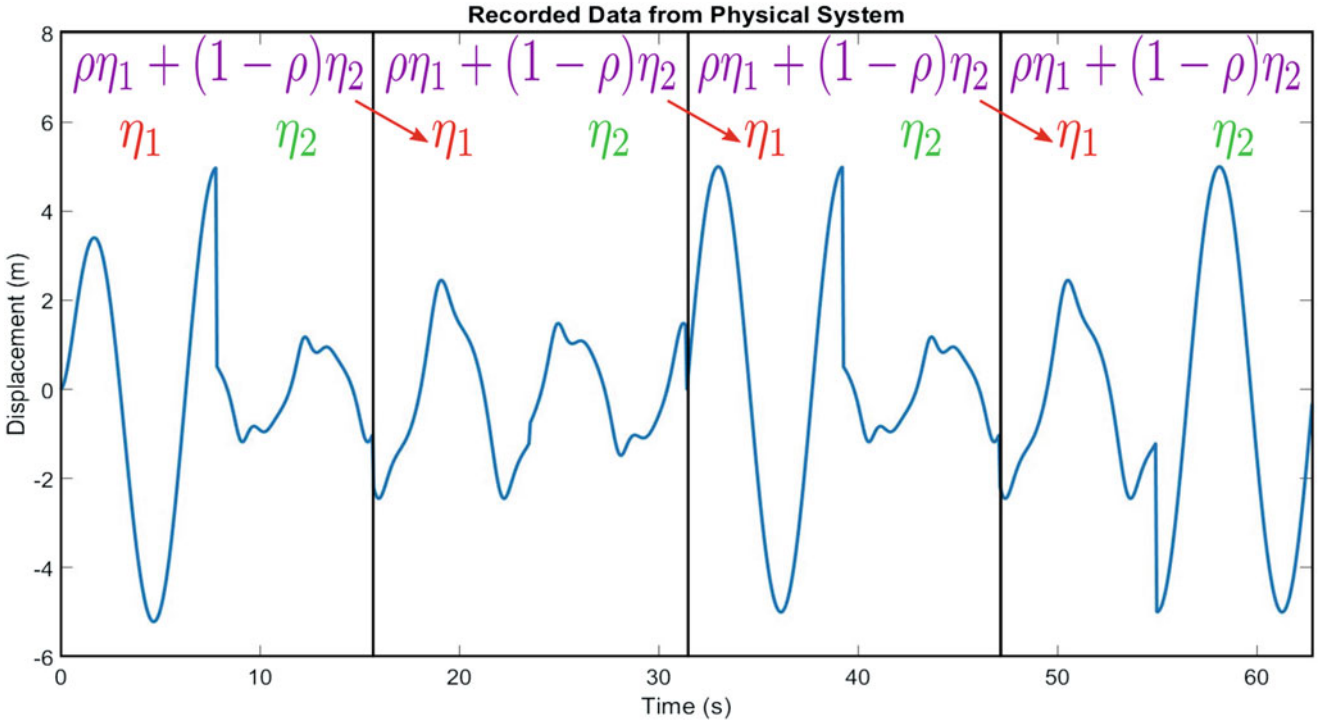

Fig. 1 Iterative implementation of the framework, applied to the recorded displacement signal (in blue) of a physical system, to incorporate temporal evolution

with each section as necessary. Figure 1 illustrates the iterative process on a changing recorded displacement signal, where the red, green, and purple expressions represent the PBM, DBM, and digital twin, respectively. Each "window" within the figure identifies a new section of the data.

3 Single Degree-of-Freedom Oscillator

The initial framework was first applied to a computationally simulated single degree-of-freedom (SDOF) Duffing oscillator, the response of which was generated to act as data measured from a "physical system" by numerically integrating the equation of motion using the ode45 MATLAB solver. This measured data was sectioned into quarters to allow for four iterations of the framework. The SDOF system to be analysed is described by Eq. (11), where m, c, k, and k_3 are the system parameters, $\mathbf{y}$ is the displacement response to input $\mathbf{x}$, and the dot denotes the derivative with respect to time.

$$m\ddot{\mathbf{y}} + c\dot{\mathbf{y}} + k\mathbf{y} + k_3\mathbf{y}^3 = \mathbf{x}. \tag{11}$$

The physical system had parameters $m = 10\,\text{kg}$, $c = 20\,\text{N·s/m}$, $k = 10\,\text{N/m}$, and a cubic stiffness value of $k_3 = 10\,\text{N/m}^3$ until time $t = 31.4\,\text{s}$ (the beginning of the third section), when it changed to $k_3 = 1\,\text{N/m}^3$. The input was $\mathbf{x} = 100\cos(\mathbf{t})$, where $\mathbf{t}$ is a vector of time values with sampling frequency $F_s = (100/2\pi)\,\text{Hz}$.

An initial linear PBM was assumed by ignoring the cubic nonlinearity to introduce some model-form error. It was intended that the framework would detect the nonlinearity and update the corresponding parameter as it changed in the "physical system". The DBM parameters were learnt using polynomial regression, with $\ddot{\mathbf{y}}$, $\dot{\mathbf{y}}$, $\dot{\mathbf{y}}^2$, $\dot{\mathbf{y}}^3$, $\mathbf{y}$, $\mathbf{y^2}$, and $\mathbf{y^3}$ as the feature vectors and $\mathbf{x}$ as the target vector. This meant the DBMs of the four sections were not restricted to the form of a Duffing system, as the nature of the nonlinearity was assumed unknown. To ensure the digital twin parameters could be determined for the first iteration, using Eq. (9), any nonlinear DBM parameters were assigned counterparts in the initial linear PBM of value 0.

The training data used to learn the four DBMs were the recorded simulated system input and response, which were noise-free, and a test dataset was produced by adding random noise to the training response (resp. input) sampled from distribution $\mathcal{N}(0, 0.5)$ (resp. $\mathcal{N}(0, 100)$). Once trained, the DBMs were compared to the PBMs by applying either the training input or a

Table 1 MSE of the models and ρ values over each section of training data

	MSE			ρ	
Data section	J_{PBM}	J_{DBM}	Original J_{DT}	Original	Updated
1	7.684	3.373×10^{-4}	6.128×10^{-4}	0.007	0
2	2.822×10^{-4}	4.434×10^{-5}	8.539×10^{-5}	0.284	0
3	2.685	6.382×10^{-6}	4.926×10^{-6}	0.002	0.002
4	1.356×10^{-4}	8.319×10^{-6}	3.763×10^{-6}	0.199	0.199

Table 2 MSE of the models and ρ values over each section of test dataset

	MSE			ρ	
Data section	J_{PBM}	J_{DBM}	Original J_{DT}	Original	Updated
1	12.467	1.032	1.623	0.223	0
2	0.990	0.991	0.990	0.500	1
3	3.900	1.003	1.373	0.336	0
4	0.998	0.997	0.997	0.500	0.500

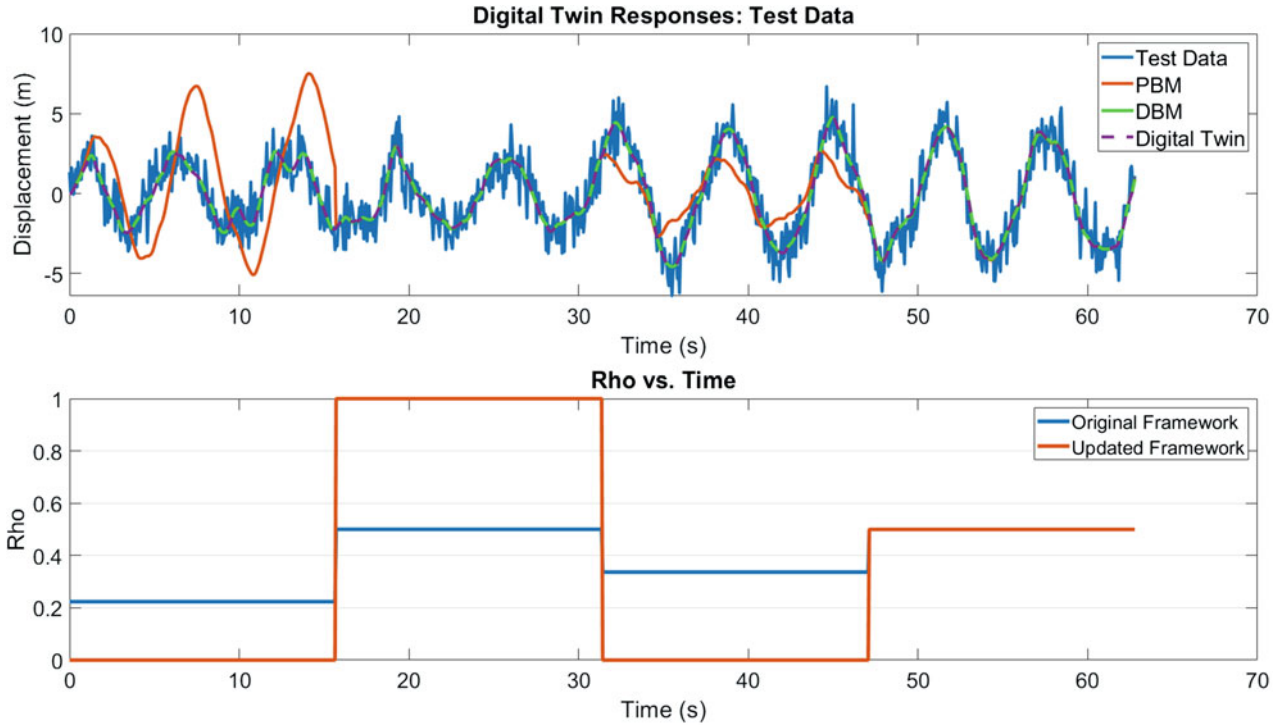

Fig. 2 (Top) Comparison of PBM, DBM, and digital twin model responses to the sectioned test data response. (Bottom) Evolution of physics-to-data model ratio over time before and after the parameter updating procedure

test input to each one. The resulting responses were finally compared to the training or test response of the Duffing system to determine the four model ratios and digital twin models. Tables 1 and 2 show the MSE of each model over the four sections of the training and test data, respectively.

The resulting responses of the PBM, DBM, and digital twin compared to the test data response are displayed in Fig. 2, along with a plot illustrating the evolution of the model ratio as determined before and after the parameter updating procedure.

The framework ensures that the model ratio produces the digital twin response with the minimal error, updating ρ for the first three iterations. It is interesting to note that the original ratios for sections two and four of the test data show the PBM is almost exactly as accurate as the DBM, so there is very little improvement to be made after just one iteration. It is clear that, for both datasets, the framework was successful in significantly improving the initial PBM by utilising the measured data from the "physical system", and again once the system's nonlinear stiffness parameter changed. The results show that the digital twin model is a good approximation of the system, with MSEs under 2.

4 Three Storey Building

Its simplistic nature meant the simulated Duffing system was ideal for trialling the beginnings of the framework. However, it did not reflect a realistic application, and so the error-based framework was also applied to an experimental multiple degree-of-freedom system set-up, with the aim of improving parameter estimates of a PBM. The three storey building system analysed by Wagg et al. [9] was taken as the focus of the proceeding work. Two input signals and the corresponding acceleration responses of the building were taken as a training and test set, which were both sectioned into quarters to produce an evolving digital twin model.

The system in [9] incorporated a buffer which introduced a harsh nonlinearity at certain displacements; however, this paper only considers the acceleration responses that were recorded when the buffer was not activated. For this reason, both the PBM and DBM were assumed to be linear 3 degree-of-freedom systems. The PBM parameters were estimated by adding errors to those identified by Wagg et al.; the mass values were all chosen as $m_1 = m_2 = m_3 = 10\,\text{kg}$, damping values as $c_1 = c_2 = c_3 = 1\,\text{N·s/m}$, and stiffness values as $k_1 = k_2 = k_3 = 1000\,\text{N/m}$.

The DBM was trained using self-adaptive differential evolution (SADE), a form of genetic algorithm, which improves an initial population of randomly sampled values by iteratively proposing new potential solutions, comparing them with a cost function and keeping only the best options [13]. In this case, the solution was the collection of system parameters and the cost function, J, determined from the normalised MSE:

$$J(\boldsymbol{\theta}) = \frac{1}{3}\sum_{i=1}^{3}\left(\frac{100}{N\sigma^{(i)2}}\sum_{j=1}^{N}\left[z_j^{(i)} - \ddot{y}_{d,j}^{(i)}(\boldsymbol{\theta})\right]^2\right), \tag{12}$$

where $i = 1, 2, 3$ denotes the floor, $j = 1, 2, \ldots, N$ denotes the training data point, σ^2 is the variance of the training dataset, z is the data response, $\ddot{y}_d$ is the DBM response, and $\boldsymbol{\theta}$ is the potential solution. The SADE algorithm implemented had the following parameters: crossover ratio 0.5, scaling factor 1.5, population size 200, and maximum generations 100, with 5 runs. The initial ranges selected for the mass, damping, and stiffness values were [4, 8], [0, 10], and $[0, 10^4]$, respectively.

With responses of three masses (instead of one), there were three different ρ values calculated for the system. These three values were averaged into a singular physics-to-data model ratio which was employed in determining $\boldsymbol{\theta}_{DT}$. The framework was successful in improving the PBM of the building, as it was for the SDOF system, and this is shown by the MSE of the model responses compared to the training and test data in Tables 3 and 4.

The model responses compared to the test data responses are shown in Fig. 3 and the evolution of the physics-to-data model ratio (as determined before and after the parameter updating procedure) in Fig. 4.

The results show that, by the 3rd section, the digital twin was a very good fit and the improvement in the PBM was most significant over the first iteration, decreasing with each further iteration after this. This is not surprising given that the precise initial conditions of the system were unknown, hence the transient responses would affect the accuracy of the initial DBM. However, it also suggests that the framework extracts most of its information from the data within the first couple of iterations, given the system properties are not changing and the forcing is relatively constant. The relative improvement of the

Table 3 MSE (averaged over all floors) of PBM, DBM, and digital twin model and ρ values over each section of training data

	MSE			ρ	
Data section	J_{PBM}	J_{DBM}	Original J_{DT}	Original	Updated
1	0.5812	0.0722	0.6255	0.2606	0
2	0.2841	0.0615	0.0750	0.3175	0
3	0.0609	0.0130	0.0230	0.3162	0
4	0.0285	0.0361	0.0213	0.5295	0.5295

Table 4 MSE (averaged over all floors) of PBM, DBM, and digital twin model and ρ values over each section of test data

	MSE			ρ	
Data section	J_{PBM}	J_{DBM}	Original J_{DT}	Original	Updated
1	0.7361	0.1520	0.7770	0.3124	0
2	0.1472	0.1059	0.0879	0.4589	0.4589
3	0.0458	0.0156	0.0180	0.3859	0
4	0.0300	0.0372	0.0278	0.5270	0.5270

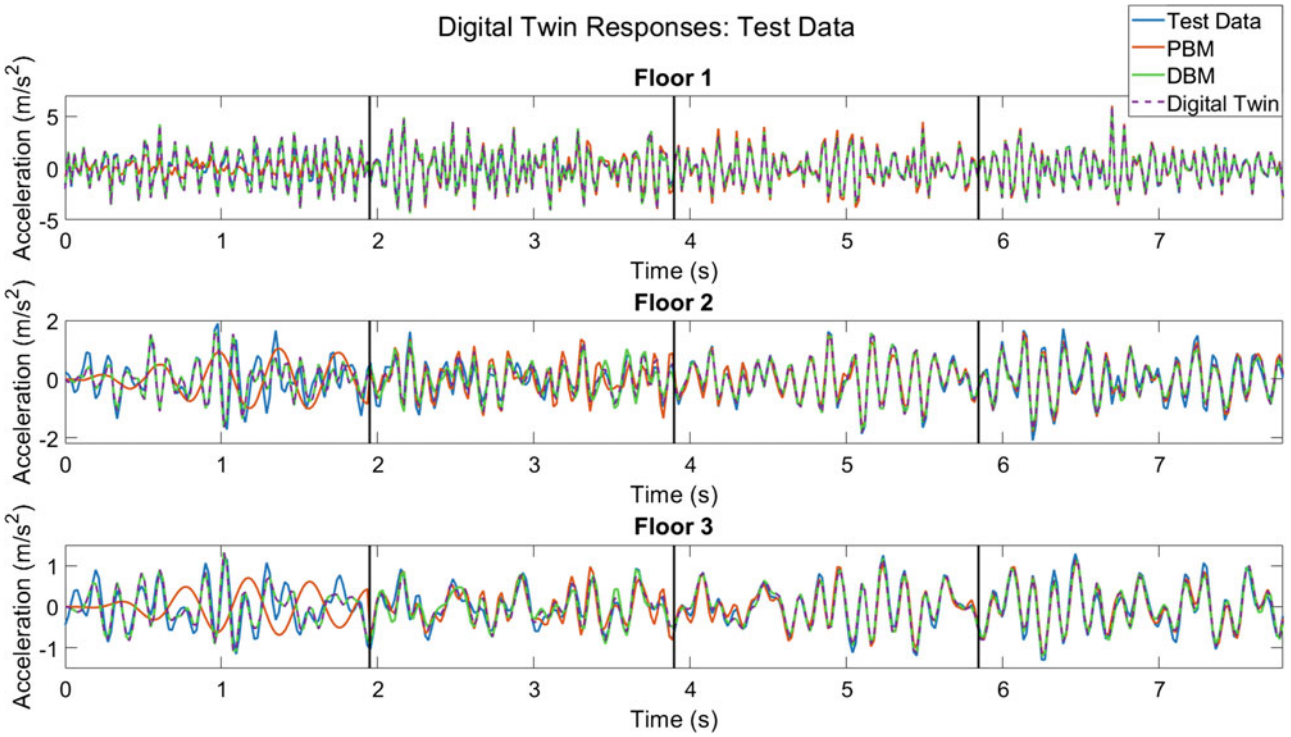

Fig. 3 Comparison of PBM, DBM, and digital twin model responses to the sectioned test data response for (top) floor 1, (middle) floor 2, and (bottom) floor 3

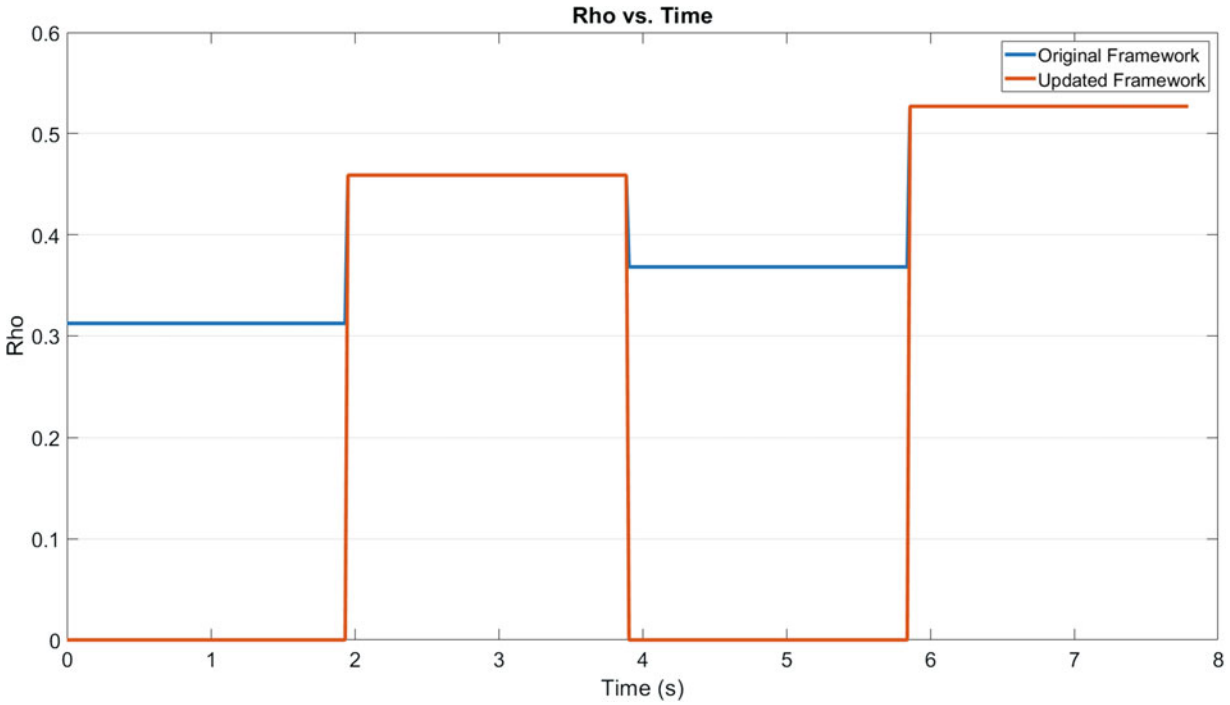

Fig. 4 Evolution of physics-to-data model ratio (averaged over all floors) over time before and after the parameter updating procedure

PBM compared to the DBM is illustrated by the evolution of the original model ratio, which shows that the PBM discrepancy is roughly equal to that of the DBM (which itself has been noticeably reduced) by the final section. The framework updated the model ratio for the first and third sections because the weighted average model did not produce the minimal MSE of the three model options, as confirmed by Table 4. However, the framework did produce a better weighted average model for sections two and four so offered an advantage over simply fitting one model to a system.

5 Discussion

The systems analysed in the presented work were simplistic, although the objective of the work was to clearly demonstrate the framework itself and not to produce extremely high-fidelity digital twins of complex systems. However, in progressing with this work, other techniques could be employed to produce models of less simplistic systems; the presented DBMs were produced using methods which made assumptions on underlying physics, but more "black-box" methods such as Gaussian processes [14, 15], neural networks [16], or support vector machines [17] would not be constrained by such assumptions. Another consideration is the computational cost of the models, as the SADE algorithm used for the three storey building was highly intensive, and this would affect the ability of the resulting digital twin to update in real time as required. However, this was more a concern of the specific application of the framework and not of the framework itself.

The temporal evolution aspect of the initial framework could also be improved. The existing work arbitrarily splits the data signals into four sections, which was suitable for demonstrating the iterative process clearly, but did not produce frequently updated digital twin models. It may give better results to shorten the sections (although this would be at the expense of less training data for the DBMs), or to maintain a longer section but translating it as a "window" along the signal. This method of updating the digital twin model as it receives new data has similarities to model predictive control [18], which involves controlling a system's independent variables by following an algorithm to minimise some cost function so that its outputs (dependent variables) optimally reflect a given reference.

Other elements would need to be incorporated into the existing mathematical framework if it was to be realistically useful for digital twins of dynamic systems. For example, some form of uncertainty quantification is required to assign a level of trust to a digital twin's predictions, which may be introduced using measures of entropy or Bayesian regression techniques. There is also further work to be considered in terms of the optimisation element of the framework, such as employing more model options for the framework to choose from, using different optimisation criteria, and using decision trees to enable the digital twin to act as a decision-maker.

6 Conclusion

The digital twin is a concept which has recently garnered significant interest amidst the current data-driven industrial revolution and is set to offer a whole range of potential benefits to many disciplines. However, there arguably exist as many obstacles to the development and application of the digital twin, one of which is the inconsistency in the employed definitions of the concept and it is a challenge to reliably compare and evaluate the performance of different digital twin models as a result.

This paper presented the beginnings of an error-based mathematical framework, with the aim of starting to address this issue by introducing a means to quantify the performance of digital twins of dynamic engineering systems. The foundational concept of the framework is that a digital twin model could be produced from an evolving, optimal combination of a PBM and a DBM, the contribution of each related to their relative discrepancies from data measured from the physical system.

This initial framework was applied to two simplistic systems for clear demonstration: a SDOF Duffing oscillator, assuming a linear PBM and aiming to improve the incorrect model form, and the physical three storey building analysed by Wagg et al. [9] in order to improve PBM parameter estimates. The framework was successful in improving the models in both examples, but must be further developed to incorporate other aspects of a digital twin before it may realistically be applied to a range of engineering systems.

Acknowledgments The support of the University of Sheffield Department of Mechanical Engineering departmental studentship and the UK EPSRC via the *Digital twins for improved dynamic design* (EP/R006768/1) EPSRC grant is greatly acknowledged.

References

1. Grieves, M., Vickers, J.: Digital twin: Mitigating unpredictable, undesirable emergent behavior in complex systems. In:Transdisciplinary Perspectives on Complex Systems, pp. 85–113. Springer, Berlin (2017)
2. Tuegel, E.J., Ingraffea, A.R., Eason, T.G., Spottswood, S.M.: Reengineering air-craft structural life prediction using a digital twin. Int. J. Aerosp. Eng. **2011**, 154798 (2011)
3. Kapteyn, M.G., Knezevic, D.J., Willcox, K.: Toward predictive digital twins via component-based reduced-order models and interpretable machine learning. In: AIAA Scitech 2020 Forum, p. 0418 (2020)
4. Reifsnider, K., Majumdar, P.: Multiphysics stimulated simulation digital twin methods for fleet management. In: 54th AIAA/ASME/ASCE/AHS/ASC Structures, Structural Dynamics, and Materials Conference, p. 1578 (2013)
5. Kraft, E.M.: The air force digital thread/digital twin-life cycle integration and use of computational and experimental knowledge. In: 54th AIAA Aerospace Sciences Meeting, p. 0897 (2016)
6. Seshadri, B.R., Krishnamurthy, T.: Structural health management of damaged aircraft structures using digital twin concept. In: 25th AIAA/AHS Adaptive Structures Conference, p. 1675 (2017)
7. Karve, P.M., Guo, Y., Kapusuzoglu, B., Mahadevan, S., Haile, M.A.: Digital twin approach for damage-tolerant mission planning under uncertainty. Eng. Fract. Mech. **225**, 106766 (2020)
8. Sivalingam, K., Sepulveda, M., Spring, M., Davies, P.: A review and methodology development for remaining useful life prediction of offshore fixed and floating wind turbine power converter with digital twin technology perspective. In: 2018 2nd International Conference on Green Energy and Applications (ICGEA), pp. 197–204. IEEE, Piscataway (2018)
9. Wagg, D., Worden, K., Barthorpe, R., Gardner, P.: Digital twins: state-of-the-art and future directions for modeling and simulation in engineering dynamics applications. ASCE-ASME J Risk and Uncert in Engrg Sys Part B Mech Engrg **6**(3), 030901 (2020)
10. Worden, K., Cross, E., Barthorpe, R., Wagg, D., Gardner, P.: On digital twins, mirrors, and virtualizations: Frameworks for model verification and validation. ASCE-ASME J Risk and Uncert in Engrg Sys Part B Mech Engrg **6**(3), 030902 (2020)
11. Gardner, P., Dal Borgo, M., Ruffini, V., Hughes, A.J., Zhu, Y., Wagg, D.J.: Towards the development of an operational digital twin. Vibration **3**(3), 235–265 (2020)
12. Kennedy, M.C., O'Hagan, A.: Bayesian calibration of computer models. J. Roy. Stat. Soc. Ser.B (Stat. Methodol.) **63**(3), 425–464 (2001)
13. Storn, R., Price, K.: Differential evolution – a simple and efficient heuristic for global optimization over continuous spaces. J. Global Opt. **11**(4), 341–359 (1997)
14. Kocijan, J., Murray-Smith, R., Rasmussen, C.E., Girard, A.: Gaussian process model based predictive control. In: Proceedings of the 2004 American Control Conference, vol. 3, pp. 2214–2219. IEEE, Piscataway (2004)
15. Camacho, E.F., Alba, C.B.: Model Predictive Control. Springer Science & Business Media, Berlin (2013)
16. Azman, K., Kocijan, J.: Application of Gaussian processes for black-box modelling of biosystems. ISA Trans. **46**(4), 443–457 (2007)
17. Sjoberg, J., Hjalmarsson, H., Ljung, L.: Neural Networks in System Identification. Linkoping University, Linköping (1994)
18. Gretton, A., Doucet, A., Herbrich, R., Rayner, P.J., Scholkopf, B.: Support vector regression for black-box system identification. In: Proceedings of the 11th IEEE Signal Processing Workshop on Statistical Signal Processing (Cat. No. 01TH8563), pp. 341–344. IEEE, Piscataway (2001)

Hierarchical Bayesian Model Updating for Nonlinear Structures Using Response Time Histories

Xinyu Jia, Omid Sedehi, Lambros S. Katafygiotis, Babak Moaveni, and Costas Papadimitriou

Abstract This paper presents a novel hierarchical Bayesian modeling (HBM) framework for the model updating and response predictions of dynamic systems with material nonlinearity using multiple data sets consisting of measured response time histories. The proposed framework is capable of capturing the uncertainties originating from both structural and prediction error parameters. To this end, a multilevel probabilistic model is proposed aiming to characterize the variability of both model and noise parameters. Moreover, a new Laplace approximation is formulated within the HBM framework to reduce the computational burden up to a great extent. Finally, a multidegree of freedom (MDOF) nonlinear system modeled by Bouc-Wen hysteresis elements is employed to demonstrate the effectiveness of the method.

Keywords Nonlinear model updating · Hierarchical Bayesian modeling · Structural parameter uncertainty · Prediction error uncertainty · Time-domain response

1 Introduction

Updating models and predicting responses using data-driven approaches have garnered attention over the last three decades. Although most structures exhibit a nonlinear behavior to some extent, the majority of model updating techniques are applicable to linear ones. In the context of structural health monitoring, the characterization of such nonlinearities is required as it allows for more accurate and efficient representations of real structures. Thus, the calibration of nonlinear models is likely to be more appropriate for the identifications of real-life structures.

Bayesian inference is a powerful probabilistic tool for updating finite element (FE) models [1]. It provides a powerful probabilistic tool for updating nonlinear models and handling the uncertainties of nonlinear model parameters. Nevertheless, the variability of the nonlinear-model parameters owing to the alterations of environmental and loading conditions seems to be neglected in the conventional Bayesian framework. A hierarchical Bayesian modeling (HBM) framework has been introduced recently to capture this variability when dealing with linear models [2–4]. However, the implementation of nonlinear model updating based on the HBM approach is still in its early stages.

In this paper, a new time-domain HBM framework is developed for the identification of nonlinear models modeled by a Bouc-Wen hysteresis element [5], aiming to quantify the uncertainties of the nonlinear model parameters and the prediction errors and to further propagate overall uncertainties to the system outputs. The proposed methodology can capture the statistical properties of the model parameters together with the prediction error parameters by introducing a joint distribution of their hyper-parameters. The presented methodology also adopts a novel asymptotic approximation approach, which can significantly reduce the computational burden of the HBM framework. A 5-DOF spring-mass chain model with simulated, noise-contaminated, "measured" acceleration time history data is used to demonstrate the effectiveness of the proposed approach.

X. Jia · C. Papadimitriou (✉)
Department of Mechanical Engineering, University of Thessaly, Volos, Greece
e-mail: costasp@uth.gr

O. Sedehi · L. S. Katafygiotis
Department of Civil and Environmental Engineering, The Hong Kong University of Science and Technology, Hong Kong, China

B. Moaveni
Department of Civil and Environmental Engineering, Tufts University, Medford, MA, USA

Z. Mao (ed.), *Model Validation and Uncertainty Quantification, Volume 3*, Conference Proceedings of the Society for Experimental Mechanics Series, https://doi.org/10.1007/978-3-030-77348-9_14

2 Methodology

The differential equation of motion for a Bouc-Wen (BW) model is written in the form [5]:

$$\mathbf{M}\ddot{\mathbf{u}}(t) + \mathbf{C}\dot{\mathbf{u}}(t) + \alpha\mathbf{K}_0\mathbf{u}(t) + \mathbf{K}_0\,(1-\alpha)\,\mathbf{z}(t) = \mathbf{P}(t) \tag{1}$$

where $\mathbf{M}$ and $\mathbf{C}$ are the mass and the viscous damping matrices, $\mathbf{u}(t)$ is the displacement response, $\mathbf{K}_0$ denotes the initial tangent stiffness, α defines the share of linear part while $1-\alpha$ defines the share of nonlinear hysteretic part, and $\mathbf{z}(t)$ is the virtual hysteretic displacement. Without including the pinching effect and degradation functions in this paper, the formulation of the implemented hysteretic displacement $\mathbf{z}(t)$ can be simplified as:

$$\dot{\mathbf{z}}(t) = A\dot{\mathbf{u}}(t) - \beta\,|\dot{\mathbf{u}}(t)|\,\mathbf{z}(t)|\mathbf{z}(t)|^{n-1} - \gamma\dot{\mathbf{u}}(t)|\mathbf{z}(t)|^{n} \tag{2}$$

where the parameter A determines the tangent stiffness and the parameters β, γ and n affect the shape and smoothness of the hysteretic model, respectively. The implemented BW model can be fully parameterized by six parameters. However, due to the fact that the nonlinear parameters are interrelated, various combinations of those parameters can simulate similar model responses, which may cause difficulties in updating the model parameters [6]. The nonlinear parameters α, β, γ, along with the linear parameter $\mathbf{K}_0$, are calibrated in this paper, and the remaining parameters will be fixed in further applications.

Let $D_i = \left\{\hat{\mathbf{Y}}_i\,(j\Delta t) \in R^{N_0},\ \ i = 1, 2, \ldots, N_{\mathrm{D}},\ \ j = 1, 2, \ldots, N_{\mathrm{d}}\right\}$ be the i - th experimental data set consisting of a sequence of acceleration data measured at N_0 degrees of freedoms (DOFs), where N_{d} is the number of the sampled data using a sampling rate Δt. Consider a parameterized class of nonlinear structural model M with a Bouc-Wen hysteresis type. Let $\boldsymbol{\theta} \in R^{N_{\boldsymbol{\theta}}}$ be the set of structural model parameters composing the parameters $\mathbf{K}_0, \alpha, A, \beta, \gamma, n$, where $N_{\boldsymbol{\theta}}$ is the total number of the unknown updated parameter $\boldsymbol{\theta}$. Herein, uncertainties are embedded into the model parameters by assigning Gaussian distribution for $\boldsymbol{\theta}$ with hyper-mean $\boldsymbol{\mu}_{\boldsymbol{\theta}}$ and hyper-covariance matrix $\Sigma_{\boldsymbol{\theta}}$ [7]. The realization of $\boldsymbol{\theta}$ is free to vary across the data sets, where $\boldsymbol{\theta}_i$ corresponds to D_i and is considered as an independent sample from $N(\boldsymbol{\theta}|\,\boldsymbol{\mu}_{\boldsymbol{\theta}}, \Sigma_{\boldsymbol{\theta}})$. Let also $g_i\,(t;\boldsymbol{\theta}_i) = \left\{\mathbf{Y}_i\,(t;\boldsymbol{\theta}_i) \in R^{N_{\mathrm{s}}}, t = j\Delta t\right\}$ be the predicted response time histories generated from the model M corresponding to a particular value of the i - th model parameter set $\boldsymbol{\theta}_i$, where N_{s} denotes the number of DOFs. The discrepancy between the i - th experimental data set and the i - th predicted response time histories can be defined as:

$$\boldsymbol{\varepsilon}_{i,l} = g_{i,l}\,(j\Delta t;\boldsymbol{\theta}_i) - \hat{\mathbf{Y}}_{i,l}(j\Delta t) \tag{3}$$

where l denotes the l - th DOF of the system and $l = 1, 2, \ldots, N_0$. The notation $\boldsymbol{\varepsilon}_{i,\,l}$ represents the prediction error modeled by Gaussian variables $\boldsymbol{\varepsilon}_{\mathrm{r}} \sim N(\,\boldsymbol{\varepsilon}_{\mathrm{r}}|\,\mathbf{0}, \Sigma_{i,\,l})$ with zero mean and covariance matrix $\Sigma_{i,\,l} = (\sigma_i a_{i,\,l})^2 I$, where σ_i^2 is the variance corresponding to the i - th data set and $a_{i,\,l}$ denotes the intensity of the response time histories in the l - th DOF, given as $a_{i,l} = \sqrt{\frac{1}{N_{\mathrm{d}}}\sum_{j=1}^{N_{\mathrm{d}}}\hat{\mathbf{Y}}_{i,l}^2\,(j\Delta t)}$. Note that the parameter $\sigma^2 = \left\{\sigma_i^2,\ \ i = 1, 2, \ldots, N_{\mathrm{D}}\right\}$ is the one that needs to be identified, and it is used to elucidate the uncertainty of the prediction error arising from a modeling error or measurement noise. Inverse gamma (IG) distribution is employed here for the prediction error, as shown below:

$$p\left(\sigma^2;\lambda_1,\lambda_2\right) = \mathrm{IG}\left(\sigma^2;\lambda_1,\lambda_2\right) = \frac{(\lambda_2)^{\lambda_1}}{\Gamma\,(\lambda_1)}\left(\sigma^2\right)^{-\lambda_1-1}\exp\left(-\frac{\lambda_2}{\sigma^2}\right) \tag{4}$$

The parameters λ_1 and λ_2 are the shape parameter and scale parameter, respectively.

According to Bayes rules, the joint posterior distribution of all parameters is built as follows:

$$\begin{aligned} p\left(\{\boldsymbol{\theta}_i\}_{i=1}^{N_{\mathrm{D}}}, \left\{\sigma_i^2\right\}_{i=1}^{N_{\mathrm{D}}}, \boldsymbol{\mu}_{\boldsymbol{\theta}}, \Sigma_{\boldsymbol{\theta}}, \lambda_1, \lambda_2 | \{D_i\}_{i=1}^{N_{\mathrm{D}}}\right) \propto\ & p\left(\{\boldsymbol{\theta}_i\}_{i=1}^{N_{\mathrm{D}}}, \left\{\sigma_i^2\right\}_{i=1}^{N_{\mathrm{D}}}, \boldsymbol{\mu}_{\boldsymbol{\theta}}, \Sigma_{\boldsymbol{\theta}}, \lambda_1, \lambda_2\right) \\ & p\left(\{D_i\}_{i=1}^{N_{\mathrm{D}}} | \{\boldsymbol{\theta}_i\}_{i=1}^{N_{\mathrm{D}}}, \left\{\sigma_i^2\right\}_{i=1}^{N_{\mathrm{D}}}, \boldsymbol{\mu}_{\boldsymbol{\theta}}, \Sigma_{\boldsymbol{\theta}}, \lambda_1, \lambda_2\right) \end{aligned} \tag{5}$$

The joint prior distribution is taken as:

$$p\left(\{\boldsymbol{\theta}_i\}_{i=1}^{N_{\mathrm{D}}}, \left\{\sigma_i^2\right\}_{i=1}^{N_{\mathrm{D}}}, \boldsymbol{\mu}_{\boldsymbol{\theta}}, \Sigma_{\boldsymbol{\theta}}, \lambda_1, \lambda_2\right) = p\left(\boldsymbol{\mu}_{\boldsymbol{\theta}}, \Sigma_{\boldsymbol{\theta}}, \lambda_1, \lambda_2\right)\prod_{i=1}^{N_{\mathrm{D}}} p\left(\boldsymbol{\theta}_i|\boldsymbol{\mu}_{\boldsymbol{\theta}}, \Sigma_{\boldsymbol{\theta}}\right)\mathrm{IG}\left(\sigma_i^2|\lambda_1,\lambda_2\right) \tag{6}$$

The likelihood function can be simplified as the product of individual function $p\left(D_i|\boldsymbol{\theta}_i, \sigma_i^2\right)$, and therefore the joint posterior distribution can be rewritten as:

$$p\left(\{\boldsymbol{\theta}_i\}_{i=1}^{N_\mathrm{D}}, \{\sigma_i^2\}_{i=1}^{N_\mathrm{D}}, \boldsymbol{\mu}_{\boldsymbol{\theta}}, \boldsymbol{\Sigma}_{\boldsymbol{\theta}}, \lambda_1, \lambda_2|\{D_i\}_{i=1}^{N_\mathrm{D}}\right) \propto p\left(\boldsymbol{\mu}_{\boldsymbol{\theta}}, \boldsymbol{\Sigma}_{\boldsymbol{\theta}}, \lambda_1, \lambda_2\right) \prod_{i=1}^{N_\mathrm{D}} p\left(D_i|\boldsymbol{\theta}_i, \sigma_i^2\right) N\left(\boldsymbol{\theta}_i|\boldsymbol{\mu}_{\boldsymbol{\theta}}, \boldsymbol{\Sigma}_{\boldsymbol{\theta}}\right) \mathrm{IG}\left(\sigma_i^2|\lambda_1, \lambda_2\right) \tag{7}$$

The posterior PDF of the hyper-parameters are obtained through the marginalization of Eq. (7). Using an efficient asymptotic approximation to evaluate each one of the N_D independent multidimensional integrals over the space of the parameters $\boldsymbol{\theta}_i$ that arise in the marginalization process, and carrying out the marginalization integrals over the prediction error parameters exactly, one can derive the marginal distribution over σ_i^2 as:

$$p\left(\{\boldsymbol{\theta}_i\}_{i=1}^{N_\mathrm{D}}, \boldsymbol{\mu}_{\boldsymbol{\theta}}, \boldsymbol{\Sigma}_{\boldsymbol{\theta}}, \lambda_1, \lambda_2|\{D_i\}_{i=1}^{N_\mathrm{D}}\right) \propto p\left(\boldsymbol{\mu}_{\boldsymbol{\theta}}, \boldsymbol{\Sigma}_{\boldsymbol{\theta}}, \lambda_1, \lambda_2\right) T\left(\hat{\boldsymbol{\theta}}_i, \lambda_1, \lambda_2\right) \prod_{i=1}^{N_\mathrm{D}} \left[N\left(\boldsymbol{\theta}_i|\boldsymbol{\mu}_{\boldsymbol{\theta}}, \boldsymbol{\Sigma}_{\boldsymbol{\theta}}\right) N\left(\boldsymbol{\theta}_i|\hat{\boldsymbol{\theta}}_i, \boldsymbol{\Sigma}_L\left(\hat{\boldsymbol{\theta}}_i, \lambda_1, \lambda_2\right)\right)\right] \tag{8}$$

where $\hat{\boldsymbol{\theta}}_i$ is obtained by minimizing $L\left(\boldsymbol{\theta}_i, \lambda_1, \lambda_2\right) = f\left(\lambda_1\right) \ln\left(\frac{1}{2} J\left(\boldsymbol{\theta}_i\right) + \lambda_2\right)$ and $\boldsymbol{\Sigma}_L\left(\hat{\boldsymbol{\theta}}_i, \lambda_1, \lambda_2\right)$ is the inverse of the Hessian matrix of L, $f\left(\lambda_1\right) = \frac{N_\mathrm{d} N_0 + 2\lambda_1}{2}$, and $J\left(\boldsymbol{\theta}_i\right) = \sum_{l=1}^{N_0} \frac{1}{a_{i,l}^2} \sum_{j=1}^{N_\mathrm{d}} \left(\hat{\mathbf{Y}}_{i,l}(j) - g_{i,l}\left(j; \boldsymbol{\theta}_i\right)\right)^2$. Herein $T\left(\hat{\boldsymbol{\theta}}_i, \lambda_1, \lambda_2\right)$ is calculated as:

$$T\left(\hat{\boldsymbol{\theta}}_i, \lambda_1, \lambda_2\right) = \left[\frac{(\lambda_2)^{\lambda_1}}{\Gamma\left(\lambda_1\right)} \Gamma\left(f\left(\lambda_1\right)\right)\right]^{N_\mathrm{D}} \prod_{i=1}^{N_\mathrm{D}} \left[\frac{1}{2} J\left(\hat{\boldsymbol{\theta}}_i\right) + \lambda_2\right]^{-f\left(\lambda_1\right)} \sqrt{\left|\boldsymbol{\Sigma}_L\left(\hat{\boldsymbol{\theta}}_i, \lambda_1, \lambda_2\right)\right|} \tag{9}$$

Then the marginal distribution of the hyper-parameters can be obtained analytically by integrating with the model parameters to yield the following expression:

$$p\left(\boldsymbol{\mu}_{\boldsymbol{\theta}}, \boldsymbol{\Sigma}_{\boldsymbol{\theta}}, \lambda_1, \lambda_2|\{D_i\}_{i=1}^{N_\mathrm{D}}\right) \propto p\left(\boldsymbol{\mu}_{\boldsymbol{\theta}}, \boldsymbol{\Sigma}_{\boldsymbol{\theta}}, \lambda_1, \lambda_2\right) T\left(\hat{\boldsymbol{\theta}}_i, \lambda_1, \lambda_2\right) \prod_{i=1}^{N_\mathrm{D}} N\left(\boldsymbol{\mu}_{\boldsymbol{\theta}}|\hat{\boldsymbol{\theta}}_i, \boldsymbol{\Sigma}_{\boldsymbol{\theta}} + \boldsymbol{\Sigma}_L\left(\hat{\boldsymbol{\theta}}_i, \lambda_1, \lambda_2\right)\right) \tag{10}$$

The aforementioned formula requires solving N_D optimization problems and computing the Hessian N_D times, which involve FE model runs. The posterior distribution of the model parameters and prediction error parameter can be then obtained as:

$$p\left(\boldsymbol{\theta}, \sigma^2|D\right) \approx \frac{1}{N_\mathrm{s}} \sum_{m=1}^{N_m} N\left(\boldsymbol{\theta}|\boldsymbol{\mu}_{\boldsymbol{\theta}}^{(m)}, \boldsymbol{\Sigma}_{\boldsymbol{\theta}}^{(m)}\right) \mathrm{IG}\left(\sigma^2|{\lambda_1}^{(m)}, {\lambda_2}^{(m)}\right) \tag{11}$$

where N_m is the number of samples. The transitional Markov chain Monte Carlo (TMCMC) algorithm [8] is used to generate the samples. The FE model parameter uncertainty and prediction error can be then propagated for predicting the system output.

3 Application

Consider a 5-DOF spring-mass chain system representing a shear building model excited at the first floor and suppose the same nonlinear properties in each floor. The nominal values of nonlinear parameters are assumed as $\alpha = 0.1$, $\beta = 1$, $\gamma = 1$, $A = 10$, and $n = 1$. One hundred acceleration data sets are generated from a mass-perturbed FE model, where the nominal mass is added by a 2% error. As mentioned before, the linear parameter K_0 and nonlinear parameters α, β, γ are assumed to be estimated. Grouping strategy is employed herein to reduce the total number of identified parameters. Each parameter

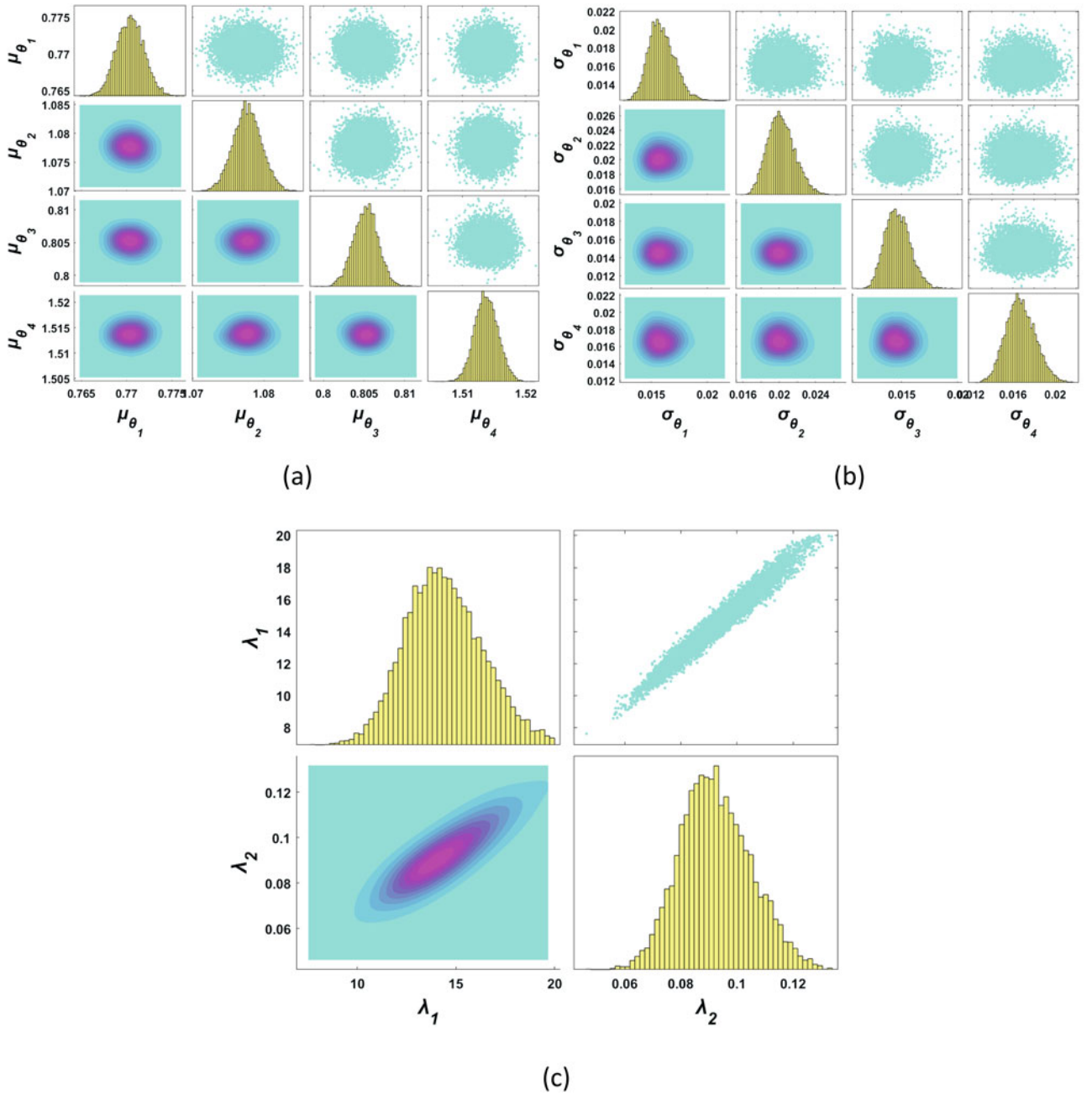

Fig. 1 Posterior distribution of (**a**) hyper-means, (**b**) hyper-standard deviations, and (**c**) hyper-parameters of prediction error

is assembled in a specific group. For normalization purposes, four unknown parameters $\boldsymbol{\theta} = (\theta_1, \theta_2, \theta_3, \theta_4)$ are introduced and respectively multiply the nominal values of the corresponding quantities. The proposed HBM framework is then applied to estimate the hyper-parameters of the model parameters and prediction error parameter, as shown in Fig. 1. It is noted that the hyper-means are deviated from their nominal values; this is because of the presence of model error. It is also noted that the hyper-standard deviations are around 2%, which shows the variability uncertainty of each parameter. The parameters λ_1, λ_2 aim to capture the statistical properties of the prediction error parameter. It is obvious that the two parameters are strongly correlated, as shown in its sample region and contour plot. This is reasonable since those two parameters determine the distribution of the prediction error parameter. The obtained uncertainties are then propagated to the quantities of interest (QoI). Two cases are considered for predicting the responses. The first case only considers the variability uncertainty for the predictions of the accelerations of the fifth floor, while the second case includes the prediction error as well. Figure 2 shows the results of case 1 by using the conventional Bayesian method (CBM) and hierarchical Bayesian method (HBM). It can be

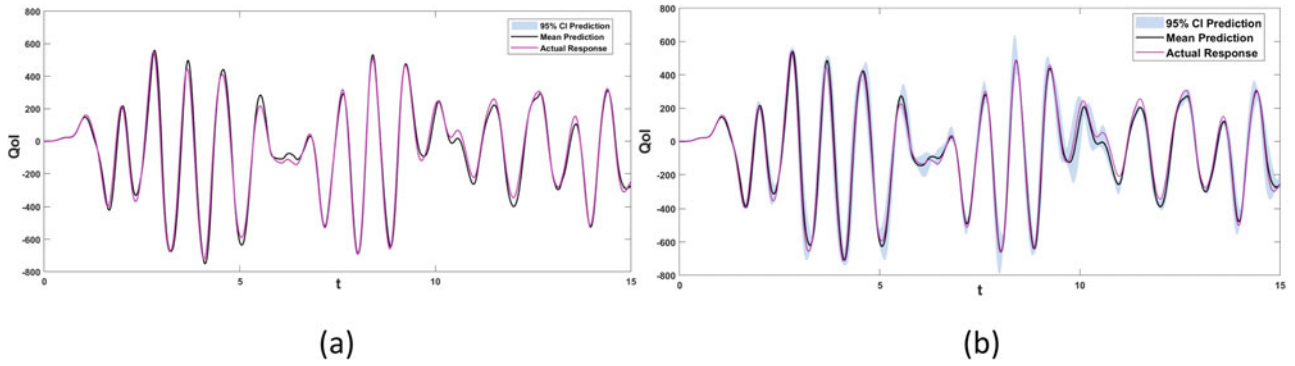

Fig. 2 Predictions of accelerations of the fifth floor considering only variability uncertainty using (**a**) CBM and (**b**) HBM

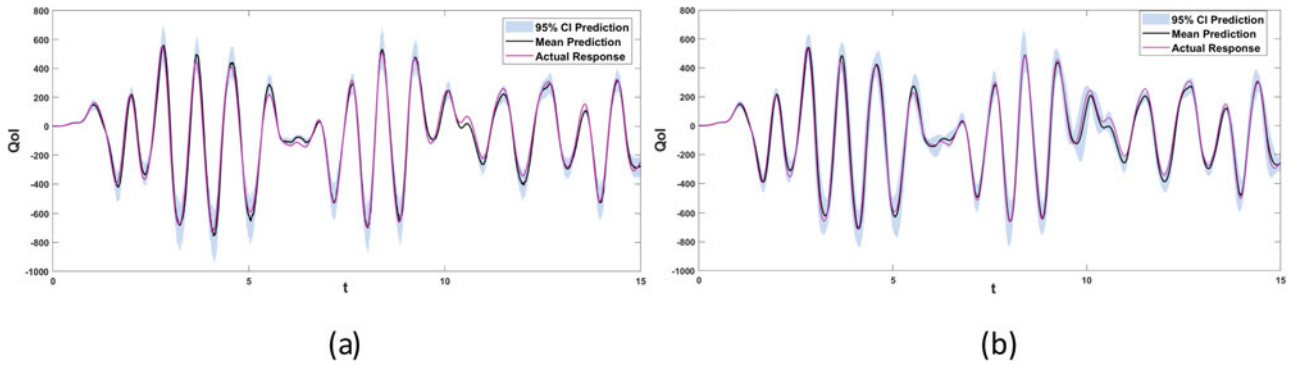

Fig. 3 Predictions of accelerations of the fifth floor considering the overall uncertainties using (**a**) CBM and (**b**) HBM

seen that the proposed HBM delivers a reasonable confidence interval (CI) of the predictions, which contains the most part of the measurement, while the CBM gives an extremely thin uncertainty bound where the measurement falls outside. Figure 3 shows the results of considering both uncertainties for the predictions. The uncertainty bounds for the HBM are slightly affected by the model error, while the CBM approach provides also reasonable uncertainty bounds, similar to the HBM, only if the prediction error model uncertainties are included. However, for unobserved quantities, prediction error models are not available, and so the CBM approach will severely underestimate uncertainties, while the proposed HBM is expected to provide reasonable uncertainty bounds.

Acknowledgements This project has received funding from the European Union's Horizon 2020 research and innovation program under Marie Skłodowska-Curie grant agreement No 764547.

References

1. Beck, J.L., Katafygiotis, L.S.: Updating models and their uncertainties. I: Bayesian statistical framework. J. Eng. Mech. **124**, 455–461 (1998)
2. Behmanesh, I., Moaveni, B.: Accounting for environmental variability, modeling errors, and parameter estimation uncertainties in structural identification. J. Sound Vib. **374**, 92–110 (2016)
3. Sedehi, O., Papadimitriou, C., Katafygiotis, L.S.: Probabilistic hierarchical Bayesian framework for time-domain model updating and robust predictions. Mech. Syst. Signal Process. **123**, 648–673 (2019)
4. Sedehi, O., Katafygiotis, L.S., Papadimitriou, C.: Hierarchical Bayesian operational modal analysis: theory and computations. Mech. Syst. Signal Process. **140**, 106663 (2020)
5. Ismail, M., Ikhouane, F., Rodellar, J.: The hysteresis Bouc-Wen model, a survey. Arch. Comput. Meth. Eng. **16**, 161–188 (2009)
6. Asgarieh, E., Moaveni, B., Barbosa, A.R., Chatzi, E.: Nonlinear model calibration of a shear wall building using time and frequency data features. Mech. Syst. Signal Process. **85**, 236–251 (2017)
7. Behmanesh, I., Moaveni, B., Lombaert, G., Papadimitriou, C.: Hierarchical Bayesian model updating for structural identification. Mech. Syst. Signal Process. **64–65**, 360–376 (2015)
8. Ching, J., Chen, Y.-C.: Transitional Markov chain Monte Carlo method for Bayesian model updating, model class selection, and model averaging. J. Eng. Mech. **133**, 816–832 (2007)

SLS Integrated Modal Test Uncertainty Quantification Using the Hybrid Parametric Variation Method

Daniel C. Kammer, Paul Blelloch, and Joel Sills

Abstract Uncertainty in structural loading during launch is a significant concern in the development of spacecraft and launch vehicles. Small variations in launch vehicle and payload mode shapes and their interaction can result in significant variation in system loads. In many cases involving large aerospace systems, it is difficult, not economical, or impossible to perform a system modal test. However, it is still vital to obtain test results that can be compared with analytical predictions to validate models. Instead, the "Building Block Approach" is used in which system components are tested individually. Component models are correlated and updated to agree as best they can with test results. The Space Launch System consists of a number of components that are assembled into a launch vehicle. Finite element models of the components are developed, reduced to Hurty/Craig-Bampton models, and assembled to represent different phases of flight. The only opportunity to obtain modal test data from an assembled Space Launch System will be during the Integrated Modal Test. There is always uncertainty in every model, which flows into uncertainty in predicted system results. Uncertainty quantification is used to determine statistical bounds on prediction accuracy based on model uncertainty. For the Space Launch System, model uncertainty is at the Hurty/Craig-Bampton component level. Uncertainty in the Hurty/Craig-Bampton components is quantified using the hybrid parametric variation approach, which combines parametric and nonparametric uncertainties. Uncertainty in model form is one of the biggest contributors to uncertainty in complex built-up structures. This type of uncertainty cannot be represented by variations in finite element model input parameters and thus cannot be included in a parametric approach. However, model-form uncertainty can be modeled using a nonparametric approach based on the random matrix theory. The hybrid parametric variation method requires the selection of dispersion values for the Hurty/Craig-Bampton fixed-interface eigenvalues and the Hurty/Craig-Bampton stiffness matrices. Component test/analysis frequency error is used to identify fixed-interface eigenvalue dispersions, while test/analysis cross-orthogonality is used to identify stiffness dispersion values. The hybrid parametric variation uncertainty quantification approach is applied to the Space Launch System Integrated Modal Test configuration. Monte Carlo analysis is performed, and statistics are determined for modal correlation metrics, frequency response from Integrated Modal Test shakers to selected accelerometers, as well as other metrics for determining how well target modes are excited and identified. If the predicted uncertainty envelopes future Integrated Modal Test results, then there will be increased confidence in the utility of the component-based hybrid parametric variation uncertainty quantification approach.

Keywords Uncertainty quantification · Hurty/Craig-Bampton · Random matrix · Model form

Acronyms

CAA	Crew Access Arm
CL	Centerline
CS	Core stage
CT	Crawler Transporter
DCGM	Diagonal cross-generalized mass

D. C. Kammer (✉) · P. Blelloch
ATA Engineering, Inc, San Diego, CA, USA
e-mail: daniel.kammer@wisc.edu

J. Sills
NASA Johnson Space Center, Houston, TX, USA

Z. Mao (ed.), *Model Validation and Uncertainty Quantification, Volume 3*, Conference Proceedings of the Society for Experimental Mechanics Series, https://doi.org/10.1007/978-3-030-77348-9_15

DOF	Degree of freedom
FEM	Finite element model
FI	Fixed interface
GP	Gaussian process
HCB	Hurty/Craig-Bampton
HPV	Hybrid parametric variation
ICPS	Interim Cryogenic Propulsion Stage
ISPE	Integrated Spacecraft Payload Element
IVGVT	Integrated Vehicle Ground Vibration Test
IMT	Integrated Modal Test
LSRB	Left Solid Rocket Booster
LV	Launch vehicle
LVSA	Launch Vehicle Stage Adapter
MC	Monte Carlo
MEM	Modal effective mass
ML	Mobile Launcher
MPCV	Multipurpose Crew Vehicle
MSA	MPCV Stage Adapter
MSO	Mass Simulator for Orion
NMIF	Normal mode indicator function
NPV	Nonparametric variation
RMS	Root mean square
RMT	Random matrix theory
RSRB	Right Solid Rocket Booster
RSS	Root sum square
RV	Residual vector
SLS	Space Launch System
SRB	Solid Rocket Booster (Solid Rocket Motor)
TAM	Test-analysis model
UQ	Uncertainty quantification
VAB	Vertical Assembly Building
XO	Cross-orthogonality

1 Introduction

The National Aeronautics and Space Administration (NASA) has historically tested launch vehicles in an integrated configuration with boundary conditions controlled to approximate the boundary conditions expected in flights. Integrated Vehicle Ground Vibration Tests (IVGVT) increase the confidence that the structural loads predicted using system finite element models are within specified limits with respect to accuracy and uncertainty. However, to save cost and schedule, a cross-program decision was made to not perform the IVGVT for the Space Launch System (SLS) and rely more heavily on analytical methods supported by component test results. This process is referred to as the "building-block approach," in which system components are tested individually and component models are correlated and updated to agree with test results as closely as possible.

In spite of this decision, an integrated SLS system will still undergo testing, referred to as the Integrated Modal Test (IMT). The IMT is a ground test of the integrated vehicle, assembled on the Mobile Launcher (ML) in the Vehicle Assembly Building (VAB) facility at Kennedy Spaceflight Center. The results of the IMT will provide an opportunity to validate or update previously correlated SLS component models such that, in an assembled configuration, they provide agreement with integrated system test results. For this test, the integrated SLS is mounted to the launch pad at the base of the Solid Rocket Boosters with the Multi-Purpose Crew Vehicle (MPCV) being replaced by the Mass Simulator for Orion (MSO). The IMT/MSO configuration, shown in Fig. 1, is resting on the six VAB support posts with no Crawler Transporter (CT). The analytical model used in this study consists of SLS Hurty/Craig-Bampton (HCB) components developed based on the IMT integrated finite element model (FEM). The Interim Cryogenic Propulsion Stage (ICPS) and core stage (CS) are empty, with CS pressurization stiffness included corresponding to approximately 4 psi. The integrated model was divided into six HCB

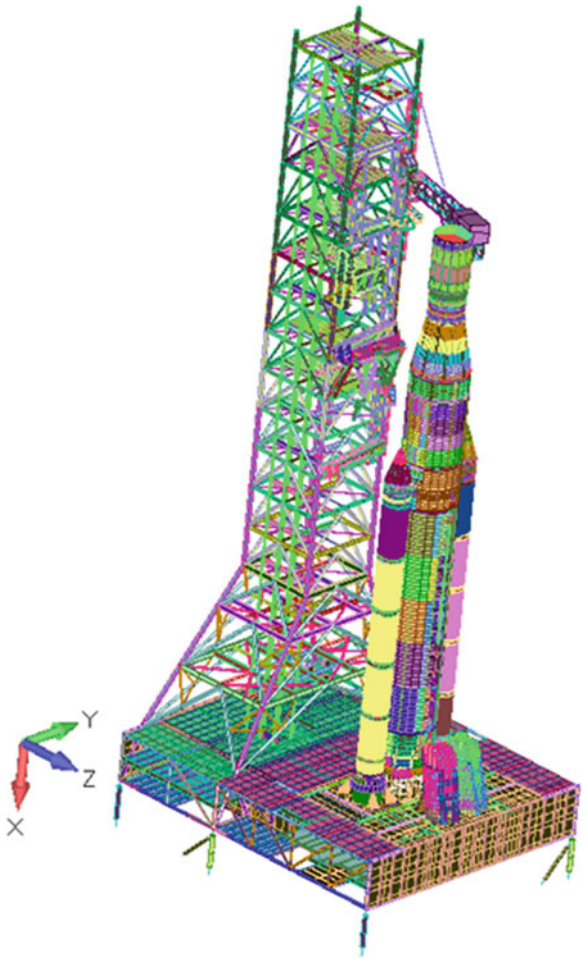

Fig. 1 IMT with MSO on six VAB mounts

[1] components, including the MSO combined with the MPCV Spacecraft Adaptor (MSA), a combined ICPS and Launch Vehicle Stage Adapter (LVSA), the CS, left and right Solid Rocket Boosters (LSRB, RSRB), and the ML.

There is some level of uncertainty in every analytical model, which flows to a level of uncertainty in predicted results. The purpose of uncertainty quantification (UQ) is to provide statistical bounds on prediction accuracy based on model uncertainty. This is distinct from model updating, which attempts to modify models to improve their accuracy. Uncertainty quantification does not improve the accuracy of models but accepts the fact that the models are inaccurate and attempts to quantify the impact of that inaccuracy on predicted results. Previously, a new method for UQ, called the hybrid parametric variation (HPV) method, was applied to SLS HCB components to predict system-level statistics for SLS attitude control transfer functions [2] and CS section loads due to buffet [3]. The HPV method combines a parametric variation of the HCB fixed-interface (FI) modal frequencies with a nonparametric variation (NPV) method that randomly varies the HCB mass and stiffness matrices as Wishart [4] random matrix distributions using the random matrix theory (RMT). The HPV method anchors uncertainty at the HCB level to component modal test results by matching HCB modes to test configuration modes based on either modal effective mass (MEM) or mode descriptions and then applying differing levels of frequency variation. The specific variations depend on the degree to which a component FEM has been verified through modal testing. The NPV method is then layered on top of the frequency variation to match the modal test cross-orthogonality (XO) results. Component uncertainty is propagated to the system level using a Monte Carlo (MC) approach, which generates statistics for system-level results. This provides a UQ method that can be traced directly to available test data and that can be updated as additional data, and better correlated models become available.

The purpose of this study was to apply the HPV UQ approach to the IMT/MSO ground vibration test. Projection of component test-based uncertainty into the system provides estimates of the system-level uncertainty that can be expected in target modal parameters, such as frequencies and mode shapes. Component uncertainty is also propagated into system-level frequency response and normal mode indicator functions (NMIF) [5]. Statistics for NMIF and modal orthogonality can be used during pretest analysis to determine the probability that the target modes will be adequately excited and separated

during the modal test using the proposed sensor and shaker configurations. This study was completed prior to the IMT; however, during a future posttest analysis, the test results can be compared to the UQ predictions. If the uncertainty predicted by the UQ analysis covers the test results, there is increased confidence that the HPV UQ method and the approach used to assign component uncertainty models are valid. This paper presents a brief summary of the theory behind the NPV and HPV methods, including new developments, a description of the IMT components and the corresponding component uncertainty models, followed by the presentation of MC-based statistics for target modal parameters, selected frequency response functions, and normal mode indicator functions. At the time of this study, model correlation and updating of the ML were still in progress, meaning that the sensor set and shaker locations were still evolving. It has been found that the ability of the shaker configuration to adequately excite the target modes is very much dependent on the most recent updated ML model version. Therefore, some of the statistics presented in this report must be considered preliminary.

2 Theory

The SLS consists of components that are assembled into the launch vehicle. In order to predict system performance, FEMs of the components are developed, reduced to HCB representations, and assembled to represent different phases of flight. The same approach is used for IMT. There is always uncertainty in every model, which flows into uncertainty in predicted system results. For the SLS, it is natural to treat the model uncertainty at the HCB component-model level. The HCB component-model displacement vector is given by $u_{\text{HCB}} = \left\{ x_{\text{t}}^T \quad q^T \right\}^T$, where x_{t} is the vector of physical displacements at the component interface and q is the vector of generalized coordinates associated with the component fixed-interface (FI) modes. Given the assumption that the FI modes are mass normalized, the corresponding HCB mass and stiffness matrices have the form

$$M_{\text{HCB}} = \begin{bmatrix} M_{\text{S}} & M_{\text{tq}} \\ M_{\text{tq}}^T & I \end{bmatrix} \quad K_{\text{HCB}} = \begin{bmatrix} K_{\text{S}} & 0 \\ 0 & \lambda \end{bmatrix} \tag{1}$$

in which M_{S} and K_{S} are the component physical mass and stiffness matrices statically reduced to the interface, M_{tq} is the mass coupling between the interface and the fixed-interface modes, I is an identity matrix, and λ is a diagonal matrix of the FI mode eigenvalues. Details of the HCB component-model derivation can be found in reference [1].

In this work, uncertainty in the component HCB representations is quantified using the HPV approach, which combines parametric with nonparametric uncertainty. Purely parametric uncertainty approaches are the most common in the structural dynamics community. Component parameters that are inputs to the FEM, such as Young's modulus, mass density, geometric properties, etc., are modeled as random variables. Parametric uncertainty can be propagated into the system response using a method such as stochastic finite element analysis [6]. The advantage of the parametric approach is that each random set of model parameters represents a specific random FEM. However, there are disadvantages associated with the parametric method: it can be very time-consuming, there are infinite number of ways to parameterize the model, and the selected parameter probability distributions are generally not available. The most significant drawback is that the uncertainty represented is limited to the form of the nominal FEM. It is known that most errors in a FEM stem from modeling assumptions or model-form errors, not parametric errors. Therefore, in practice, the parameter changes are merely surrogates for the actual model errors. In the case of HPV, the HCB components are parameterized in terms of the FI eigenvalues, not the inputs to the original FEM. While there is not a simple direct connection between the random FI eigenvalues and a random component FEM, there is a direct connection to the corresponding random HCB component.

Model form is likely the largest contributor to uncertainty in complex built-up structures as it cannot be directly represented by model parameters and thus cannot be included in a parametric approach. Familiar examples include unmodeled nonlinearities, errors in component joint models, etc. Instead, model-form uncertainty can be represented using RMT, where a probability distribution is developed for the matrix ensemble of interest. RMT was introduced and developed in mathematical statistics by Wishart [4], and more recently, Soize [7, 8] developed an NPV approach to represent model-form uncertainty in structural dynamics applications. Soize's approach was extended by Adhikari [9, 10] using Wishart distributions to model random structural mass, damping, and stiffness matrices. The nonparametric matrix-based approach to representing structural uncertainty has been used previously in several aeronautics and aerospace engineering applications [11–13].

The maximum entropy (ME) principle was employed by Soize [8] to derive the positive and positive-semidefinite ensembles SE^{+} and SE^{+0}, which follow a matrix variate gamma distribution and are capable of representing random structural matrices. This means that the matrices in the ensembles are real and symmetric and possess the appropriate sign

definiteness to represent structural mass, stiffness, or damping matrices. As the dimension of the random matrix n increases, the matrix variate gamma distribution converges to a matrix variate Wishart distribution. The matrix dimensions in structural dynamics applications are usually sufficient to give a negligible difference between the two distributions. In letting ensemble member random matrix G be any of the random mass, stiffness, or damping matrices, it is assumed that G follows a matrix variate Wishart distribution, $G \sim W_n(p, \Sigma)$. A Wishart distribution with parameters p and Σ can be thought of as the sum of the outer product of p independent random vectors X_i all having a multivariate normal distribution with zero mean and covariance matrix Σ. Parameter p is sometimes called the shape parameter. The random matrix G can be written as

$$G = \sum_{i=1}^{p} X_i X_i^T \quad X_i \sim N_n(0, \Sigma) \tag{2}$$

where the expected value is given by

$$E(G) = \overline{G} = p\Sigma \tag{3}$$

The dispersion or normalized standard deviation of the random matrix G is defined by the relation

$$\delta_G^2 = \frac{E\left(\left\|G - \overline{G}\right\|_{\mathrm{F}}^2\right)}{E\left(\left\|\overline{G}\right\|_{\mathrm{F}}^2\right)} \tag{4}$$

in which $\|*\|_{\mathrm{F}}^2$ is the Frobenius norm squared, or trace$({}_*{}^T{}_*)$. It can be shown that Eq. (4) reduces to the expression

$$\delta_G^2 = \frac{1}{p}\left[1 + \frac{\left(\mathrm{tr}\left(\overline{G}\right)\right)^2}{\mathrm{tr}\left(\overline{G}^T\overline{G}\right)}\right] = \frac{1}{p}\left[1 + \gamma_G\right] \tag{5}$$

where $\gamma_G = \frac{\left(\mathrm{tr}\left(\overline{G}\right)\right)^2}{\mathrm{tr}\left(\overline{G}^T\overline{G}\right)}$ can be thought of as a measure of the magnitude of the matrix. The uncertainty in the random matrix G is dictated by the shape parameter p, the number of inner products in Eq. (2). The larger the value of p, the smaller the dispersion δ_G. There may be instances when it is desirable to have the same amount of uncertainty in two or more substructures. Suppose G_1 and G_2 represent structural matrices, such as stiffness, from two different system components. In order to have equivalent uncertainty in the two matrices, the shape parameter p must be the same for both ensembles. However, Eq. (5) shows that even if $p_1 = p_2 = p$, the dispersion values are not the same in general, $\delta_{G_1}^2 \neq \delta_{G_2}^2$, unless $\gamma_1 = \gamma_2$. A more useful definition of matrix dispersion is the normalized dispersion

$$\delta_{G_n} = \frac{\delta_{G_1}}{\sqrt{1+\gamma_1}} = \frac{\delta_{G_2}}{\sqrt{1+\gamma_2}} = \frac{1}{\sqrt{p}} \tag{6}$$

which is independent of the matrix magnitude γ_G.

Adhikari [9] referred to the random matrix method developed by Soize [7, 8] as Method 1. The Wishart parameters are selected as p and $\Sigma = G_\mathrm{o}/p$ where G_o is the nominal value of G. The mean of the distribution is given by Eq. (3) as $\overline{G} = p\Sigma = p\left(G_\mathrm{o}/p\right) = G_\mathrm{o}$. Therefore, Method 1 preserves the nominal matrix as the mean of the ensemble. In general, the nominal matrix can be decomposed in the form

$$G_\mathrm{o} = LL^T \tag{7}$$

In the case of a positive definite matrix, this would just be the Cholesky decomposition. Let $(n \times p)$ matrix X be given by

$$X = \left[x_1 \; x_2 \cdots x_p\right] \tag{8}$$

in which x_i is an $(n \times 1)$ column vector containing standard random normal variables such that $x_i \sim N_n(0, I_n)$. Note that $p \geq n$ must be satisfied in order for G to be full rank. An ensemble member $G \sim W_n(p, G_\mathrm{o}/p)$ can then be generated for MC analysis using the expression

$$G = \frac{1}{p} L X X^T L^T \tag{9}$$

It has been found that ensembles of random component mass matrices are best represented using Method 1. Adhikari [9] noted that Method 1 does not maintain the inverse of the mean matrix as the mean of the inverse; that is

$$E\left(G^{-1}\right) \neq [E(G)]^{-1} = \overline{G}^{-1} \tag{10}$$

The two can be vastly different in some cases, which is clearly not physically realistic. Instead, he proposed Method 3, in which the Wishart parameters are selected as p and $\Sigma = G_o/\theta$, where

$$\theta = \frac{1}{\delta_G^2}\left[1 + \gamma_G\right] - (n+1) \tag{11}$$

An ensemble member $G \sim W_n(p, G_o/\theta)$ can then be generated using the relation

$$G = \frac{1}{\theta} L X X^T L^T \tag{12}$$

In this case, the inverse of the mean matrix is preserved as the mean of the ensemble inverses, where the mean matrix is now given by

$$\overline{G} = p\Sigma = p\left(G_o/\theta\right) = \frac{p}{\theta} G_o \tag{13}$$

In Method 3, the dispersion defined in Eq. (4) is now calculated with respect to the mean given in Eq. (13), while Eqs. (5) and (6) still hold. It has been determined that ensembles of random component stiffness matrices are best represented using Method 3. Therefore, the nonparametric portion of the HPV method is based on a Method 1 randomization of the component mass matrix and a Method 3 randomization of the component stiffness matrix. In IMT application, only the component stiffness matrices are randomized. The component mass matrices are assumed to have little uncertainty and are considered to be deterministic.

The Wishart matrix uncertainty model results in uncertainty in both frequencies and mode shapes. However, an extensive amount of MC simulation and analysis performed during this and previous assessments has shown that, in comparison to modal frequencies, the corresponding component mode shapes tend to be much more sensitive to the nonparametric matrix randomization provided by Methods 1 and 3. Therefore, the HPV approach possesses a parametric component of uncertainty in which the eigenvalues of the FI modes in the component HCB representation are assumed to be random variables. The FI eigenvalues are then random parameters within the HCB component stiffness matrix. During each iteration within an MC analysis, a random draw of HCB FI eigenvalues is selected to generate a random HCB component stiffness matrix. Note that the mean of this ensemble would just be the nominal HCB stiffness matrix. However, for the current iteration, the parametrically randomized HCB stiffness is treated as the nominal matrix for NPV, and Method 3 is applied to provide model-form uncertainty on top of the FI eigenvalue uncertainty. This is analogous to the approach proposed by Capiez-Lernout [11] for separating parametric and nonparametric uncertainty. In contrast to the nonparametric model-form uncertainty, the mode shapes are relatively insensitive to the parametric FI eigenvalue uncertainty. Therefore, the HPV approach provides the capability to almost independently adjust the uncertainty in the component frequencies and mode shapes when the uncertainty levels are not too high.

The HPV method also has the capability of preserving rigid body motion and rigid body mass properties. It can also preserve the certainty of subsets of component modes. For example, in previous assessments, the component slosh modes were assumed to have no uncertainty. Details on how to handle these special cases are presented in reference [2].

2.1 Randomization of Component FI Eigenvalues Using Gaussian Process Models

In past work [2, 3], the component FI eigenvalues were considered as independent random variables. It was shown in reference [3] that even though the variation of the FI eigenvalues is parametric with respect to the HCB representation, if they are varied independently, it results in a nonparametric variation of the stiffness matrix in physical space. In contrast, if

the FI eigenvalues are varied in unison, i.e. perfectly correlated, it produces a purely parametric variation of the component stiffness matrix in physical space. As a component stiffness matrix varies, it is common to see the corresponding eigenvalues vary in a correlated manner to some extent, especially when they are closely spaced. Therefore, reality is somewhere between treating the FI eigenvalues as totally independent and treating them as perfectly correlated.

In this study, Gaussian process (GP) modeling [14] was used to represent the random space of component FI eigenvalues. This means that any finite ensemble of component FI eigenvalue realizations follows a multivariate normal distribution. The characteristics of the realizations therefore are completely determined by the mean vector $\overline{\lambda}$ and covariance matrix Σ or covariance function $\Sigma(x, x^{'})$. In general, the covariance matrix or function corresponding to the FI eigenvalues of a component is unknown. However, a robust assumption [14] that was used in this study is that the covariance function can be defined based on Euclidean distance. Therefore, if $Y(x)$ is a realization of the FI eigenvalues, the covariance function is defined as

$$\mathrm{Cov}\left(Y(x), Y\left(x'\right)\right) = \Sigma\left(x, x'\right) = \exp\left(-\left\|x - x'\right\|^2\right) \tag{14}$$

where x and $x^{'}$ are two points in FI eigenvalue space. The covariance between $Y(x)$ and $Y(x^{'})$ decays exponentially fast as the distance between x and $x^{'}$ increases. The covariance matrix Σ_n is then generated by evaluating $\Sigma(x_i, x_j)$ in Eq. (14) at all pairs of the n component FI eigenvalues.

It is apparent that the covariance matrix derived based on Eq. (14) corresponds to unit scale or variance. In practice, it is desired to have the variance of the FI eigenvalues be based on the difference between the FEM and test eigenvalues or frequencies from the component modal test. Suppose that $\Delta\lambda$ is a vector of root-mean-square (RMS) uncertainties assigned to the FI eigenvalues based on the component modal test correlation results. In the case of a Gaussian distribution, the RMS uncertainty is just the standard deviation. The FI eigenvalue covariance matrix with the proper variance is then given by

$$\Sigma_{\mathrm{nv}} = \mathrm{diag}\left(\Delta\lambda\right) * \Sigma_n * \mathrm{diag}\left(\Delta\lambda\right) \tag{15}$$

where diag($\Delta\lambda$) is a diagonal matrix. If the jth eigenvalue λ_j is not uncertain, then $\Delta\lambda_j = 0$ and the jth row and column of Σ_{nv} are null, meaning that Σ_{nv} is positive semi-definite. Within MATLAB®, the command

$$Y = \mathrm{mvnrnd}\left(\overline{\lambda}, \Sigma_{\mathrm{nv}}, 1\right) \tag{16}$$

produces a finite realization of the random FI eigenvalues under a GP prior with a specific mean and covariance, which can be easily implemented within an MC analysis.

2.2 *Mixed-Boundary Approach for Assigning HCB Eigenvalue Dispersions*

The HPV approach for modeling component uncertainty requires the selection of dispersion values for the HCB component FI eigenvalues, mass matrix, and stiffness matrix. Ideally, these dispersion values are selected for each component based on component modal test results. This is because test-analysis modal correlation metrics are used to determine the dispersions. Test-analysis frequency error is used to identify the HCB FI eigenvalue uncertainties, but one of the biggest challenges in the propagation of component test-analysis frequency error into uncertainty in the HCB flight configuration FI modes is that the component test configuration and the component flight configuration boundary conditions and/or hardware are almost never the same. Because of this, it is difficult to match test configuration modes with flight configuration FI modes. The boundary condition mismatch can be alleviated using a mixed-boundary approach. In general, the HCB flight configuration FI modes will be overconstrained when compared with the test configuration modes. Therefore, the HCB stiffness matrix in Eq. (1) can be written as

$$K_{\mathrm{HCB}} = \begin{bmatrix} K_{\mathrm{S}} & 0 \\ 0 & \lambda \end{bmatrix} = \begin{bmatrix} K_{\mathrm{cc}} & K_{\mathrm{cb}} & 0 \\ K_{\mathrm{bc}} & K_{\mathrm{bb}} & 0 \\ 0 & 0 & \lambda \end{bmatrix} \tag{17}$$

where the HCB flight configuration set of boundary degrees of freedom (DOFs) has been divided into two subsets: the c-set contains all DOFs that are free in the component test configuration, and the b-set contains the DOFs that are constrained in

the component test configuration. When the HCB flight configuration is constrained at the test configuration interface DOF (b-set), it produces mass and stiffness matrices

$$M_{\mathrm{C}} = \begin{bmatrix} M_{\mathrm{cc}} & M_{\mathrm{cq}} \\ M_{\mathrm{qc}} & M_{\mathrm{qq}} \end{bmatrix} \quad K_{\mathrm{C}} = \begin{bmatrix} K_{\mathrm{cc}} & 0 \\ 0 & \lambda \end{bmatrix} \tag{18}$$

with corresponding eigenvalues λ_{C} and mass normalized eigenvectors $\phi_{\mathrm{C}} = \begin{bmatrix} \phi_{\mathrm{cc}}^T & \phi_{\mathrm{cq}}^T \end{bmatrix}^{\mathrm{T}}$. These eigenvalues and eigenvectors are consistent with the boundary conditions of the test configuration modes used in the component test-analysis correlation. Error or uncertainty in the analytical test configuration eigenvalues can be much more easily mapped onto uncertainty $\Delta\lambda_{\mathrm{C}}$ in the eigenvalues of the system in Eq. (18). The HCB representation of the component using λ_{C} and ϕ_{C} as FI modal properties has the stiffness matrix and corresponding displacement vector given by

$$K_{\mathrm{B}} = \begin{bmatrix} K_{\mathrm{Sb}} & 0 \\ 0 & \lambda_{\mathrm{C}} \end{bmatrix} \quad u_{\mathrm{B}} = \left\{ x_{\mathrm{b}}^T \; q_{\mathrm{C}}^T \right\}^T \tag{19}$$

where $K_{\mathrm{S}b}$ is K_{S} statically reduced to the b-set, x_b is the physical displacement of the b-set, and q_{C} are the modal coordinates of the FI modes with the c-set free. The transformation between the displacement vector u_{B} and the original HCB displacement vector u_{HCB} is given by

$$u_{\mathrm{HCB}} = \begin{Bmatrix} x_{\mathrm{c}} \\ x_{\mathrm{b}} \\ q \end{Bmatrix} = \begin{bmatrix} \psi & \phi_{\mathrm{cc}} \\ I & 0 \\ 0 & \phi_{\mathrm{cq}} \end{bmatrix} \begin{Bmatrix} x_{\mathrm{b}} \\ q_{\mathrm{C}} \end{Bmatrix} = T u_{\mathrm{B}} \tag{20}$$

The relation between K_{B} and K_{HCB} is then

$$K_{\mathrm{B}} = T^T K_{\mathrm{HCB}} T \tag{21}$$

The test configuration HCB FI eigenvalues λ_{C} can be randomized (λ_{Cr}) based upon the component test-analysis correlation results, and the uncertainty can be propagated into the random flight configuration HCB component stiffness (K_{HCBr}) using the expression

$$K_{\mathrm{HCBr}} = T^{-T} K_{\mathrm{Br}} T^{-1} = T^{-T} \begin{bmatrix} K_{\mathrm{Sb}} & 0 \\ 0 & \lambda_{\mathrm{Cr}} \end{bmatrix} T^{-1} \tag{22}$$

3 Hurty/Craig-Bampton Uncertainty Models

The IMT/MSO components used in this UQ analysis were based on the integrated FEM. The FEM was divided into six components and reduced to HCB representations for an efficient MC UQ analysis. The frequency range of interest for the IMT is approximately 0.0–7.0 Hz; therefore, component FI modes were calculated to 15.0 Hz and augmented with residual vectors (RV) corresponding to the component interfaces and the IMT shaker locations. A few of the component uncertainty models are described in detail, while the remaining are summarized.

3.1 Mass Simulator for Orion

Due to possible scheduling conflicts and the fact that the MPCV would add a multitude of complexities to the IMT, the MPCV was replaced by a mass simulator. The IMT MSO and MSA, shown in Fig. 2, were combined into a single FEM and reduced to an HCB component representation. The HCB component contains 152 DOFs, including 144 physical DOFs at the interface between the MSA and the ICPS and eight FI modal DOFs. Only two of the FI modes have frequencies below 15.0 Hz. The component test/analysis correlation results for the updated MSO are listed in Table 1.

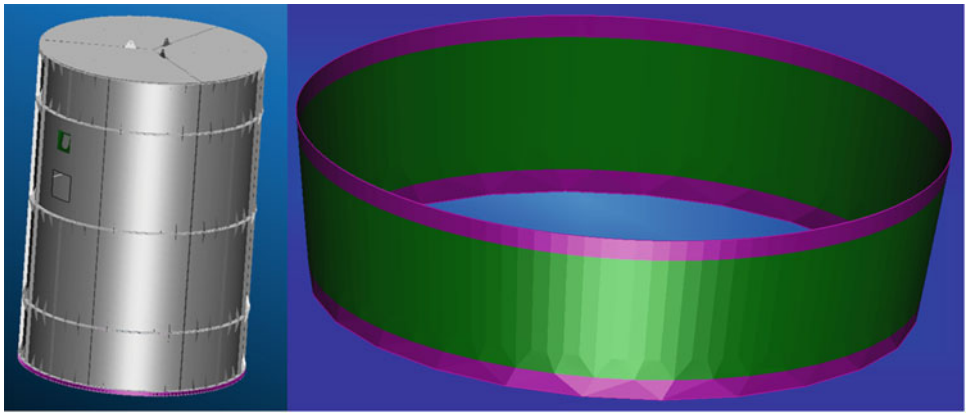

Fig. 2 CAD representations of MSO and MSA

Table 1 Test/analysis correlation results for updated MSO

Mode	% Error		XO
	Freq	Eigen	
1	2.42	4.90	99
2	−3.91	−7.97	99
3	3.57	7.27	97
4	4.83	9.89	93
5	3.03	6.15	89
6	5.14	10.55	89
7	3.83	7.81	95
8	1.59	3.20	96
9	5.25	10.78	96
10	3.86	7.88	80
11	4.62	9.44	72
12	6.26	12.92	80
13	5.24	10.76	92
14	3.97	8.09	75

Note that the percentage modal frequency errors are computed relative to the FEM frequencies for UQ analysis. There were not enough sensors in the modal test to describe modes 10–14; therefore, they were excluded in the formulation of the MSO/MSA uncertainty model. Based on the results in Table 1, the first MSO/MSA HCB FI mode (1st bending along Y) was assigned an RMS uncertainty of 7.97%, and the second MSO/MSA HCB FI mode (1st bending along Z) was assigned an RMS uncertainty of 4.90%. The remaining six FI modes, corresponding to RVs, were assigned an eigenvalue uncertainty of 7.81%, which corresponds to the median eigenvalue uncertainty in MSO FEM test configuration modes 3–9 listed in Table 1. During the process of combining the MSO and MSA FEMs, it was found that the MSO/MSA fixed-base modal frequencies could vary by as much as 10%, depending on just how the interface between the MSO and MSA was modeled. This additional uncertainty was addressed by adding an extra 10% frequency uncertainty, corresponding to approximately 21% eigenvalue uncertainty, to the uncertainties already assigned to the MSO/MSA FI eigenvalues based on the test results. This results in an eigenvalue uncertainty of 28.97% for FI mode one, 25.90% for FI mode two, and 28.81% for the other six FI modes.

Once the eigenvalue uncertainty is applied to the HCB stiffness matrix, the dispersion of the stiffness matrix is then applied using the NPV method. The dispersion level is determined based on the diagonal cross-generalized mass (DCGM) metric, which is the RMS value of the diagonal of the test/analysis XO matrix. Based on the XO results listed in Table 1, the value of DCGM for the MSO test over the first nine modes is given by $\text{DCGM}_{\text{Test}} = 94.84$. An MC analysis was then performed in which the HCB stiffness matrix dispersion was selected and then 3000 random MSO/MSA components were generated. The XO between the nominal and random HCB modes and the corresponding DCGM value were computed for each of the ensemble members for the first nine nominal modes, analogous to the test. The root-sum-square (RSS) cross-orthogonality [15] was computed as the cross-orthogonality for a linear combination of random modes within 3% of the frequency of the unique-best-fit mode. The most probable value of DCGM was then computed over the ensemble and compared with the test value. The stiffness matrix dispersion was adjusted such that the most probable DCGM value for the corresponding ensemble

matched the test value. For the MSO/MSA, a stiffness dispersion of $\delta_K = 21\%$ produced a most probable DCGM value of 94.54, which is comparable to the test value. The average RMS frequency uncertainty over the nine HCB modes is 6.72%.

3.2 *Interim Cryogenic Propulsion Stage*

The IMT ICPS and LVSA, shown in Fig. 3, were combined, and the corresponding FEM was reduced to a single HCB component. The HCB representation contains 306 DOFs, including 288 physical DOFs, 144 at the interface between the MSA and the ICPS, and 144 at the interface between the LVSA and the CS. There are 18 HCB FI modes. The IMT ICPS is empty, so there are no slosh modes. Dispersion values for the updated ICPS/LVSA HCB component were based on the Integrated Spacecraft Payload Element (ISPE) modal test-analysis correlation results. There were 11 FEM target modes matched to 11 of the 19 test modes. Only these target modes were considered in this analysis because the other eight modes were dominated by the MSA/MPCV simulator, which is not part of the ICPS/LVSA component. The test-analysis frequency correlation results are listed in Table 2.

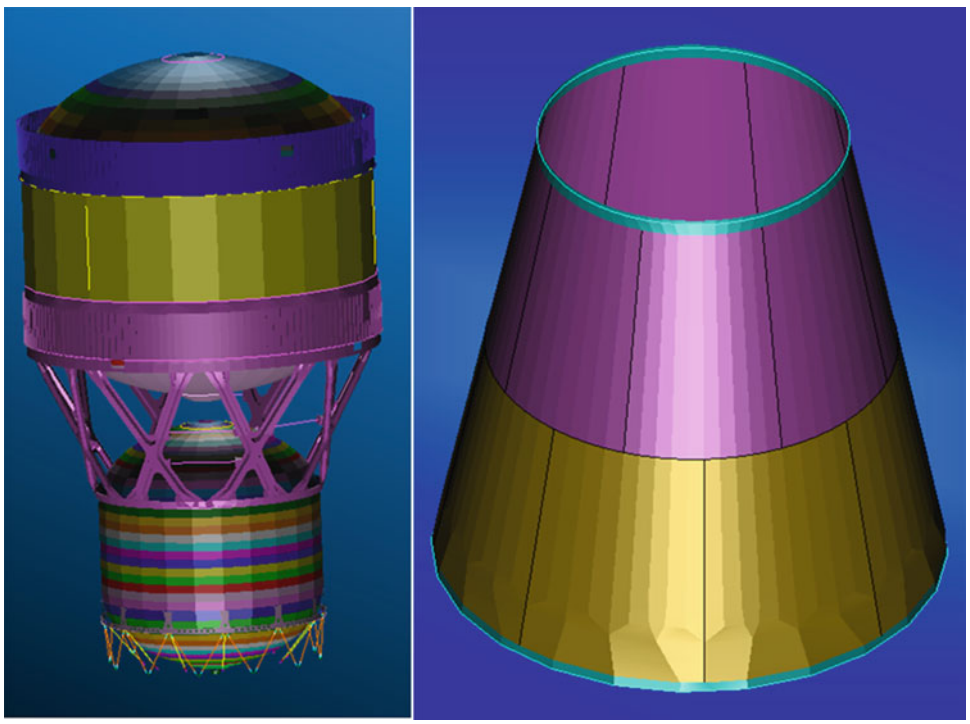

Fig. 3 CAD representations of ICPS and LVSA

Table 2 Test-analysis frequency comparison for configuration 3 updated model

FEM mode	Test mode	% error	XO
5	2	−2.70	94
6	1	−0.89	95
7	3	1.43	95
8	4	1.23	95
9	5	3.96	97
10	6	3.50	96
13	10	−0.57	97
14	9	−0.23	97
19	15	−0.33	95
20	14	−0.01	94
24	19	−4.72	94

Table 3 ISPE updated FEM MEM magnitude by bin

ISPE FEM mode	MEM (%)	Bin	% Freq. dispersion		% Eigen. dispersion
6	22.30	1	2.02		4.08
5	22.26	1	2.02		4.08
24	2.19	2	4.72		9.66
20	0.02	3	1.95		3.93
19	0.02	3	1.95		3.93
8	0.01	3	1.95		3.93
7	0.00	3	1.95		3.93
9	0.00	3	1.95		3.93
10	0.00	3	1.95		3.93
14	0.00	3	1.95		3.93
13	0.00	3	1.95		3.93

The ISPE was tested in a fixed-base configuration, while the ICPS/LVSA HCB FI modes are constrained at both the base, which is at the interface between the LVSA and the CS and at the interface between the ICPS and the MSA. This mismatch in boundary conditions makes it difficult to directly match ISPE test configuration modes with the HCB FI modes to assign modal frequency uncertainty. Therefore, the mixed-boundary approach was used on the ICPS/LVSA HCB component. The DOF at the interface between the ICPS and the MSA were released during the component mode calculation, resulting in 162 fixed-base component modes that were compared with the fixed-base modes from the test configuration. However, there are still significant differences between the ICPS/LVSA flight article and the ISPE used in the test. For example, there was no fuel in the test article and the test article included the MSA, a CS simulator, and an MPCV simulator. This makes it difficult to use frequency to match ICPS/LVSA fixed-base modes with ISPE test configuration modes. In many cases, test mode descriptions can be used to match modes, but this works best when the modes are low order and the descriptions are relatively simple. In the case of the ISPE, only three of the 11 target modes were easily described and probably insensitive to the hardware differences. Therefore, test-analysis frequency or eigenvalue error was mapped to the ICPS/LVSA fixed-base modes using modal effective mass (MEM). The updated FEM ISPE configuration 3 MEM is dominated by the fundamental bending and, to a lesser extent, the second-order bending modes. The LVSA shell modes have little or no MEM. Table 3 lists the updated ISPE configuration 3 FEM modes matched to test modes sorted by uncertainty bin based on the MEM Euclidean norm, normalized to a maximum length of $\sqrt{6}$ and multiplied by 100.

Bin 1 was assigned a frequency dispersion of 2.02%, corresponding to the RMS error in the prediction of the first bending test mode pair. Bin 2 was assigned a frequency dispersion of 4.72%, corresponding to the test-analysis frequency error of the second-order bending test mode. The remaining LVSA shell test modes have little or no MEM. These modes define uncertainty Bin 3 with a frequency dispersion of 1.95%, corresponding to the RMS frequency error in the LVSA shell modes. MEM was also computed for the ICPS/LVSA fixed-base modes. The first 22 modes to approximately 91 Hz account for approximately 99% of the effective mass over all six rigid body directions. Table 4 lists the first 25 ICPS/LVSA HCB fixed-base modes matched to the test configuration modes sorted by uncertainty bins based on the normalized MEM Euclidean norm. During the UQ analysis, the fixed-base mode uncertainty is then mapped into the HCB FI mode uncertainty.

Based on the XO results listed in Table 2, the value of DCGM for the ISPE configuration 3 test over the 11 FEM/test mode pairs is given by $\mathrm{DCGM}_{\mathrm{Test}} = 95.44$. An MC analysis was performed in which the stiffness matrix dispersion was selected and then 3000 random ICPS/LVSA components were generated. The 3% RSS XO between the nominal and random HCB modes and the corresponding DCGM value were computed for each of the ensemble members for the first 19 nominal modes below 15 Hz. A stiffness dispersion of $\delta_{\mathrm{K}} = 15\%$ produced a most probable DCGM value of 95.74, which is comparable to the test value. The average RMS frequency uncertainty over the 19 HCB modes is 2.78%.

3.3 Core Stage

The IMT CS FEM, shown in Fig. 4, was reduced to an HCB component with 224 DOFs, including 168 physical DOFs, 144 at the interface between the LVSA and the CS, and another 24 DOFs at the interfaces between the CS and the SRBs. There are 56 HCB FI modes. The IMT CS is empty, so there are no slosh modes, but CS pressurization stiffness is included. The IMT CS test-analysis correlation results are shown in Table 5. Eight test configuration IMT CS modes were matched with eight test modes. The CS was tested in a simulated free-free configuration; therefore, as in the case of the ICPS/LVSA, there is a

Table 4 IMT ICPS/LVSA HCB fixed-base sorted MEM magnitude and frequency uncertainty by bin

Bin	Number	FB mode	MEM	% Freq. dispersion	% Eigen dispersion
1	1	14	31.91	2.02	4.08
	2	22	27.29	2.02	4.08
	3	18	25.60	2.02	4.08
	4	13	24.52	2.02	4.08
	5	21	14.54	2.02	4.08
	6	15	12.51	2.02	4.08
	7	9	11.34	2.02	4.08
	8	6	10.18	2.02	4.08
2	9	19	6.68	4.72	9.66
	10	20	5.00	4.72	9.66
	11	5	3.98	4.72	9.66
	12	16	3.79	4.72	9.66
	13	10	3.69	4.72	9.66
	14	4	3.66	4.72	9.66
	15	3	1.21	4.72	9.66
	16	2	1.21	4.72	9.66
	17	7	1.13	4.72	9.66
	18	17	0.97	4.72	9.66
3	19	23	0.61	1.95	3.93
	20	25	0.51	1.95	3.93
	21	8	0.29	1.95	3.93
	22	1	0.17	1.95	3.93
	23	11	0.16	1.95	3.93
	24	24	0.05	1.95	3.93
	25	12	0.03	1.95	3.93

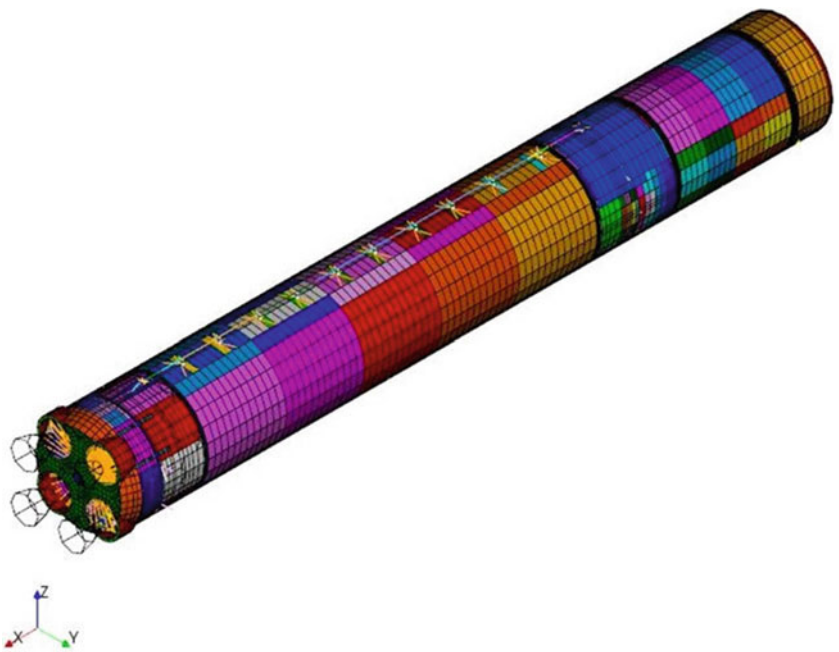

Fig. 4 CS finite element model

Table 5 IMT CS modal test-analysis correlation results

Test mode	% error		XOR
	Freq	Eigen	
1	−2.90	5.88	99
2	−6.90	14.27	98
3	10.71	22.58	43
4	3.27	6.66	79
5	4.23	8.65	87
6	0	0	89
7	−0.44	0.89	95
8	−0.29	0.59	89

Table 6 IMT CS HCB free-free mode eigenvalue dispersions

	% dispersion	
Mode	Freq	Eigen
23	2.90	5.88
24	6.90	14.27
25	2.90	5.88
26	10.72	22.58
28	10.72	22.58
31	10.72	22.58
32	10.72	22.58
36	3.28	6.66
45	10.72	22.58
46	10.72	22.58
47	10.72	22.58
48	10.72	22.58
57	0.44	0.89
67	0.29	0.59
72	4.24	8.65
73	4.24	8.65
78	4.24	8.65
79	4.24	8.65

mismatch between the test configuration boundary conditions and the boundary conditions applied to the CS HCB FI modes. Therefore, the mixed-boundary approach was also applied to the IMT CS. In order to match the test configuration boundary conditions, all 168 HCB interface DOFs were released, resulting in 224 free-free CS HCB modes that were compared with the CS test configuration modes. The eigenvalue dispersions of the HCB component modes were based on the test-analysis correlation results listed in Table 5. However, matching modes between the two sets to determine uncertainty could not be performed using MEM, as in the case of the ICPS/LVSA, because the modes are unconstrained, so they possess no MEM. Instead, the free-free CS HCB component modes were matched to the eight test configuration modes purely by the mode description listed in Table 5. The corresponding test-analysis eigenvalue error was then assigned to the HCB free-free component mode as the RMS eigenvalue uncertainty. The resulting eigenvalue uncertainties for the IMT CS HCB free-free component modes are listed in Table 6. Note that there are 18 HCB modes matched to the eight test configuration modes because there are eight HCB engine pendulum modes and the HCB bending modes are not purely bending and instead are more complex bending mode pairs. In addition, to be conservative, all HCB modes that were matched to the second bending about Z test configuration mode were given an eigenvalue uncertainty that is equal to the 8.65% uncertainty corresponding to the second bending about Y test configuration mode instead of the 0% uncertainty listed in Table 5. The remaining 188 elastic HCB free-free modes were assigned an eigenvalue dispersion of 6.27%, which corresponds to the median eigenvalue uncertainty in the eight test configuration modes listed in Table 4. The median was used instead of the mean such that no one mode would have too much influence.

Based on the XO results listed in Table 4, the value of DCGM for the CS test over the seven FEM/test mode pairs, excluding the engine pendulum mode pair, is given by $\mathrm{DCGM}_{\mathrm{Test}} = 91.09$. The XO value for the engine pendulum mode was excluded because it was uncommonly low and not reflective of the overall quality of the test. An MC analysis using 3000 ensemble members and 3% RSS XO was performed to determine the HCB stiffness matrix dispersion. The DCGM metric for each ensemble member was calculated over the first 48 elastic modes. For the CS HCB, a stiffness dispersion of

Table 7 Test-analysis correlation results for IMT ML on VAB support posts

Test	FEM	% error		
mode	mode	Freq	Eigen	XO
1	1	0.30	0.60	98
2	2	1.97	3.97	100
3	3	−23.36	−52.19	95
4	4	3.30	6.72	98
5	5	0.49	0.99	92
6	6	−2.57	−5.21	94
7	7	−3.17	−6.43	95
8	8	−0.43	−0.87	95
9	9	1.24	2.50	86
10	10	3.59	7.32	98
11	11	−2.56	−5.20	93
12	12	−0.81	−1.64	82
13	13	−1.36	−2.74	88
14	14	3.39	6.89	70
16	21	−0.77	−1.55	57

$\delta_K = 8.5\%$ produced a most probable DCGM value of 91.03, which approximates the test value. The average RMS frequency uncertainty over the 48 HCB modes is 4.70%.

Uncertainty models were also generated for the SRBs and the ML using the approaches outlined in the previous subsections. There was no specific modal test performed for the SLS SRBs; however, due to the SRB's heritage, the uncertainty models for the IMT SRB HCB components were assumed to be at the updated level. It was also assumed that the SRBs have approximately the same level of test-analysis correlation, or uncertainty, as found in the updated ISPE, listed in Table 3. This means that the three HCB FI eigenvalue uncertainty bins are given by 4.08%, 9.66%, and 3.93%, and the HCB stiffness dispersion of 2.5% was adjusted to produce a most probable DCGM value of 95.44 corresponding to the updated ISPE DCGM test value. The RSRB HCB component was assigned the same uncertainty model as the LSRB.

The IMT ML FEM was constrained at the six VAB support posts and reduced to an HCB representation with 401 DOFs, including 24 DOFs that interface with other components, 366 FI modes to 15.0 Hz, and 11 RVs. A modal survey of the ML only on the VAB support posts was performed at Kennedy Space Center on June 16–26, 2019. Test-analysis correlation results for the IMT ML are shown in Table 7 for 15 target modes, 14 primary and one secondary. Note that target mode 3 is a Crew Access Arm (CAA) mode that was in a different orientation during the modal test than what was modeled in the ML, therefore producing the large frequency error listed. For that reason, ML mode 3 was eliminated from the target mode set during the derivation of the IMT ML uncertainty model.

There is a mismatch between the ML test configuration boundary conditions and those applied to the ML HCB FI modes. Therefore, the mixed-boundary approach was also applied to the ML HCB to assign eigenvalue dispersions. The 24 HCB interface DOFs were released during HCB mode computation, resulting in 401 fixed-base modes. The HCB fixed-base modes were directly matched to the test configuration target modes listed in Table 7 using MEM and mode descriptions. The corresponding test configuration eigenvalue errors were assigned as dispersions to the corresponding HCB fixed-base modes. The remaining HCB fixed-base modes were assigned an eigenvalue dispersion of 3.35%, corresponding to the median eigenvalue error for the 14 target modes remaining after mode 3 was removed. Based on the XO values in Table 7, the test value of the DCGM metric over the 14 target modes is 89.77. During the MC stiffness dispersion analysis, the DCGM metric was computed for each ensemble member for the first 44 elastic modes with frequencies less than 8.0 Hz. An HCB stiffness dispersion of 4% produced a most probable DCGM value of 90.58, which was comparable to the test value. The corresponding mean RMS frequency uncertainty was 2.25% over the 44 modes.

4 IMT UQ Analysis

A UQ analysis was performed for the IMT configuration using MC analysis with an ensemble of 10,105 random models. The goal of the analysis was to determine the amount of primary target mode frequency and shape uncertainty that could be expected during the actual IMT, as well as the corresponding probability that the selected shaker and sensor configurations will adequately excite and separate the primary target modes. This work was completed prior to the IMT; however, during a

Table 8 IMT primary target modes

No.	Mode	Description
1	1	SLS rocking XZ plane
2	2	ML tower 1st bending XZ plane
3	3	SLS 1st XY bending
4	4	ML tower 1st bending XY plane
5	6	Core 1st torsion
6	7	SLS 1st XZ bending
7	8	SLS 2nd XZ bending
8	9	SLS 2nd XY bending
9	10	SRB 1st bending
10	11	SLS 3rd XY bending
11	12	ML tower torsion
12	13	ML tower 2nd XZ bending
13	14	ML tower/SLS 2nd XY bending
14	15	ML trampoline
15	16	CAA vertical/SLS bending
16	17	CAA vertical/SLS bending
17	18	CAA vertical
18	19	ML twisting/tower torsion
19	21	SLS 2nd torsion
20	22	ML tower bounce/3rd bending
21	23	ML tower 3rd XZ bending
22	27	SRB 2nd XY bending/CAA lateral

Table 9 IMT uncertainty model

Component	Uncertainty level	Assigned HCB FI frequency dispersion %	Stiffness dispersion %	Normalized stiffness dispersion %
MSO	Updated	Modes: 3.91, 2.42; RVs: 3.83	21	3.11
ICPS/LVSA	Updated	3 bins: 2.02, 4.72, 1.95	15	1.78
CS	Updated	Table 6	8.5	0.88
LSRB	Updated	3 bins: 2.02, 4.72, 1.95	2.5	0.75
RSRB	Updated	3 bins: 2.02, 4.72, 1.95	2.5	0.75
ML	Updated	Table 7	4	1.16

future posttest analysis, it is expected that the test results will be compared to the UQ predictions. If the uncertainty predicted by the UQ analysis covers the test results, there will be increased confidence in the HPV UQ method and the approach used to assign component uncertainty models.

The reduced IMT model contains 941 DOFs, and there are 70 modes below approximately 7 Hz. Twenty-two primary target modes were considered in this assessment. Table 8 lists the primary target modes with partial mode descriptions. The component uncertainty models described previously are summarized in Table 9.

Based on the UQ analysis, the RMS uncertainty for the 22 target modes is illustrated in Fig. 5. The greatest uncertainty, 3.23%, is in mode 19, which corresponds to the ML twisting/tower torsion mode. Figure 6 presents error bars for the target mode frequencies representing the range between the upper tolerance level at P99/90 and the lower tolerance level at P01/90. The corresponding interval provides an estimate of 98% enclosure with 90% confidence (P98/90). It can be seen that all of the modes possess a relatively small amount of frequency uncertainty. The nominal and median target mode frequencies are close in all 22 target modes. Figure 7 shows the corresponding primary target mode RMS XO. Twenty of the target modes possess an RMS XO value greater than 0.90, while two have values between 0.80 and 0.90. Note that no RSS analysis was performed to compute the XO values in this case.

The IMT sensor set contains 195 accelerometers. Figure 8 shows the XO between the nominal primary target modes and the nominal IMT modes below approximately 6 Hz, with unobservable modes 20, 24, and 32 removed. The XO was computed using the IMT test-analysis model (TAM) with the modes' mass normalized with respect to the TAM mass. The largest off-diagonal value of 0.058 indicates that the target modes are nicely decoupled from the other observable IMT modes using the IMT sensor configuration and TAM mass matrix.

During each iteration of the MC analysis, the random system modes were uniquely matched to the nominal system modes. The random modes were then recovered at the sensor DOF and mass normalized with respect to the nominal TAM

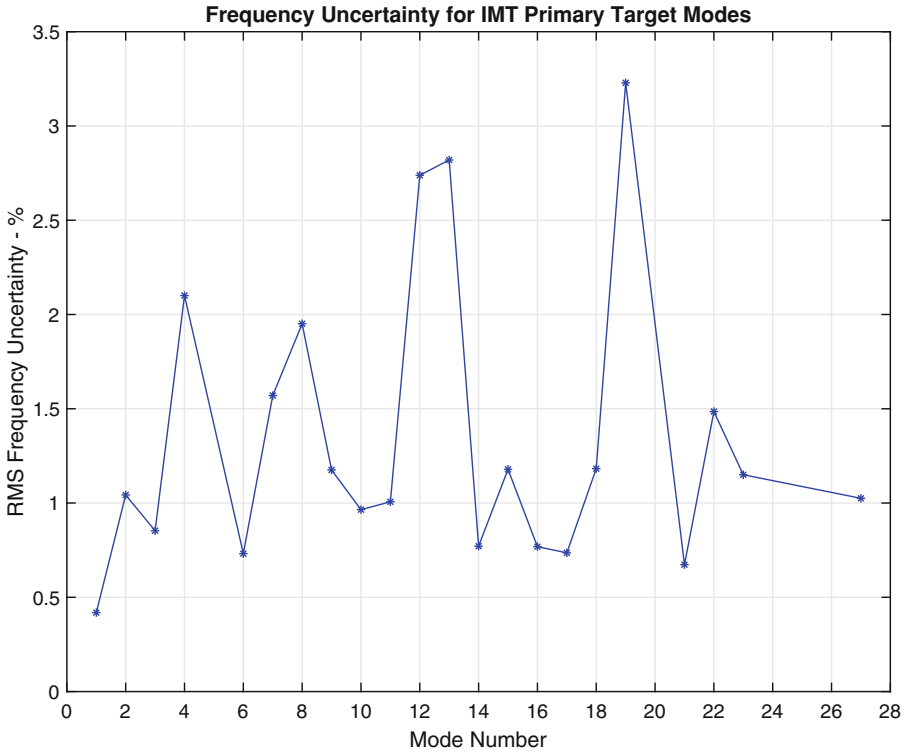

Fig. 5 RMS frequency uncertainty for IMT primary target modes

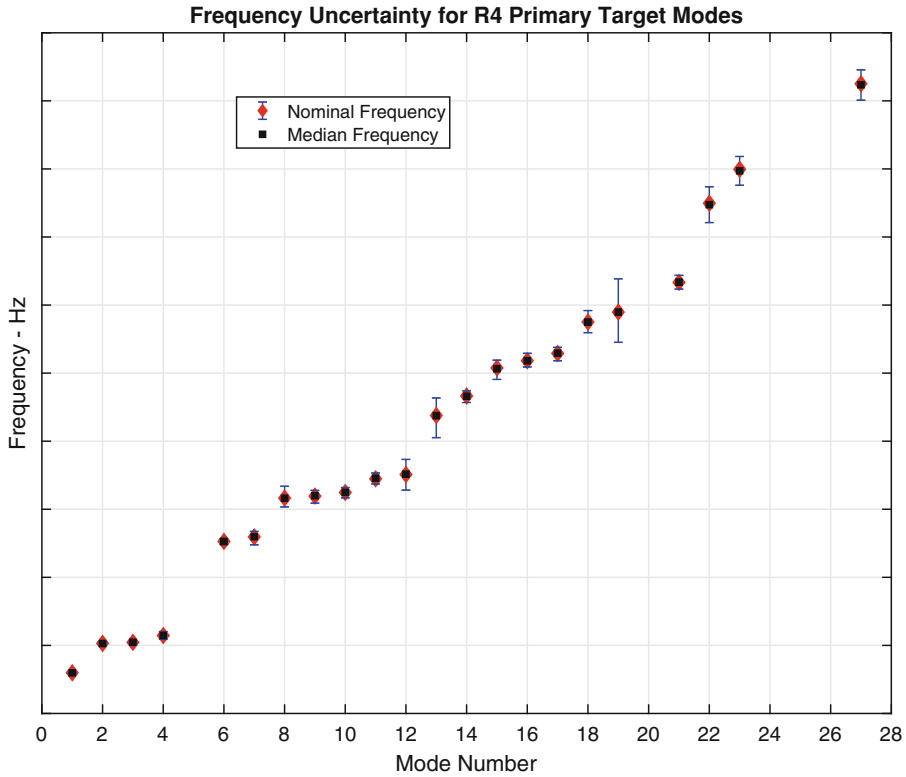

Fig. 6 P98/90 coverage intervals for IMT primary target mode frequencies

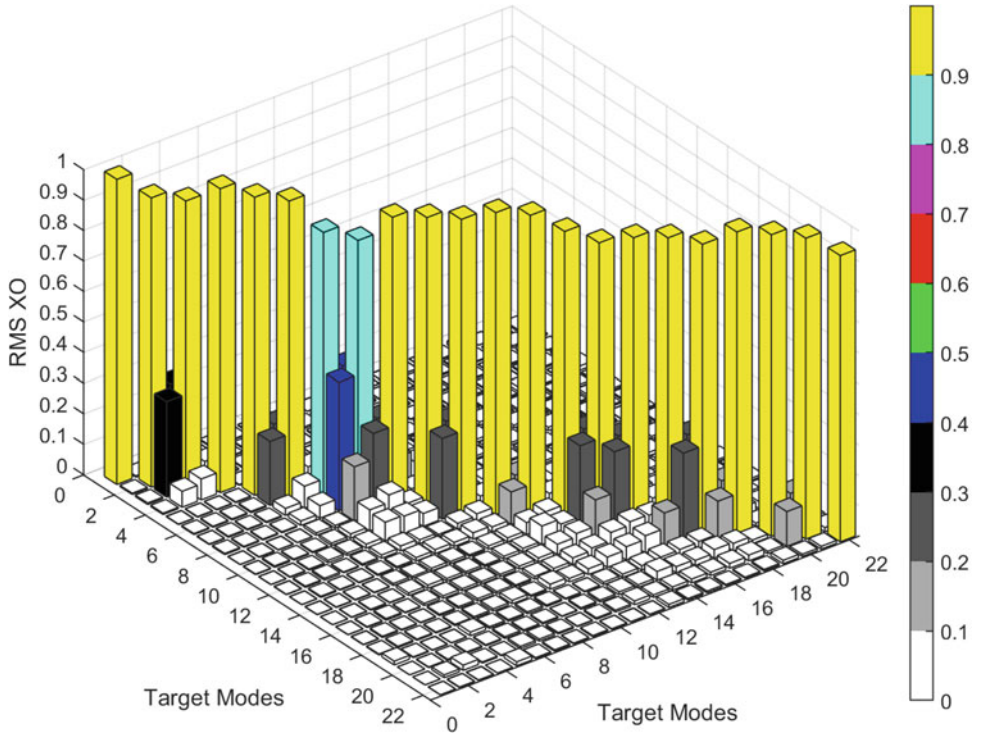

Fig. 7 IMT primary target mode RMS cross-orthogonality

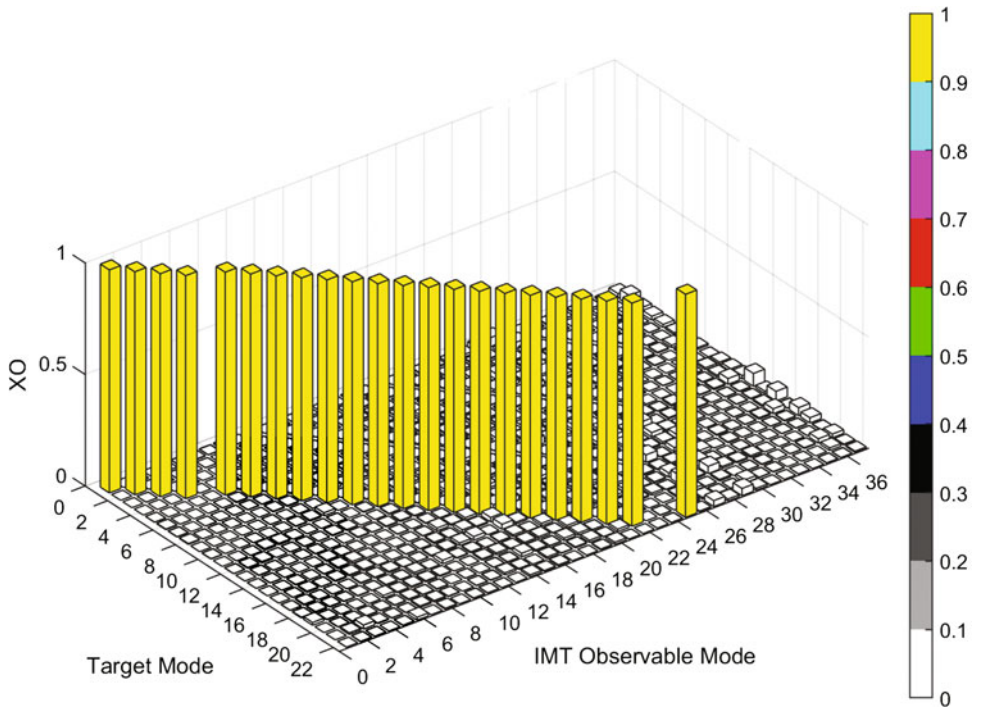

Fig. 8 XO between target modes and all observable IMT modes below 5.46 Hz

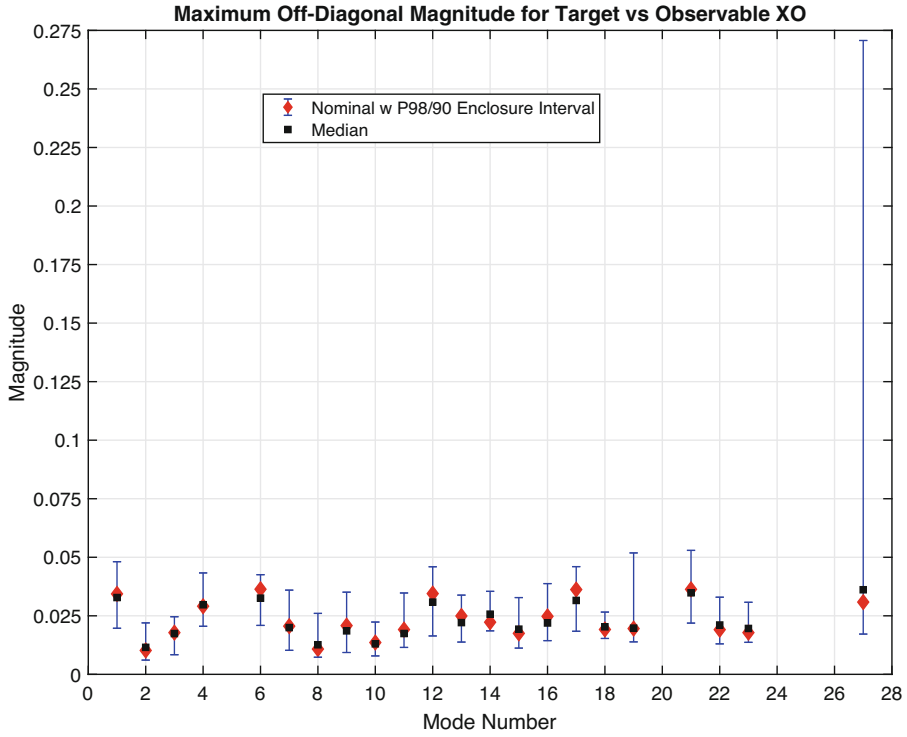

Fig. 9 Maximum off-diagonal statistics for XO between target and all observable IMT modes below 6 Hz

Table 10 IMT shaker configuration

	Shaker label	Dir.
1	S32	X
2	S35	X
3	S36	X
4	S38	Y
5	S40	Z
6	S50	X
7	S51	Y

mass matrix. The XO between the random target modes and the random observable modes using the TAM mass matrix was computed, and the largest off-diagonal magnitude for each target mode was saved. Figure 9 shows the nominal, median, and P98/90 enclosure intervals for the maximum off-diagonal values for each of the target modes. All nominal values are below 0.04. For the most part, the median values are close to the nominal values. The P99/90 maximum off-diagonal values are less than 0.06 for all the target modes, except target mode 27, which is the SRB second bending/CAA lateral bending mode. Figure 9 shows that the P99/90 value for mode 27 is much larger than both the nominal and median values, indicating that there is a large tail in the distribution of the maximum off-diagonal values. Even though the P99/90 maximum off-diagonal value is greater than 0.25, it can be shown that there is over a 92% probability that the maximum off-diagonal value is less than or equal to 0.10, which is often cited as the orthogonality criterion. These results indicate that during the actual IMT, there is a high probability and confidence that the first 21 target modes can be separated from the observable modes below approximately 6 Hz. In addition, there is a significant probability that target mode 27 can also be separated.

Statistics were also computed for acceleration frequency response and normal mode indicator functions for the selected shaker and sensor configurations. A modal damping level of 1.0% and modes up to 16.0 Hz were included in the simulations. The shaker configuration selected for this assessment is listed in Table 10. A typical acceleration frequency response in the Y direction on the ICPS/LVSA due to input at shaker S36 along X is shown in Fig. 10. The nominal as well as the P99/90 and P01/90 response levels are illustrated. During IMT posttest analysis, the corresponding test result can be compared with the predicted uncertainty interval shown in the figure. If the test result lies within the uncertainty interval, confidence in the validity of the HPV UQ method is enhanced.

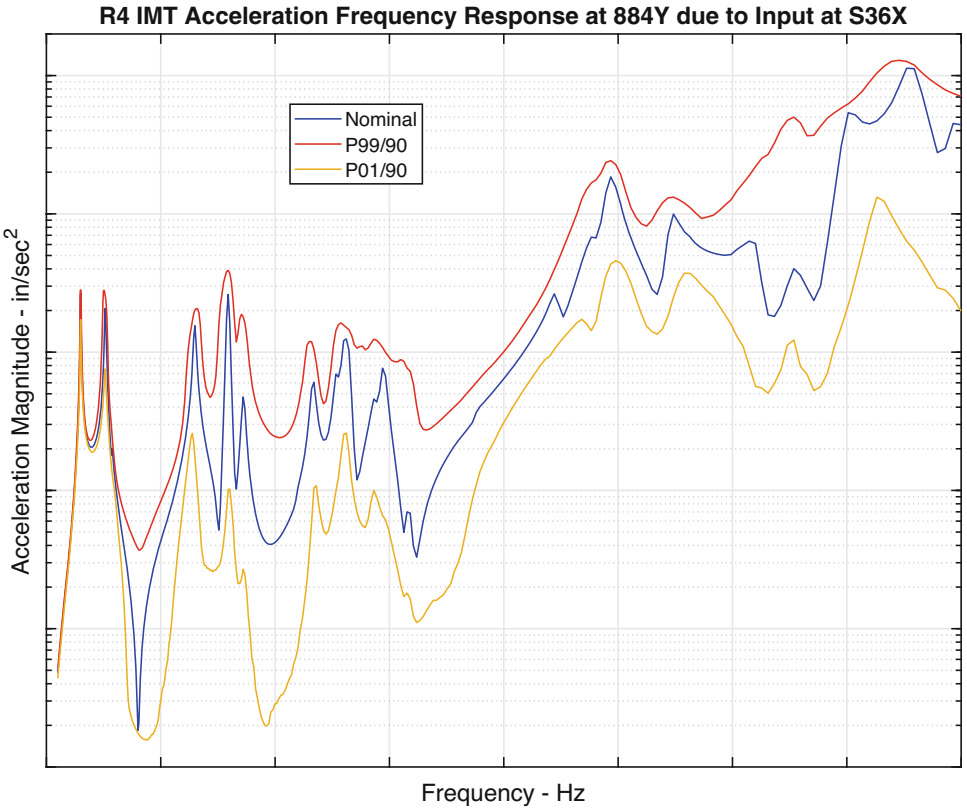

Fig. 10 Acceleration frequency response on ICPS along *Y* due to input from shaker S36X

The NMIF can be used to determine how effectively each of the primary target modes is excited and measured using the proposed shaker/sensor configuration. In practice, an NMIF value of 0.3 or smaller indicates that the mode is sufficiently excited and measured to be extracted from the test frequency response data. Therefore, for a mode to be sufficiently excited and measured, it must have an NMIF value less than or equal to 0.30 for any of the shakers. Figure 11 illustrates the minimum NMIF value over all of the shakers for each of the primary target modes for the nominal system. The values were determined by evaluating the NMIF functions at the nominal target mode frequencies. This approach is conservative because the minimum of the NMIF does not in general occur at the resonance, so this approach does not always capture the true minimum value. Using the criterion of NMIF being less than or equal to 0.30, 20 of the 22 primary IMT target modes are sufficiently excited and measured using the proposed IMT shaker/sensor configuration. Figure 11 also shows the minimum P99/90 and P01/90 NMIF values for each target mode over all seven shakers. The NMIF values corresponding to the random systems are determined by uniquely matching each of the nominal system target modes to a random mode and then evaluating the random NMIF function at the corresponding random resonant frequency. It can be seen from the figure that there is a significant amount of uncertainty in the NMIF values for all of the target modes except the first. The median values of the target mode NMIF values over the ensemble are also presented in Fig. 10. In many cases, the median NMIF values are close to the nominal values. Applying the 0.30 criterion to the median NMIF values, the figure indicates that there is a 50% probability of identifying all of the target modes during the IMT. Seven of the target modes have P99/90 NMIF values less than 0.30.

5 Conclusion

NASA has historically tested launch vehicles in an integrated configuration with boundary conditions controlled to approximate the boundary conditions expected in flight. However, to save cost and schedule, a cross-program decision was made to not perform an IVGVT and rely on analytical methods supported by component test results. However, there will still be an integrated system that will undergo testing, called the Integrated Modal Test. The IMT is a ground test of the

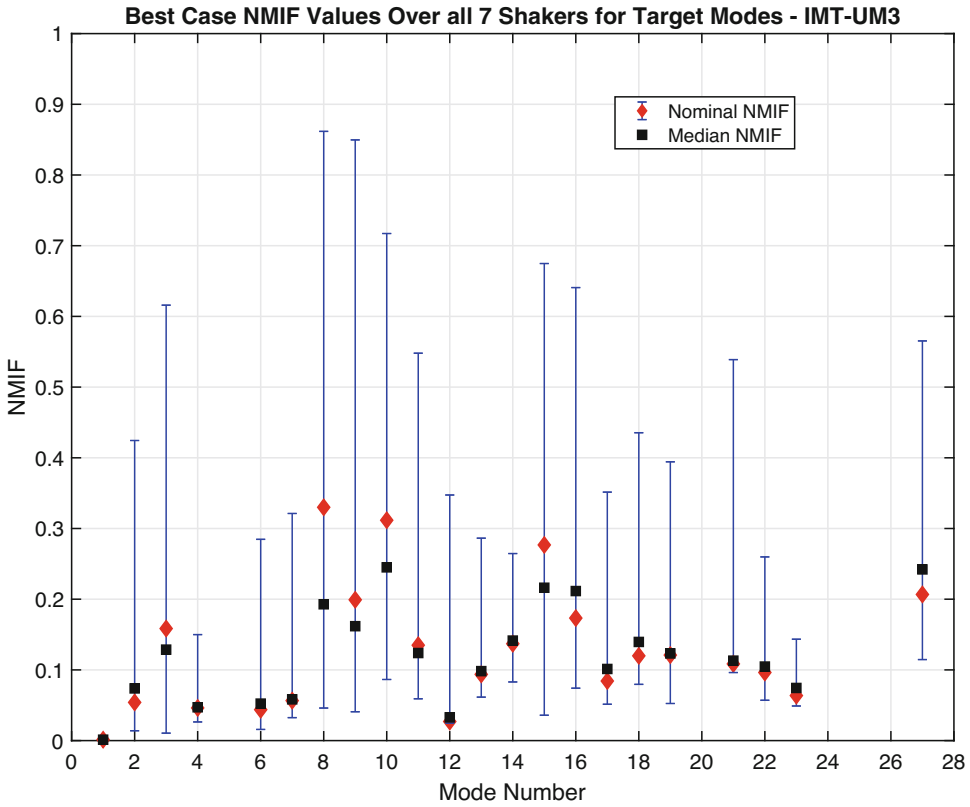

Fig. 11 IMT primary target mode NMIF statistics for seven shakers

integrated vehicle, assembled on the ML in the VAB facility at Kennedy Space Center. The results of the IMT will provide an opportunity to validate or update previously correlated SLS component models such that, in an assembled configuration, they provide agreement with integrated system test results. The purpose of this assessment was to apply the HPV UQ approach to the IMT/MSO ground vibration test configuration. Projection of component test-based uncertainty into the system provided estimates of the system-level uncertainty that can be expected in IMT target modal parameters, such as frequencies and mode shapes. Component uncertainty was also propagated into system-level acceleration frequency response and the corresponding mode indicator functions. The HPV method combines a parametric variation of the HCB FI modal frequencies with an NPV method that randomly varies the HCB stiffness matrices as Wishart random matrix distributions using RMT. Uncertainty models were developed for each of the HCB components using the test-analysis correlation results from component test configuration modal tests. Component uncertainty was propagated to the system level using an MC approach that generated statistics for system-level results. This provided a UQ method that can be traced directly to available test data and that can be updated as additional data, and better correlated models become available. In order to be more consistent with future IMT test and analysis, the most recent IMT configuration model was used in the UQ analysis. The finite element model was divided into six elements and reduced to the corresponding HCB components. Model correlation and updating of the ML is still in progress, meaning that the sensor set and shaker locations are still evolving. It has been found that the ability of the shaker configuration to adequately excite the target modes is very dependent on the most recent updated ML model version.

During the MC analysis, the off-diagonal elements in the XO between the random target modes and the random observable modes using the TAM mass matrix were computed and the largest off-diagonal magnitude for each target mode tracked. All nominal system maximum off-diagonal values were below 0.05, except target mode 14. The P99/90 maximum off-diagonal values were less than 0.10 for all the target modes, except target mode 27, which is the SRB second bending/CAA lateral bending mode. Even though the P99/90 maximum off-diagonal value for mode 27 was greater than 0.25, there was still more than a 92% probability that its value would be less than or equal to 0.10, which is often cited as the orthogonality criterion. These results indicate that during the actual IMT, there is a high probability and confidence that the first 21 target modes can be separated from the observable modes below approximately 6 Hz. In addition, there is a significant probability that target mode 27 can be separated. Using the criterion that the NMIF must be less than or equal to 0.30, 20 of the 22 primary IMT target modes are sufficiently excited and measured using the proposed IMT seven-shaker/sensor configuration. Applying

the 0.30 criterion to the median NMIF values, there is a 50% probability of identifying all of the target modes during the IMT. Seven of the target modes have P99/90 NMIF values less than 0.30. While the results of this UQ assessment provide meaningful insight into the effects of component uncertainty on system-level results, the assessment was not meant to be a comprehensive UQ analysis of the SLS IMT. For simplicity, noteworthy sources of uncertainty, such as component damping, were neglected in this assessment. In future work, it is believed that the HPV approach can also be applied to the dispersion of the component damping matrix. Finally, while the HPV method provides a valuable tool for complex system UQ analysis using only a limited amount of data, it is believed that confidence in predicted results could be improved through a rigorous validation program.

References

1. Craig, R.R., Bampton, M.C.C.: Coupling of substructures for dynamic analysis. AIAA J. **6**, 1313–1319 (1968)
2. Kammer, D., Blelloch, P., Sills, J.: Test-based uncertainty quantification and propagation using Hurty/Craig-Bampton substructure representations. In: IMAC, Orlando, 2019
3. Kammer, D., Blelloch, P., Sills, J.: Variational coupled loads analysis using the hybrid parametric variation method. In: IMAC, Houston, 2020
4. Wishart, J.: Generalized product moment distribution in samples. Biometrika. **20A**(1–2), 32–52 (1928)
5. Rades, M.: Performance of various mode Indicator functions. Shock. Vib. **17**, 473–482 (2010)
6. Ghanem, R., Spanos, P.: Stochastic Finite Elements: A Spectral Approach. Springer, New York (1991)
7. Soize, C.: A nonparametric model of random uncertainties for reduced matrix models in structural dynamics. Probab. Eng. Mech. **15**(3), 277–294 (2000)
8. Soize, C.: Maximum entropy approach for modeling random uncertainties in transient elastodynamics. J. Acoust. Soc. Am. **109**(5), 1979–1996 (2001)
9. Adhikari, S.: Generalized Wishart distribution for probabilistic structural dynamics. Comput. Mech. **45**, 495–511 (2010)
10. Adhikari, S.: Wishart random matrices in probabilistic structural mechanics. J. Eng. Mech. **134**(12), 1029–1044 (2008)
11. Capiez-Lernout, E., Pellissetti, M., Pradlwarter, H., Schueller, G.I., Soize, C.: Data and model uncertainties in complex aerospace engineering systems. J. Sound Vib. **295**(3–5), 923–938 (2006)
12. Pellissetti, M., Capiez-Lernout, E., Pradlwarte, H., Soize, C., Schueller, G.: Reliability analysis of a satellite structure with a parametric and a non-parametric probabilistic model. Comput. Methods Appl. Mech. Eng. **198**(2), 344–357 (2008)
13. Mignolet, M., Soize, C., Avalos, J.: Nonparametric stochastic modeling of structures with uncertain boundary conditions/coupling between substructures. AIAA J. **51**(6), 1296–1308 (2013)
14. Gramacy, R.: Surrogates, Gaussian Process Modeling, Design, and Optimization for the Applied Sciences. CRC Press, Boca Raton (2020)
15. Blelloch, P.: Cross-orthogonality of closely spaced modes. In: IMAC, 2006

A Forward Model Driven Structural Health Monitoring Paradigm: Damage Detection

Robert J. Barthorpe, Aidan J. Hughes, and Paul Gardner

Abstract Structural Health Monitoring (SHM) involves determining the health state of an engineered structure based upon measured, damage-sensitive features such as natural frequencies, modeshapes and time-domain model coefficients. One of the key challenges in SHM is the difficulty associated with gathering experimental data from a structure in its damaged state. This challenge is particularly acute for purely data-based supervised learning methods. Numerical modelling offers the potential to overcome the lack-of-data problem by making physically informed predictions of how the structure will behave once damaged. However, numerical modelling raises challenges of its own, with a major question being how one incorporates uncertainties and errors arising from the model prediction process within SHM decision-making. In addition, variability inevitably arises in the observed experimental responses and this, too, should be incorporated in the decision process. Finally, it is desirable that the cost of misclassification be incorporated within the decision process, with risk-based approaches being an attractive option for moving from classification to decision-making. This paper introduces a practical application of a Forward Model Driven (FMD) paradigm for SHM. A key tenet of the approach is that numerical model predictions may be used to inform a statistical classifier. The method is demonstrated for the case of damage detection on an experimental truss bridge structure for which an associated finite element (FE) model has been developed. A framework based upon a sequence of binary classifiers is introduced, with attention drawn to the importance both of the choice of individual classifier and the strategy for their combination.

Keywords Structural health monitoring · Finite element modelling · Damage identification

1 Introduction

Structural Health Monitoring (SHM) refers to the process of assessing the health state of a structure via changes in global dynamic response. The SHM process involves the continual or periodic gathering of data from a network of sensors attached to a structure, application of appropriate data normalisation and cleansing techniques, extraction of damage-sensitive features from the processed data, and statistical analysis of these features to make a statement of system health. The potential benefits of such systems if they can be developed range from the life-safety benefits that arise from being able to identify defects before they progress to system failure, through to the economic benefits that arise through increased maintenance efficiency and the potential to either extend the life of existing systems or to create new systems that are designed to be damage-tolerant. Various paradigms exist for tackling the SHM problem. The method that has received most attention in the literature is the data-driven approach, which makes use of measured data and statistical pattern recognition (SPR) to identify the damage state of the structure (see [1] for a comprehensive overview of approaches). This has been demonstrated to be extremely effective in detecting, locating and classifying damage in both laboratory-based and real-world structures in cases where damaged-state data is available. An alternative approach which has also received significant attention, referred to herein as the inverse model-based approach, makes use of physics-based models and inverse methods in order to infer the location and extent of damage in the structure [2]. These techniques are often found to suffer from non-identifiability issues due the nature of the inverse problem solved, with individual model parameters or subsets of parameters updated on the basis of observed data [3].

R. J. Barthorpe (✉) · A. J. Hughes · P. Gardner
Dynamics Research Group, Department of Mechanical Engineering, University of Sheffield, Sheffield, UK
e-mail: r.j.barthorpe@sheffield.ac.uk; AJHughes2@sheffield.ac.uk; p.gardner@sheffield.ac.uk

Z. Mao (ed.), *Model Validation and Uncertainty Quantification, Volume 3*, Conference Proceedings of the Society for Experimental Mechanics Series, https://doi.org/10.1007/978-3-030-77348-9_16

A third approach, referred to herein as the forward model driven approach, represents a hybrid of the above, with the physics-based model used in a predominantly forward mode in order to make predictions that are subsequently used to inform a statistical classifier [4, 5]. In this way, physics-based modelling offers the possibility of generating feature predictions for those damage scenarios of interest that it is not possible to observe experimentally. The potential advantages of such an approach include:

- Enabling the application of model validation and uncertainty quantification (UQ) concepts to build systems that are robust to identified sources of uncertainty.
- The possibility of performing SHM system evaluation at the design stage, enabling rigorous assessment of feature sensitivity and the identifiability of health states.
- The major computational expense—generating feature predictions for health states—being incurred at the design stage, with the ongoing costs of solving an inverse problem online either reduced or avoided completely.

A fuller review of recent trends in forward model driven SHM is presented in [6]. This approach naturally faces challenges of its own. Perhaps the greatest of these is in overcoming the perception that physics-based models are (1) expensive to produce and (2) nonetheless offer insufficient predictive accuracy for use in an SHM context. The latter point may be addressed to some extent by application of methods for model validation, although this gives rise to the linked question of how models of the structure in its damaged state may be validated given that such data is hard to come by. Possibilities here include the pursuit of validation at the component or sub-system level, where damaged-state testing may be feasible. The contention in this paper, however, is that by selecting a classification architecture that allows for a degree of error in the damaged-state model predictions, a classifier may be trained that offers satisfactory performance without reliance on the availability of damaged-state data. The paper thus introduces a practical application of a Forward Model Driven (FMD) paradigm for SHM, with the focus initially being restricted to the damage detection stage. The methodology employed is described in Sect. 2, with an experimental case study presented in Sect. 3. Outcomes and future work are briefly summarised in Sect. 4.

2 Methodology

The work presented in this study focuses initially on the damage detection case, with extension to the more challenging case of damage localisation to be pursued in follow up studies. The detection strategy pursued broadly follows that presented in [7], which set out a Bayesian risk minimisation framework for optimal sensor placement focusing on active sensing. This approach enables the costs associated with different actions to be included in the decision-making process. In this way, a design that minimises risk under uncertainty may be found, where 'design' is taken to incorporate sensor placement, feature selection and the setting of localised damage thresholds. The presented approach essentially casts damage identification as a set of binary hypothesis testing problems, weighted by the cost of making a correct/incorrect decision. The structure is considered to consist of $k = 1 \ldots K$ discrete regions. In the simple case of binary local damage states (i.e. the local region is either considered 'damaged' or 'undamaged') the local health state in region k is denoted h_{k0} in the undamaged case and h_{k1} in the damaged case. The approach proceeds by setting local thresholds on the features arising from each damage state using a principled Bayesian approach that incorporates the costs involved with both correct and incorrect health state decisions. In order to facilitate this approach, a number of simplifying assumptions are made: only single-site damage is considered; the features used for damage detection are assumed to be Gaussian distributed; a simple linear detector is employed; and features are drawn from a deterministic physics-based model, with no model uncertainty quantification considered.

The aim of the present study is to move towards a general forward model driven (FMD) SHM classification framework. This will be pursued through (1) investigation of generalised classification options based on SPR methods and (2) incorporation of both the uncertainty associated with the model predictions and the variability observed in the experimental data in the predictions of $p(\mathbf{x}_{trn}|h_{k0})$ and $p(\mathbf{x}_{trn}|h_{k1})$, where $\mathbf{x}_{trn}$ are the feature values associated with each health state that are used to train the SPR classifier. Initially this will be demonstrated for the case of damage detection, with the ultimate goal being extension to damage localisation and classification of damage type.

The strategy adopted for damage detection in this context is as follows:

1. A physics-based model is used to make system-level predictions across health states of interest, with appropriate uncertainty quantification applied to capture modelling and experimental uncertainties.
2. An acceptable local damage threshold is defined and applied within each discrete region. This could be a maximum permissible crack length, for example.

3. The model-predicted feature vectors are labelled as belonging to either the undamaged class h_{k0} or damaged class h_{k1} for each local region k.
4. For each region k, a classifier is developed using training data $\mathbf{x}_{trn}$ and used to predict the local health state of the structure when presented with new test data $\mathbf{x}_{tst}$. Classification options include:
   - Using a generative method. Here, the joint distribution of the training data and the class labels $p(\mathbf{x}_{trn}|h_{k0})$ and $p(\mathbf{x}_{trn}|h_{k1})$ is learnt. When test data $\mathbf{x}_{tst}$ are presented, the joint distribution is used to report probabilities of class membership $P(h_{k0}|\mathbf{x}_{tst})$ and $P(h_{k1}|\mathbf{x}_{tst})$.
   - Using a discriminative method. In this case, the class conditional distributions $P(h_{k0}|\mathbf{x}_{trn})$ and $P(h_{k1}|\mathbf{x}_{trn})$ are learnt directly using labelled training data $\mathbf{x}_{trn}$. When test data $\mathbf{x}_{tst}$ are presented, the predicted local class label h_{k0} or h_{k0} is reported.
5. An appropriate decision rule is applied to combine the outputs of the individual classifiers.

The latter option for classifier training is explored in the current paper. In this instance, Support Vector Machine (SVM) classification is adopted, with the predictions of multiple binary classifiers being combined. While the above is conceptually simple, challenges nonetheless arise and a number of decisions must be taken by the system designer. Setting of the local thresholds (alternatively *decision boundaries*) on acceptable damage is key among these. The compromise here is between maximising the true positive rate (equivalently minimising the false negative rate, promoting detectability) while minimising the false positive rate. The risk-based framework proposed in [7] offers a principled means of making such decisions on the basis of the costs associated with each outcome; note that while not explored in this study, the SPR classifiers adopted remain amenable to use within a risk-based framework.

3 Case Study

The approach introduced in Sect. 2 is demonstrated in this paper via an experimental case study on a truss bridge structure, shown in Fig. 1. The finite element (FE) model developed to make predictions of the dynamic response of the structure in the presence of damage is introduced in Sect. 3.1 with the experimental procedure adopted introduced in Sect. 3.2. The selection of comparable features is discussed in Sect. 3.3, alongside details of the classification architecture in Sect. 3.4. The results of applying a classifier trained purely on the FE results to data from the experimental structure are presented and discussed in Sect. 3.5.

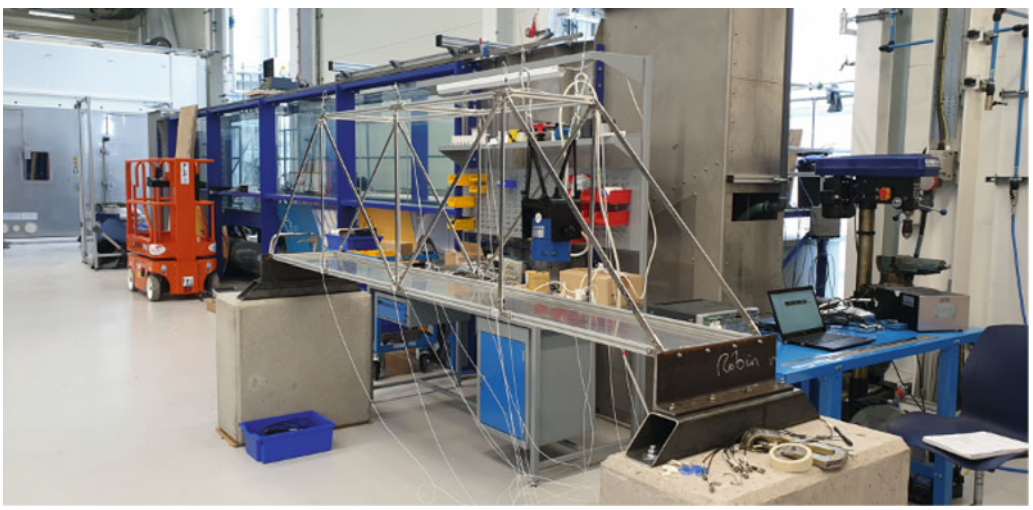

Fig. 1 The experimental truss bridge structure, here set up for testing using shaker excitation

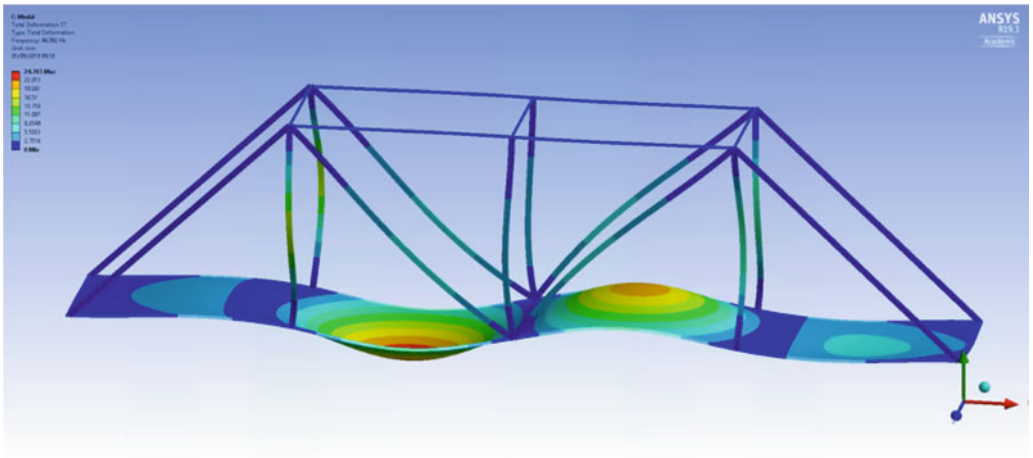

Fig. 2 Finite element model of the truss bridge structure

3.1 Model Description

A finite element model of the truss bridge structure was developed in ANSYS. The trusses were modelled using Timoshenko beam elements and the deck with shell elements. Damage was introduced via a geometric reduction in the beams at the same dimensions as the saw cut, simulating the type of damage in the physical structure. The model was used to extract modal properties that could be compared with the test data, with modal coordinates being extracted at nodes equivalent to the locations where sensors had been positioned on the structure. An illustrative example of the model output is shown in Fig. 2. In this instance, no calibration of the model to test data was performed—the model may be considered purely white box in nature.

3.2 Experimental Procedure

Damage was introduced, in turn, on the three vertical struts lying on the front elevation of the structure as shown in Fig. 3. The damage itself consisted of sawcuts implemented at the midpoint of the truss. These were increased in 2.5 mm increments from the undamaged state through to a maximum extent of 17.5 mm, with the trusses being 20 mm in depth. Between each introduction of damage, the structure was returned to its undamaged state by replacing the damaged truss. All tests were conducted in ambient conditions at a nominal temperature of 20 °C. Data acquisition was performed using a Siemens Mobile SCADAS system, with the test programme proceeding in two stages. First, an impact hammer test was conducted at a total 54 locations with the aim of establishing a comprehensive dataset for modal matching between the experimental data and model predictions. Secondly, the structure was set up for shaker excitation, with sensor locations informed by the modeshape observations from the impact hammer test. Accelerometers were placed as closely as possible to the 'nodes' on the deck of the structure, where the vertical and diagonal truss elements meet. The sensor layout was repeated on front and rear elevations, resulting in 12 sensors locations. Uniaxial PCB 353B16 accelerometers were used, all oriented in the vertical direction (denoted as the y-direction in Fig. 3). The shaker was also mounted in the vertical direction, suspended via bungee cords. The shaker attachment point lay at deck level on the rear elevation of the structure with a PCB force transducer used for force acquisition. Band limited white noise excitation in the range 0–1024 Hz was applied via the shaker. Modal analysis was performed using the PolyMax algorithm.

3.3 Feature Selection

Accurately matching the features predicted by the model to those observed experimentally represents an important step in the presented paradigm. In this paper, changes in the natural frequencies were adopted as the damage-sensitive features of interest. The selection of those features that it was deemed most important to match was principally guided by their sensitivity

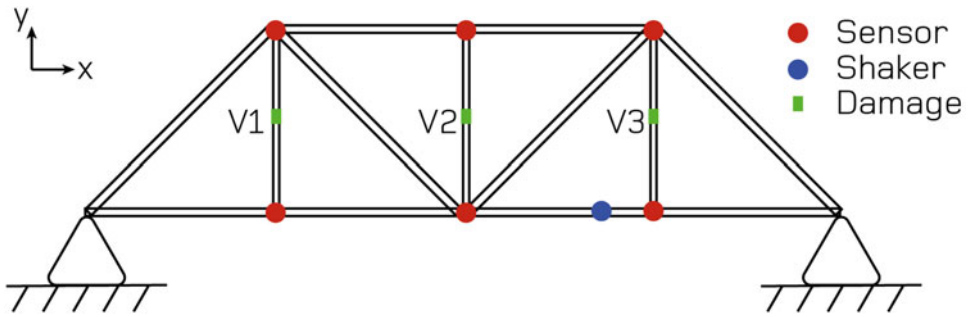

Fig. 3 Schematic diagram of the truss bridge structure, indicating damage scenarios and shaker and excitation locations

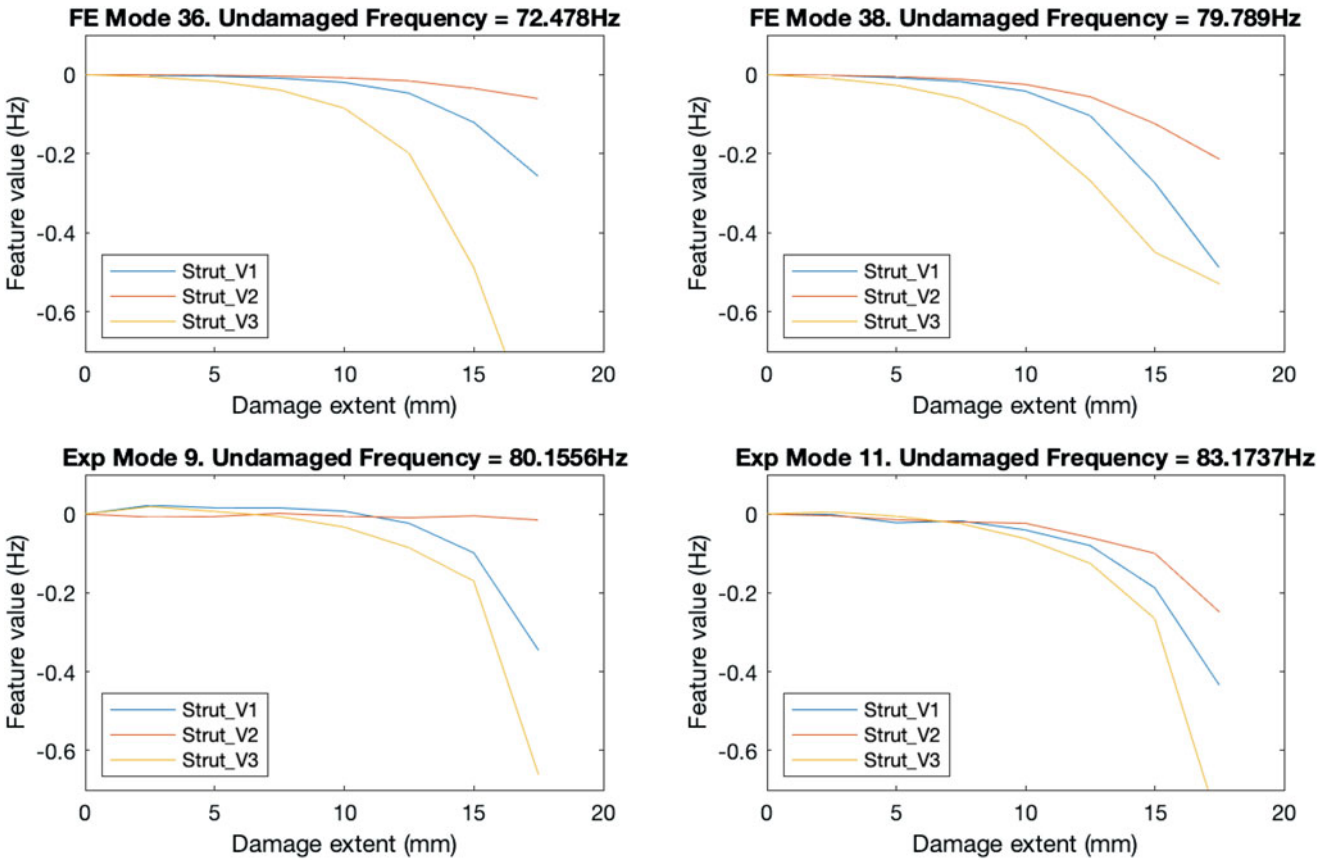

Fig. 4 Features adopted for damage detection

to damage as indicated by model. Mode matching was pursued using data from the impact hammer test, comprising responses at 54 locations. An initial set of 10 'well-matched' mode pairs was identified based on comparison of modeshapes and associated natural frequencies. Good agreement was observed in the modeshapes, and these proved central to successfully pairing the modes. As may be expected from an uncalibrated model of a comparatively complex structure, substantial deviation was observed in the natural frequency values. In this paper, just two of the available paired features are adopted for illustration, enabling simple visualisation of the feature space without recourse to dimensionality reduction techniques. The individual matched features are presented in Fig. 4, with the two-dimensional feature space visualised in Fig. 5. Note that in practical applications of the approach one would not have access to experimental damaged-state data at the feature selection stage; the results are included here to offer an initial visual indication of the agreement between model predictions and experimental observations.

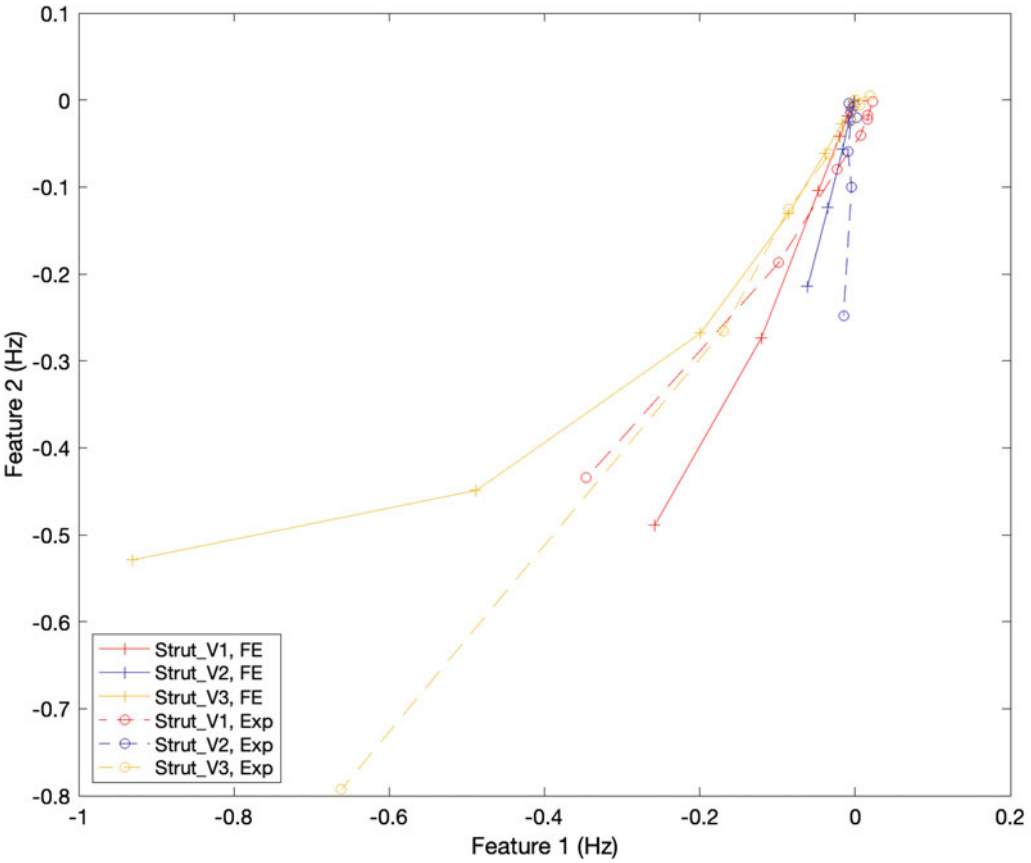

Fig. 5 Schematic diagram of the truss bridge structure

3.4 Classifier Training

A global damage classifier was developed using training data from the FE model only. In this case, the damage threshold was set such that local damage of greater than or equal to 12.5 mm would be labelled as damaged. Experimental variability was simulated via the addition of multivariate Gaussian distributed noise, with a variance of $\sigma = 0.01$ Hz on each feature. The overall classification architecture comprised K 'one-vs-one' classifiers, in this instance with $K = 3$ local regions to consider. Each binary classifier was trained to separate predicted feature vectors resulting from damage in one of the local regions from those of the undamaged state. Classification was pursued using a binary SVM for each region. A linear kernel was adopted for each SVM, with the classifier hyperparameters (the scale parameter and misclassification tolerance) set via k-folds cross-validation. In order to provide an overall label for the predicted damage state of the structure, a decision rule must be adopted in order to combine the classification labels returned by the K individual classifiers. In this case, the decision rule used was that the structure should be labelled as globally damaged $(+1)$ if the health state of any local region is labelled as damaged.

A useful outcome of the model driven approach is that the predicted performance of the SHM system may be evaluated at this stage. At its simplest, this may be conducted by assessing the overall classifier performance on the training set used to develop the individual binary classifiers (i.e. via *recall*). For the case study presented, this evaluation returned an overall probability of detection of $P_D = 99.33\%$ and probability of false alarm $P_{FA} = 17.73\%$. It may be noted from these metrics that while the probability of detection was exceptionally high, this came at the cost of a substantial number of false positives. By considering the confusion matrices for the individual binary classifiers, it was apparent that this false positive rate could be ascribed to the performance of Classifiers 1 and 3, relating to damage at struts V1 and V3, respectively. This information is useful as it enables tailoring of the system design through, for example, the adoption of further features to offer greater discrimination of damaged health states or tailoring of the classification thresholds. As highlighted in Sect. 2, one attractive possibility here is that risk-based approaches may be utilised to inform the choice of decision boundary.

Table 1 Classifier outcomes for strut V1

	Classifier			
Damage (mm)	1	2	3	Prediction
0.0	−1	−1	−1	−1
2.5	−1	−1	−1	−1
5.0	−1	−1	−1	−1
7.5	−1	−1	−1	−1
10.0	−1	−1	−1	−1
12.5	1	1	−1	1
15.0	1	1	−1	1
17.5	1	1	1	1

Table 2 Classifier outcomes for strut V2

	Classifier			
Damage (mm)	1	2	3	Prediction
0.0	−1	−1	−1	−1
2.5	−1	−1	−1	−1
5.0	−1	−1	−1	−1
7.5	−1	−1	−1	−1
10.0	−1	−1	−1	−1
12.5	−1	1	−1	1
15.0	1	1	−1	1
17.5	1	1	−1	1

Table 3 Classifier outcomes for strut V3

	Classifier			
Damage (mm)	1	2	3	Prediction
0.0	−1	−1	−1	−1
2.5	−1		−1	−1
5.0	−1	−1	−1	−1
7.5	−1	−1	−1	−1
10.0	−1	1	−1	1
12.5	1	1	−1	1
15.0	1	1	1	1
17.5	1	1	1	1

3.5 Classification Results

Having trained the damage detector purely on model-predicted data (with an assumed level of experimental variation), the classifier was applied to the features observed from experimental damage cases. The results observed for damage introduced into each strut are summarised in Tables 1, 2, and 3. The undamaged class is denoted −1 and the damaged class 1. As can be observed from the tables, completely accurate classification was seen for both struts V1 and V2. For strut V3, the classifier returned a false positive for the 10 mm damage case, arising from a misclassification by Classifier 2. Overall, this can be viewed as an extremely promising result given that only two features were used for classification and no model calibration was performed.

4 Conclusion

The aim of the current paper has been to present a forward model driven methodology for structural health monitoring. This represents a generalisation of earlier approaches to allow consideration of SPR classification techniques and incorporation of model uncertainty and measurement variability. An experimental case study based on a truss bridge structure has been presented with a classifier trained purely using FE model predictions being shown to perform extremely well on experimentally observed data. The case study represents a successful application of this paradigm to an experimental structure for the purposes of damage detection. The immediate focus of future work will be extension to the localisation

case. This comprises a much more nuanced classification task, with greater sensitivity to discrepancies in model predictions being expected.

Reference

1. Farrar, C.R., Worden, K.: Structural Health Monitoring: A Machine Learning Perspective. Wiley, New York (2012)
2. Friswell, M.I.: Damage identification using inverse methods. Philos. Trans. R. Soc. A Math. Phys. Eng. Sci. **365**(1851), 393–410 (2007)
3. Friswell, M.I., Mottershead, J.E., Ahmadian, H.: Combining subset selection and parameter constraints in model updating. J. Vib. Acoust. Trans. ASME **120**, 854–859 (1998)
4. Barthorpe, R.J.: On model- and data-based approaches to structural health monitoring. Ph.D. thesis, University of Sheffield (2011)
5. Gardner, P.: On novel approaches to model-based structural health monitoring. Ph.D. thesis, University of Sheffield (2019)
6. Gardner, P., Barthorpe, R.J.: On current trends in forward model-driven SHM. In: 12th International Workshop on Structural Health Monitoring (2019)
7. Flynn, E., Todd, M.: A Bayesian approach to optimal sensor placement for structural health monitoring with application to active sensing. Mech. Syst. Signal Process. **24**, 891–903 (2010)

Uncertainty Quantification of Inducer Eigenvalues Using Conditional Assessment of Models and Modal Test of Simpler Systems

Andrew M. Brown, Jennifer L. DeLessio, and Timothy J. Wray

Abstract The low-pressure fuel pump inducer of the new Space Launch System RS25 core stage engine operates in a highly complex environment that substantially affects its modal characteristics. Some of the more important effects are fluid-added mass (FAM) resulting from operation within a light liquid (hydrogen) and the magnification of this effect due to tight tip clearance (TC). Since higher-order cavitation has been identified as a significant harmonic driver, knowledge of the natural frequency of potentially excitable modes is critical for safe operation, but this frequency cannot be measured during the severe operational environment. A comprehensive testing and analysis program has therefore been performed over the last 4 years to identify the nominal value and uncertainty of the frequency by modeling and testing two simpler structures in several configurations that share some of the characteristics of the operational inducer. This testing was used to assess and adjust modeling techniques, and an excellent correlation was achieved. Identification of the uncertainty in the inducer frequency itself was still problematic, however. This difficulty led to an investigation of Bayesian uncertainty quantification techniques and to the application of the relatively simple technique of multivariate normal conditional distributions to calculate the inducer natural frequency uncertainty. Assumptions on the prior distributions of the uncertainty of the fluid-added mass and tip clearance effect are initially applied to the models of each of the simple structures and the inducer itself, and these uncertainties are propagated to generate natural frequencies using the design of experiments. Simple response surfaces are then created from this data in order to calculate a covariance matrix relating all of these natural frequencies. Finally, the results from the modal test of the simple structures are considered to be observations and used to calculate the conditional variance of the desired inducer frequencies. As this method is less rigorous than more complicated Bayesian methods reported in the literature, a conservative factor is applied to the result, but the resulting uncertainty is still significantly less than originally estimated and will greatly assist the certification of the inducer for use in the engine.

Keywords Uncertainty quantification · Structural dynamics · Modal test · Liquid hydrogen · Bayesian techniques · Model updating

Nomenclature

CB	Cantilever beam
DOF	Degrees of freedom
DOE	Design of experiments
E	Young's modulus
FS	Full scale
HOC	Higher-order cavitation
HOSC	Higher-order surge cavitation
LH2	Liquid hydrogen

A. M. Brown (✉)
NASA/Marshall Space Flight Center, ER41/Propulsion Structural & Dynamic Analysis, Huntsville, AL, USA
e-mail: andy.brown@nasa.gov

J. L. DeLessio
JSEG/ESSCA – NASA/Marshall Space Flight Center, ER41/Propulsion Structural & Dynamic Analysis, Huntsville, AL, USA

T. J. Wray
NASA/Marshall Space Flight Center, ER41/Propulsion Structural & Dynamic Analysis, Huntsville, AL, USA

Z. Mao (ed.), *Model Validation and Uncertainty Quantification, Volume 3*, Conference Proceedings of the Society for Experimental Mechanics Series, https://doi.org/10.1007/978-3-030-77348-9_17

LPFP	Low pressure fuel pump2
MAC	Modal Assurance Criterion
ND	Nodal diameter
PDF	Probability density function
RT	Room temperature
ρ_f	Fluid mass density
RV	Primitive random variable
SLS	Space Launch System
SSME	Space Shuttle Main Engine
SS	Subscale
SSP	Simply supported plate
Ti	Titanium

1 Introduction

Liquid rocket engines are powered by the combustion of two propellants at very high pressure, a fuel and an oxidizer. Frequently, the fuel is liquid hydrogen (LH2). While the pressure can be provided by a very-high-strength storage tank, usually this would be weight prohibitive, so a turbopump or a series of turbopumps is required to provide these extremely high pressures. The staged-combustion cycle of the RS-25 engine powering the core stage of the National Aeronautics and Space Administration's (NASA's) Space Launch System, which is an adaption of the Space Shuttle Main Engines (SSME) that operated successfully for 30 years, has low- and high-pressure fuel and oxidizer turbopumps. The low-pressure fuel pump, which is fed directly by the fuel tank via ducting, uses an inducer to pressurize the liquid hydrogen fuel to several hundred psi (Fig. 1).

As with most other turbopump inducers, there is some level of cavitation, which is a "phenomenon in which rapid changes of pressure in a liquid lead to the formation of small vapor-filled cavities in places where the pressure is relatively low" [1]. The usual problem with cavitation is that these cavities collapse, and the liquid then impacts the blade surface, causing extensive damage, but in the RS-25 inducer, a different type of cavitation field is formed, called "higher-order surge cavitation (HOSC)" [2], which forms an acoustic wave that emanates both upstream and downstream. This wave has been empirically determined to be at a frequency between 6.4 and 6.7 times the engine speed for this inducer and has a high enough magnitude to resonate with modes of structures impinging on the wave, especially the inducer blades.

It was recognized during the design of the RS-25 that the differing operating conditions would cause operation in HOSC, which was not seen during the SSME operation. Although no empirical evidence of cracking in this inducer had been seen during testing or operation, this new potentially resonant condition requires a structural dynamic assessment for assured safe operation. The assessment requires knowledge of the natural frequency of potentially excitable modes, of course, but

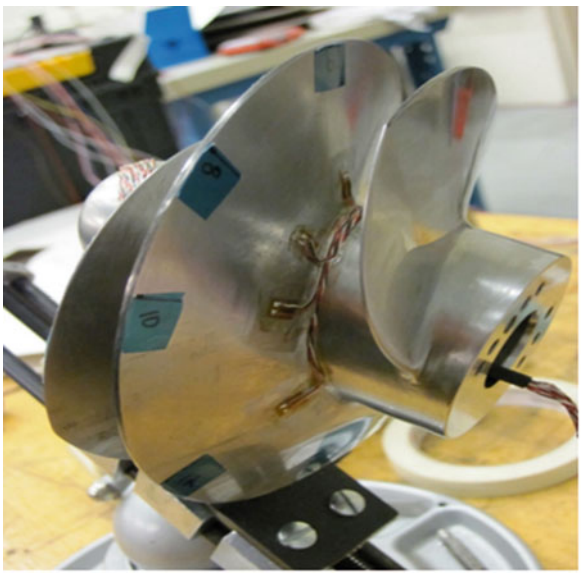

Fig. 1 Typical rocket engine turbopump inducer (not to scale)

in this case a large number of complicating factors cause both considerable adjustments from in vacuo natural frequencies and uncertainty in those adjustments. These include a large adjustment of Young's modulus of the titanium alloy used because of operation in a cryogenic (−423 °F) environment, the effect of the fluid-added mass of the liquid hydrogen, the magnification of this effect due to tight blade tip clearances with the housing, the effect of structural-acoustic interaction for a slightly compressible fluid, and the effect of multiphase fluid density where the liquid is cavitating. The magnitude of these adjustments was initially estimated by Aerojet Rocketdyne (the engine contractor) by using either available test data from similar structures or closed-form, theoretical extrapolations from the underlying physics. The uncertainties in each adjustment, on the other hand, were based purely on subjective "low, medium, or high" confidence levels, which were translated into percentages of the adjustment. As the actual values of the natural frequencies cannot be measured in operation due to the extreme environment and sensitive nature of the hardware, these adjustment and uncertainty estimates play a critical role in qualifying the turbopump for flight. This qualification uses a combination of physics-based and empirically based techniques, which will not be discussed here.

An extensive analytical and testing campaign was initiated in 2017 to help determine these adjustments, as documented by the authors [3, 4]. This campaign consisted of four modal/ping tests of hardware that have some similarity to the actual hardware and in environments that have some similarity to the actual environment. Those performed in LH2 are the first documented in the literature. These tests consisted of the following (Fig. 2):

1. Ping tests in air and LH2 of cantilever beam (CBeam) made of the same titanium alloy as the actual inducer
2. Ping test of cantilever beam in LH2 with a tight tip clearance
3. Modal test of subscale inducer with medium tight tip clearance in water
4. Modal test of stainless steel subscale (SS) inducer in air and water, ping test in LH2

These tests were largely successful, with consistent results that enabled updates to the adjustments and modeling techniques due to a number of various effects. In particular, the effect of cryogenic temperatures on the stiffness properties of the titanium alloy, the effect of fluid-added mass (for both LH2 and water), and the effect of tight tip clearance were refined.

However, it was still unclear how to improve the subjective uncertainty estimates. Table 1 shows the test/analysis error of the updated models, and it is not clear how to implement these into a global uncertainty estimate for a particular effect.

After a considerable study, a methodology based on the Bayesian updating of the variance of correlated random variables was identified as a reasonable technique to quantify the total uncertainty in the full-scale (FS) operational inducer. In particular, the eigenvalues from the four tested configurations and the untested actual configuration are used as the correlated random variables, and the modal tests give information that can be used with the correlation to infer an improved (reduced variance) posterior distribution of the desired eigenvalue. This application of the Bayesian techniques in this way has not been previously presented in the literature and is the subject of this paper.

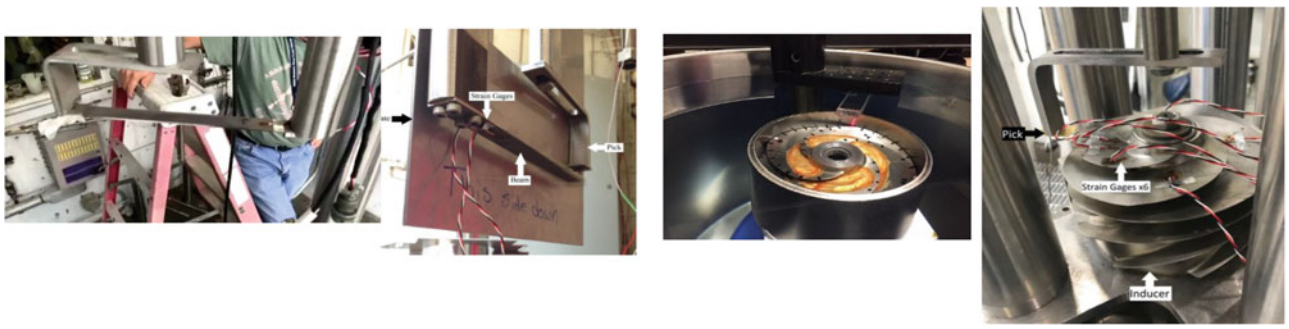

Fig. 2 Modal and ping test series

Table 1 Test/analysis error summary

Description	Error analysis from test	Error note	Effect tested
SS inducer, LH2, open	−3.23%		Fluid-added mass
SS inducer, water, open	−3.70%		Fluid-added mass
SS inducer, water, tight	−1.80%		Fluid-added mass, tip clearance
Ti CBeam water, open	0.80%	Approximate weighted average of modes	Fluid-added mass
Ti CBeam, water tight	3.00%	Approximate weighted average of modes	Fluid-added mass, tip clearance
Ti CBeam, LH2, open	0.80%	Approximate weighted average of modes	Fluid-added mass, $E = $ f(temp),
Ti CBeam, LH2, tight	2.00%	Approximate weighted average of modes	Fluid-added mass, tip clearance, $E = $ f(temp)

2 Literature Survey

An extensive literature survey was undertaken to determine an approach for quantifying the uncertainties of numerous complicating effects on the dynamic characteristics of the full-scale actual inducer. Investigation into the implementation of this concept led to a vast number of papers on uncertainty quantification (UQ), with a small subset focused on structural dynamics. Atamturktur et al. [5] looked at the UQ of the natural frequencies and modes of the National Cathedral in Washington, D.C., based upon a correlation to primitive random variables (RVs), such as material properties, and formulated a Bayesian approach to quantifying the inference uncertainty of these properties using Gaussian process emulators. The final result was a new posterior distribution of the dynamic characteristics, which is what is being sought here. As with our study, the experiment used to make this updated inference is the modal test. The experimental data are used to quantify the primitives, which are then filtered and propagated to obtain the desired output variance. These techniques are also applied to the dynamics of wind turbine blades by Van Buren and Atamturktur [6]. As defined here, inference UQ is the determination of a posterior that "is the probability law that leads to predictions of resonant frequencies that are statistically consistent with the experimental data." In these two papers, the Markov chain Monte Carlo methodology, which essentially is the development of output statistics by numerous expensive simulations of the finite element models, is replaced by Gaussian process emulators. The end result of this model updating process is a nondeterministic model rather than a typical deterministic one. Marwala also uses the modal test to update the model via a Bayesian updating of the primitive random variables [7].

Mullins and Mahadevan do not look at structural dynamics specifically but do generate a Bayesian framework encompassing all of the issues in the discipline, examining differences in propagation for aleatory versus epistemic uncertainties, evaluating the impact of sparse data, incorporating experimental results, and examining model-form errors. The number of considerations brought up in this paper is somewhat overwhelming, and the techniques necessary to address them are quite advanced [8].

3 Conditional Covariance

As the focus of this study was only to quantify the uncertainty of the final model of the full-scale inducer rather than update the model, which had been previously performed, it was deemed excessively complex to apply the techniques shown in the literature, which focus on improving the primitive random variable posterior distributions and generating nondeterministic models that would then be propagated. The initial concept was generated based on studies by the lead author identifying the uncertainty in the new NASA Space Launch System Flight vehicle primary mode based on a ground modal testing of the vehicle [9]. In that study, a quartile linear regression technique was used to obtain the flight mode purely as a regression on a single ground mode, as opposed to this case, where dependence on a number of modes from different configurations was sought.

Here, we have four different modal-tested configurations whose resulting dynamic data could be used to improve the posterior distribution of the full-scale inducer natural frequency of concern. Based on the papers discussed above, a text on the Gaussian processes by Gramacy was examined, which led to the definition of multivariable conditional covariance [10]. Derived from the Bayes theorem, which is

$$p\left(\theta|x\right) = \frac{p\left(x|\theta\right)\, p\left(\theta\right)}{p(x)} \tag{1}$$

where $\boldsymbol{\theta}$ is the parameter being inferred and $\mathbf{x}$ is the variable observed experimentally, it is stated that for a multivariate random distribution where the random variables are expressed as vector $\mathbf{x}$, this vector can be partitioned into $\mathbf{x_1}$, which is the random variables for which updated statistics are sought, and $\mathbf{x_2}$, which is the random variable that has data that can be used for inference:

$$x = \begin{bmatrix} x_1 \\ x_2 \end{bmatrix} \text{ with sizes } \begin{bmatrix} q \times 1 \\ (N-q) \times 1 \end{bmatrix} \tag{2}$$

The means of the RVs are partitioned similarly, and the covariance matrix relating the RVs is partitioned as

$$\Sigma = \begin{bmatrix} \Sigma_{11} & \Sigma_{12} \\ \Sigma_{21} & \Sigma_{22} \end{bmatrix} \text{ with sizes } \begin{bmatrix} q \times q & q \times (N-q) \\ (N-q) \times q & (N-q) \times (N-q) \end{bmatrix} \tag{3}$$

The distribution of $\mathbf{x_1}$ conditional on $\mathbf{x_2}$ equaling $\mathbf{a}$, a known vector (in our case, the vector of modal test natural frequencies), is therefore multivariate normal $(\mathbf{x_1} | \mathbf{x_2} = \mathbf{a}) \sim \mathrm{N}(\overline{\mu}, \overline{\Sigma})$, where

$$\overline{\mu} = \mu_1 + \Sigma_{12}\Sigma_{22}^{-1}(a - \mu_2) \quad \text{and covariance matrix} \quad \overline{\Sigma} = \Sigma_{11} - \Sigma_{12}\Sigma_{22}^{-1}\Sigma_{21}. \tag{4}$$

The concept of how this conditional calculation improves (reduces) the posterior variance is somewhat illustrated graphically in Fig. 4. The multivariate surface is reduced to a two-dimensional (2-D) curve by taking a slice where the information (the modal test natural frequency results) is given. This explains the odd fact that the information from the modal test (i.e., $\boldsymbol{x_2} = \boldsymbol{a}$) is not in the formula for the covariance, which can be understood by realizing that for a multivariate normal, any 2-D slice will have the exact same probability distribution function. Of course, this is based on the assumption of normality, so an error depending on the level of nonnormality will exist.

The applicability of eigenvalue covariance as used here to infer a reduction in the posterior variance of a correlated desired output eigenvalue is not conclusive (the authors do not claim to be experts in this complex discipline). However, the methodology was presented to the author of the Gaussian process text, R. Gramacy, who believed that it was legitimate [11]. In addition, although this technique itself was not found in the study of numerous papers, no rejection of the idea was discovered either. Some ideas for technique validation will be proposed in the concluding section of this paper.

4 Application of Technique to Pathfinder Case

Although somewhat simplified from more advanced techniques presented in the literature, implementation onto the complex fluid/structure models of the four modal tests as well as the actual inducer was anticipated to be a large challenge. A much simple "pathfinder" case was first processed, therefore, to at least verify the mathematical accuracy of the techniques. The ANSYS™ Workbench and Six-Sigma toolboxes proved critical for enabling the technique. For this case, a cantilever plate (CP) in water with a tight clearance from the sides was modeled and a pseudo-modal test value assigned to the first two natural frequencies. A model of a simply supported plate (SSP) in water was also modeled, with its fundamental frequency being the sought-after variance to be reduced by conditioning upon the cantilever plate (CP) eigenvalues. The model of the beam, cutaway of the surrounding fluid mesh, and model of the simply supported plate (SSP) with a partial visualization of the fluid mesh are shown in Fig. 3. After much effort, it was realized that for this technique to work, every conceivable source of error in the modal-tested structure (and only those sources) needed to be represented by primitive random variables. Therefore, RVs "fluid-added mass (FAM) with tight tip clearance (TC) factor," "cantilever plate geometric imperfection factor (GIF)," and "flat plate geometric imperfection factor" with means of 1.0 and standard deviations of 0.05 were created. The FAM factor was multiplied by the density of the water in both models, and as a simplification on varying the actual geometry, the GIF factors were multiplied by the Young's modulus of their models.

The goal of the process is to generate an accurate covariance matrix relating selected eigenvalues from both systems. Rather than go through the Markov chain Monte Carlo with the models themselves, which would be completely intractable for the complex inducer system, the ANSYS response surface system methodology is applied. Based upon the variation in the given primitive random variables, a design of experiment set was established to generate the response surface. For each design point, the first two eigenvalues were calculated and a second-order polynomial response surface created. A covariance matrix between all the random variables (primitives as well as eigenvalues) was then calculated by performing a Monte Carlo on the response surfaces 10,000 times. Statistics for each RV were also calculated. To ensure that the pseudo modal test value was physically realizable, samples from the primitives were selected and a modal analysis performed to obtain these values for the two cantilever plate modes.

A smaller covariance matrix relating only the eigenvalues was then selected and imported into Matlab, which is shown in Table 2. The means and standard deviations of the eigenvalues as well as the pseudo-modal test values were also inputted into Matlab and are shown in Table 3. The conditional mean and covariance values were then calculated using Eq. (4).

For this test case, only a small improvement in the coefficient of variation is obtained, but this is consistent given the poor correlation between the two systems. For illustration, the response surface polynomial was imported into Matlab to enable a separate Monte Carlo analysis to show the correlation between the fundamental modes of each system. A multivariate normal probability density surface from this calculation for the fundamental modes is shown in Fig. 4, and a red line identifies the pseudo-modal test value of the cantilever plate. The 2-D PDF curve obtained by slicing the surface at this point will be posterior PDF of the simply supported plate given only that single input modal test. A great deal was learned from this pathfinder case, particularly the importance of the selection of relevant random variables.

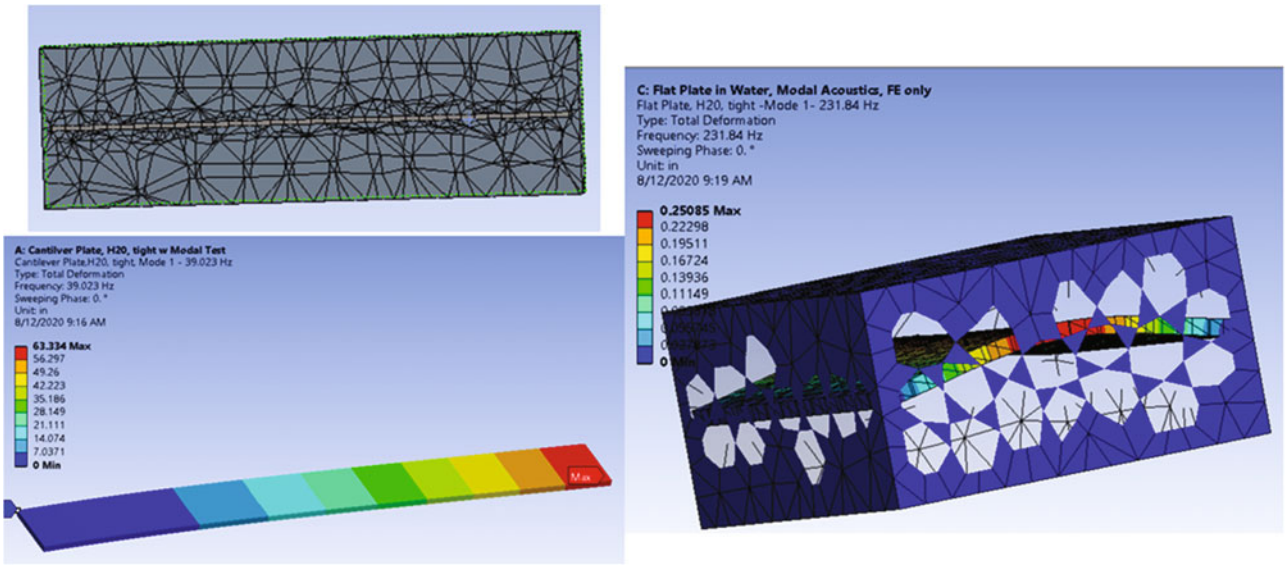

Fig. 3 Cantilever plate with fluid mesh cutaway, simply supported plate in fluid

Table 2 Eigenvalue correlation matrix

CP M1	CP M2	SSP M1	SSP M2
1.0	1.0	0.3803	0.2995
1.0	1.0	0.3565	0.2821
0.3803	0.3565	1.0	1.0
0.2995	0.2821	1.0	1.0

Table 3 Eigenvalue initial statistical parameters, modal test values, and conditional results

Mode	Mean	Coeff variation	Modal test
Cant plate mode 1	39.02 Hz	2.56%	42.991
Cant plate mode 2	258.01	2.49%	278.52
			Conditional coeff variation
SS plate mode 1	231.9	2.79%	2.40%
SS plate mode 2	434.33	2.43%	2.24%

5 Application of Technique to Inducer

As usual, the implementation of the technique to the actual inducer case proved orders of magnitude that are much more difficult than those for the pathfinder case. Based upon the extensive literature survey and the pathfinder, five primitive random variables were chosen to represent the first three of the modal test configurations (the SS inducer in LH2 was not used to save modal-tracking review time, which will be discussed below). These primitive random factors are the fluid-added-mass (FAM) effect on liquid density, tip clearance (TC) effect on liquid density, cryogenic (Cryo) effect on the titanium alloy, geometric imperfection effect on the subscale inducer, and geometric imperfection effect on titanium tight clearance and open clearance cantilever beams. As with the pathfinder case, the geometric effects are multiplied by the appropriate Young's modulus. Since only the effect on the full-scale inducer of the variances for FAM, TC, and Cryo are sought, it was decided (after much debate) that a geometric imperfection factor for the FS inducer was not necessary; i.e., the correlation of the FS inducer relative to the modal-tested cases needs to include all potential uncertainties in the tested cases but only those effects whose variance will be conditionally inferred in the FS. There is a substantial incentive for reducing the number of primitive RVs as each one doubles the number of design points, but this reasoning may not be rigorous and could lead to error in the results if it is incorrect.

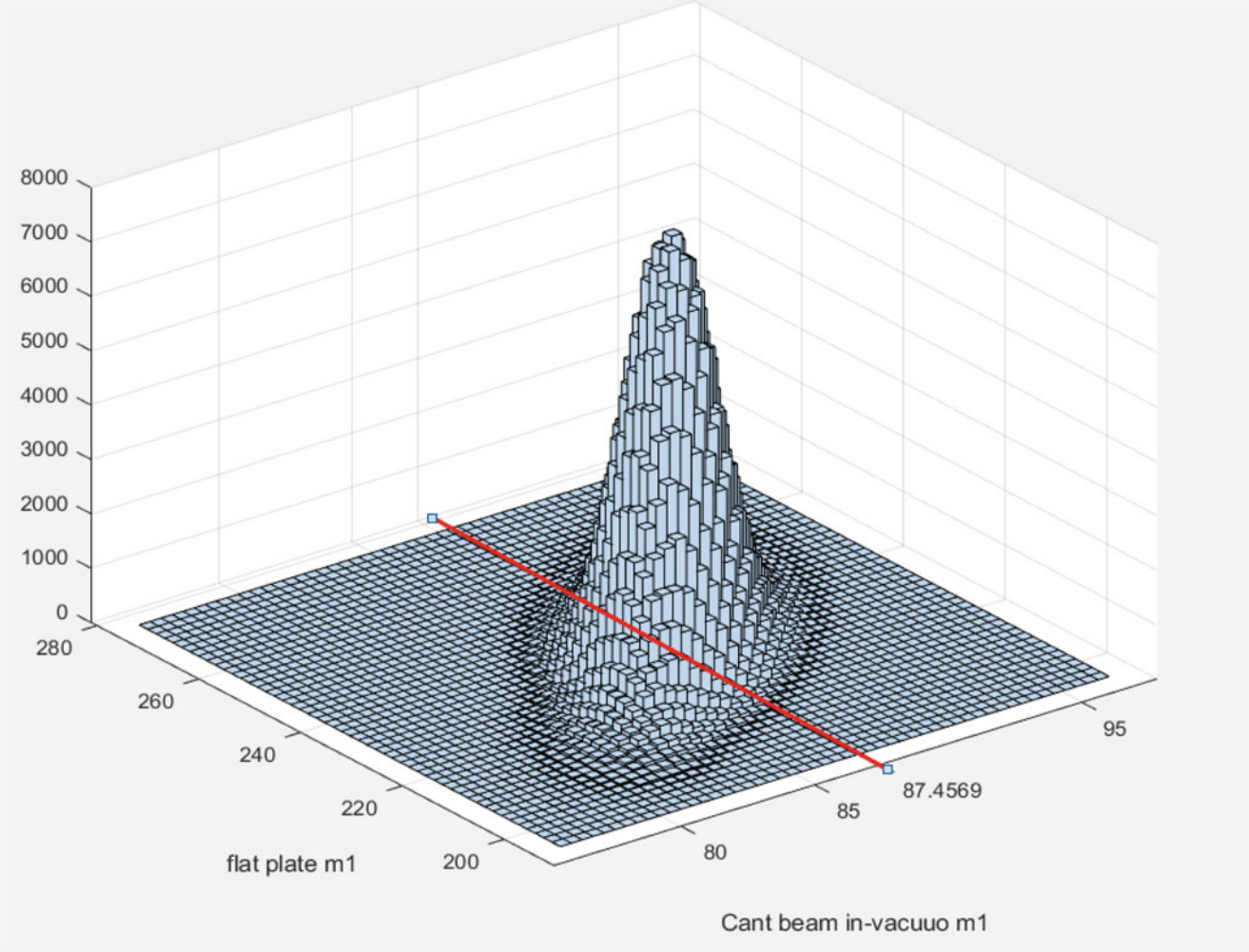

Fig. 4 Multivariate normal probability density function with 2-D slice at given information value

Some simplifying assumptions were made to limit the number of independent primitive RVs. One is that the tip clearance effect factor was assumed to be the same for the SS inducer in water with a medium tip clearance (see description in reference [4]), the cantilever beam in LH2 with a tighter clearance, and the full-scale inducer with the tightest clearance. We believe that the acoustic modeling technique for the tight tip regions, which is consistent for all of these models and gave excellent results upon a direct test/analysis, will have this same unknown error.

One complicating factor is the modeling of the cavitating region on the full-scale inducer. That has not been discussed in the author's previous papers, and the details will be discussed in a future paper. For now, we simply state that there are two cavitating regions on the blade, and different void fractions are assumed for each region. Each of these regions is assumed to have the same effect of uncertainty due to the use of FAM and TC as the noncavitating regions.

The same general procedure using ANSYS was followed as with the pathfinder. Even though the FS 0ND second bending mode was being sought, it is clear that this mode would be correlated with more than one of the other system's modes, so both the first and second of the cantilever beam modes were chosen, as well as the 0ND and 1ND modes of the SS inducer. Upon completion and further understanding of the process, we realize that since these pairs are almost fully correlated with each other, they probably do not yield any additional useful information to the final posterior inference, so they could be deleted. In reality, the geometry imperfections might cause different correlations with the FS inducer mode, so if a more precise method of representing that uncertainty was used, the extra mode would be useful. Another way to implement this extra information would be to include a separate modal test error for each mode, but each extra parameter doubles the design points, as noted earlier.

Compared to the pathfinder, though, this procedure had two additional severe complications. First, the acoustic/structure models are each quite large, and since the five primitives require 54 design points (as determined automatically by ANSYS),

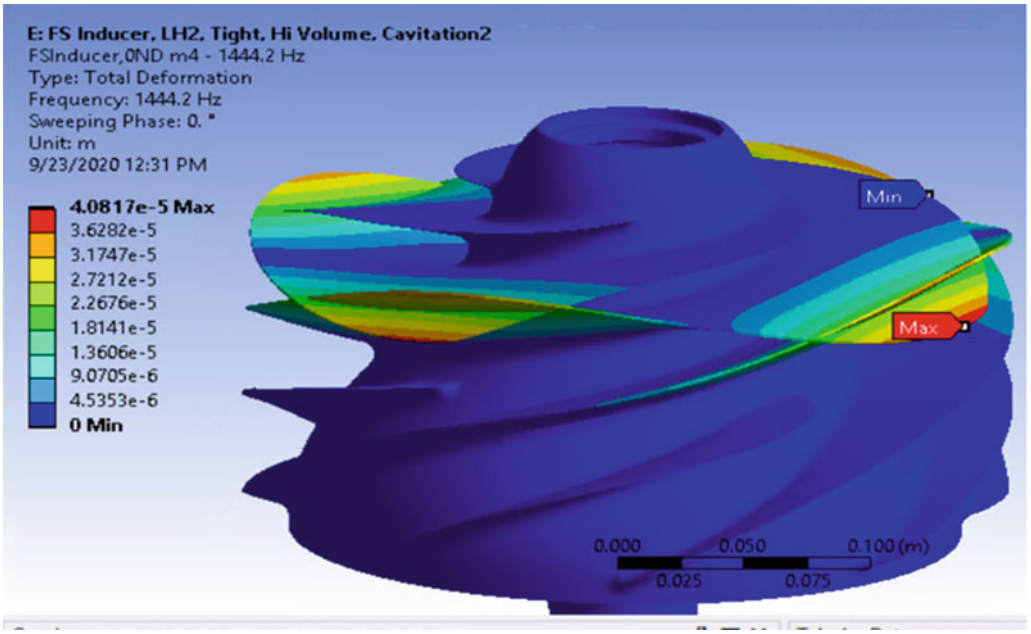

Fig. 5 Zero nodal diameter, second bending mode of FS inducer (illustration warped)

the analyses had to be ported from a local computer to a Linux server and then results ported back using the ANSYS RSM utility. As this utility is fairly new, and since the Linux server does not easily run more than a few analyses in parallel, this effort resulted in quite a few failed runs before a step-by-step procedure for running the many design points developed. The second complication was that it was determined that the modes chosen from each model switched in order quite frequently as the primitives were altered from their nominal values in the design points. Although identifying the correct mode potentially could have been performed automatically using a Modal Assurance Criterion calculation, implementing this would have been quite difficult, so instead the modes for each design point were animated and reviewed manually to determine which mode was the correct one to be tracked. The particular mode shape of the FS inducer is shown in Fig. 5. Table 4 shows the information of most of the parameters used in the study (titanium alloy cryogenic Young's modulus not shown due to export control concerns).

As with the pathfinder case, the correlation matrix was calculated based on the response surface and so is dependent on the accuracy of the surfaces. Both a full second-order polynomial and Kriging fits were attempted. ANSYS enables the creation of a normalized plot of the response surface prediction versus actual design point calculation, where the closer the points are to the diagonal the better the prediction is. As the plot for the second-order polynomial method shows in Fig. 6, the match is fairly good. A 3D plot of the response surface and design points can also be generated (obviously only two of the five primitives can be examined on a single plot), and this also shows a good match since most of the points lie on the surface (some of those that do not are hidden) (Fig. 7). The Kriging technique, in contrast, does a better job of matching the surface to the design points, but the response surface has large local warpages to try to match every point, so the second order was chosen as an overall better predictor of the output eigenvalue parameter correlation, which outliers should not overly influence.

6 Conditional Variance Results for FS Inducer 0ND Mode

The correlation matrix resulting from the process described results in the values shown in Table 5. The results are in the range that would indicate useful answers as the correlations are good (generally above 0.5) and yet not perfect, which would indicate that uncertainty is not being captured. This matrix and the parameter statistics were inputted into the Matlab code and the conditional variance calculated as described in the pathfinder case. The results yield a posterior coefficient of variation of the FS inducer 0ND mode of 0.68%, substantially yet believably improved from the unimproved value obtained directly from the propagation of the primitive RVs of 1.18%. While this improvement may not sound noteworthy, it is multiplied by three to incorporate a "three-sigma" overall range and is double sided, so the actual reduction in uncertainty is 3.02%,

Table 4 Inducer parameters

Parameter	Nominal/mean value	Standard deviation	Modal test	Notes
FAM effect on liquid density **ρ** (FAM)	1	0.05	Not applicable	Primitive random variable
Tip clearance effect on liquid density **ρ** (TC)	1	0.05	NA	Primitive random variable
Cryogenic effect on Ti **E** (Cryo)	1	0.05	NA	Primitive random variable
Geometric uncertainty effect on SS inducer **E** (GeomSSE)	1	0.05	NA	Primitive random variable
Geometric uncertainty effect on cant beams **E** (GeomCBE)	1	0.05	NA	Primitive random variable
SS inducer H_2O tight tip clearance **ρ*** FAM*TC	998.52 kg/m^3	56.323 kg/m^3	NA	Derived input RV
SS inducer **E***GeomSSE	2.001e11 Pa	8.0037e9	NA	Derived input RV
Ti CBeam, open clearance LH2 **ρ** *FAM	70.8 kg/m^3	2.832	NA	Derived input RV
Ti CBeam, open, **E***GeomCBE*Cryo	Not shown	Not shown	NA	Derived input RV
Ti CBeam, tight clearance LH2 **ρ** *FAM*TC	70.8 kg/m^3	3.9935	NA	Derived input RV
Ti CBeam, tight clearance LH2 **E***GeomCBE*Cryo	Not shown	Not shown	NA	Derived input RV
Full-scale inducer, tight clearance, noncavitating region **ρ** *FAM*TC	70.8 kg/m^3	3.9935	NA	Derived input RV
FS inducer, tight LH2 cavitating region 5% void fraction **ρ** *FAM*TC	67.26 kg/m^3	3.7939	NA	Derived input RV
FS inducer, tight LH2 cavitating region 5% void fraction **ρ** *FAM*TC	63.72 kg/m^3	3.5942	NA	Derived input RV
SS inducer H_2O tight tip clearance 0ND 2nd bending mode	1477.7 Hz	46.623 Hz	1509.4 Hz*	Output parameter *Modal test adjusted by 95.8% to account for not modeling fillet
SS inducer H_2O tight tip clearance 1ND mode	1693 Hz	49.454 Hz	1689.6 Hz	Output parameter
Ti CBeam, open clearance LH2 1st bending mode	41.182 Hz	1.554 Hz	42.5 Hz	Output parameter
Ti CBeam, open clearance LH2 2nd bending mode	259.71 Hz	7.279 Hz	267.5 Hz	Output parameter
Ti CBeam, tight clearance LH2 1st bending mode	38.437 Hz	1.1013 Hz	40.252 Hz	Output parameter
Ti CBeam, tight clearance LH2 2nd bending mode	245.16 Hz	6.9753 Hz	256 Hz	Output parameter
FS inducer 0ND 2nd bending mode	1505.3 Hz	17.859 Hz	NA	Sought-after uncertainty

which is quite significant in achieving the programmatic goals of the effort. Because of the considerable uncertainties in the methodology itself, this value was compared with the test/analysis errors shown in Table 1, and a rough "upper bound" on uncertainty of 3% is chosen for use in the final inducer assessment. As this value still reduces the original estimated total range of uncertainty by 3%, it is of major value.

7 Conclusion and Future Work

A new methodology for quantifying the uncertainty of a fundamental natural frequency of a complex, untested system based upon the Bayesian conditional covariance with modal-tested models of simpler systems has been presented. Although it was intended on being somewhat simpler than other methodologies presented in the literature, the final process was still extremely difficult due to the logistics of running a large number of central processing unit (CPU)-intensive simulations and because of mode switching. In addition, a number of questions remain on the accuracy of the final variance value obtained,

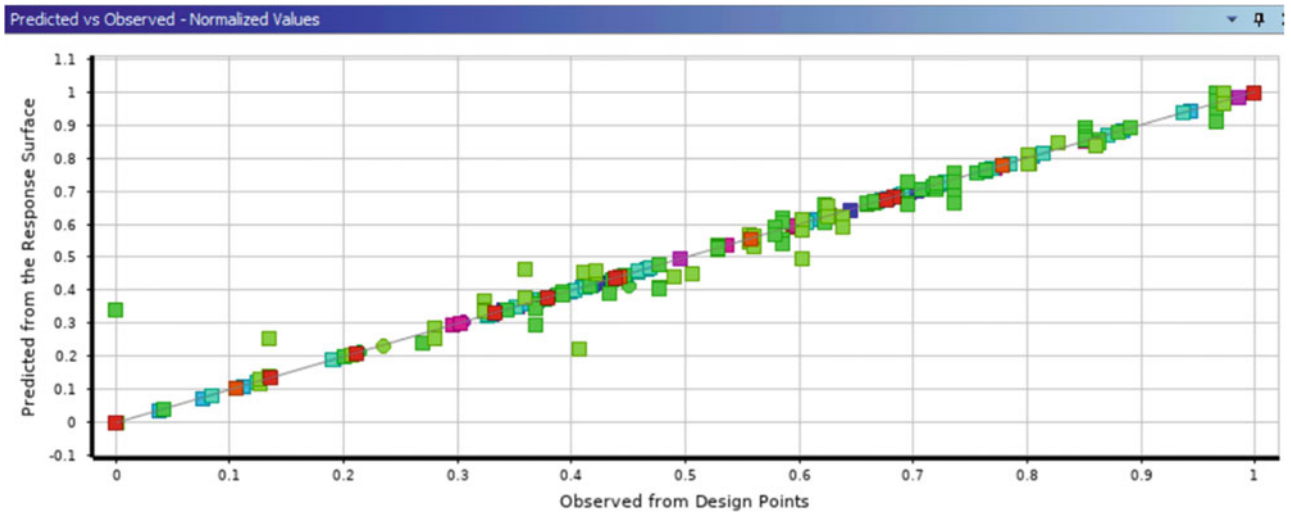

Fig. 6 Matching capability of second-order response surface

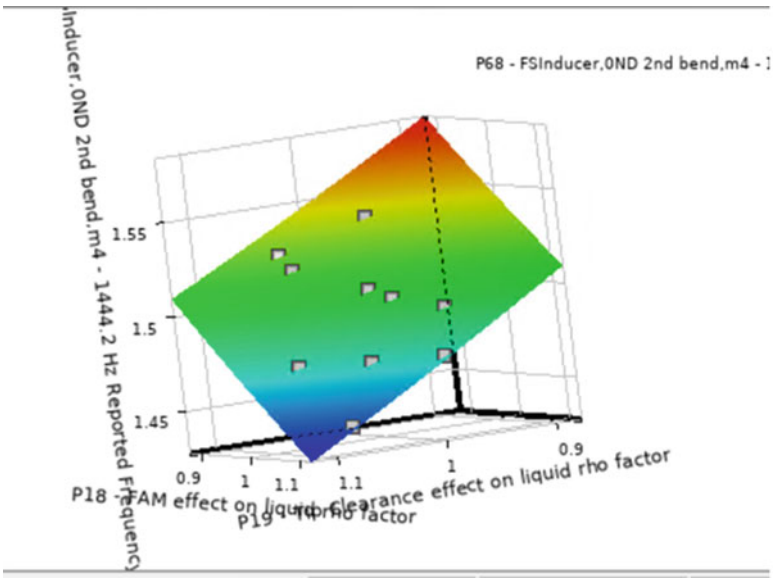

Fig. 7 Response surface for FAM and TC

in particular exactly how many and which uncertainties to represent for each configuration, how this value should relate to test/analysis error, and the theoretical accuracy of this methodology in the context of the overall Bayesian UQ hierarchy (as presented by Mahadevan). Nevertheless, if this value is considered along with simple test/analysis errors of the simpler modal-tested systems, the resulting conservative estimate of the variance still has proven to be of tremendous value to the program in assessing the susceptibility of the inducer to possible resonant excitation.

There are a number of possible courses of future work that could help assess the validity of the technique. The most valuable would be to generate a somewhat simpler system of tested structures informing a more complex structure for which the modes could actually be measured; it is not clear to the authors, however, exactly how the uncertainties themselves could be measured for comparison to prediction. In addition, the primitive RV-focused methodology described by Atamturktur could be implemented and the results compared with this eigenvalue covariance conditional technique. Finally, more study on the response surface validation, normality of the multivariate PDF, and implementation of automatic modal tracking based on the MAC would add information to the validation efforts.

Table 5 Correlation matrix for inducer systems

Correlation matrix	P34 – SS Inducer, MedWa-ter,OND,2nd Bend	P35-SSInducer,MedWater.IND	P3S-TiCantBeam,Lh20pen,lstBend	P37-TiCantBeam,Lh20pen,2ndBend	P38 TiCant-Beam,LH2Tight,lstBend	P39-TiCantBeam,LH2tight,2ndB end	P68 FSInducer,0ND 2nd bend
P34 – SS lnducer,MedWater,0ND, 2ndBend	1.000	0.871	0.465	0.464	0.590	0.573	0.716
P35 - SSInducer,MedWater,lND	0.871	1.000	0.588	0.587	0.682	0.668	0.557
P36- TiCant-Beam,Lh20pen,lstBend	0.465	0.588	1.000	1.000	0.979	0.983	0.058
P37- TiCant-Beam,Lh20pen,2ndBend	0.464	0.587	1.000	1.000	0.979	0.983	0.058
P38- TiCant-Beam,LH2Tight,lstBend	0.590	0.682	0.979	0.979	1.000	0.999	0.207
P39- TiCant-Beam,LH2tight,2ndBend	0.573	0.668	0.983	0.983	0.999	1.000	0.188
P68 – FSInducer ,OND 2nd bend	0.716	0.557	0.058	0.058	0.207	0.188	1.000

References

1. Wikipedia: Cavitation, 4 December 2020
2. Subbaraman, M., Burton, K.: Cavitation-induced vibrations in turbomachinery: Water model exploration. In: Fifth International Symposium on Cavitation, Osaka, 1–4 November 2003
3. Brown, A.M., DeLessio, J.L., Jacobs, P.W.: Natural frequency testing and model correlation of rocket engine structures in liquid hydrogen – phase I, cantilever beam. In: IMAC-XXXVI Conference and Exposition on Structural Dynamics, Orlando, 12–15 February 2018, paper 469
4. Brown, A.M., DeLessio, J.L.: Test-analysis modal correlation of rocket engine structures in liquid hydrogen – phase II. In: IMAC-XXXVIII Conference and Exposition on Structural Dynamics, Houston, 10–13 February 2020, paper 8732
5. Atamturktur, S., Hemez, F.M., Laman, J.A.: Uncertainty quantification in model verification and validation as applied to large scale historic masonry monuments. Eng. Struct. **43**, 221–234 (2012)
6. Van Buren, K.L., Molliineaux, M.G., Hemez, F.M., Atamturktur, S.: Simulating the dynamics of wind turbine blades: Part II, model validation and uncertainty quantification. In: Los Alamos National Laboratory paper LA-UR-11-4997
7. Marwala, T., Sibisi, S.: Finite element model updating using Bayesian framework and modal properties. J. Aircr. **42**(1), 275–278 (2005)
8. Mullins, J., Mahadevan, S.: Bayesian uncertainty integration for model calibration, validation, and prediction. J. Verif. Valid. Uncert. Quantification. **1**(1), 011006 (2016) (10 pages)
9. Brown, A.M., Peck, J.A., Stewart, E.C.: Quantification of dynamic model validation metrics using uncertainty propagation from requirements. In: IMAC-XXXVI Conference and Exposition on Structural Dynamics, Orlando, 12–15 February, 2018, paper 468
10. Gramacy, R.B.: Surrogates: Gaussian Process Modeling, Design, and Optimization for the Applied Sciences. CRC Press (2020)., ISBN 9781000766202
11. Personal Correspondence with Robert Gramacy, 5 August 2020

Application of Speaker Recognition *x*-Vectors to Structural Health Monitoring

Kyle L. Hom, Homayoon Beigi, and Raimondo Betti

Abstract The domain overlap between speech and structural vibration presents opportunities to leverage advances in speaker recognition for structural health monitoring. Classification of x-vectors, which are the outputs of a pre-final layer from a time-delay neural network (TDNN) acoustic model, has been used to recent success in speaker discrimination. x-Vectors present a flexible speaker representation for increased classification robustness, as they contain intermediate speaker parameterizations rather than distinct class predictions for a specific identification task. In investigation of the parallels between speech and structural acoustics, this paper explores the viability of the x-vector speaker recognition system for structural damage detection. A TDNN following the x-vector structure is trained to classify damage scenarios from the Z24 Bridge Benchmark, using cepstral and pitch features from accelerometer measurements. x-Vectors are calculated for each measurement, which are used to train a probabilistic linear discriminant analysis (PLDA) model for Z24 damage scenario categorization. This approach yields strong performance in damage detection and classification, and we attempt a transfer learning approach to use this developed TDNN for training a modified x-vector system for local damage. We also apply the developed x-vector system to the LANL SHM Alamosa Canyon Bridge and UC-Irvine Bridge Column studies to explore generalization of this method, obtaining strong results in damage detection. We find that the x-vector system demonstrates the feasibility of speaker recognition techniques for structural health monitoring and shows significant potential for output-only structural health assessment.

Keywords Structural health monitoring · Time-delay neural networks · x-Vectors · Transfer learning · Z24 bridge

1 Introduction

Structural health monitoring (SHM) and speaker recognition both leverage hidden information to find dynamic behavior and recognize identifying characteristics of an acoustic system. The challenges unique to SHM are often difficult to disentangle; natural degradation over the life of a structure is often unrecorded until failure, and the necessary sparsity of sensor instrumentation provides limited representation of modified dynamics. Though much work in SHM has focused on constitutive models to improve observation of hidden dynamics, there may be much to be gained from investigating developments in speaker recognition. For example, nonlinear dynamics have been captured by data-driven mapping techniques such as neural networks, i-vectors, and Gaussian mixture models, which are topical to the current research efforts in speaker recognition [1]. In this paper, we introduce a recently developed technique in speaker recognition to improve damage detection for SHM.

As both speech and structural vibrations fall under the acoustic domain, we can use a structural measurement dataset to test speaker recognition techniques. One established resource is the Z24 Bridge Benchmark provided by the KU Leuven Structural Mechanics Section for development of damage detection techniques [2, 3]. Efforts in constitutive modeling have yielded some success in identifying damage for the Z24 Bridge Benchmark, though limited by how slight the changes in spectral features are over the progressive introduction of damage [4, 5]. However, with current integration of techniques from

K. L. Hom (✉) · R. Betti
Department of Civil Engineering and Engineering Mechanics, Columbia University, New York, NY, USA
e-mail: klh2136@columbia.edu; rb68@columbia.edu

H. Beigi
Recognition Technologies, Inc., Yorktown Heights, NY, USA
e-mail: beigi@recotechnologies.com

Z. Mao (ed.), *Model Validation and Uncertainty Quantification, Volume 3*, Conference Proceedings of the Society for Experimental Mechanics Series, https://doi.org/10.1007/978-3-030-77348-9_18

machine learning into conventional structural analysis tools [6], and the success of speaker recognition features in damage identification [7, 8], nonlinear structural behaviors may be better captured via data-driven methods.

To explore this research path, we use Kaldi, a robust open-source speech recognition toolkit [9]. The Kaldi team at Johns Hopkins University has recently developed the x-vector speaker recognition technique, which is leading the field in speaker classification [10–12]. x-Vectors are the intermediate layer outputs from a time-delay neural network (TDNN) trained to classify speakers from speech audio. TDNNs were first used in 1989 to learn temporal relationships between speech sequences for phoneme recognition [13], and were recently rediscovered as effective and computationally efficient alternatives to other sequence-detecting neural networks, such as RNNs or LSTMs. Once trained as an acoustic model to find these temporal relationships within speech, the TDNN's penultimate layers provide outputs, or embeddings, which represent speaker characteristics. By extracting these embeddings for classification, instead of using the final, discrete output classes of the TDNN, the x-vector formulation can robustly tolerate variations of the speaker's behavior.

As speaker classification is an analogous problem to damage classification in structural health monitoring, this paper applies the x-vector formulation to damage classification for the Z24 Bridge Benchmark to assess the technique's potential value in the field. We present three tasks to this x-vector method: global damage scenario classification using x-vectors, local damage severity classification using the damage relationships learned in the damage scenario task, and application of the global damage scenario x-vector system to identify structural modification for unseen LANL SHM datasets.

2 Data Preparation

2.1 Data Resources

We use the Z24 Bridge Benchmark Progressive Damage Test (PDT) provided from the KU Leuven Structural Mechanics Section [2, 3]. The PDT dataset has 17 cases of applied damage (Table 1) for the instrumentation in Fig. 1 with ambient and forced vibration testing. The sensor measurements are sampled at 100 Hz for 65k samples, for a total of approximately 5800 min of data per damage case. Anomalies in the sensor data are recorded in the test documentation and are removed or addressed with the recommended processing from the documentation.

The accelerometer measurements must be adjusted so that the frequency content is mapped to the Mel-frequency ranges used for Kaldi's speech features. As the relationship between frequency and Mel-frequency is nearly linear up to 1 kHz, we perform a frequency warping of the waveforms to stretch the native sampling rate of 100 Hz to 2 kHz and the Nyquist frequency from 50 Hz to 1 kHz. The waveforms are normalized by the largest amplitude in the dataset, to preserve low-amplitude signals from the quantization inherent in conversion to audio file formats. Detrending is performed for all waveforms, as several instances of sensor drift are recorded in the Z24 documentation.

2.2 Training and Test Data

Assignment of class labels corresponds to the damage scenarios in Table 1. The damage case numbers are assigned to all sensor waveforms from the same damage scenario. Sensor locations for the training set are selected after removing sensor locations which have absent or degraded waveforms during at least one damage scenario, as we want to train the TDNN on a balanced number of waveforms per damage scenario. All removed sensor locations are shown in Fig. 1, and we supplement the test set with these sensors' valid waveforms from the other damage scenarios. Hence, the test set in Fig. 1 is constructed from the Z24 reference sensor locations (R1, R2, and R3), a 3-DOF sensor opposite R1 (208), two column 3-DOF sensors (432, 531), and the available non-degraded waveforms from the degraded accelerometer set (99V, 199L, 203L, 512L, 512V). These 19 sensor waveforms per scenario in our test set constitute approximately 7% of the 263 total available waveforms per scenario from the Z24 PDT test. Consequently, the training set consists of the remaining 244 sensor waveforms.

2.3 Local Damage Labeling

In the interest of leveraging the granularity of the Z24 PDT sensor arrangement, local damage severity ('Estimated Location' and 'Assigned Severity') is assigned in Table 1. Severity is labeled as described in the Z24 documentation, from a scale of 1 to 7. We assign severity to sensor measurements at the given Location Label (e.g. only waveforms from HH4 are assigned

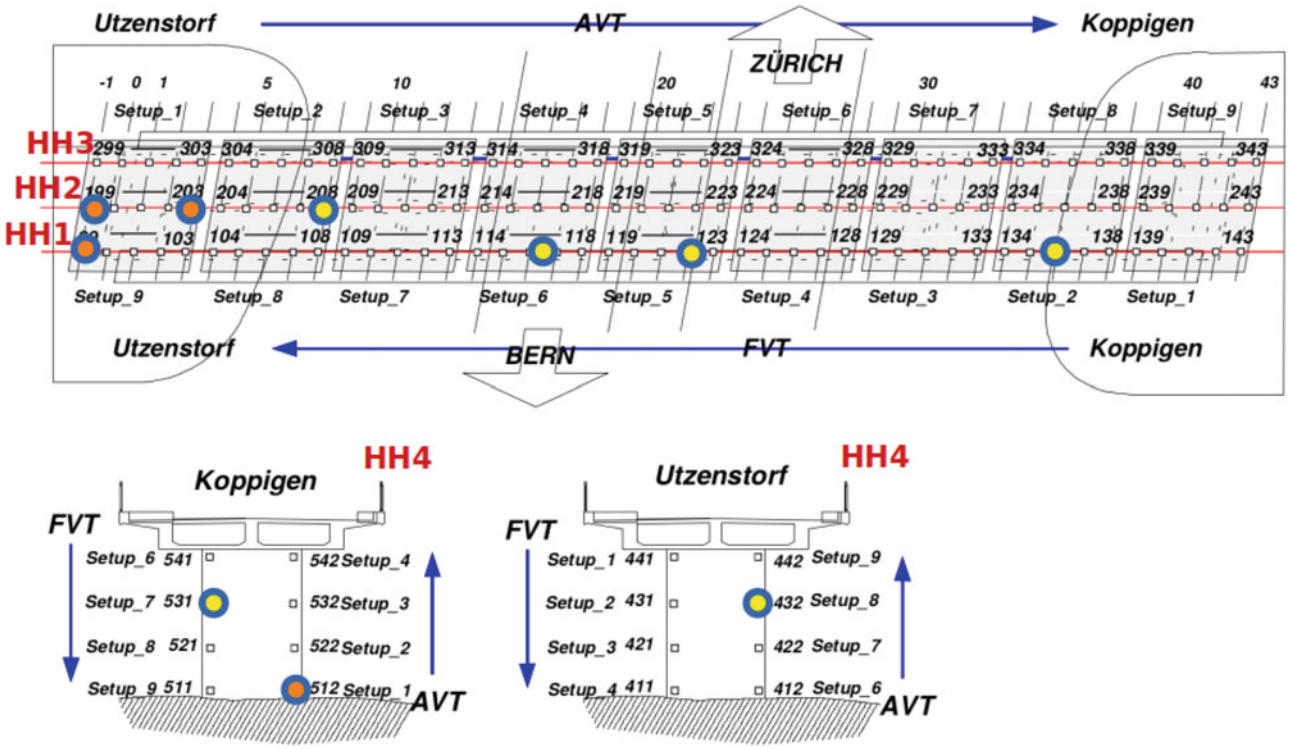

Fig. 1 Front and top view of the Z24 bridge instrumentation [3, 14]. Sensor locations reserved from the training dataset R1V, R2(L,V,T), R3V, 208(L,V,T), 432(L,V,T), and 531(L,V,T) are represented by the yellow-filled circles, and sensors with missing data from damage tests 99V, 199L, 203L, 512L, 512V are represented by the orange-filled circles. Both orange and yellow sensors are used in the test set

Table 1 Z24 progressive damage tests and assigned local damage severity

Damage case	Estimated location	Assigned severity	Damage scenario	Damage case	Estimated location	Assigned severity	Damage scenario
1	None	0	Undamaged condition	9	HH1,2,3	3	Spalling of concrete at soffit, 12 m^2
2	HH4	1	Installation of pier settlement system	10	HH1,2,3	3.5	Spalling of concrete at soffit, 24 m^2
3	HH4	2	Lowering of pier, 20 mm	11	Setup1,9	4	Landslide of 1 m at abutment
4	HH4	2	Lowering of pier, 40 mm	12	Setup1,9	4.5	Failure of concrete hinge
5	HH4	3	Lowering of pier, 80 mm	13	Setup1,9	5	Failure of 2 anchor heads
6	HH4	3	Lowering of pier, 95 mm	14	Setup1,9	5.5	Failure of 4 anchor heads
7	None	1	Lifting of pier, tilt of foundation	15	HH1,3	6	Rupture of 2 out of 16 tendons
8	None	1	New reference condition	16	HH1,3	6.5	Rupture of 4 out of 16 tendons
–	–	–	–	17	HH1,3	7	Rupture of 6 out of 16 tendons

Severity 1–3 for Cases 2–8). As damage for cases 9–17 are cumulative, severity only increases at the location of induced damage (e.g. waveforms from HH1-3 shifts in Severity from 3.5 to 6 due to Cases 10–15).

3 Analysis

3.1 Data Augmentation

The available sensor data for training a neural network can be increased, or augmented, through speed perturbation and addition of foreground and background noise [12]. Speed variation of 0.9×, 1.0×, and 1.1× is performed before noise

corruption. The augmentation is applied with three independent noise sources, consisting of foreground and background white and brown noise, and background traffic recordings from [15]. In total, this augmentation expands the dataset approximately eightfold.

3.2 Feature Selection

Mel-Frequency Cepstral Coefficients (MFCCs), pitch, delta-pitch, and probability of voicing features are standard features used in speaker recognition, and are chosen for a preliminary foray into damage detection. Each measurement is divided into evenly spaced sections, or frames, of 25 ms duration sliding over 10 ms intervals, over which features are calculated and mean- and variance-normalized.

In Kaldi, the MFCCs are calculated from an inverse discrete cosine transform of the log of the signal's power spectral density [9]. MFCCs represent periodic behavior of frequency spectra over an auditory frequency warping. The dynamics of spectral shifting captured in cepstra is assumed to be of similar utility in the structural domain as it is in the speech domain. As damage is introduced to a structure, modes may shift and new acoustic behaviors may appear, as illustrated in Fig. 2. In this study, we assess the effect of varying MFCC resolution on damage detection. We use speech standards of high and low MFCC resolution, or 13 and 30 coefficients, respectively. We refer the reader to [1] for a formal description of the calculation of MFCCs.

Normalized pitch, delta-pitch, and probability of voicing features calculated in Kaldi [16] are analogous to a structure's natural frequency, shifts in natural frequency, and the likelihood of such a shift happening. These features are appended to the MFCC features to construct the feature vector per frame, resulting in 16-dimensional and 33-dimensional feature vectors.

3.3 Time-Delay Neural Network Architecture

We use a TDNN with the same structure presented in the x-vector formulation [12] to find distinguishing structural damage characteristics across the Z24 PDT scenarios. The TDNN captures vibration dynamics by learning relationships between features over a sequence of frames corresponding to the damage scenario. Exposure to past or future features from a given point in the sequence is accomplished by defining a range of frames, or context, that are connected in a layer. As the input layer is restricted to an ordered sequence of time-dependent features, the outputs of the following hidden layer are a compressed representation of structural damage dynamics over the defined context.

As shown in Fig. 3, the first four layers (TDNN1–TDNN4) collect several frames of context from the sensor waveform before and after the frame being assessed. To reduce sensitivity to the selection of frames when segmenting the signal, a statistics pooling layer is inserted after sufficient frame-level representations are collected. This statistics pooling layer collects all of the TDNN5 outputs in the segment of the measurement input and returns the mean and standard deviation for the segment, compressing the context of the following layers into segment-level representations. The following layers (TDNN6, TDNN7) fit the statistics from the T sequences to the corresponding damage scenarios, and a softmax output layer provides the predicted class of the 17 damage scenarios. This TDNN is trained over eight epochs and thus sees all training data eight times.

The x-vectors for each accelerometer signal are obtained from the outputs of TDNN6, yielding 512×1 dimensional vectors. We can improve the damage classification performance by attempting to use an intermediate layer's output as the identifier of damage [11, 12]. The final output of the network is supposed to be the best-estimate of the classes, but this is often not the case; variations in the test dataset may be uncaptured by the network, and the output at the end of the network may be inflexible in distinguishing between classes (as the final layer is a softmax output layer, and tends to learn the 'strongest' separations between discrete classes). We hope that extracting outputs at a layer close, but not at the final output layer may yield better class representations and reduce the effect of overfitting the network to particular damage scenarios.

3.4 PLDA Classification

We apply a LDA transformation to the x-vectors for dimensionality reduction from 512 to 200 dimensions. To perform classification in the LDA-transformed space, a Probabilistic LDA (PLDA) classifier [17] is developed from the training set

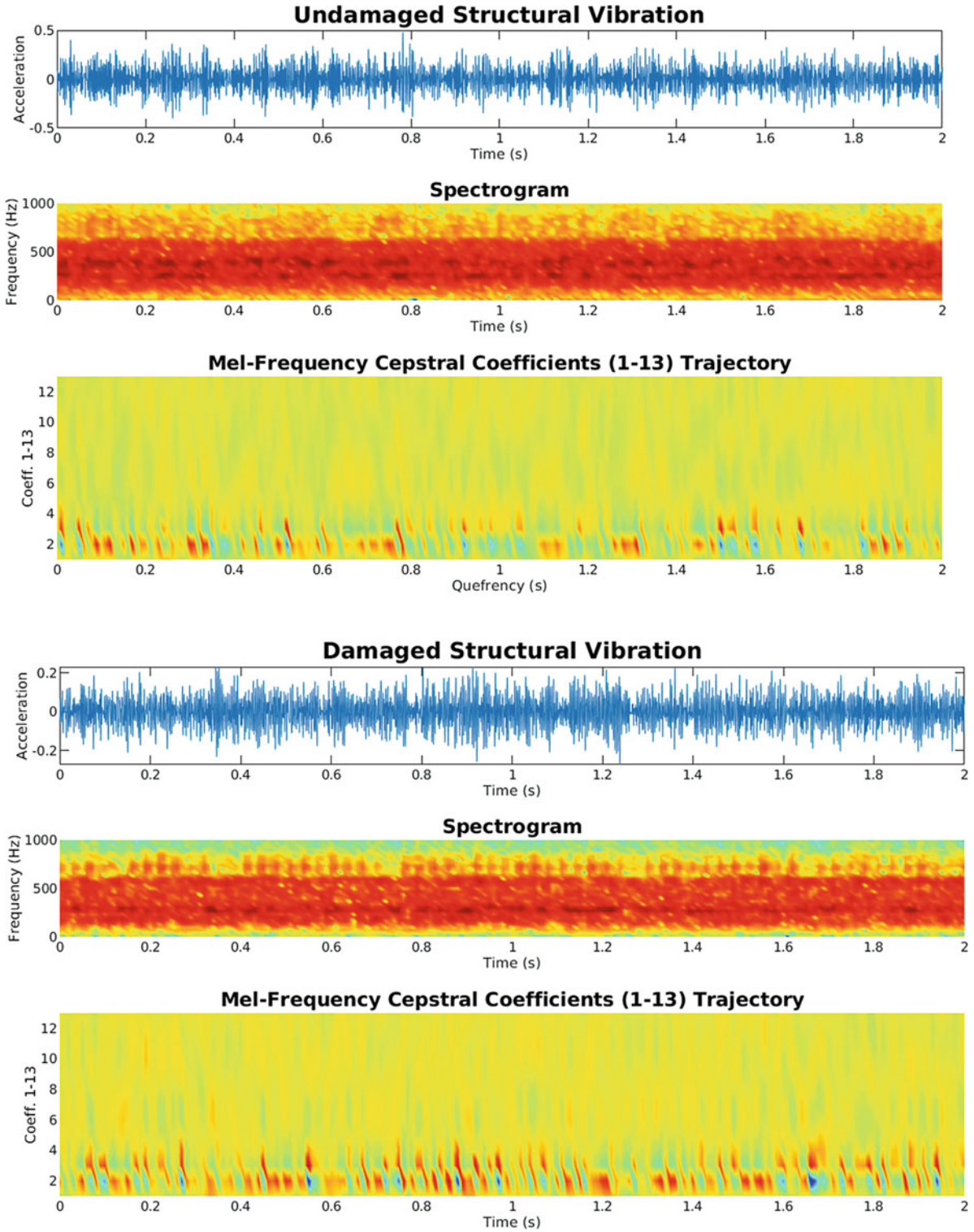

Fig. 2 Timeseries, spectrogram, and the first six MFCCs for R1V from damage cases 1 (left) and 17 (right). Though the spectral content has some characteristic banding after the full damage procedure is performed on case 17, the differences between signals are more readily apparent from the MFCC trajectory. In particular, case 17 has sharper and closer bands of MFCCs around durations of 0.0–0.2s and 0.7–1.0 s corresponding to the 'clicks' and 'pops' audible around that periodicity, likely due to the anchor and tendon failures

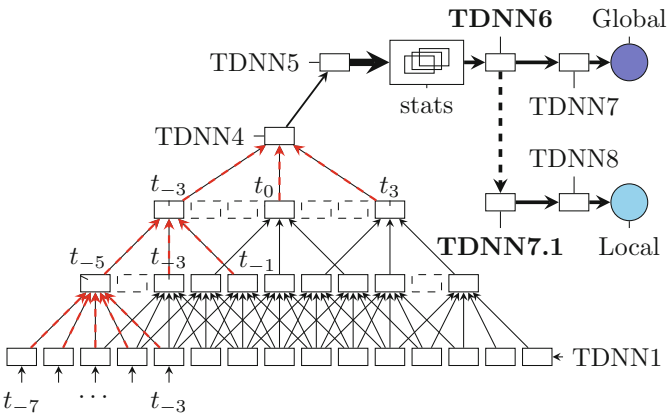

Layer	Layer Context	Total Context	Input × Output
TDNN1	[-2,-1,0,1,2]	5	(N-D×5)×512
TDNN2	[-2,0,2]	9	(512×3)×512
TDNN3	[-3,0,3]	15	(512×3)×512
TDNN4	[0]	15	(512×1)×512
TDNN5	[0]	15	512×1500
stats	[0:T)	T	(1500×T)×3000
TDNN6	[0]	T	3000×512
TDNN7	[0]	T	512×512
Global	[0]	T	512×17
TDNN7.1	[0]	T	512×512
TDNN8	[0]	T	512×512
Local	[0]	T	512×12

Fig. 3 15 Frames ($t_{-7} \leq t_0 \leq t_7$) are provided to the input layer (TDNN1). Following the red arrows, TDNN2's t_{-5} node receives 5 frames (corresponding to $t_{-7} \leq t_{-5} \leq t_{-3}$) of N-D features (where $N = 16$ or $N = 33$) as inputs. The TDNN for global damage scenario classification follows the standard x-vector configuration, while the TDNN for local damage severity appends two additional layers (TDNN7.1, TDNN8) to the TDNN6 layer and is retrained on the local severity labels. Bold indicates layers for intermediate output extraction

of x-vectors and the LDA transform. The PLDA technique assigns continuous probabilities to the classes used in LDA, and so can be used to determine log-likelihood ratios for the test set's membership in the probability distributions of the damage scenarios, within the LDA-transformed space. Hence, where LDA presents the 'primary directions' to maximize between-class scatter and minimize within-class scatter, PLDA provides the probability an example belongs in the class groupings separated along these 'primary directions'. Classification is then performed based on the log-likelihood ratios, scoring a test example against the clusters of training examples (as visualized in Fig. 4).

3.5 Local Damage Identification

Given the spatial granularity of the Z24 PDT sensor grid, we attempt to identify local damage severity over the damage scenarios, utilizing the learned structural acoustic relationships from the previous TDNN. Following the transfer learning technique from [18–20], we initialize a new network with the pretrained Z24 damage scenario TDNN's TDNN1-TDNN6 layers, and append new layers TDNN7.1, TDNN8, and a softmax output layer as shown in Fig. 3. This local damage TDNN is trained on the 12 local damage severity labels from Table 1 for only three epochs, as less training is required after initializing with the pretrained global damage TDNN. We then follow the same LDA/PLDA classification procedure, extracting local damage embeddings at TDNN7.1.

3.6 Validation on LANL Datasets

Though the Z24 damage scenario TDNN's output layer is fitted to the Z24 PDT's 17 damage scenarios, we can use this TDNN to provide x-vectors for other structures. Using the Los Alamos National Lab SHM Experimental Datasets for the Alamosa Canyon Bridge and UCI Column tests [21, 22], we perform the aforementioned data preparation procedure and feed the converted measurements forward through the TDNN. The resulting x-vectors are then classified via the PLDA procedure to assess how well they distinguish between structural modifications. For the Alamosa Bridge, we attempt to detect the addition of a stiffener placed on the midspan of the bridge. For the UCI Column tests, we attempt to distinguish between six cases of progressive loading for two columns with different reinforcement techniques.

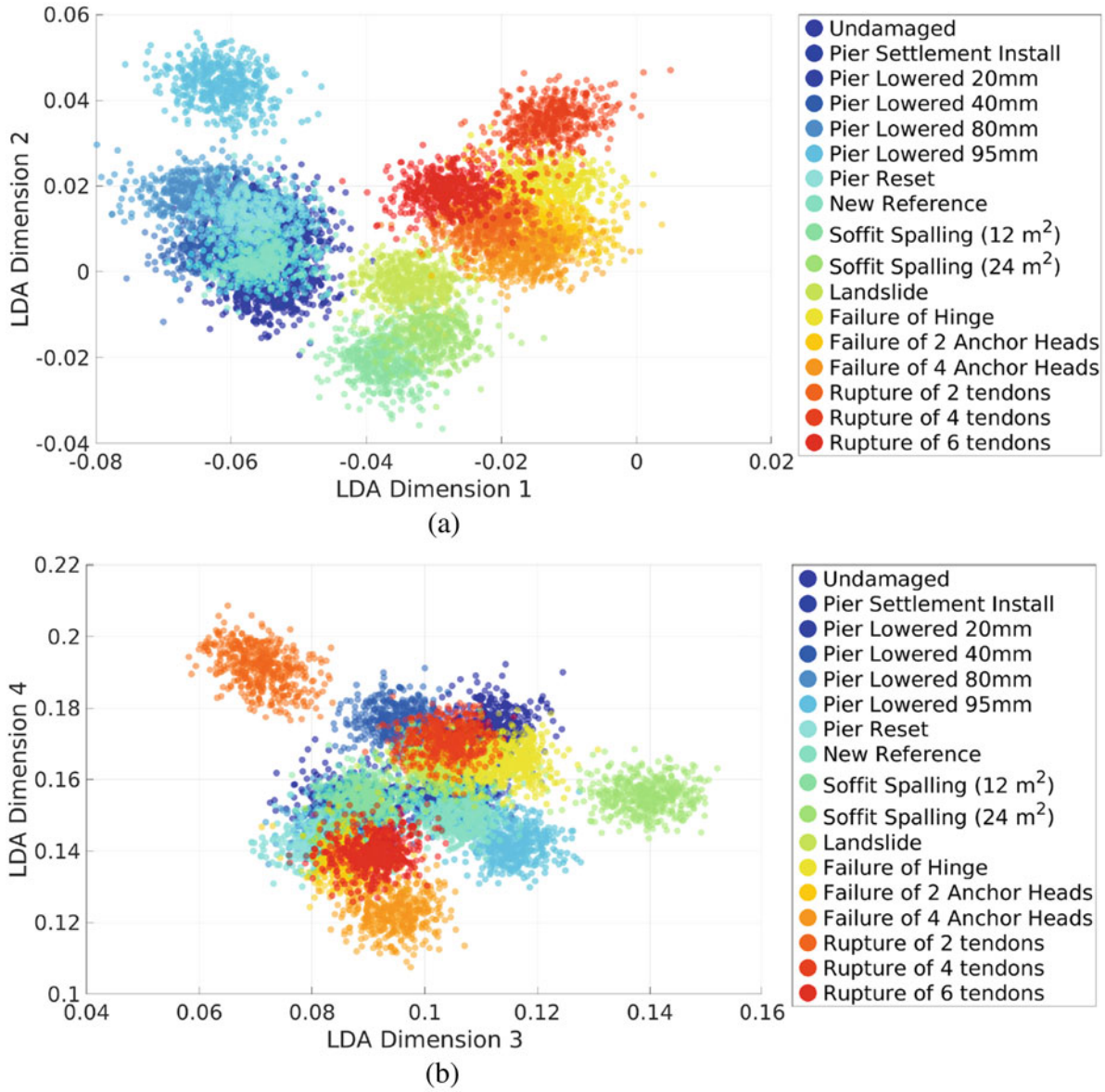

Fig. 4 Visualization of the LDA-transformed x-vectors from the first four largest eigenvalues (or LDA dimensions), demonstrating separability of the x-vectors. Separation appears to follow intuitive groupings of the damage scenarios and order of importance for discrimination (where first and second eigenvalues correspond to damage mechanisms, and third and fourth to levels of severity). The PLDA technique finds the centers and covariances of these clusters, and provides a log-likelihood ratio for class membership scoring of a presented test example. (**a**) Separation of pier lowering, spalling/landslide, and failure with first and second LDA dimensions. (**b**) Delineation of pier lowering depth with third LDA dimension, failure severity with fourth LDA dimension

4 Results

The results for applying the x-vector formulation to the Z24, Alamosa, and UCI datasets are provided in Table 2. We use accuracy, equal-error rate (EER), and area-under-the-curve (AUC) to assess the performance of this technique on these datasets. Our best-performing x-vector damage scenario setup has an EER of 3.919%, which is comparable to the x-vector performance on the VoxCeleb corpus and Speakers in the Wild Core with a minimum EER of 4.16% [12].

For the global damage scenarios in Fig. 5, the softmax output performs best, as it was directly trained to predict the classes. Though the x-vectors do not perform as well in identifying damage type for low-damage scenarios, we see in later results that their flexibility proves beneficial for classifying unseen data.

Table 2 Damage classification via x-vector approach

			13 MFCCs, 3 Pitch			30 MFCCs, 3 Pitch		
		Augmentation	Acc.(%)	EER(%)	AUC	Acc.(%)	EER(%)	AUC
Z24 Global	x-vector	–	87.977	5.938	0.989	**91.372**	**3.919**	**0.994**
	x-vector	(aug.)	83.451	7.525	0.983	88.967	5.658	0.986
	softmax	–	97.171	0.643	0.999	**98.161**	**0.455**	**0.999**
	softmax	(aug.)	95.757	1.225	0.999	96.322	1.067	0.999
Z24 Local	TDNN7.1	–	71.146	11.376	0.954	**72.419**	**12.414**	**0.951**
	TDNN7.1	(aug.)	63.366	14.120	0.929	66.195	13.626	0.932
	softmax	–	80.057	6.909	0.969	82.885	6.376	0.9709
	softmax	(aug.)	85.572	6.244	0.977	**85.997**	**5.741**	**0.979**
Alamosa	x-vector	–	**99.972**	**0.023**	**0.999**	99.954	0.046	0.999
	x-vector	(aug.)	99.954	0.037	0.999	99.935	0.065	0.999
UCI Column	x-vector	–	96.005	5.261	0.991	98.707	3.063	0.996
	x-vector	(aug.)	99.745	1.592	0.999	**99.530**	**1.364**	**0.999**

Bold indicates best-performing configuration.

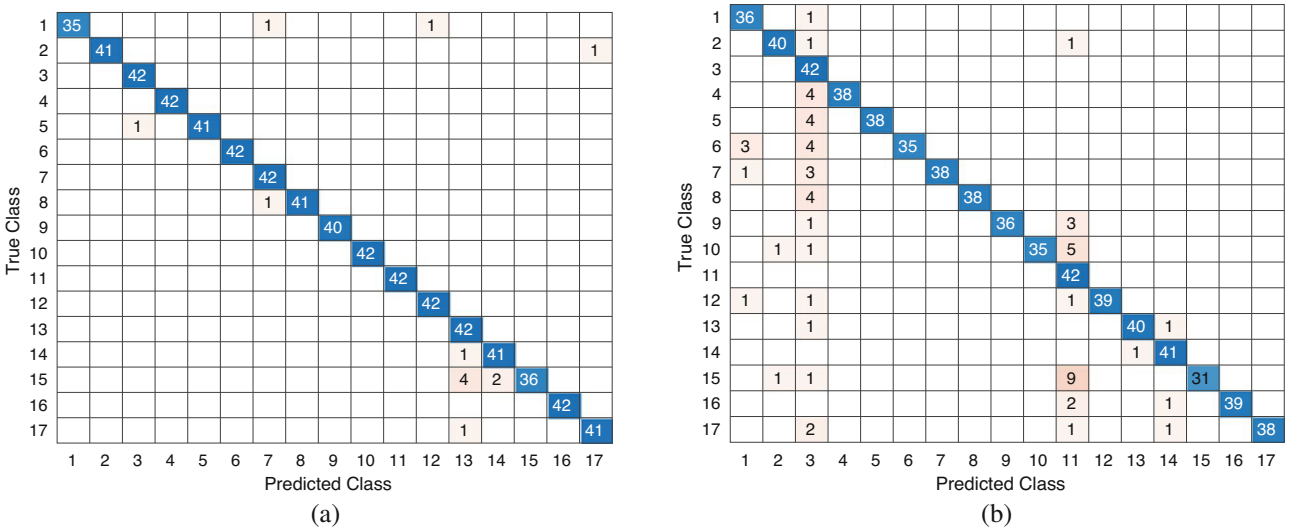

Fig. 5 Selected damage scenario confusion matrices. The x-vector approach appears to be biased towards predicting damage case 3, which is the first instance of pier lowering. This may be a level of damage that is not well associated with increased pier lowering, and may emulate effects of other damage cases. (**a**) Unaugmented 30 MFCCs, 3 Pitch Softmax Output. (**b**) Unaugmented 30 MFCCs, 3 Pitch x-Vector Output

When classifying local damage severities, the TDNN7.1 output confuses lower severities for higher severities more often than the softmax output in Fig. 6. We believe this was caused by the population bias towards lower damage across the sensor locations. This is in part due to the localization of damage methods: for example, tendon failures only increase severity for the sensor locations distributed along the tendon. However, the flexibility of the intermediate layer output classification appears to manifest for prediction of higher severity damage, as the TDNN7.1 output predicts this severity more accurately.

The detection-error-threshold (DET) curves for the damage classification tradeoff space indicate how much we can tolerate false alarms in exchange for lower detection of damage scenarios [1]. From Fig. 7, we observe that the miss probability for global damage can be reduced to 1% if we accept a 15% false alarm probability, indicating that the x-vector approach for global damage classification may be effective for use in bridge inspections and damage assessments.

Strong performance is observed from the x-vector classification for the unseen LANL datasets. Of note is the improvement which data augmentation during training of the Z24 TDNN provides for classifying the UCI Column damage: both low-resolution MFCC and high-resolution MFCC feature configurations perform well with data augmentation. Speaker recognition with x-vectors has shown improved performance with training on noise-corrupted and speed-perturbed signals, and it is postulated that this sort of variation in data 'loosens' the fit of the x-vectors to the particular training data [12]. In applying the learned acoustic knowledge from the Z24 dataset in the developed TDNN, this sort of data augmentation may have increased the flexibility of the network in separating damage types across different structures.

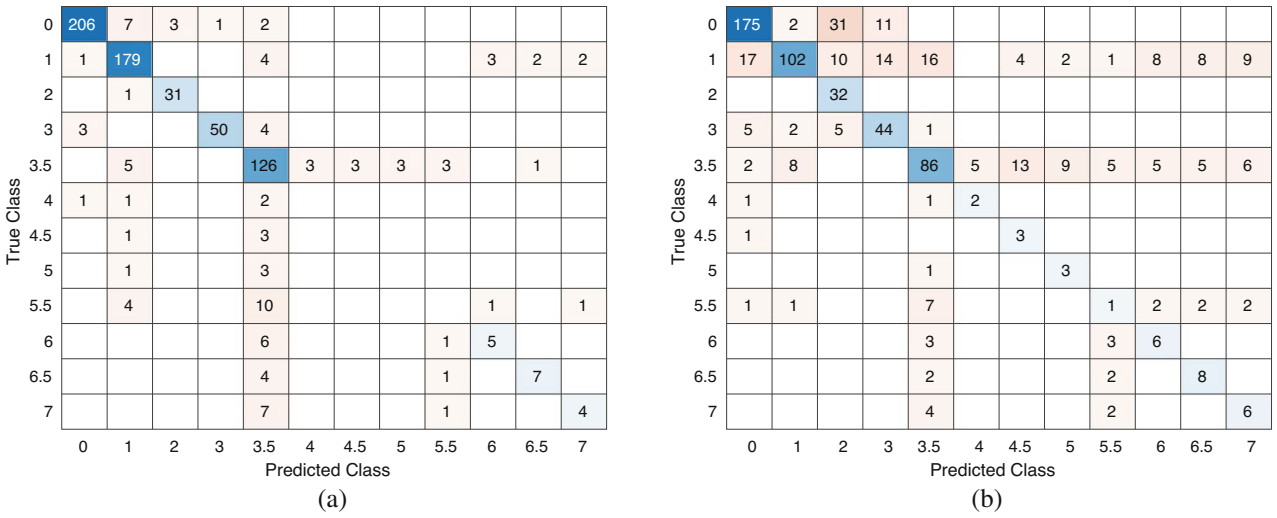

Fig. 6 Selected local damage severity confusion matrices. The TDNN7.1 output classification performs worse on the lower damage severities, but errs on the side of conservatism in predicting more severe damage at more sensor locations. It correctly identifies severe damage more often than the softmax outputs. (**a**) Augmented 30 MFCCs, 3 Pitch, Softmax Output. (**b**) Augmented 30 MFCCs, 3 Pitch, TDNN-7.1 Output

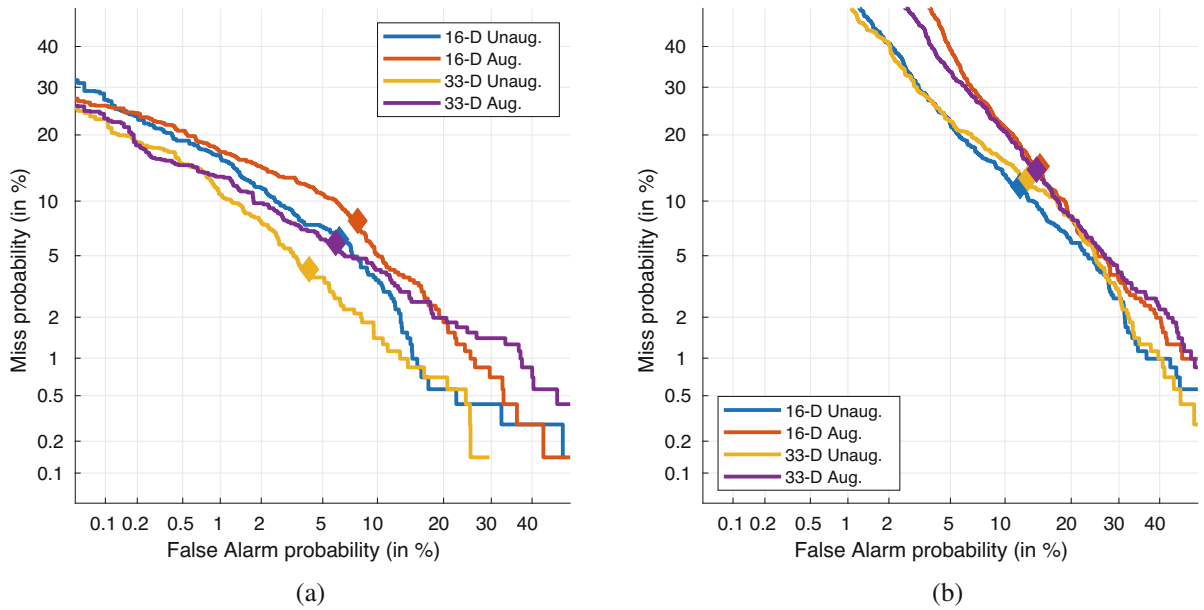

Fig. 7 DET curves for x-vectors. (**a**) Global damage scenario. (**b**) Local damage severity

5 Conclusion

The application of x-vectors for structural damage recognition has been investigated using the Z24 Bridge Benchmark and the LANL SHM Dataset. Damage scenario and local damage identification were performed, through development of two TDNNs for these tasks and PLDA classification of their intermediate outputs. Several feature enhancement techniques were explored to assess impact on damage assessment performance of these methods, including MFCC resolution and noise augmentation. These acoustic representations replicated the success of their parent models for speaker recognition in application to structural damage detection, with very strong results in distinguishing between damage scenarios across various SHM datasets. The x-vector system developed on the Z24 Bridge Benchmark demonstrated flexible and accurate performance in diagnosing structural health for all structures presented to the model.

In particular, the extension of damage scenario classification to local damage at particular sensors presents a promising field for investigation. As this approach does not explicitly utilize the physical interactions between adjacent sensors,

constitutive modeling may contribute physics-based structure to the x-vector framework's adaptation to empirical data. Future work in this area will encompass merging data-driven approaches (such as those presented in this paper) with constitutive analysis methods, and extension of this technique to assess bridges with sparse instrumentation.

Acknowledgments The authors would like to thank the KU Leuven Structural Mechanics Section for providing the Z24 Bridge Benchmark dataset, and the Los Alamos National Laboratory for providing the Alamosa Canyon Bridge and UCI Bridge Column datasets.

References

1. Beigi, H.: Fundamentals of Speaker Recognition. Springer, New York (2011). ISBN: 978-0-387-77591-3. https://doi.org/10.1007/978-0-387-77592-0
2. Maeck, J., De Roeck, G.: Description of Z24 benchmark. Mech. Syst. Signal Process **17**, 127–131 (2003). https://doi.org/10.1006/mssp.2002.1548
3. Reynders, E., De Roeck, G.: Continuous vibration monitoring and progressive damage testing on the Z24 bridge. In: Encyclopedia of Structural Health Monitoring. Wiley (2009). ISBN: 978-04-70061-62-6. https://doi.org/10.1002/9780470061626.shm165
4. Masciotta, M.-G., et al.: A spectrum-driven damage identification technique: application and validation through the numerical simulation of the Z24 Bridge. Mech. Syst. Signal Process. **70–71**, 578–600 (2016). ISSN: 0888-3270. https://doi.org/10.1016/j.ymssp.2015.08.027
5. Masciotta, M., Ramos, L., Lourenco, P., Vasta, M.: Damage detection on the Z24 bridge by a spectral-based dynamic identification technique. In: Dynamics of Civil Structures, vol. 4, pp. 197–206. Springer International Publishing, Cham (2014). https://doi.org/10.1007/978-3-319-04546-7_23
6. Azimi, M., Eslamlou, A.D., Pekcan, G.: Data-driven structural health monitoring and damage detection through deep learning: state-of-the-art review. Sensors **20**(10) (2020). ISSN: 1424-8220. https://doi.org/10.3390/s20102778
7. Balsamo, L., Betti, R., Beigi, H.: A structural health monitoring strategy using cepstral features. J. Sound Vib. **333**, 4526–4542 (2014). https://doi.org/10.1016/j.jsv.2014.04.062
8. Balsamo, L., Betti, R., Beigi, H.: Damage Detection Using Large-Scale Covariance Matrix, vol. 5 (2014). https://doi.org/10.1007/978-3-319-04570-2_10
9. Povey, D., et al.: The Kaldi speech recognition toolkit. IEEE 2011 Workshop on Automatic Speech Recognition and Understanding. IEEE Catalog No.: CFP11SRW-USB. Hilton Waikoloa Village, Big Island, Hawaii, US: IEEE Signal Processing Society (Dec 2011)
10. Snyder, D., Garcia-Romero, D., Povey, D., Khudanpur, S.: Deep neural network embeddings for text-independent speaker verification. In: Proc. Interspeech 2017, pp. 999–1003 (2017). https://doi.org/10.21437/Interspeech.2017-620
11. Snyder, D., et al.: Spoken language recognition using X-vectors, pp. 105–111, June 2018. https://doi.org/10.21437/Odyssey.2018-15
12. Snyder, D., et al.: x-Vectors: robust DNN embeddings for speaker recognition, pp. 5329–5333, April 2018. https://doi.org/10.1109/ICASSP.2018.8461375
13. Waibel, A.H., et al.: Phoneme recognition using time-delay neural networks. IEEE Trans. Acoust. Speech Signal Process. **37**, 328–339 (1989)
14. De Roeck, G., Peeters, B., Maeck, J.: Dynamic monitoring of civil engineering structures. In: Computational Methods for Shell and Spatial Structures IASS-IACM 2000 (2000)
15. Soundjay Traffic and Transportation Ambience. https://www.soundjay.com/transportation-ambience-1.html. Accessed 13 May 2020
16. Ghahremani, P., et al.: A pitch extraction algorithm tuned for automatic speech recognition. In: 2014 IEEE International Conference on Acoustics, Speech and Signal Processing (ICASSP), pp. 2494–2498. IEEE, Piscataway (2014)
17. Ioffe, S.: Probabilistic linear discriminant analysis. In: Leonardis, A., Bischof, H., Pinz, A. (eds.) Computer Vision – ECCV 2006, pp. 531–542. Springer, Berlin (2006). ISBN: 978-3-540-33839-0
18. Ghahremani, P., et al.: Investigation of transfer learning for ASR using LF-MMI trained neural networks. In: 2017 IEEE Automatic Speech Recognition and Understanding Workshop (ASRU), pp. 279–286 (2017). https://doi.org/10.1109/ASRU.2017.8268947
19. Ananthram, A., Saravanakumar, K., Huynh, J., Beigi, H.: Multi-modal emotion detection with transfer learning. In: Natural Language, Dialog and Speech Symposium (NDS2020). New York Academy of Science, New York City (2020). https://doi.org/10.13140/RG.2.2.31373.97760
20. Zhou, S., Beigi, H.: A transfer learning method for speech emotion recognition from automatic speech recognition. Recognition Technologies Technical Report No. RTI-2020330-01, March 2020
21. Farrar, C., Cornwell, P., Doebling, S., Prime, M.: Structural health monitoring studies of the Alamosa Canyon and I-40 bridges, July 2000. https://doi.org/10.2172/766805
22. Farrar, C., et al.: Damage identification with linear discriminant operators, July 2003

Equation Discovery Using an Efficient Variational Bayesian Approach with Spike-and-Slab Priors

Rajdip Nayek, Keith Worden, and Elizabeth J. Cross

Abstract A major challenge in the field of nonlinear system identification is the problem of selecting models that are not just good in prediction but also provide insight into the nature of the underlying dynamical system. In this study, a sparse Bayesian equation discovery approach is pursued to address the model selection problem, where it is treated as a Bayesian variable selection problem and solved via sparse linear regression using spike-and-slab priors. The spike-and-slab priors are considered the *gold standard* in Bayesian variable selection; however, Bayesian inference with spike-and-slab priors is not analytically tractable and often Markov chain Monte Carlo techniques are employed, which can be computationally expensive. This study proposes to use a computationally efficient variational Bayes algorithm for facilitating Bayesian equation discovery with spike-and-slab priors. To illustrate its performance, the algorithm has been applied to four systems of engineering interest, which include a baseline linear system, and systems with cubic stiffness, quadratic viscous damping, and Coulomb friction damping. The results of model selection and parameter estimation demonstrate the effectiveness and efficiency of the variational Bayesian inference compared to the conventional Markov-chain-Monte-Carlo-based Bayesian inference.

Keywords Equation discovery · Nonlinear system identification · Spike-and-slab prior · Sparse Bayesian learning · Variational Bayes

1 Introduction

Characterising the behaviour of nonlinear structural dynamical systems plays a key role in shaping the fundamental understanding of the underlying phenomena manifested by such systems. In forward analyses of these systems, generative models are derived from first principles, in the form of governing differential equations of motion, which are then utilised to analyse the behaviour of nonlinear structural dynamical systems and predict the possible future states. These governing differential equations of motion for structural dynamical systems can often be conveniently represented in the state-space form,

$$\dot{\boldsymbol{x}} = \mathcal{M}(\boldsymbol{x}) + \boldsymbol{u} \tag{1}$$

where $\boldsymbol{x}$ is the state vector of system responses, $\dot{\boldsymbol{x}}$ is the time derivative of the state vector, $\boldsymbol{u}$ is the external input force, and $\mathcal{M}(\boldsymbol{x})$ is the generative model embedding the equation of motion of the structure. When dealing with inverse problems, the form of $\mathcal{M}$ is treated as unknown and one is tasked with positing a suitable generative model of $\mathcal{M}$ that best describes the system dynamics, given some measurement data. This task constitutes the problem of model selection in nonlinear structural system identification. One commonly estimates a *black-box* approximation [1, 2] to $\mathcal{M}$, if the goal lies in only predicting the future states, given some past measurements. However, when the goal extends beyond prediction and the user aspires to select *interpretable* models—to understand the physics of the observed phenomenon—there arises a need to uncover the full parametric form of an underlying governing equation of motion.

In the pursuit of interpretable dynamical models, standard model selection procedures postulate a small set of candidate models based on expert intuition and use information-theoretic measures to select a best-fit model [3]. However, such

R. Nayek (✉) · K. Worden · E. J. Cross
Dynamics Research Group, Department of Mechanical Engineering, University of Sheffield, Sheffield, UK
e-mail: r.nayek@sheffield.ac.uk; k.worden@sheffield.ac.uk; e.j.cross@sheffield.ac.uk

Z. Mao (ed.), *Model Validation and Uncertainty Quantification, Volume 3*, Conference Proceedings of the Society for Experimental Mechanics Series, https://doi.org/10.1007/978-3-030-77348-9_19

procedures can become prohibitive when very little expert knowledge is available and the pool of candidate models is large. With the rapid development of data-driven modelling, there has been an emergence of alternative frameworks of model selection for nonlinear dynamical systems that depend more on data and much less on expert knowledge. An early effort in this setting include the data-driven symbolic regression [4, 5] that searches through a library (or *dictionary*) of simple and interpretable functional forms to identify the model structure or the governing equations of a nonlinear dynamical system. While this strategy works well for discovering interpretable physical models, its dependence on evolutionary optimisation for selecting the *relevant* variables from the dictionary makes it computationally expensive and unsuited to large-scale problems. In a more recent study [6], the discovery process was reformulated in terms of sparse linear regression, which makes the variable selection process amenable to solution using efficient sparsity-promoting algorithms, thus providing a computationally cheaper alternative.

This study follows a sparse linear regression approach to equation discovery of nonlinear structural dynamical systems. To describe the approach, consider a Single Degree-of-Freedom (SDOF) oscillator with equation of motion of the form,

$$m\ddot{q} + c\dot{q} + kq + g\left(q, \dot{q}\right) = u \tag{2}$$

where m, c, k are the mass, damping, and stiffness, g is an arbitrary nonlinear function of displacement q and velocity $\dot{q}$, and u is the input forcing function. The first-order state-space formulation for this system is,

$$\dot{x}_1 = x_2 \tag{3}$$

$$\dot{x}_2 = \frac{1}{m}\left(u - kx_1 - cx_2 - g(x_1, x_2)\right) \tag{4}$$

with $x_1 = q$ and $x_2 = \dot{q}$. Equation (3) can be ignored as it simply provides the definition of velocity; Eq. (4) captures the governing equation of the structure's motion. To uncover the underlying structure of the right hand side of equation (4), a dictionary of basis functions is constructed, containing several simple and interpretable functional forms of the system states and the input. The right hand side of equation (4) is then expressed as a weighted linear combination of the basis functions of the dictionary as follows:

$$\dot{x}_2 = \theta_1 f_1(x_1, x_2) + \theta_2 f_2(x_1, x_2) + \cdots + \theta_l f_l(x_1, x_2) + \theta_{l+1} u \tag{5}$$

where, $\{f_1(x_1, x_2), \ldots, f_l(x_1, x_2), u\}$ represent the collection of basis functions/variables and $\{\theta_1, \cdots, \theta_l, \theta_{l+1}\}$ correspond to the set of weights. Given noisy observations of time-series measurements of the system $\left\{x_{1,j}, x_{2,j}, \dot{x}_{2,j}, u_j\right\}_{j=1}^{N}$, where j in the subscript indicates time point t_j, the above problem reduces to a linear regression problem,

$$\underbrace{\begin{bmatrix} \dot{x}_{2,1} \\ \dot{x}_{2,2} \\ \vdots \\ \dot{x}_{2,N} \end{bmatrix}}_{\boldsymbol{y}} = \underbrace{\begin{bmatrix} f_1\left(x_{1,1}, x_{2,1}\right) & f_2\left(x_{1,1}, x_{2,1}\right) & \cdots & f_l\left(x_{1,1}, x_{2,1}\right) & u_1 \\ f_1\left(x_{1,2}, x_{2,2}\right) & f_2\left(x_{1,2}, x_{2,2}\right) & \cdots & f_l\left(x_{1,2}, x_{2,2}\right) & u_2 \\ \vdots & \vdots & \ddots & \vdots & \vdots \\ f_1\left(x_{1,N}, x_{2,N}\right) & f_2\left(x_{1,N}, x_{2,N}\right) & \cdots & f_l\left(x_{1,N}, x_{2,N}\right) & u_N \end{bmatrix}}_{\mathbf{D}} \underbrace{\begin{bmatrix} \theta_1 \\ \theta_2 \\ \vdots \\ \theta_l \\ \theta_{l+1} \end{bmatrix}}_{\boldsymbol{\theta}} + \underbrace{\begin{bmatrix} \epsilon_1 \\ \epsilon_2 \\ \vdots \\ \epsilon_N \end{bmatrix}}_{\boldsymbol{\epsilon}} \tag{6}$$

where, $\boldsymbol{y}$ is the time-series vector of observations of the derivatives of x_2, $\mathbf{D}$ is the dictionary matrix of basis variables, and $\boldsymbol{\epsilon}$ denotes the vector of residuals, taking into account model inadequacies and measurement errors. The task is now to select which basis variables from the dictionary are to be included in the final model. The equation discovery approach followed here assumes that only a few basis variables from the dictionary would actively contribute to the governing dynamics. As such, the solution of $\boldsymbol{\theta}$ would be *sparse*, i.e. would have only a few non-zero weights; hence, it is reasonable to seek sparse solutions of $\boldsymbol{\theta}$ in the above linear regression problem, as illustrated in Fig. 1.

There exists a variety of classical penalisation methods [7] such as lasso, elastic-net, etc. that promote sparsity by adding a penalty term to the ordinary least-squares objective. Another deterministic sparsity-promoting method is the sequential threshold least-squares, which runs a least-squares algorithm iteratively while eliminating the small weights at each iteration. This method underpins the Sparse Identification of Nonlinear Dynamics (SINDy) algorithm—introduced by Brunton et al. [6] in their pioneering work on equation discovery of nonlinear dynamical systems. Nevertheless, the performance of classical penalisation as well as sequential threshold least-squares often critically depends on a regularisation parameter that needs

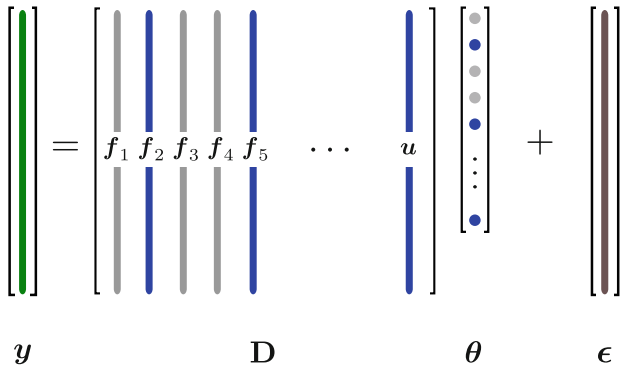

Fig. 1 Sparse linear regression for selection of relevant basis variables (shown in blue)

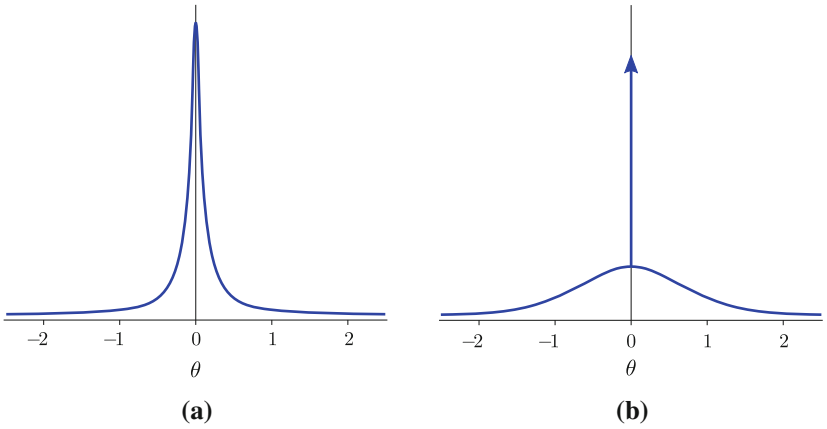

Fig. 2 Probability density functions of (**a**) the Student's-*t* prior, and (**b**) the spike-and-slab prior (with the spike displayed by an arrow pointing upwards)

tuning via cross-validation. A sparse Bayesian framework [8, 9] provides a more appealing alternative in this context; apart from the usual advantage of uncertainty quantification, it offers natural penalisation via sparsity-promoting prior distributions and allows simultaneous estimation of model and regularisation parameters, thereby avoiding the need for cross-validation.

In a Bayesian framework, sparse solutions to Eq. (6) are obtained by placing sparsity-promoting (or *shrinkage*) priors on the unknown weight vector $\boldsymbol{\theta}$. The densities of such priors feature a strong peak at zero and heavy tails: the peak at zero enforces most of the values to be (near) zero while heavy tails allow a few non-zero values. Examples of such priors include Laplace [10], Student's-*t* [8], Horseshoe [11], and spike-and-slab [12]. Previous studies [13, 14] on sparse Bayesian model discovery approaches employed the Relevance Vector Machine (RVM) [15]—a popular implementation of the Student's-*t* prior. Despite its remarkable computational efficiency, an issue with the RVM is that it often results in false discoveries [16]. This issue with the RVM arises due to the use of the Student's-*t* prior, and is undesirable, as false discoveries introduce more complexity and hinder the interpretability of the estimated model.

Compared to a Student's-*t* prior, a spike-and-slab (SS) prior is capable of producing sparser solutions and reducing false discoveries. An SS prior represents a mixture of two distributions—a point mass at zero (the *spike*) for small weights, and a diffused density (the *slab*) for the large weights—and is considered as the gold standard in Bayesian variable selection (BVS) [17]. It is capable of shrinking the small weights to exactly zero; hence, it has the potential to induce a greater degree of sparsity among the weights compared to a Student's-*t* prior. Figure 2 provides a visual depiction of the densities of the Student's-*t* and SS priors.

A disadvantage of the SS prior is that the Bayesian inference can be computationally demanding: the posterior computation with the SS prior is analytically intractable and one typically employs Markov Chain Monte Carlo (MCMC)-based approaches—most commonly Gibbs sampling—to draw samples from the posterior distribution. Employing a Gibbs sampler, it was shown that equation discovery with SS priors lends to more interpretable models [18] compared to the RVM, although the runtime of the Gibbs sampler could be prohibitive for large systems. A faster alternative to MCMC-based approaches is to use a variational Bayesian approach. A few studies [19, 20] have previously proposed Variational Bayes

(VB) algorithms with SS priors to reduce the computational burden in BVS. The implementation in [19] assumed complete independence of the variational distributions of the model parameters, and it led to severe underestimation of the posterior covariance of the model parameters. On the other hand, [20] relaxed the independence assumption to a greater extent and was able to better control the underestimation of posterior covariance.

This paper presents a novel application of VB to Bayesian equation discovery of dynamical systems with SS priors. A VB algorithm is derived for posterior inference with SS priors, and its performance has been compared with an MCMC-based sampling approach. Furthermore, the efficiency of the proposed approach has been compared with two other algorithms: (a) RVM (that uses a Student's-t prior) and (b) the deterministic SINDy algorithm [6]. The rest of the paper is structured as follows: Sect. 2 describes the SS prior model for linear regression, followed by Sect. 3 describing the variational Bayesian approach for BVS. Section 4 presents numerical demonstrations of equation discovery for four SDOF oscillators: a linear oscillator, a Duffing oscillator with cubic nonlinearity, an oscillator with quadratic viscous damping, and one with Coulomb damping. Finally, Sect. 5 summarises the conclusions of the paper.

2 Linear Regression Model with Spike-and-Slab Prior

Consider once again the linear regression problem in Eq. (6), rewritten here in a compact matrix-vector form,

$$\boldsymbol{y} = \mathbf{D}\boldsymbol{\theta} + \boldsymbol{\epsilon} \tag{7}$$

where, $\boldsymbol{y}$ is a $N \times 1$ vector of state derivatives (also referred to as the target vector), $\mathbf{D}$ is a $N \times P$ dictionary matrix,[1] $\boldsymbol{\theta}$ is the $P \times 1$ weight vector, and $\boldsymbol{\epsilon}$ is the $N \times 1$ residual error vector. The residual error $\boldsymbol{\epsilon}$ is modelled as a vector of independent Gaussian noise with diagonal covariance matrix $\sigma^2\mathbf{I}_N$ $\left(\boldsymbol{\epsilon} \sim \mathcal{N}\left(\mathbf{0}, \sigma^2\mathbf{I}_N\right)\right)$. With a known dictionary $\mathbf{D}$, the likelihood function can be written as,

$$\boldsymbol{y} \mid \boldsymbol{\theta}, \sigma^2 \sim \mathcal{N}\left(\mathbf{D}\boldsymbol{\theta}, \sigma^2\mathbf{I}_N\right) \tag{8}$$

To perform BVS with the SS prior, the linear regression problem is considered as part of a hierarchical model. The key feature of the hierarchical model is that each component of $\boldsymbol{\theta}$ is assigned an independent SS prior, defined as follows:

$$\theta_i \mid z_i, v_s \sim (1 - z_i)\delta(\theta_i) + z_i\mathcal{N}\left(0, \sigma^2 v_s\right) \tag{9}$$

The spike part of the prior is modelled by a Dirac delta function at zero [12], while the slab part is modelled by a continuous zero-mean Gaussian density with a variance $\sigma^2 v_s$. Here v_s is the slab variance and it is multiplied with σ^2 so that the prior naturally scales with the scale of the outcome, that is, the results would not depend on the measurement units of $\boldsymbol{y}$. Whether a weight θ_i belongs to the spike or the slab is determined by an indicator variable z_i: $z_i = 0$ implies $\theta_i = 0$, and $z_i = 1$ implies $\theta_i \sim \mathcal{N}(0, v_s)$. In other words, $z_i = 0$ or $z_i = 1$ determines the inclusion or exclusion of the ith basis variable in the model. Furthermore, each indicator variable z_i is assigned an independent Bernoulli prior, controlled by a common parameter p_0,

$$z_i \mid p_0 \sim \text{Bern}(p_0) \tag{10}$$

Equation (10) implies that the selection of a basis variable is independent of the inclusion of any other basis variables from the dictionary $\mathbf{D}$. The parameter $p_0 \in (0, 1)$ represents the probability of $z_i = 1$ and controls the degree of sparsity imposed by the SS prior. Together, the weight vector $\boldsymbol{\theta}$ and the vector of indicator variables $\boldsymbol{z}$ constitute the main parameters of the SS prior model for linear regression. Finally, inverse-Gamma priors are assigned to the error variance σ^2,

$$\sigma^2 \sim \mathcal{IG}(a_\sigma, b_\sigma) \tag{11}$$

Note that v_s, p_0, a_σ, b_σ appearing in Eqs. (9)–(11) are treated as deterministic parameters, controlling the shape of the respective priors. The hierarchical SS model for linear regression is illustrated in Fig. 3.

[1] Note the number of columns in the dictionary has been redefined as $P = l + 1$.

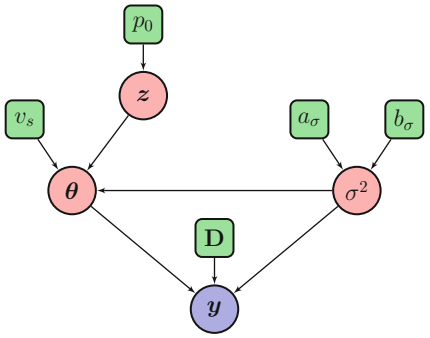

Fig. 3 Graphical structure of the hierarchical spike-and-slab model for linear regression; the variables in circles represent random variables, while those in squares represent deterministic parameters

3 Variational Bayesian Inference for Variable Selection

The information required for BVS using the SS prior is derived from the joint posterior distribution of the model parameters $p\left(\boldsymbol{\theta}, z, \sigma^2 \mid \boldsymbol{y}\right)$, which can be computed using Bayes' rule in the form,

$$p\left(\boldsymbol{\theta}, z, \sigma^2 \mid \boldsymbol{y}\right) = \frac{p\left(\boldsymbol{y} \mid \boldsymbol{\theta}, \sigma^2\right) p\left(\boldsymbol{\theta} \mid z, \sigma^2\right) p\left(z\right) p\left(\sigma^2\right)}{p\left(\boldsymbol{y}\right)} \tag{12}$$

Here $p\left(\boldsymbol{y} \mid \boldsymbol{\theta}, \sigma^2\right)$ is the likelihood, $p\left(\boldsymbol{\theta} \mid z, \sigma^2\right) p\left(z\right)$ is the SS prior over z and $\boldsymbol{\theta}$, $p\left(\sigma^2\right)$ is the prior over measurement noise variance, and $p\left(\boldsymbol{y}\right)$ is the normalising constant. Unfortunately, the posterior in Eq. (12) cannot be computed analytically, and using MCMC-based sampling methods can be computationally expensive. Therefore, in this section, a VB methodology is pursued for approximating the joint posterior distribution $p\left(\boldsymbol{\theta}, z, \sigma^2 \mid \boldsymbol{y}\right)$ by a simpler distribution. However, the presence of the Dirac delta function in the SS prior makes the derivation of the VB algorithm difficult, and hence the linear regression model with SS prior is reparameterised in a form that is more amenable to VB inference methods. Specifically, the form of the SS prior is rewritten as [20],

$$\begin{aligned} &\boldsymbol{y} \mid \boldsymbol{\theta}, z, \sigma^2 \sim \mathcal{N}\left(\mathbf{D}\boldsymbol{\Gamma}\boldsymbol{\theta}, \sigma^2 \mathbf{I}_N\right), \quad \sigma^2 \sim \mathcal{IG}\left(a_\sigma, b_\sigma\right), \\ &\theta_i \sim \mathcal{N}\left(0, \sigma^2 v_s\right), \quad \text{and} \quad z_i \sim \text{Bern}(p_0), \; i = 1, \ldots, P \end{aligned} \tag{13}$$

where the newly introduced term represents $\boldsymbol{\Gamma} = \text{diag}\left(z_1, \ldots, z_P\right)$.

3.1 Variational Bayes

In VB inference, a factorised distribution $q(\boldsymbol{\theta}, z, \sigma^2)$ is chosen from a predetermined family of simple distributions $\mathcal{Q}$ and then the distributional parameters are optimised such that the Kullback–Leibler (KL) divergence between the true posterior $p\left(\boldsymbol{\theta}, z, \sigma^2 \mid \boldsymbol{y}\right)$ and the optimised variational approximation $q^*(\boldsymbol{\theta}, z, \sigma^2)$ is a minimum. Put formally,

$$q^*(\boldsymbol{\theta}, z, \sigma^2) = \underset{q \in Q}{\arg\min}\, \text{KL}\Big[q(\boldsymbol{\theta}, z, \sigma^2) \,||\, p\left(\boldsymbol{\theta}, z, \sigma^2 \mid \boldsymbol{y}\right)\Big] = \underset{q \in Q}{\arg\min}\, \mathbb{E}_{q(\boldsymbol{\theta}, z, \sigma^2)}\left[\ln\left(\frac{q(\boldsymbol{\theta}, z, \sigma^2)}{p\left(\boldsymbol{\theta}, z, \sigma^2 \mid \boldsymbol{y}\right)}\right)\right] \tag{14}$$

where $\mathbb{E}_{q(\boldsymbol{\theta}, z, \sigma^2)}\left[\cdot\right]$ denotes the expectation with respect to the variational distribution $q(\boldsymbol{\theta}, z, \sigma^2)$. The expansion of the KL divergence term in Eq. (14) leads to an expression for the evidence lower bound (ELBO), which plays a key role in assessing the convergence of VB methods.

$$\text{KL}\Big[q(\boldsymbol{\theta}, z, \sigma^2) \,||\, p\left(\boldsymbol{\theta}, z, \sigma^2 \mid \boldsymbol{y}\right)\Big] = \mathbb{E}_{q(\boldsymbol{\theta}, z, \sigma^2)}\left[\ln\left(\frac{q(\boldsymbol{\theta}, z, \sigma^2)}{p\left(\boldsymbol{\theta}, z, \sigma^2 \mid \boldsymbol{y}\right)}\right)\right]$$

$$
\begin{aligned}
&= \mathbb{E}_{q(\boldsymbol{\theta},z,\sigma^2)}\left[\ln q\left(\boldsymbol{\theta},z,\sigma^2\right)\right] \\
&\quad - \mathbb{E}_{q(\boldsymbol{\theta},z,\sigma^2)}\left[\ln\left(p\left(\boldsymbol{y}\mid\boldsymbol{\theta},z,\sigma^2\right)p\left(\boldsymbol{\theta},z,\sigma^2\right)\right)\right] + \ln p\left(\boldsymbol{y}\right) \\
&= \mathbb{E}_{q(\boldsymbol{\theta},z,\sigma^2)}\left[\ln\left(\frac{q\left(\boldsymbol{\theta},z,\sigma^2\right)}{p\left(\boldsymbol{\theta},z,\sigma^2\right)}\right)\right] - \mathbb{E}_{q(\boldsymbol{\theta},z,\sigma^2)}\left[\ln p\left(\boldsymbol{y}\mid\boldsymbol{\theta},z,\sigma^2\right)\right] + \ln p\left(\boldsymbol{y}\right) \\
&= \underbrace{\mathrm{KL}\left[q\left(\boldsymbol{\theta},z,\sigma^2\right)\mid\mid p\left(\boldsymbol{\theta},z,\sigma^2\right)\right] - \mathbb{E}_{q(\boldsymbol{\theta},z,\sigma^2)}\left[\ln p\left(\boldsymbol{y}\mid\boldsymbol{\theta},z,\sigma^2\right)\right]}_{-\mathrm{ELBO}} + \ln p\left(\boldsymbol{y}\right) \\
&= \ln p\left(\boldsymbol{y}\right) - \mathrm{ELBO} \geq 0
\end{aligned} \tag{15}
$$

Since the KL divergence is non-negative and $\ln p\left(\boldsymbol{y}\right)$ is constant with respect to the variational distribution $q(\boldsymbol{\theta},z,\sigma^2)$, the ELBO can be seen as the lower bound to $\ln p\left(\boldsymbol{y}\right)$, and hence, minimising $\mathrm{KL}\left[q\left(\boldsymbol{\theta},z,\sigma^2\right)\mid\mid p\left(\boldsymbol{\theta},z,\sigma^2\mid\boldsymbol{y}\right)\right]$ is equivalent to maximising the ELBO, thus,

$$
q^*(\boldsymbol{\theta},z,\sigma^2) = \underset{q\in Q}{\arg\max}\ \underbrace{\mathbb{E}_{q(\boldsymbol{\theta},z,\sigma^2)}\left[\ln p\left(\boldsymbol{y}\mid\boldsymbol{\theta},z,\sigma^2\right)\right] - \mathrm{KL}\left[q\left(\boldsymbol{\theta},z,\sigma^2\right)\mid\mid p\left(\boldsymbol{\theta},z,\sigma^2\right)\right]}_{\mathrm{ELBO}} \tag{16}
$$

In this study, $q(\boldsymbol{\theta},z,\sigma^2)$ has been chosen to have the following factorised form [20]:

$$
q\left(\boldsymbol{\theta},z,\sigma^2\right) = q\left(\boldsymbol{\theta}\right)q\left(\sigma^2\right)\prod_{i=1}^{P} q\left(z_i\right) \tag{17}
$$

and the corresponding individual variational distributions are selected as,

$$
\begin{aligned}
q\left(\boldsymbol{\theta}\right) &= \mathcal{N}\left(\boldsymbol{\mu}^q,\boldsymbol{\Sigma}^q\right), \\
q\left(\sigma^2\right) &= \mathcal{IG}\left(a_\sigma^q,b_\sigma^q\right), \\
q\left(z_i\right) &= \mathrm{Bern}\left(w_i^q\right), \text{ for } i=1,\ldots,P
\end{aligned} \tag{18}
$$

Here, $\left\{\boldsymbol{\mu}^q,\boldsymbol{\Sigma}^q,a_\sigma^q,b_\sigma^q,w_i^q\right\}$ represents a set of deterministic variational parameters whose values need to be optimised to draw the approximate variational distribution closer to the true posterior distribution, in the sense of KL divergence (see Eq. (14)). The optimal choice of the set of variational parameters that maximise the ELBO in Eq. (16) satisfies the following relations [21, 22]:

$$
\begin{aligned}
q^*(\boldsymbol{\theta}) &\propto \mathbb{E}_{q(z)q(\sigma^2)}\left[\ln p\left(\boldsymbol{y},\boldsymbol{\theta},z,\sigma^2\right)\right] \\
q^*(z) &\propto \mathbb{E}_{q(\boldsymbol{\theta})q(\sigma^2)}\left[\ln p\left(\boldsymbol{y},\boldsymbol{\theta},z,\sigma^2\right)\right] \\
q^*(\sigma^2) &\propto \mathbb{E}_{q(\boldsymbol{\theta})q(z)}\left[\ln p\left(\boldsymbol{y},\boldsymbol{\theta},z,\sigma^2\right)\right]
\end{aligned} \tag{19}
$$

and on solving the above, the expression for the variational parameters can be obtained as

$$
\boldsymbol{\Sigma}^q = \left[\tau\left(\left(\mathbf{D}^T\mathbf{D}\right)\odot\boldsymbol{\Omega} + v_s^{-1}\mathbf{I}_P\right)\right]^{-1}, \tag{20}
$$

$$
\boldsymbol{\mu}^q = \tau\boldsymbol{\Sigma}^q\mathbf{W}^q\mathbf{D}^T\boldsymbol{y}, \tag{21}
$$

$$
a_\sigma^q = a_\sigma + 0.5N + 0.5P, \tag{22}
$$

$$
b_\sigma^q = b_\sigma + 0.5\left[\boldsymbol{y}^T\boldsymbol{y} - 2\boldsymbol{y}^T\mathbf{D}\mathbf{W}^q\boldsymbol{\mu}^q + \mathrm{tr}\left\{\left(\left(\mathbf{D}^T\mathbf{D}\right)\odot\boldsymbol{\Omega} + v_s^{-1}\mathbf{I}_P\right)\left(\boldsymbol{\mu}^q\boldsymbol{\mu}^{q\,T} + \boldsymbol{\Sigma}^q\right)\right\}\right], \tag{23}
$$

$$\tau = a_\sigma^q / b_\sigma^q, \tag{24}$$

$$\eta_i = \text{logit}(p_0) - 0.5\tau \left((\mu_i^q)^2 + \Sigma_{i,i}^q \right) \boldsymbol{f}_i^T \boldsymbol{f}_i + \tau \boldsymbol{f}_i^T \left[\boldsymbol{y} \mu_i^q - \mathbf{D}_{-i} \mathbf{W}_{-i}^q \left(\boldsymbol{\mu}_{-i}^q \mu_i^q + \boldsymbol{\Sigma}_{-i,i}^q \right) \right], \tag{25}$$

$$w_i^q = \text{expit}(\eta_i) \tag{26}$$

In the above expressions, $\text{logit}(A) = \ln(A) - \ln(1 - A)$, $\text{expit}(A) = \text{logit}^{-1}(A) = \exp(A)/(1 + \exp(A))$, $\boldsymbol{w}^q = \left[w_1^q, \ldots, w_P^q \right]^T$, $\mathbf{W}^q = \text{diag}(\boldsymbol{w}^q)$, $\boldsymbol{\Omega} = \boldsymbol{w}^q \boldsymbol{w}^{q\,T} + \mathbf{W}^q (\mathbf{I}_P - \mathbf{W}^q)$, and the symbol $\odot$ denotes the element-wise product between two matrices. Additionally, $\boldsymbol{f}_i$ denotes the ith column of $\mathbf{D}$, and $\mathbf{D}_{-i}$ represents the dictionary matrix with the ith column removed. As the variational parameters do not have explicit solutions and their update expressions are dependent upon each other, an iterative coordinate-wise updating procedure is followed for optimising them, in which they are first initialised and then cyclically updated conditional on the updates of other parameters.

3.2 Initialisation and Convergence

To implement the VB algorithm, one needs to set the values of the prior parameters $\{v_s, p_0, a_\sigma, b_\sigma\}$ and initialise the variational parameters $\{\boldsymbol{w}^q, \tau\}$. The prior parameters are set as follows: a slab variance $v_s = 10$, noise prior parameters $a_\sigma = 10^{-4}$, $b_\sigma = 10^{-4}$, and a small probability $p_0 = 0.1$ to favour the selection of simpler models. The VB algorithm is found to be quite sensitive to the initial choice of the variational parameter $\boldsymbol{w}^q$ which represents the vector of inclusion probabilities of the basis variables. To provide a good initial guess, a grid-search procedure was suggested in [20]; however, such an initialisation procedure is time-consuming and deemed inconvenient here. In this work, $\boldsymbol{w}^q$ is initialised by setting it to the model diagnostic parameter vector $\boldsymbol{\gamma}$ output by the RVM algorithm. The RVM diagnostic parameter, $\gamma_i \in (0, 1)$, can be interpreted as a probabilistic measure of how important the ith basis variable is in explaining the target vector $\boldsymbol{y}$ [8]; as such, it relates well with the idea of variable inclusion probabilities. Moreover, a RVM run is cheap, and therefore getting a good initial point for $\boldsymbol{w}^{(0)}$ takes very little time. Lastly, the initial value of τ, which represents the expected precision of the noise σ^2, is set to $\tau^{(0)} = 1000$.

The VB algorithm iteratively and monotonically maximises the ELBO and converges to a local maximum of the bound. Starting with the initial variational parameters, the VB iterations are continued until the relative increase in the ELBO between two successive VB iterations is very small, that is, when

$$\text{ELBO}^{(t)} - \text{ELBO}^{(t-1)} < \rho \tag{27}$$

the iterations are terminated. Here, $\rho = 10^{-6}$ is considered. The value of ELBO, at each iteration t, is computed using the simplified expression:

$$\begin{aligned} \text{ELBO}^{(t)} = {} & 0.5P - 0.5N \ln(2\pi) - 0.5P \ln(v_s) + a_\sigma \ln(b_\sigma) - \ln \Gamma(a_\sigma) + \ln \Gamma(a_\sigma^{(t)}) - a_\sigma^{(t)} \ln \Gamma(b_\sigma^{(t)}) \\ & + 0.5 \ln|\boldsymbol{\Sigma}^{(t)}| + \sum_{i=1}^{P} \left[w_i^{(t)} \ln \left(\frac{p_0}{w_i^{(t)}} \right) + (1 - w_i^{(t)}) \ln \left(\frac{1 - p_0}{1 - w_i^{(t)}} \right) \right] \end{aligned} \tag{28}$$

where $\Gamma(\cdot)$ is the Gamma function, and $a_\sigma^{(t)}$, $b_\sigma^{(t)}$, $\boldsymbol{\mu}^{(t)}$, $\boldsymbol{\Sigma}^{(t)}$, $\boldsymbol{w}^{(t)}$ denote the variational parameters at the tth iteration, dropping the 'q' superscript. Upon convergence, the variational parameters from the final step are denoted by a_σ^*, b_σ^*, $\boldsymbol{\mu}^*$, $\boldsymbol{\Sigma}^*$, $\boldsymbol{w}^*$.

3.3 Bayesian Variable Selection

With a total of P basis variables in the dictionary, there are 2^P possible models, where a model is indexed by which of the z_is equal one and which equal zero. For example, the model with zero basis variables has $\boldsymbol{z} = \mathbf{0}$, whereas the model that includes all basis variables has $\boldsymbol{z} = \mathbf{1}$. The *relevant* basis variables to be included in the final model are selected based on the marginal *posterior inclusion probabilities* (PIP), $p(z_i = 1 \mid \boldsymbol{y})$. Specifically, the basis variables whose corresponding PIPs

are greater than half, i.e. $p\left(z_i = 1 \mid \boldsymbol{y}\right) > 0.5,\ i = 1, \ldots, P$, are included in the final estimated model. The corresponding model is popularly known as the median probability model and is considered optimal for prediction [23]. In VB inference, the estimated w_i^*s can be interpreted as an approximation to the posterior probability of $p\left(z_i = 1 \mid \boldsymbol{y}\right)$. Therefore, post inference, the set of basis variables which correspond to $w_i^* > 0.5$ are included in the estimated model. Furthermore, the estimated mean and covariance of the vector of weights $\boldsymbol{\theta}$, denoted by $\hat{\boldsymbol{\mu}}_{\boldsymbol{\theta}}$ and $\hat{\boldsymbol{\Sigma}}_{\boldsymbol{\theta}}$, are respectively populated with values of $\boldsymbol{\mu}^*$ and $\boldsymbol{\Sigma}^*$ at the indices corresponding to the selected set of basis variables, and the rest of the entries of $\hat{\boldsymbol{\mu}}_{\boldsymbol{\theta}}$ and $\hat{\boldsymbol{\Sigma}}_{\boldsymbol{\theta}}$ are set to zero. Thereafter, predictions with the estimated model can be made using the mean and the covariance of the weights, as shown below,

$$\boldsymbol{\mu}_{\boldsymbol{y}^*} = \mathbf{D}^* \hat{\boldsymbol{\mu}}_{\boldsymbol{\theta}} \tag{29}$$

$$\mathbf{V}_{\boldsymbol{y}^*} = \mathbf{D}^* \hat{\boldsymbol{\Sigma}}_{\boldsymbol{\theta}} \mathbf{D}^{*T} + \left(a_\sigma^*/b_\sigma^*\right)^{-1} \mathbf{I}_{N^*} \tag{30}$$

where $\mathbf{D}^*$ is the $N^* \times P$ test dictionary, defined at a set of N^* previously unseen test data points, $\boldsymbol{\mu}_{\boldsymbol{y}^*}$ is the $N^* \times 1$ predicted mean of the target vector, and $\mathbf{V}_{\boldsymbol{y}^*}$ is the predicted covariance associated with the target vector.

4 Numerical Studies

This section presents numerical studies for exploring the performance of the SS-prior-based VB inference for model/equation discovery. Four SDOF oscillators of the form expressed by Eq. (4) are considered, each having different forms of the nonlinear term $g(x_1, x_2)$, as enumerated in Table 1.

The four systems are simulated using the following parameters:

- The parameters of the linear system are taken as: $m = 1$, $c = 2$, and $k = 10^3$.
- The three other nonlinear systems use the same values of parameters for the underlying linear part and only differ in the additional nonlinear term $g(x_1, x_2)$. The respective forms and the values of $g(x_1, x_2)$ are provided in Table 1.
- The systems are excited using a band-limited Gaussian excitation with standard deviation of 50 and passband of 0 to 100 Hz.
- The displacement x_1 and velocity x_2 for each system are simulated using a fixed-step fourth-order Runge–Kutta numerical integration scheme, with a sampling rate of 1 kHz.
- The acceleration $\dot{x}_2$ is obtained using Eq. (4).

Noisy observations of the displacement x_1, the velocity x_2, the acceleration $\dot{x}_2$, and the input force u are assumed, and the noise is modelled as sequences of zero-mean Gaussian white noise with a standard deviation equal to 5% of the standard deviation of the simulated quantities.

The equation discovery approach commences with a dictionary of candidate basis variables. In this work, the dictionary $\mathbf{D}$ is composed of 36 basis variables, where each basis variable represents a certain function of the noisy measurements x_1, x_2,

$$\mathbf{D} = \left\{ P^1(\boldsymbol{x}), \ldots, P^6(\boldsymbol{x}), \operatorname{sgn}(\boldsymbol{x}), |\boldsymbol{x}|, \boldsymbol{x} \otimes |\boldsymbol{x}|, u \right\} \tag{31}$$

where, $P^\gamma(\boldsymbol{x})$ denotes the polynomial expansion of order γ of the sum of state vectors $(x_1 + x_2)^\gamma$. The dictionary consists of basis variables that are terms from polynomial orders up to $\gamma = 6$ and certain other terms. The term $\operatorname{sgn}(\boldsymbol{x})$ represents the signum functions of states, i.e., $\operatorname{sgn}(x_1)$ and $\operatorname{sgn}(x_2)$. Similarly, $|\boldsymbol{x}|$ denotes the absolute functions of states, i.e., $|x_1|$ and $|x_2|$. The tensor product term $\boldsymbol{x} \otimes |\boldsymbol{x}|$ represents the following set of functions: $x_1|x_1|$, $x_1|x_2|$, $x_2|x_1|$, and $x_2|x_2|$. Finally, the measured input force u is included directly in the dictionary. Note that the total number of models that can be formed by

Table 1 Simulation cases

System	Name	$g(x_1, x_2)$	
1	Linear	0	
2	Duffing	$k_3 x_1^3$	$k_3 = 10^5$
3	Quadratic viscous damping	$c_2 x_2 \lvert x_2 \rvert$	$c_2 = 2$
4	Coulomb friction damping	$c_F \operatorname{sgn}(x_2)$	$c_F = 1$

combinatorial selection of all 36 basis variables in the dictionary is 2^{36}, and it grows exponentially as the number of basis variables increases.

The constructed dictionary in Eq. (31) is often ill-conditioned, due to a combined effect of large-scale difference among the basis variables and the presence of strong linear correlation between certain basis variables. Appropriate scaling of the columns (i.e. the basis variables) helps to reduce the difference in scales and improve the conditioning of the dictionary. For the purpose of Bayesian inference, the columns of the training dictionary are standardised (i.e. they are centred and scaled to have zero mean and unit standard deviation) and the training target vector is detrended to have zero mean. Formally put, the transformed pair of dictionary and the target vector $\left(\mathbf{D}_s, \boldsymbol{y}_s\right)$ input to the Bayesian inference algorithm in the training phase has the form,

$$\begin{aligned} \mathbf{D}^s &= \left(\mathbf{D} - \mathbf{1}\boldsymbol{\mu}_{\mathbf{D}}\right) \boldsymbol{S}_{\mathbf{D}}^{-1} \\ \boldsymbol{y}^s &= \boldsymbol{y} - \mathbf{1}\mu_{\boldsymbol{y}} \end{aligned} \tag{32}$$

where, $\mathbf{1}$ denotes a column vector of ones, $\boldsymbol{\mu}_{\mathbf{D}}$ is a row vector of the column-wise means of $\mathbf{D}$, $\boldsymbol{S}_{\mathbf{D}}$ is a diagonal matrix of the column-wise standard deviations of $\mathbf{D}$, and $\mu_{\boldsymbol{y}}$ is the mean of the target training vector $\boldsymbol{y}$. Note that this modification implies that, post Bayesian inference, the estimated mean and covariance of the scaled weights $\boldsymbol{\theta}^s$, denoted by $\hat{\boldsymbol{\mu}}_{\boldsymbol{\theta}^s}$ and $\hat{\boldsymbol{\Sigma}}_{\boldsymbol{\theta}^s}$, have to be transformed back to the original space using the relations: $\hat{\boldsymbol{\mu}}_{\boldsymbol{\theta}} = \boldsymbol{S}_{\mathbf{D}}^{-1}\hat{\boldsymbol{\mu}}_{\boldsymbol{\theta}^s}$ and $\hat{\boldsymbol{\Sigma}}_{\boldsymbol{\theta}} = \boldsymbol{S}_{\mathbf{D}}^{-1}\hat{\boldsymbol{\Sigma}}_{\boldsymbol{\theta}^s}\boldsymbol{S}_{\mathbf{D}}^{-1}$.

As the VB methodology is based on approximating the posterior, it is worthwhile to compare the results of the VB inference to that of the MCMC-based Bayesian inference that can yield arbitrarily accurate posteriors. In this study, the MCMC-based Bayesian inference is conducted with a Gibbs sampler, with sampling steps as follows:

$$\begin{aligned} \boldsymbol{\theta}_r \mid \boldsymbol{y}, \sigma^2 &\sim \mathcal{N}\left(\boldsymbol{a}_r, \sigma^2\mathbf{A}_r\right), \text{with } \mathbf{A}_r = \left(\mathbf{D}_r^T\mathbf{D}_r + v_s^{-1}\mathbf{I}_r\right)^{-1}, \quad \boldsymbol{a}_r = \mathbf{A}_r\mathbf{D}_r^T\boldsymbol{y} \\ \sigma^2 \mid \boldsymbol{y}, \boldsymbol{\theta}_z &\sim \mathcal{IG}\left(a_\sigma + 0.5N, \quad b_\sigma + 0.5\left(\boldsymbol{y}^T\boldsymbol{y} - \boldsymbol{a}_r^T\mathbf{A}_r^{-1}\boldsymbol{a}_r\right)\right) \\ z_i \mid \boldsymbol{y} &\sim \text{Bern}(\xi_i), \text{with } \xi_i = \frac{p_0}{p_0 + R_i(1-p_0)}, \quad R_i = \frac{p\left(\boldsymbol{y} \mid z_i = 0, \boldsymbol{z}_{-i}\right)}{p\left(\boldsymbol{y} \mid z_i = 1, \boldsymbol{z}_{-i}\right)}, \quad i = 1, \ldots, P \end{aligned} \tag{33}$$

where $\boldsymbol{\theta}_r$ is a $r \times 1$ vector consisting of components of $\boldsymbol{\theta}$ which belong to the slab (i.e. corresponding to $z_i = 1$), $\mathbf{D}_r$ is a $N \times r$ matrix that includes only those columns of $\mathbf{D}$ whose corresponding components of $\boldsymbol{z}$ are unity, and the calculation of R_i uses the marginal likelihood of $\boldsymbol{y}$ given $\boldsymbol{z}$

$$p\left(\boldsymbol{y} \mid \boldsymbol{z}\right) = \frac{\Gamma(a_\sigma + 0.5N)}{(2\pi)^{N/2}(v_s)^{r/2}} \frac{(b_\sigma)^{a_\sigma}}{\Gamma(a_\sigma)} \frac{\left|\left(\mathbf{D}_r^T\mathbf{D}_r + v_s^{-1}\mathbf{I}_r\right)^{-1}\right|^{1/2}}{\left(b_\sigma + 0.5\boldsymbol{y}^T\left(\mathbf{I}_N - \mathbf{D}_r\left(\mathbf{D}_r^T\mathbf{D}_r + v_s^{-1}\mathbf{I}_r\right)^{-1}\mathbf{D}_z^T\right)\boldsymbol{y}\right)^{(a_\sigma + 0.5N)}} \tag{34}$$

The Gibbs sampler is run with four chains, each chain having a total of 5000 samples and the first 1000 samples are discarded as burn-in. The following values were set for the deterministic prior parameters: $a_\sigma = 10^{-4}$, $b_\sigma = 10^{-4}$, $p_0 = 0.1$, and $v_s = 10$. The measurement noise variance $\sigma^{2^{(0)}}$ for each chain was initialised with slightly perturbed values about a nominal mean value—set equal to the residual variance from an ordinary least-squares regression. To facilitate faster convergence of the Gibbs sampler to a good solution, the initial vector of binary latent variables $\boldsymbol{z}^{(0)}$ was computed by starting off with $z_1, \ldots, z_P$ set to zero and then activating the components of $\boldsymbol{z}$ that reduce the mean-squared error on the training target vector, until an integer number ($\approx p_0 P$) of components of $\boldsymbol{z}$ is equal to one. The multivariate potential scale reduction factor $\hat{R}$ [24], which estimates the potential decrease in the between-chain variance with respect to the within-chain variance, was applied to assess the convergence of the generated samples of $\boldsymbol{\theta}$. A value of $\hat{R} < 1.1$ was adopted to decide if convergence had been reached.

Figure 4 demonstrates the procedure of basis variable selection applied to the four SDOF oscillator systems using PIP. In the case of MCMC, the PIP is calculated for the ith basis variable by averaging over the posterior samples of z_i, $i = 1, \ldots, 36$. For VB, the PIP for the ith basis variable is approximated by w_i^*. Basis variables with higher values of PIP imply greater relevance, and as mentioned in Sect. 3.3, only those basis variables are selected whose PIPs are greater than 0.5 (shown by a dotted line in red). It can be seen that the estimated models for all the four systems are able to select the true basis variables out of the pool of 36 basis variables. In all cases, the computed PIPs corresponding to the true basis variables are close to one, which indicates very strong selection probability; however, that may not always be the case. For example, in

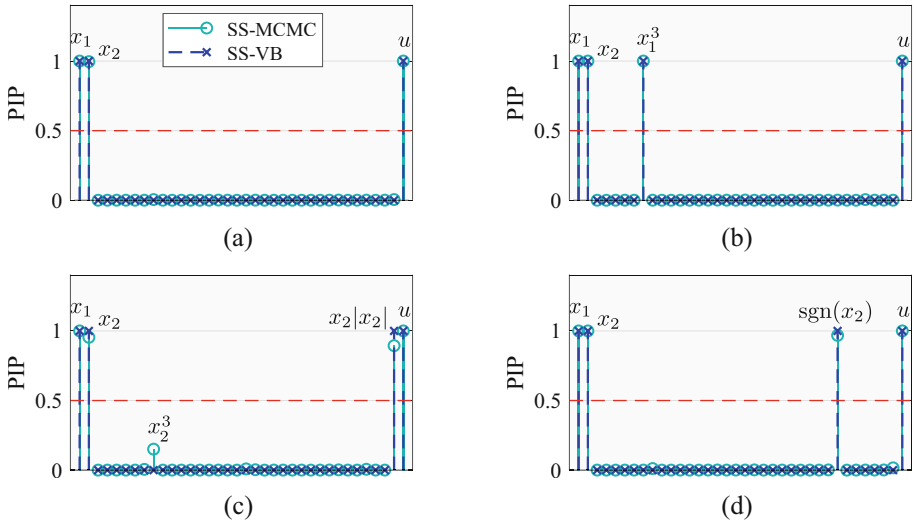

Fig. 4 Illustration of Bayesian variable selection using posterior inclusion probability (PIP), computed by $p\,(z_i = 1 \mid \boldsymbol{y})$ in case of MCMC (SS-MCMC) and approximated by w_i^* in case of VB (SS-VB). (**a**) Linear. (**b**) Duffing. (**c**) Viscous damping. (**d**) Friction damping

the quadratic viscous damping case (see Fig. 4c), the SS-MCMC algorithm selects the true basis variable $x_2|x_2|$ with a PIP of 0.9, while it discards a correlated basis function x_2^3 with a PIP of 0.15. Such situations can arise when there exist strong correlations between certain basis variables, causing the Bayesian algorithm to get confused as to which among the set of correlated basis variables should be selected.

For the sake of comparison, Fig. 5 plots the pairwise joint posteriors of the model parameters obtained from MCMC samples and those obtained from VB (using means and 95% confidence ellipses). Posteriors using SS priors often tend to be multimodal, as is demonstrated by the scatterplots from MCMC samples. Since VB uses a single approximating distribution, it is impossible to capture the multiple modes of the true posterior. Instead, VB methods approximate the true posterior around its maximum *a posteriori* (MAP) estimate. This feature is clearly indicated in the above plots where the mean of the VB distribution (labelled by $\times$) is found to coincide with the MCMC MAP estimate (depicted by the regions where the MCMC samples are most concentrated). Alongside the VB means, 95% confidence ellipses—representing the joint 95% confidence bounds—of the model parameters are also plotted (shown by yellow lines). It is noted that the 95% confidence ellipses from VB are always smaller than the support of posterior samples from MCMC, which signify the underestimation of posterior covariances from VB—a well known issue with VB methods [25].

4.1 Performance Comparison Using Monte Carlo Simulations

In this section, Monte Carlo simulations are used to compare the performance of equation discovery by the VB algorithm with that of MCMC. In addition, results from the popular sparse Bayesian RVM algorithm [8] and the deterministic SINDy algorithm [6] are also included for comparison. The RVM is implemented following the algorithm outlined in [15]. As mentioned in Sect. 1, SINDy implements a sequential threshold least-squares to promote sparsity and requires selection of the value of a regularisation parameter via cross-validation. A naive sweep over a sequence of regularisation parameter values was performed, and a value was selected for which the corresponding test set prediction error was a minimum.

Thousand different realisations for each of the four systems, as summarised in Table 1, were considered. The realisations were created by introducing random perturbations of 0.1κ to the nominal values of the parameters c, k, k_3, c_2, c_F, such that the new realisations have parameters $\bar{c} = (1 + 0.1\kappa)c$, $\bar{k} = (1 + 0.1\kappa)k$, and so on. The variable κ was sampled from a standard Gaussian distribution $\mathcal{N}(0, 1)$ for each realisation. Note that the nominal values of parameters are the ones that were used in the previous numerical study. In order to assess the performance, the following performance metrics are defined:

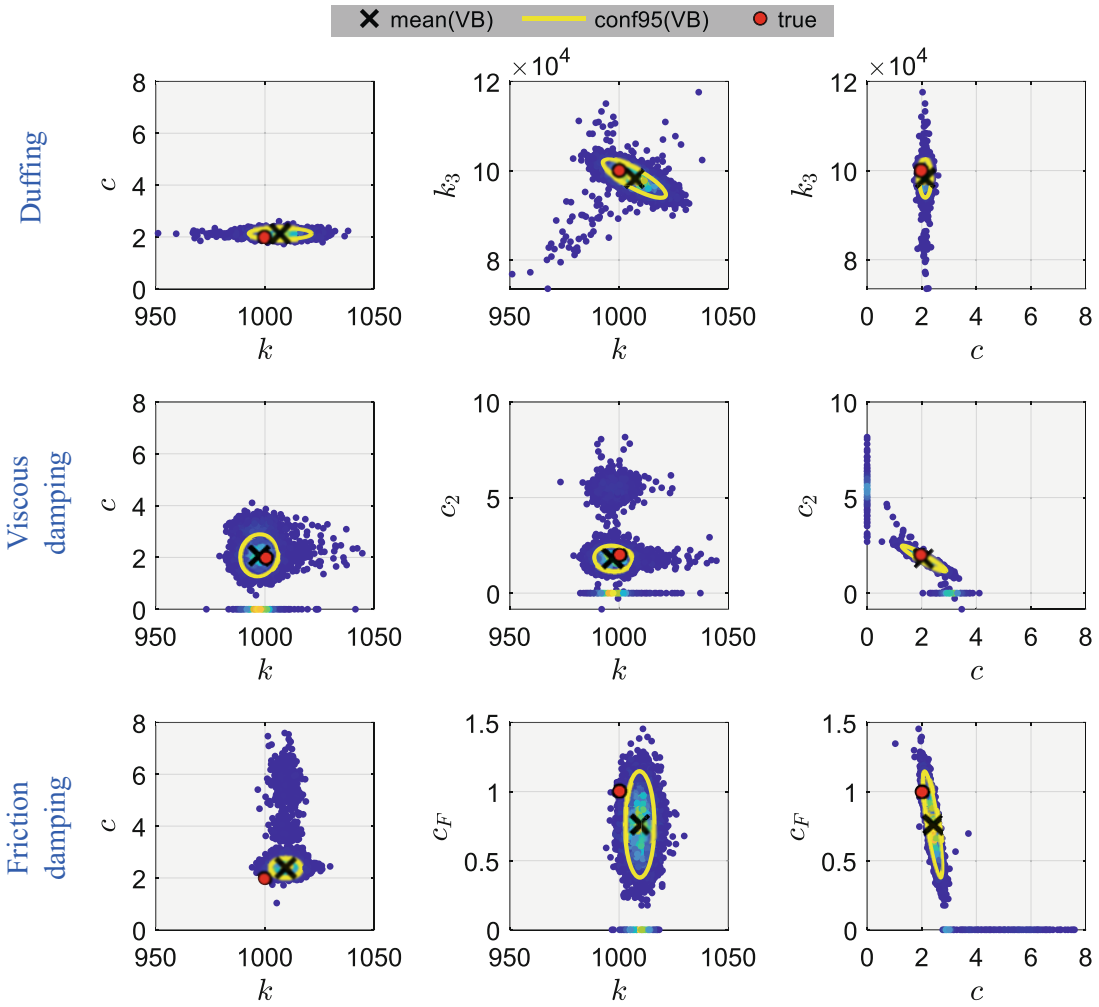

Fig. 5 Comparison of pairwise joint posteriors of the model parameters obtained by MCMC (shown as scatter-plot with posterior samples) and VB (depicted by mean and 95% confidence ellipse) for the three nonlinear oscillators: Duffing, quadratic viscous damping, and Coulomb friction damping; the red circle shows the true parameter values

- Weight estimation error, $e_\theta = \frac{\|\hat{\boldsymbol{\theta}}-\boldsymbol{\theta}\|_2}{\|\boldsymbol{\theta}\|_2}$, where $\hat{\boldsymbol{\theta}}$ is the estimate of the true (unscaled) weight vector $\boldsymbol{\theta}$ corresponding to the unscaled dictionary. Similarly, one can also define a scaled weight estimation error, $e_{\theta^s} = \frac{\|\boldsymbol{S}_\mathbf{D}(\hat{\boldsymbol{\theta}}-\boldsymbol{\theta})\|_2}{\|\boldsymbol{S}_\mathbf{D}\boldsymbol{\theta}\|_2}$. In the case of SS priors, $\hat{\boldsymbol{\theta}}$ is set to the estimated mean of the weights, whereas in the case of RVM, it is obtained as the MAP estimate.
- Test set prediction error, $e_p = \frac{\|\boldsymbol{y}^*-\mathbf{D}^*\hat{\boldsymbol{\theta}}\|_2}{\|\boldsymbol{y}^*\|_2}$, where $\boldsymbol{y}^*$ is the test set of responses, $\mathbf{D}^*$ is the unscaled test dictionary, and $\hat{\boldsymbol{\theta}}$ is the estimate of weight vector obtained using training data. 2000 data points were used for training and another 2000 data points for testing.
- False discovery rate (FDR), defined as the ratio of the number of false basis variables selected to the total number of basis variables included in the estimated model.
- Exact model selection indicator, $\hat{\mathcal{M}} = \mathcal{M}$, is a variable that takes value one when the estimated model $\hat{\mathcal{M}}$ has the exact same basis variables as the true model $\mathcal{M}$, and is zero otherwise.
- Superset model selection indicator, $\hat{\mathcal{M}} \supset \mathcal{M}$, is a variable that takes value one when the estimated model $\hat{\mathcal{M}}$ includes all the basis variables present in the true model $\mathcal{M}$, and is zero otherwise.

The above performance metrics are evaluated for each of the 1000 different realisations for all four systems, and the averages of the results are reported in Table 2.

Table 2 Comparison of results from SINDy, RVM, SS-MCMC, and SS-VB algorithms, averaged over 1000 realisations; bold numbers highlight the best performing metric

Type	Alg.	e_{θ^s}	e_θ	e_p	FDR	$\hat{\mathcal{M}} = \mathcal{M}$	$\hat{\mathcal{M}} \supset \mathcal{M}$
Linear	SINDy	0.168	$\approx 3 \times 10^4$	0.302	0.580	0.190	0.778
	RVM	0.010	502.261	0.097	0.576	0.005	0.999
	SS-MCMC	**0.004**	5.863	0.072	**0.002**	**0.992**	**1.000**
	SS-VB	0.004	**0.164**	**0.071**	0.003	0.991	0.997
Duffing	SINDy	0.253	609.134	0.168	0.558	0.113	0.742
	RVM	0.070	47.377	0.091	0.560	0.001	0.976
	SS-MCMC	**0.026**	**4.116**	0.078	**0.037**	**0.846**	**0.977**
	SS-VB	0.034	4.631	**0.076**	0.041	0.845	0.971
Quadratic damping	SINDy	0.147	$\approx 4 \times 10^5$	0.097	0.488	0.106	0.520
	RVM	0.017	1546.542	0.073	0.497	0.003	**0.931**
	SS-MCMC	0.017	0.004	0.072	0.030	0.859	0.865
	SS-VB	**0.012**	**0.004**	**0.071**	**0.019**	**0.886**	**0.892**
Coulomb damping	SINDy	0.216	$\approx 4 \times 10^5$	0.257	0.592	0.021	0.371
	RVM	0.013	1034.780	0.092	0.496	0.003	**0.993**
	SS-MCMC	0.011	**0.004**	0.071	0.018	**0.847**	0.850
	SS-VB	**0.009**	0.026	**0.070**	**0.003**	0.762	0.765

Table 3 Average computational runtimes for a single run of SINDy, RVM, SS-MCMC (single chain), and SS-VB

SINDy	RVM	SS-MCMC	SS-VB
3.65s	0.03s	34.23s	0.33s

It is noted that for all four systems, the model selection and parameter estimation performance using SS priors are superior to that using RVM and SINDy, with the deterministic SINDy algorithm performing worst among the four algorithms. Overall, it can be inferred that SINDy and the RVM very rarely find the exact true model and will likely include many false discoveries. The occurrence of false discoveries can be regarded a major deterrent in equation discovery, where selecting the correct set of basis variables is crucial for drawing scientific conclusions from the estimated model. Both implementations of SS priors do remarkably well, particularly in reducing the false discovery rate and in increasing the exact model selection rate. Moreover, the results from VB are seen to closely match those from MCMC, even outperforming them on many occasions. Such competitive performance demonstrated by VB makes it efficient compared to MCMC, as the VB takes much less run time than MCMC. The average runtimes of the four algorithms on a PC with 64-bit Windows 10 with 128GB RAM and Intel Xeon E5-2698 (version 4) CPU at 2.20 GHz are enumerated in Table 3. The RVM is the cheapest in terms of computational time, while the SS-MCMC is the most expensive. The SINDy algorithm run with a known regularisation parameter is often faster than the RVM; however, when accounting for the time to find the appropriate regularisation parameter, the SINDy can be much slower than RVM, as is shown in Table 3. The time reported for SS-VB is the combined time of running both the RVM (required for initialising the VB) and the VB algorithm, and it is apparent that the SS-VB is much faster than SS-MCMC, taking only 1/100th of the time used by SS-MCMC.

5 Conclusions

This paper investigates the use of an efficient variational Bayesian approach for performing equation discovery of nonlinear structural dynamic systems. Using a dictionary composed of interpretable functions, the task of Bayesian equation discovery is turned into a BVS problem, and solved using SS priors, which have the potential to derive more parsimonious and interpretable models of the underlying structural dynamics. However, MCMC-based Bayesian inference with SS priors is computationally demanding and can be prohibitive when the size of the dictionary grows and the number of observations is large. Unlike the MCMC-based approaches, the VB methodology approximates the true posterior with a simple distribution; it converts the Bayesian inference into a distribution-fitting optimisation problem and solves the optimisation at a much lower computational cost.

Using a series of numerical simulations, it has been demonstrated that the SS-VB algorithm correctly identifies the presence and type of various nonlinearities such as a cubic stiffness, a quadratic viscous damping, and a Coulomb friction

damping. Most importantly, the SS-VB algorithm yields performance on par with the MCMC-based Gibbs sampler at a much lower computational cost, making the VB approach very efficient in Bayesian equation discovery of nonlinear dynamical systems.

Acknowledgments This work has been funded by the UK Engineering and Physical Sciences Research Council (EPSRC), via the Autonomous Inspection in Manufacturing and Re-manufacturing (AIMaReM) grant EP/N018427/1. Support for K. Worden from the EPSRC via grant reference number EP/J016942/1 and for E.J. Cross via grant number EP/S001565/1 is also gratefully acknowledged.

References

1. Ljung, L.: Nonlinear Black-box modeling in system identification. Linköping University (1995)
2. Kocijan, J., Girard, A., Banko, B., Murray-Smith, R.: Dynamic systems identification with Gaussian processes. Math. Comput. Model. Dyn. Syst. **11**(4), 411–424 (2005)
3. Nakamura, T., Judd, K., Mees, A.I., Small, M.: A comparative study of information criteria for model selection. Int. J. Bifurcation Chaos **16**(08), 2153–2175 (2006)
4. Bongard, J., Lipson, H.: Automated reverse engineering of nonlinear dynamical systems. Proc. Natl. Acad. Sci. **104**(24), 9943–9948 (2007)
5. Schmidt, M., Lipson, H.: Distilling free-form natural laws from experimental data. Science **324** (5923), 81–85 (2009)
6. Brunton, S.L., Proctor, J.L., Kutz, J.N.: Discovering governing equations from data by sparse identification of nonlinear dynamical systems. Proc. Natl. Acad. Sci. **113**(15), 3932–3937 (2016)
7. Hastie, T., Tibshirani, R., Wainwright, M.: Statistical Learning with Sparsity: The Lasso and Generalizations. CRC Press, Boca Raton (2015)
8. Tipping, M.E.: Sparse Bayesian learning and the relevance vector machine. J. Mach. Learn. Res. **1**, 211–244 (2001)
9. Wipf, D.P., Rao, B.D.: Sparse Bayesian learning for basis selection. IEEE Trans. Signal Process. **52**(8), 2153–2164 (2004)
10. Seeger, M.W.: Bayesian inference and optimal design for the sparse linear model. J. Mach. Learn. Res. **9**, 759–813 (2008)
11. Carvalho, C.M., Polson, N.G., Scott, J.G.: Handling sparsity via the Horseshoe. In: Artificial Intelligence and Statistics, pp. 73–80 (2009)
12. Mitchell, T.J., Beauchamp, J.J.: Bayesian variable selection in linear regression. J. Am. Stat. Assoc. **83**(404), 1023–1032 (1988)
13. Zhang, S., Lin, G.: Robust data-driven discovery of governing physical laws with error bars. Proc. R. Soc. A Math. Phys. Eng. Sci. **474**(2217), 20180305 (2018)
14. Fuentes, R., Dervilis, N., Worden, K., Cross, E.J.: Efficient parameter identification and model selection in nonlinear dynamical systems via sparse Bayesian learning. J. Phys. Conf. Ser. **1264**, 012050 (2019). IOP Publishing
15. Tipping, M.E., Faul, A.C.: Fast marginal likelihood maximisation for sparse Bayesian models. In: Proceedings of the Ninth AISTATS Conference, pp. 1–13 (2003)
16. Nayek, R., Worden, K., Cross, E.J., Fuentes, R.: A sparse Bayesian approach to model structure selection and parameter estimation of dynamical systems using spike-and-slab priors. In: Proceedings of the International Conference on Noise and Vibration Engineering - ISMA2020 and International Conference on Uncertainty in Structural Dynamics - USD2020 (2020)
17. Polson, N.G., Scott, J.G.: Shrink globally, act locally: sparse Bayesian regularization and prediction. Bayesian Stat. **9**(501–538), 105 (2010)
18. Nayek, R., Fuentes, R., Worden, K., Cross, E.J.: On spike-and-slab priors for Bayesian equation discovery of nonlinear dynamical systems via sparse linear regression (2020). Preprint, arXiv:2012.01937
19. Carbonetto, P., Stephens, M.: Scalable variational inference for Bayesian variable selection in regression, and its accuracy in genetic association studies. Bayesian Anal. **7**(1), 73–108 (2012)
20. Ormerod, J.T., You, C., Müller, S.: A variational Bayes approach to variable selection. Electron. J. Stat. **11**(2), 3549–3594 (2017)
21. Bishop, C.M.: Pattern Recognition and Machine Learning. Springer, New York (2006)
22. Blei, D.M., Kucukelbir, A., McAuliffe, J.D.: Variational inference: a review for statisticians. J. Am. Stat. Assoc. **112**(518), 859–877 (2017)
23. Barbieri, M.M., Berger, J.O.: Optimal predictive model selection. Ann. Stat. **32**(3), 870–897 (2004)
24. Brooks, S.P., Gelman, A.: General methods for monitoring convergence of iterative simulations. J. Comput. Graph. Stat. **7**(4), 434–455 (1998)
25. Giordano, R., Broderick, T., Jordan, M.I.: Covariances, robustness and variational Bayes. J. Mach. Learn. Res. **19**(1), 1981–2029 (2018)

Bayesian Finite Element Model Updating Using an Improved Evolution Markov Chain Algorithm

M. Sherri, I. Boulkaibet, T. Marwala, and M. I. Friswell

Abstract Model updating algorithms are used to minimise the differences between the experimental results of a structure and the analytical solutions of its finite element model (FEM). In simple model updating procedures, iterative optimisation techniques can be easily used to update models and reduce the errors between experimental and analytical results. Unfortunately, experimental results as well as analytical models may have some degree of uncertainty that comes from different sources. As a result, iterative optimisation techniques may not be enough to quantify the uncertainty associated with structures. Uncertainty quantification approaches, such as the Bayesian approach, have the ability to incorporate the uncertainties associated with experiments as well as the modelling process into the updating procedure. In Bayesian finite element model updating, the uncertainty associated with the structural system is described by a posterior distribution function, while numerical tools are essential to approximate the solution of the complex posterior distribution function. In this paper, an improved evolution Markov chains Monte Carlo algorithm is used to solve the Bayesian model updating problem. In the proposed approach, the Markov chain Monte Carlo (MCMC) method is combined with the differential evolution optimising algorithm, while the final updating procedure is modified and extended with a snooker updater. The proposed approach is tested by updating a structural example, and the results are compared with the results obtained by the Metropolis-Hastings and the standard Differential Evolution Markov Chain (DE-MC) methods.

Keywords Bayesian model updating · Markov chain Monte Carlo · Differential evolution · Finite element model · Snooker updater

1 Introduction

The finite element method (FEM) is by far the most common technique for numerical analysis [1, 2]. It has wide application in engineering, including structural dynamics. The principle of FEM is based on dividing the physical system into small regions called "elements" and finding local solutions that satisfy the model equations on the boundaries of individual elements. Combining individual solutions for all elements gives the global solution for the physical system. Generally, FEM accurately predicts behaviour in simple structural dynamics. However, it can be relatively inaccurate when applied to the modelling of a complex structural system. Usually, a significant mismatch between FEM outputs and experimental results appears, and the final outcomes of FEM need to be updated to reduce the differences between modelling results and measurements.

Finite element model updating (FEMU) is a numerical procedure aimed at minimising the errors between FEM solutions and experiment data [3–6]. FEMU can be classified into two main classes: direct updating methods and iterative updating methods. The direct procedures are computationally inexpensive since no iterative process is involved. This method provides an improved model by determining the system matrices (mass and stiffness) that give the experimental modal results (natural

M. Sherri (✉)
Department of Mechanical Engineering Science, University of Johannesburg, Auckland Park, South Africa

I. Boulkaibet
College of Engineering, the American University of the Middle East, Kuwait City, Kuwait

T. Marwala
Institute of Intelligent Systems, University of Johannesburg, Auckland Park, South Africa

M. I. Friswell
College of Engineering, Swansea University, Swansea, UK

Z. Mao (ed.), *Model Validation and Uncertainty Quantification, Volume 3*, Conference Proceedings of the Society for Experimental Mechanics Series, https://doi.org/10.1007/978-3-030-77348-9_20

frequencies and mode shapes). However, the direct approach may lead to unrealistic results with no physical meaning. The iterative updating methods, also referred to as indirect updating approaches, construct an objective function, which is defined as the error between the experiment results and the FEM solutions, and then iteratively minimise this objective function. The variation of the system matrices is bounded during the minimisation process, and thus the updated parameters tend to be realistic.

Unfortunately, uncertainties are associated with FE models as well as experimental results, which consequently impacts the correctness of the FEM solutions. These uncertainties can be resolved by uncertainty quantification techniques, which can be applied during the iterative updating process. The Bayesian probability framework is well known for uncertainty quantification, where the uncertain parameters are modelled by a probability distribution function. In Bayesian theory, a posterior probability density function (PDF) is employed to identify the unknown (uncertain) parameters. However, the posterior PDF of complex structures cannot be determined analytically. Therefore, sampling techniques are used to obtain approximate solutions for the posterior PDF.

Markov chain Monte Carlo (MCMC) [7] methods are the most recognised techniques to generate samples from complex probability distributions. These methods are based on generating samples from a posterior PDF, while each new sample is either accepted or rejected according to the Metropolis acceptance criterion. However, the performance of the MCMC methods declines proportionally with the complexity of the posterior PDF, and optimums may not be discovered for complex problems during the sampling process. Thus, an extensive sampling procedure is recommended to avoid MCMC limitations. Differential evolution (DE) is an evolutionary algorithm [8–11] that is often used for optimisation problems. The DE algorithm solves the objective function by exploiting a population of particles and the interaction between these particles until the optimal solution is reached. The DE algorithm can be merged with the Metropolis-Hasting (M-H) algorithm, a basic MCMC algorithm, to generate samples at a population level instead of adopting only the local jump state. The DE-MC algorithm is an advanced algorithm that combines the DE and M-H algorithms and can be applied to draw samples from a posterior PDF. This method requires N chains to be evolved in order to provide the new samples.

Recently, more work has been conducted in order to improve the computational performance of the DE-MC algorithm. The Differential Evolution Markov Chain with snooker update (DE-MCS) algorithm requires a smaller number of chains and extends the exploration for optimal solutions to improve the DE-MC sampling procedure and sequentially solve the posterior PDF. This paper introduces the DE-MCS algorithm to solve the Bayesian finite element model updating problem. In addition, the performance of the DE-MCS method is investigated by updating a structural system. The obtained results are then compared with the M-H and DE-MC algorithms. Section 2 explains Bayesian inference for model updating. Section 3 details the theory of the updating methods. Sections 4 presents the updating results of the DE-MCS algorithm. Finally, the paper is concluded in Sect. 6.

2 Bayesian Inference

Generally, the model updating process can be formulated as a Bayesian procedure, while the uncertain parameters can be easily obtained by the numerical solution of the posterior PDF. This function can be described by Bayes' rule [12–14]:

$$P\left(\boldsymbol{\theta}|\,\mathcal{D},\mathcal{M}\right) \propto P\left(\mathcal{D}|\,\boldsymbol{\theta},\mathcal{M}\right)\;P\left(\boldsymbol{\theta}|\,\mathcal{M}\right) \tag{1}$$

where $\mathcal{M}$ represents the model class of the system, where each model class is defined by a different set of updating parameters. $\boldsymbol{\theta}$ is the vector of updating parameters $\boldsymbol{\theta} \in \boldsymbol{\Theta} \subset \mathcal{R}^d$. $\mathcal{D}$ is the experimental data of the structural system, represented by the natural frequencies f_i^{m} and mode shapes $\boldsymbol{\phi}_i^{\mathrm{m}}$. $P\left(\boldsymbol{\theta}|\,\mathcal{M}\right)$ refers to the prior PDF that expresses the initial knowledge of the uncertain parameters $\boldsymbol{\theta}$ given $\mathcal{M}$ and with the absence of $\mathcal{D}$. The likelihood function $P\left(\mathcal{D}|\,\boldsymbol{\theta},\mathcal{M}\right)$ describes the difference between the measured data and FEM solutions. $P\left(\boldsymbol{\theta}|\,\mathcal{D},\mathcal{M}\right)$is the posterior PDF of the updating parameters given a model class $\mathcal{M}$ and the measured data $\mathcal{D}$. Only one model class is studied here, and hence $\mathcal{M}$ is neglected for a simple Bayesian formulation.

The likelihood function is given by:

$$P\left(\mathcal{D}|\,\boldsymbol{\theta}\right) = \frac{1}{\left(\frac{2\pi}{\beta_{\mathrm{c}}}\right)^{N_{\mathrm{m}}/2}\prod_{i=1}^{N_{\mathrm{m}}} f_i^{\mathrm{m}}} \exp\left(-\frac{\beta_{\mathrm{c}}}{2}\sum\nolimits_i^{N_{\mathrm{m}}}\left(\frac{f_i^{\mathrm{m}}-f_i}{f_i^{\mathrm{m}}}\right)^2\right) \tag{2}$$

where N_{m} is the number of measured modes, β_{c} is a user-defined constant, and f_i^{m} and f_i are the i th measured and analytical natural frequencies.

The prior $P(\boldsymbol{\theta})$, which provides preliminary knowledge of the updating parameter $\boldsymbol{\theta}$, is defined by a Gaussian probability distribution:

$$P(\boldsymbol{\theta}) = \frac{1}{(2\pi)^{Q/2}\prod_{i=1}^{Q}\frac{1}{\sqrt{\alpha_i}}}\exp\left(-\sum_i^{Q}\frac{\alpha_i}{2}\left\|\theta^i - \theta_0^i\right\|^2\right) = \frac{1}{(2\pi)^{Q/2}\prod_{i=1}^{Q}\frac{1}{\sqrt{\alpha_i}}}\exp\left(-\frac{1}{2}(\boldsymbol{\theta}-\boldsymbol{\theta}_0)^T\ \Sigma^{-1}(\boldsymbol{\theta}-\boldsymbol{\theta}_0)\right) \tag{3}$$

where Q is the number of the uncertain parameters, $\boldsymbol{\theta}_0$ represents the mean value of the uncertain parameters, α_i is the coefficient of uncertain parameters, $i = 1, \ldots, Q$, and the Euclidean norm of $*$ is noted by $\|*\|$.

The posterior PDF $P(\boldsymbol{\theta}|\mathcal{D})$ of the updating parameters $\boldsymbol{\theta}$ given the measured data $\mathcal{D}$ can be now described by substituting Eqs. (2) and (3) with Eq. (1):

$$P(\boldsymbol{\theta}|\mathcal{D}) \propto \frac{1}{Z_{\mathrm{s}}(\alpha,\beta_{\mathrm{c}})}\exp\left(-\frac{\beta_{\mathrm{c}}}{2}\sum_i^{N_{\mathrm{m}}}\left(\frac{f_i^{\mathrm{m}}-f_i}{f_i^{\mathrm{m}}}\right)^2 - \sum_i^{Q}\frac{\alpha_i}{2}\left\|\theta^i-\theta_0^i\right\|^2\right) \tag{4}$$

where

$$Z_{\mathrm{s}}(\alpha,\beta_{\mathrm{c}}) = \left(\frac{2\pi}{\beta_{\mathrm{c}}}\right)^{N_{\mathrm{m}}/2}\prod_{i=1}^{N_{\mathrm{m}}}f_i^{\mathrm{m}}(2\pi)^{Q/2}\prod_{i=1}^{Q}\frac{1}{\sqrt{\alpha_i}} \tag{5}$$

As can be observed from Eq. (4), the more is the structural complexity, the more difficult is the acquisition of the analytical solutions for the posterior PDF. The dimensionality of the unknown parameters, along with the search space complexity, may significantly affect the updating process, and the global solutions of the uncertain parameter may not be easily obtained.

3 Markov Chain Monte Carlo Algorithms

This section explains the three sampling techniques that are applied to approximate the posterior PDF in the Bayesian framework. The methods are M-H, DE-MC, and an improved version of the stranded DE-MC referred to as the Differential Evolution Markov Chain with snooker update (DE-MCS). Finally, the three algorithms are used to update a structural example with real experimental data.

3.1 Metropolis-Hastings (M-H) Algorithm

The Metropolis-Hastings algorithm [15, 16] is one of the basic sampling algorithms used to approximate the posterior PDF through generating new samples, also known as proposals, from a predefined proposal distribution. A transition probability is later applied to accept the proposal or remain on the current Markov chain. Let $\boldsymbol{\theta} = \{\theta_1, \theta_2, \theta_3, \ldots, \theta_d\}$ be a d-dimensional updating vector, and $P(\boldsymbol{\theta}|\mathcal{D})$ is the target distribution function. To acquire proposals from the $P(\boldsymbol{\theta}|\mathcal{D})$ distribution, another proposal density function $q(\boldsymbol{\theta}|\theta_{t-1})$ is used to generate samples. Every new sample $\boldsymbol{\theta}^*$ is proposed randomly, given the value of the chain at the last iteration θ_{t-1}. Finally, the generated sample is accepted or rejected by the Metropolis-Hastings rule:

$$\alpha\left(\boldsymbol{\theta}^*, \theta_{t-1}\right) = \min\left\{1, \frac{P\left(\boldsymbol{\theta}^*|\mathcal{D}\right)\ q\left(\theta_{t-1}|\boldsymbol{\theta}^*\right)}{P\left(\theta_{t-1}|\mathcal{D}\right)\ q\left(\boldsymbol{\theta}^*|\theta_{t-1}\right)}\right\} \tag{6}$$

The M-H algorithm for FEMU is as follows:

1. Initialise the algorithm using the prior probability distribution, with vector $\boldsymbol{\theta}_o$ and set $t = 1$.
2. At each iteration t, generate a new sample $\boldsymbol{\theta}^*$ from the proposal density $q(\boldsymbol{\theta}^*|\theta_{t-1})$.
3. Update the FE model and calculate the posterior PDF, $P\left(\boldsymbol{\theta}^*|\mathcal{D}\right)$.
4. Determine the acceptance probability using the M-H rule, Eq. (6).

5. Draw u from the uniform distribution U(0, 1).
6. If $u < \alpha(\boldsymbol{\theta}^*, \theta_{t-1})$, accept $\boldsymbol{\theta}^*$; otherwise, reject $\boldsymbol{\theta}^*$.
7. Repeat 2–6 steps until the maximum number of iterations is achieved.

3.2 Standard DE-MC Algorithm

The DE-MC algorithm is an evolutionary-based MCMC algorithm that exploits the interaction among multichains to draw new proposals. Consider $\boldsymbol{\theta}$ is a d-dimensional vector of the updating parameters, $\boldsymbol{\theta} = \{\theta^1, \theta^2, \cdots, \theta^d\}$. Each updating parameter has N chains of states, $\boldsymbol{\theta}_{(d)} = \{\boldsymbol{\theta}_1, \boldsymbol{\theta}_2, \ldots, \boldsymbol{\theta}_N\}$. The entire set of chains represents the population that evolves during the iterations (generation process). The initial population is drawn from the prior probability distribution, Eq. (3). The new proposal (state) $\boldsymbol{\theta}_i^*$ of the i th chain, $i \in \{1, 2, \ldots, N\}$, is determined as [17, 18]:

$$\boldsymbol{\theta}_i^* = \boldsymbol{\theta}_i + \gamma\,(\boldsymbol{\theta}_b - \boldsymbol{\theta}_a) + \varepsilon \tag{7}$$

where $\boldsymbol{\theta}_a$ and $\boldsymbol{\theta}_b$ are two randomly selected vectors, with $\boldsymbol{\theta}_i \neq \boldsymbol{\theta}_a \neq \boldsymbol{\theta}_b$. The symbol γ is a scaling factor that controls the jumping distribution and can vary on a scale of 0.4 – 1. The default choice of γ is $2.38/\sqrt{2d}$, which gives better mixing of chains and preferable acceptance probability. The symbol ε is a small value added to the proposed chain to avoid the degeneracy problem, and it is drawn from a normal distribution with mean $\mu = 0$ and small variance σ^2; i.e., $\varepsilon \sim N(0, \sigma^2)$.

The conditional detailed balance of the new value of the chain $\boldsymbol{\theta}_i^*$ with respect to the posterior PDF is obtained by applying the Metropolis ratio to accept or reject the proposed samples:

$$r = \min\left\{1, \frac{P\left(\boldsymbol{\theta}_i^* | \mathcal{D}\right)}{P\left(\boldsymbol{\theta}_i | \mathcal{D}\right)}\right\} \tag{8}$$

The jump in Eq. (7) is almost parallel to the direction $\boldsymbol{\theta}_a$ — $\boldsymbol{\theta}_b$. If the small value ε is neglected, then all new proposed samples are contained in a space of dimension $\min(d, N-1)$. To efficiently sample over the entire search space, N must be greater than d; e.g., $N = 2d$. Figure 1 shows the sampling process of the DE-MC and M-H methods.

As shown in Fig. 1, the new proposed chain by the DE-MC algorithm is determined by the magnitude of two randomly selected chains, while the M-H method only adopts the random walk jump to propose the new sample state.

Below is the DE-MC algorithm for FEMU:

1. Initialise the population $\boldsymbol{\theta}_{i,0}$, $i \in \{1, 2, \ldots, N\}$.
2. Set the scaling factor γ ($\gamma = 2.38/\sqrt{2d}$, and d is the dimension of the updating parameters).
3. For all chains N, determine the posterior PDF $P\left(\boldsymbol{\theta}|\mathcal{D}\right)$.
4. For all chains, $i \in \{1, 2, \ldots, N\}$.
   - 4.1 Select at random two other vectors $\boldsymbol{\theta}_a$, $\boldsymbol{\theta}_b$, where $\boldsymbol{\theta}_a \neq \boldsymbol{\theta}_b \neq \boldsymbol{\theta}_i$.
   - 4.2 Sample the random term ε with small variance $\varepsilon \sim N(0, \sigma^2)$.
   - 4.3 Calculate the proposed sample, $\boldsymbol{\theta}_i^* = \boldsymbol{\theta}_i + \gamma\,(\boldsymbol{\theta}_b - \boldsymbol{\theta}_a) + \varepsilon$, then estimate $P\left(\boldsymbol{\theta}_i^* | \mathcal{D}\right)$.

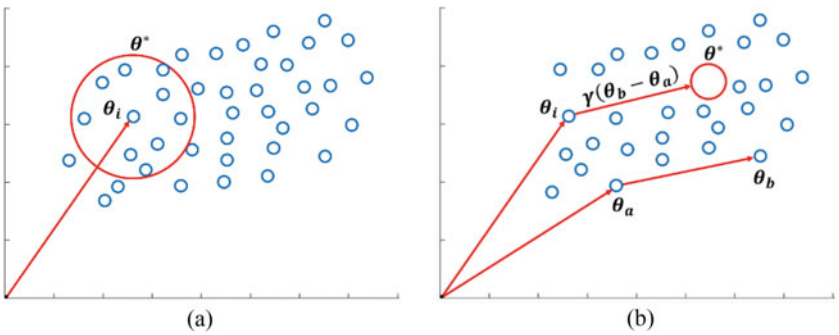

Fig. 1 Illustration of new sample proposition. Blue circles represent the chains. (**a**) M-H method. (**b**) DE-MC method

4.4 Determine the Metropolis ratio, $r = \min\left\{1, \frac{P(\boldsymbol{\theta}_i^*|\mathcal{D})}{P(\boldsymbol{\theta}_i|\mathcal{D})}\right\}$.

4.5 Accept the proposed sample $\boldsymbol{\theta}_i \leftarrow \boldsymbol{\theta}_i^*$ with probability $\min(1, r)$; otherwise, $\boldsymbol{\theta}_i$ remains.

5. Repeat steps 4.1 to 4.5 until the number of samples required is achieved.

3.3 Standard DE-MCS Algorithm

Generally, the DE-MC algorithm requires $N_s > d$ to propose a new sample $\boldsymbol{\theta}^*$, and the difference vector $(\boldsymbol{\theta}_b - \boldsymbol{\theta}_a)$ is determined by means of the current interacting chains, Eq. (7). In contrast, the modified version of the DE-MC algorithm, DE-MCS [19], requires fewer chains (e.g. $N_s = 3$), and the difference vector is obtained from the past states of the chains. As a result, reducing the value of N helps to overcome several common disadvantages:

(i) All chains from the initial population by the prior distribution must move to the high-density region of the posterior function. Thus, the convergence of the solutions is a factor of N_s.
(ii) Outlier problems occur more often with large N_s. If $N_s - 1$ chains have converged to a confidence level, it might require extensive time for the last chain (outlier) to reach the same convergence.
(iii) Real-time processing takes longer to draw large N_s chains. Accordingly, the lower is the number of chains required, the greater the practical applicability to deal with computationally demanding problems.

Generally, the DE-MCS algorithm has more algorithmic parameters than the standard DE-MC, which is due to improvements made to enhance the DE-MC performance. Let $\boldsymbol{\Theta}$ denote an $N_s \times d$ matrix that contains the states of the chains at the current iteration, and $\mathbf{M}$ is the matrix that preserves the current and past states of the chains. The initial number of rows in $\mathbf{M}$ is defined by R_0, which has a default set to $R_0 = 10d$ as a computational effective initial size of the matrix. At each generation (iteration), the updated chains (N_s rows) of $\boldsymbol{\Theta}$ are appended to $\mathbf{M}$, which expands the size of $\mathbf{M}$ through time t by $R + N_s$. Therefore, a thinning rate Z is added to reduce the storage capacity, which decreases the change of $\mathbf{M}$ by order $N_s/R = Z/t$.

The chain proposal of the DE-MCS algorithm is illustrated in Fig. 2. The proposal is generated along a reference line through the current chain $\boldsymbol{\theta}_i$ and another state $\boldsymbol{\theta}_{\mathrm{M}}^x$ from the past position matrix $\mathbf{M}$. The proposed chain $\boldsymbol{\theta}_{\mathrm{i}}^*$ is generated by randomly selecting two other chains, $\boldsymbol{\theta}_{\mathrm{M}}^a$ and $\boldsymbol{\theta}_{\mathrm{M}}^b$, then projecting them orthogonally on the reference line ($\boldsymbol{\theta}_{\mathrm{M}}^{Pa}$ and $\boldsymbol{\theta}_{\mathrm{M}}^{Pb}$) and adding the scaling factor γ_s multiplied by the difference between the projection chains $\boldsymbol{\theta}_{\mathrm{M}}^{Pa}$ and $\boldsymbol{\theta}_{\mathrm{M}}^{Pb}$ to $\boldsymbol{\theta}_i$. The proposal generation of the new chain $\boldsymbol{\theta}_{\mathrm{i}}^*$ by DE-MCS is given as:

$$\boldsymbol{\theta}_{\mathrm{i}}^* = \boldsymbol{\theta}_i + \gamma_s\left(\boldsymbol{\theta}_{\mathrm{M}}^{Pa} - \boldsymbol{\theta}_{\mathrm{M}}^{Pb}\right) \tag{9}$$

The default choices of DE-MCS parameters are $N_s = 3$, $R_0 = 10d$, $Z = 10$, and $\gamma_s = 2.38/\sqrt{2d}$. In the DE-MCS algorithm, the scaling factor γ_s uses $d = 1$ for all d; thus, $\gamma_s = 2.38/\sqrt{2} \approx 1.7$. The reason for this choice ($d = 1$) is that the projection step minimises the variance of the difference, which adjusts the resulting dimensionality. This default set returns a better acceptance rate. Finally, the generated sample $\boldsymbol{\theta}_{\mathrm{i}}^*$ is accepted by the Metropolis ratio:

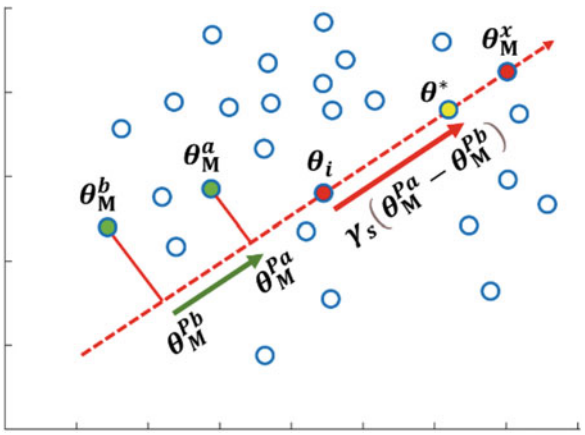

Fig. 2 DE-MCS new chain proposal. Blue circles represent the chains

$$r = \min\left\{1, \frac{P\left(\boldsymbol{\theta}_{\mathrm{i}}^{*}\middle|\mathcal{D}\right)\ \left\|\boldsymbol{\theta}_{\mathrm{i}}^{*} - \boldsymbol{\theta}_{\mathrm{M}}^{x}\right\|^{d-1}}{P\left(\boldsymbol{\theta}_{i}|\mathcal{D}\right)\ \left\|\boldsymbol{\theta}_{i} - \boldsymbol{\theta}_{\mathrm{M}}^{x}\right\|^{d-1}}\right\} \tag{10}$$

The DE-MCS algorithm for FEMU is the following:

1. Initialise the $R_0 \times d$ matrix $\mathbf{M}$.
2. Sample the initial population from the prior distribution, copy the first N_{s} rows of $\mathbf{M}$ to $\boldsymbol{\Theta}$, and set $R \leftarrow R_0$.
3. Z times update the population $\boldsymbol{\Theta}$:
   (a) Select randomly another chain from the store matrix $\boldsymbol{\theta}_{\mathrm{M}}^{x}$, and sample along the line $\boldsymbol{\theta}_{i}$—$\boldsymbol{\theta}_{\mathrm{M}}^{x}$.
   (b) Select randomly two other random chains $\boldsymbol{\theta}_{\mathrm{M}}^{a}$ and $\boldsymbol{\theta}_{\mathrm{M}}^{b}$.
   (c) Project $\boldsymbol{\theta}_{\mathrm{M}}^{a}$ and $\boldsymbol{\theta}_{\mathrm{M}}^{b}$ orthogonally on the line $\boldsymbol{\theta}_{i}$—$\boldsymbol{\theta}_{\mathrm{M}}^{x}$ yielding $\boldsymbol{\theta}_{\mathrm{M}}^{Pa}$ and $\boldsymbol{\theta}_{\mathrm{M}}^{Pb}$.
   (d) Determine the new chain proposal, $\boldsymbol{\theta}_{\mathrm{i}}^{*} = \boldsymbol{\theta}_{i} + \gamma_{s}\left(\boldsymbol{\theta}_{\mathrm{M}}^{Pa} - \boldsymbol{\theta}_{\mathrm{M}}^{Pb}\right)$.
   (e) Calculate the posterior function $P\left(\boldsymbol{\theta}_{\mathrm{i}}^{*}\middle|\mathcal{D}\right)$, then estimate the Metropolis ratio:
   $$r = \min\left\{1, \frac{P(\boldsymbol{\theta}_{\mathrm{i}}^{*}|\mathcal{D})\ \boldsymbol{\theta}^{*} - \boldsymbol{\theta}_{\mathrm{M}}^{x\ d-1}}{P(\boldsymbol{\theta}_{i}|\mathcal{D})\ \boldsymbol{\theta}_{i} - \boldsymbol{\theta}_{\mathrm{M}}^{x\ d-1}}\right\}.$$
   (f) Accept the proposal with probability $\min(1, r)$; otherwise, remain at $\boldsymbol{\theta}_{i}$.
4. Append the current rows (generations) of $\boldsymbol{\Theta}$ to $\mathbf{M}$, so that $R \leftarrow R + N_{\mathrm{s}}$.
5. Repeat steps 3 and 4 until the maximum number of iterations is achieved.

4 Application: F-shaped Structure

Figure 3 illustrates the structural system to be updated, which is constructed as an F-shaped structure [20]. The structure is assembled by four square cross-sectional beams. The vertical beams are welded to each other and fixed to the base plate. The horizontal beams are joined by bolts to the vertical side, forming an F-shaped skeleton. The structure is made of industrial steel and weighs 13.8 kg. Young's modulus is 2×10^{11} N/m^2, and the material density is 7850 kg/m^3. The cross-sectional area A, the moment of inertia I_x, and the torsional constant J are 14.21×10^{-4} m^2, 1.68×10^{-7} m^4, and 3.36×10^{-7} m^4, respectively.

The structure was excited using an impact hammer, and the response was measured using an accelerometer fixed at the upper half of the vertical beam (see Fig. 3). The experimental natural frequencies of the first five modes are

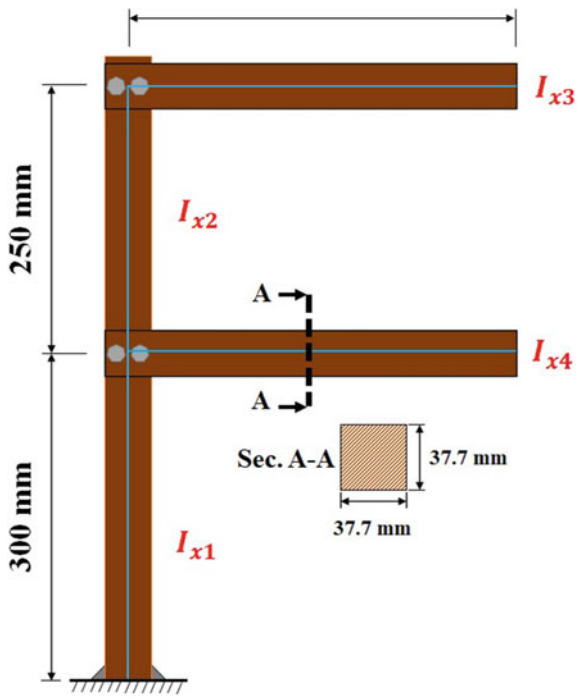

Fig. 3 The F-shaped structure

$\omega_{\mathrm{m}} = \{34.95, 104.02, 133.96, 317.52, 980.16\}$ Hz. An FE model was developed using beam elements, where each beam of the structure is divided into 50 small elements. The analytical frequencies for the first five modes of the FE model are illustrated in Table 2.

In this section, the moment of inertia I_x for the main four beams of the F-shaped structure is chosen as the updating parameter, shown by I_{xi} in Fig. 3. Thus, the updating vector is $\boldsymbol{\theta} = \{I_{x1}, I_{x2}, I_{x3}, I_{x4}\}$. The moment of inertia of beam 1 is given by I_{x1}, I_{x2} for beam 2, etc. The updating vector is bounded by $\boldsymbol{\theta}_{\max}$=$\{1.8834\times10^{-7}, 1.8834\times10^{-7}, 1.8834\times10^{-7}, 1.8834 \times 10^{-7}\}$, and $\boldsymbol{\theta}_{\min} = \{1.4834 \times 10^{-7}, 1.4834 \times 10^{-7}, 1.4834 \times 10^{-7}, 1.4834 \times 10^{-7}\}$ to keep the updating results realistic.

The number of samples is set as $T = 5000$ for all algorithms, and the dimension of the updating vector is $d = 4$. The number of chains (population) for DE-MC is $N = 10$, and the scaling factor is $\gamma = 2.38/\sqrt{2 \times 4} \approx 0.84$. The parameters of the DE-MCS method are set as the default choices, the number of chains $N_{\mathrm{s}} = 3$, the number of rows for the initial store matrix is $R_0 = 40$, the thinning rate $Z = 10$, and the scaling factor $\gamma_{\mathrm{s}} = 2.38/\sqrt{2} \approx 1.7$. For each algorithm, the updating procedure of the F-shaped structural was run more than 15 separate times for each algorithm to verify their convergence and accuracy. The outcomes for all runs are found to be almost identical for each algorithm.

Figures 4, 5, and 6 show the half boxplots with the sample distribution from the M-H, DE-MC, and DE-MCS algorithms, respectively. The plots illustrate the sampling performance of the algorithms for each updating parameter θ_i, and the median line indicates the resulting updated value for each parameter. As seen in the plots, the algorithms have converged successfully to high-density intervals, in which the generated samples are normally distributed around the mean. The outlier samples (green dots) located outside the whiskers of the boxplot (range within 1.5|QR) are observed more often in the samples of the M-H algorithm. On the other hand, the DE-MC method has fewer outliers than the M-H method, which means that the DE-MC requires only a few iterations in order to reach the area with high probability. The DE-MCS algorithm, however, has the fewest outliers overall, and only very few iterations were required to find the area with high probability. The fewer outliers demonstrate the advantage of using a population-based sampling technique to obtain sufficient sampling proposals. This means that the smaller number of chains, $N_{\mathrm{s}} \ll N$, in the DE-MCS updating method is preferable to avoid outlier solutions.

The updating parameters given by the three algorithms are listed in Table 1. As expected, the algorithms have successfully updated the uncertain parameters and produced physically realistic values. Furthermore, the table includes the coefficient of variation (c.o.v), which is defined as the ratio of the standard deviation σ_i to the mean value of θ_i. The c.o.v values are considered as a standardised measure of dispersion of probability distribution. Overall, the c.o.v values in Table 1 for all

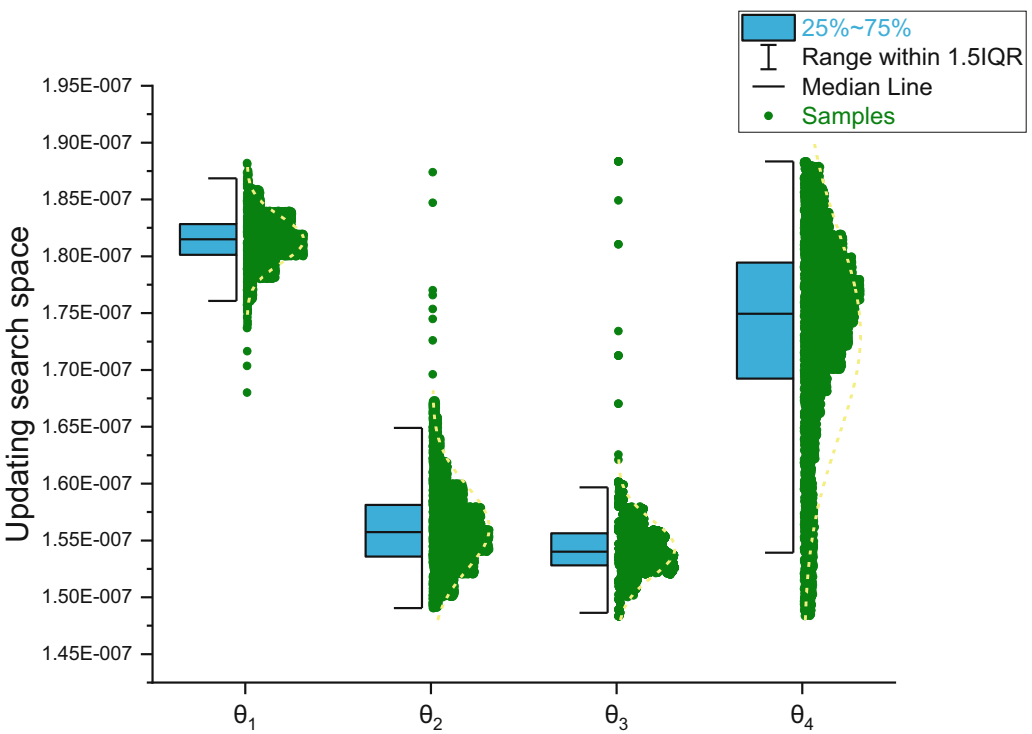

Fig. 4 Half boxplot with sample distribution (M-H method)

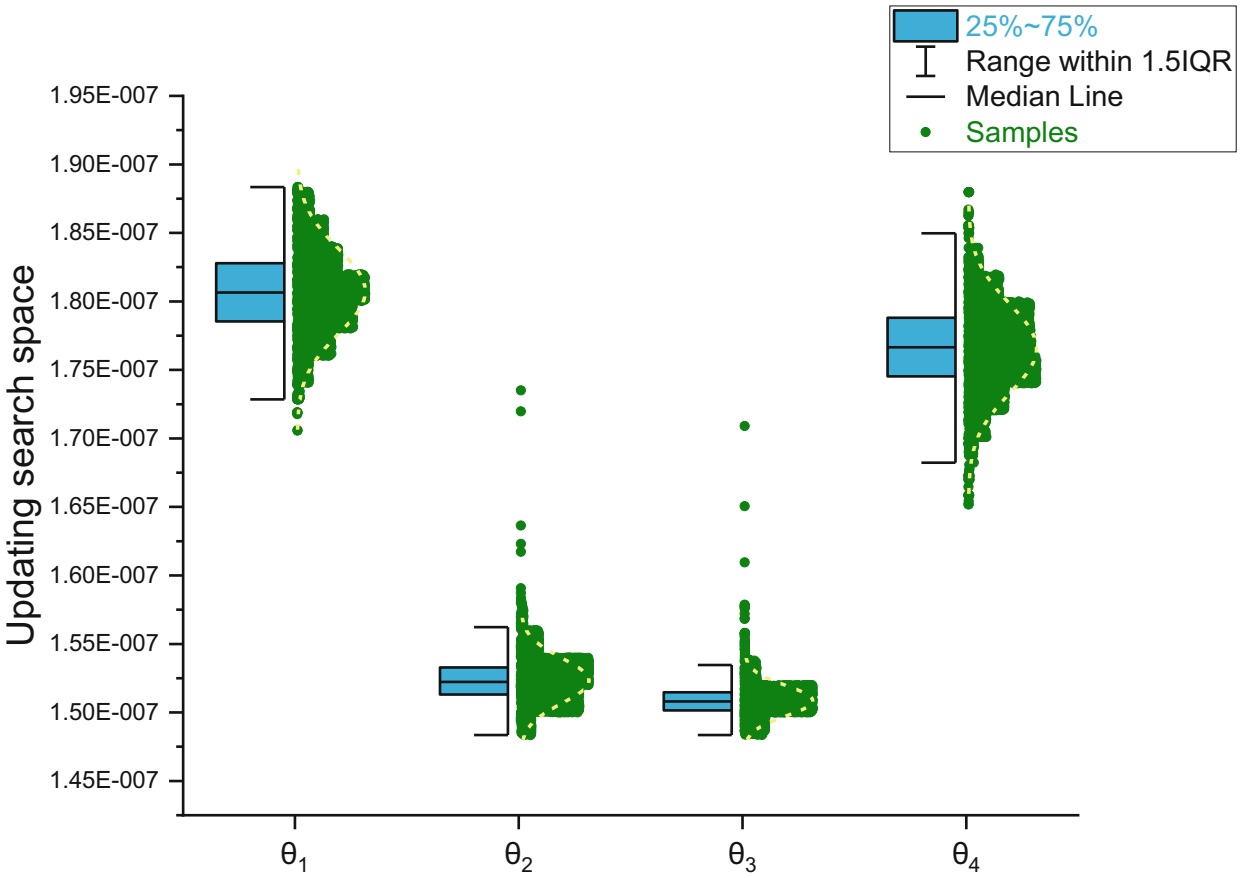

Fig. 5 Half boxplot with sample distribution (DE-MC method)

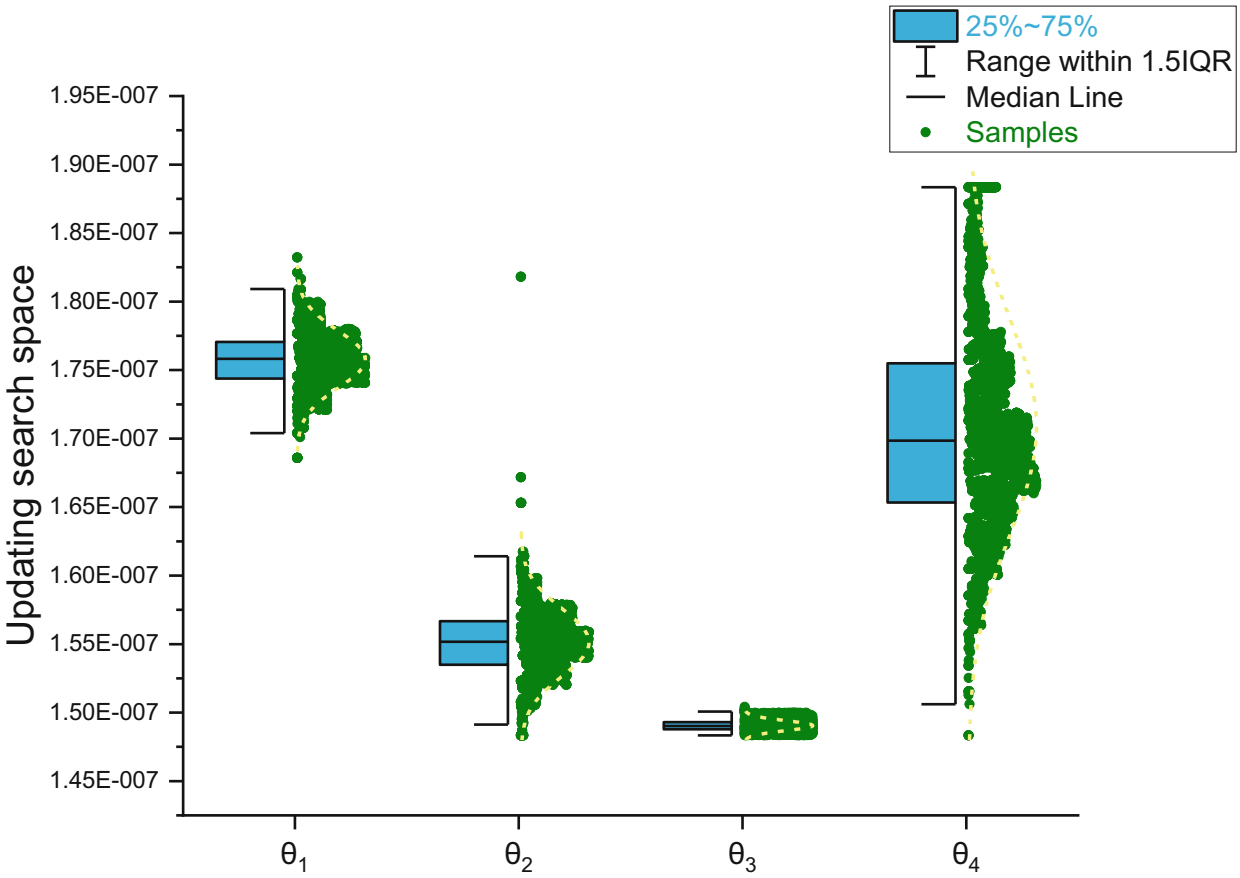

Fig. 6 Half boxplot with sample distribution (DE-MCS method)

Table 1 The updated parameters of the F-shaped structure using the M-H, DE-MC, and DE-MCS methods

Updating the moments of inertia I_x (m^4)							
	Initial	M-H method	c.o.v (%) $\frac{\sigma_i}{\theta_i}$	DE-MC method	c.o.v (%) $\frac{\sigma_i}{\theta_i}$	DE-MCS method	c.o.v (%) $\frac{\sigma_i}{\theta_i}$
I_{x1}	1.683×10^{-7}	1.815×10^{-7}	2.31	1.808×10^{-7}	2.14	1.757×10^{-7}	1.18
I_{x2}	1.683×10^{-7}	1.555×10^{-7}	3.03	1.522×10^{-7}	2.68	1.550×10^{-7}	1.58
I_{x3}	1.683×10^{-7}	1.542×10^{-7}	2.34	1.508×10^{-7}	3.02	1.490×10^{-7}	1.01
I_{x4}	1.683×10^{-7}	1.765×10^{-7}	5.55	1.770×10^{-7}	6.79	1.709×10^{-7}	4.64

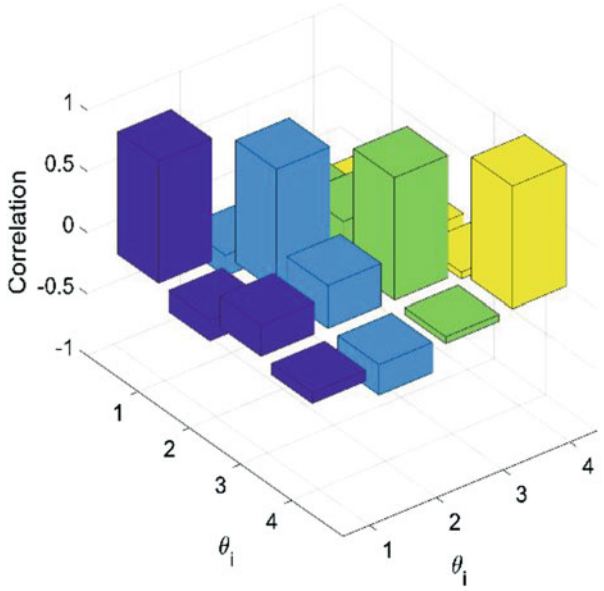

Fig. 7 Parameter correlation on MH method

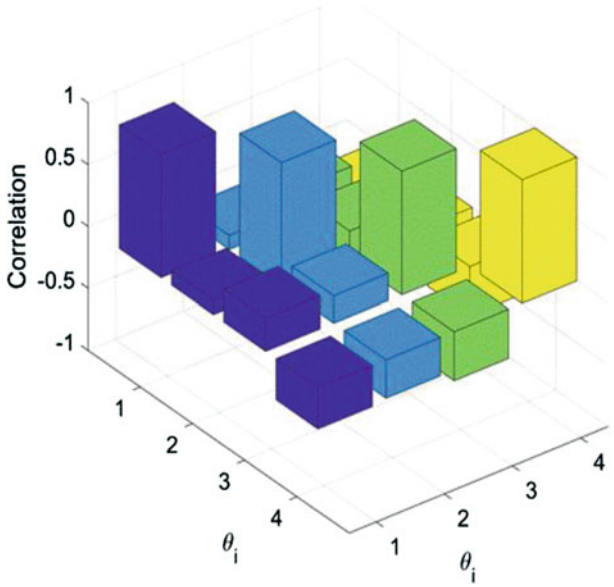

Fig. 8 Parameter correlation (DE-MC method)

updating parameters by all algorithms reflect an accurate sampling tendency toward the sampled distribution. A maximum percentage for c.o.v is noticed at I_{x4} for all algorithms. Nevertheless, DE-MCS gives the smallest c.o.v for I_{x4} as 4.64%.

Figures 7, 8, and 9 show the correlation between the updating parameters using the M-H, DE-MC, and DE-MCS methods. A small correlation means that the parameters are weakly correlated (<0.3), and a high correlation (>0.7) means there is

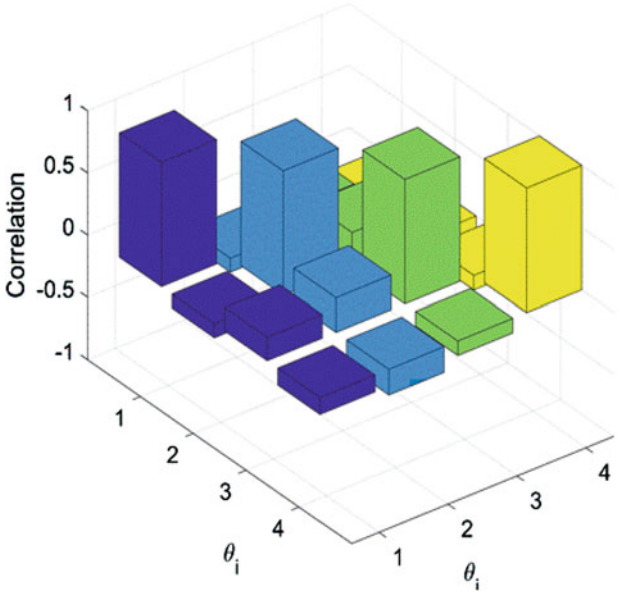

Fig. 9 Parameter correlation (DE-MCS method)

Table 2 The updated natural frequencies of the F-shaped structure using the M-H, DE-MC, and DE-MCS methods

Modes	Measured frequency (Hz)	Initial frequency (Hz)	Error (%)	M-H method frequency (Hz)	Error (%)	DE-MC method frequency (Hz)	Error (%)	DE-MCS method frequency (Hz)	Error (%)
1	34.95	34.34	1.73	34.87	0.22	34.86	0.27	34.91	0.12
2	104.02	113.42	9.04	108.49	4.30	106.71	2.59	106.19	2.09
3	133.96	129.85	3.07	125.91	6.01	129.11	3.62	130.33	2.71
4	317.52	329.85	3.88	317.99	0.15	316.66	0.27	316.55	0.31
5	980.16	1039.30	6.03	1008.40	2.88	1002.30	2.26	996.46	1.66
TAE	–		*4.75*	–	*2.71*	–	*1.80*	–	*1.38*

a logical relationship between the parameters. Correlation can be positive or negative, which indicates the way that the parameters affect each other. Usually, the updated parameters in the Bayesian framework are correlated. These figures show that all of the updated parameters estimated by the three algorithms are weakly correlated. This suggests a minimal relationship between the variables.

The updated natural frequencies are given in Table 2. The analytical and measured natural frequencies are also provided within the same table. The absolute error of each mode is estimated by $\frac{|f_i^{\mathrm{m}} - f_i|}{f_i^{\mathrm{m}}}$, and the total average error for the five modes is also estimated as $\mathrm{TAE} = \frac{1}{N_{\mathrm{m}}} \sum_{i=1}^{N_{\mathrm{m}}} \frac{|f_i^{\mathrm{m}} - f_i|}{f_i^{\mathrm{m}}}$, $N_{\mathrm{m}} = 5$. As listed in Table 2, the updated frequencies by DE-MCS give the best results compared to the other algorithms. DE-MCS has decreased the *TAE* compared to its initial state from 4.75% to 1.38%. The updated frequencies by DE-MC and M-H have better *TAE* percentages than the initial FE model. DE-MC and M-H have minimised the *TAE* down to 1.8% and 2.71%, respectively. As expected, the evolutionary-based updating techniques have demonstrated an advanced ability to explore the search space through finding new solutions by sampling at a population level. Additionally, the evolutionary-based algorithms exploit the experience of the past chains and the current interacting population to propose further accurate solutions.

The evaluation of the *TAE* at each iteration for all algorithms is plotted together in Fig. 10. The convergence for all methods has occurred in under 1000 iterations. The *TAE* in the first few iterations (<30) is affected by the very early proposed samples. This means that the selection of the solutions with experience from another sample anticipates a lower *TAE* in the first few iterations for the population-based methods. Contrastingly, the opposite result is expected for the M-H method since it only adopts the random local step to find new solutions.

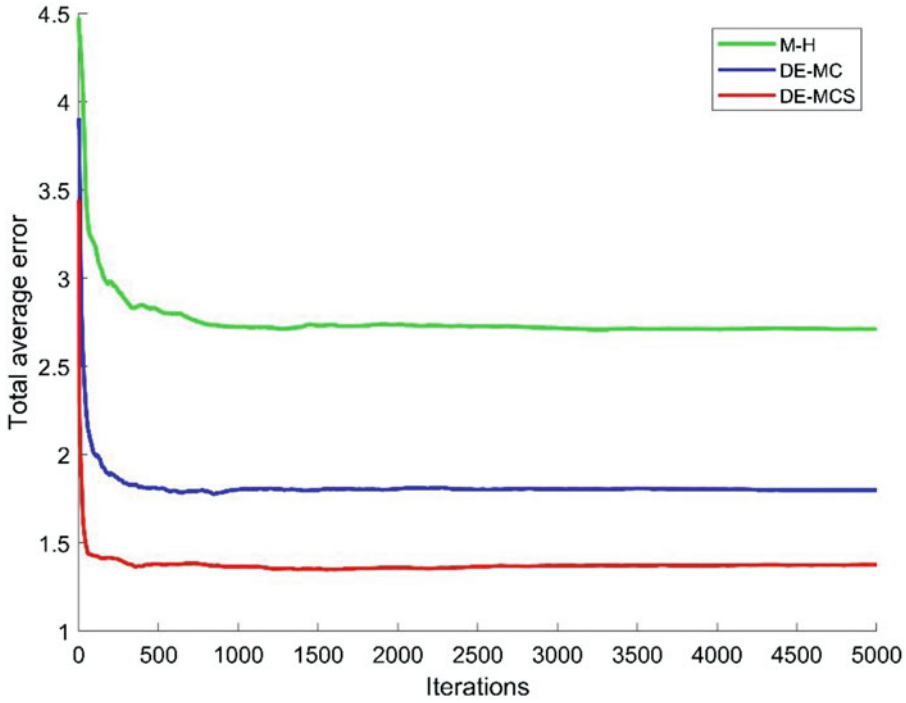

Fig. 10 Convergence of the total average error of the F-shaped structure using the M-H, DE-MC, and DE-MCS algorithms

5 Conclusion

This paper has introduced the Differential Evolution Markov Chain method with snooker update (DE-MCS) for the Bayesian FE model updating problem. The DE-MCS algorithm is an improved version of the standard Differential Evolution Markov Chain (DE-MC) algorithm that requires fewer chains and employs the past states from the storage matrix to generate new proposals. In contrast, the standard DE-MC method requires a large number of chains and uses its ongoing population to propose new solutions. In this paper, three algorithms, namely Metropolis-Hastings, DE-MC, and DE-MCS, are used to update a structural system. The F-shaped structure was employed to investigate the performance of the algorithms to solve the Bayesian FE model updating problem. The obtained results are discussed, and the differences are explained. The solutions attained by the multichain methods (DE-MC and DE-MCS) are superior to the results of the single-chain method (M-H). Furthermore, it is demonstrated that fewer chains for the DE-MCS procedure are sufficient to update the FE model. The outcomes of the DE-MCS method are the best overall, and outliers are observed less. In addition, the real-time processing required for the DE-MCS method with fewer chains is much shorter than for the standard DE-MC method since a large number of chains are involved. Finally, as future work, the DE-MCS algorithm will be compared with the performance of other evolutionary-based Markov chain Monte Carlo approaches.

References

1. Hughes, T.J.: The Finite Element Method: Linear Static and Dynamic Finite Element Analysis. Courier Corporation, New York (2012)
2. Rao, S.S.: The Finite Element Method in Engineering. Butterworth-Heinemann, Massachusetts (United States) (2017)
3. Friswell, M., Mottershead, J.E.: Finite Element Model Updating in Structural Dynamics. Springer Science & Business Media, Netherlands (2013)
4. Marwala, T.: Finite Element Model Updating Using Computational Intelligence Techniques: Applications to Structural Dynamics. Springer Science & Business Media, Verlag London (2010)
5. Marwala, T., Boulkaibet, I., Adhikari, S.: Probabilistic Finite Element Model Updating Using Bayesian Statistics: Applications to Aeronautical and Mechanical Engineering. Wiley, United Kingdom (2016)
6. Mottershead, J.E., Link, M., Friswell, M.I.: The sensitivity method in finite element model updating: a tutorial. Mech. Syst. Signal Process. **25**(7), 2275–2296 (2011)
7. Geyer, C.J.: Practical Markov chain Monte Carlo. Stat. Sci., 473–483 (1992)

8. Fortin, F.-A., De Rainville, F.-M., Gardner, M.-A.G., Parizeau, M., Gagné, C.: DEAP: evolutionary algorithms made easy. J. Mach. Learn. Res. **13**(1), 2171–2175 (2012)
9. Sherri, M., Boulkaibet, I., Marwala, T., Friswell, M.: Bayesian finite element model updating using a population Markov chain Monte Carlo algorithm. In: Special Topics in Structural Dynamics & Experimental Techniques, Volume 5, pp. 259–269. Springer, New York City, USA (2020)
10. Boulkaibet, I., Mthembu, L., Marwala, T., Friswell, M., Adhikari, S.: Finite element model updating using an evolutionary Markov chain Monte Carlo algorithm. In: Dynamics of Civil Structures, Volume 2, pp. 245–253. Springer, New York City, USA (2015)
11. Marwala, T.: Finite element model updating using wavelet data and genetic algorithm. J. Aircr. **39**(4), 709–711 (2002)
12. Marwala, T., Sibisi, S.: Finite element model updating using Bayesian framework and modal properties. J. Aircr. **42**(1), 275–278 (2005)
13. Boulkaibet, I., Marwala, T., Mthembu, L., Friswell, M., Adhikari, S.: Sampling techniques in Bayesian finite element model updating. In: Topics in Model Validation and Uncertainty Quantification, Volume 4, pp. 75–83. Springer (2012)
14. Boulkaibet, I., Mthembu, L., Marwala, T., Friswell, M., Adhikari, S.: Finite element model updating using Hamiltonian Monte Carlo techniques. Inverse Prob. Sci. Eng. **25**(7), 1042–1070 (2017)
15. Boulkaibet, I.: Finite element model updating using Markov Chain Monte Carlo techniques, University of Johannesburg, 2014
16. Boulkaibet, I., Mthembu, L., Marwala, T., Friswell, M., Adhikari, S.: Finite element model updating using the shadow hybrid Monte Carlo technique. Mech. Syst. Signal Process. **52**, 115–132 (2015)
17. Ter Braak, C.J.: A Markov chain Monte Carlo version of the genetic algorithm differential evolution: easy Bayesian computing for real parameter spaces. Stat. Comput. **16**(3), 239–249 (2006)
18. Sherri, M., Boulkaibet, I., Marwala, T., Friswell, M.: A differential evolution Markov chain Monte Carlo algorithm for Bayesian model updating. In: Special Topics in Structural Dynamics, Volume 5, pp. 115–125. Springer, New York City, USA (2019)
19. ter Braak, C.J., Vrugt, J.A.: Differential evolution Markov chain with snooker updater and fewer chains. Stat. Comput. **18**(4), 435–446 (2008)
20. Arora, V.: Comparative study of finite element model updating methods. J. Vib. Control. **17**(13), 2023–2039 (2011)

Using Dead and Thermal Loads to Capture the Behavioral Changes of a Cable-Stayed Bridge

Christos Aloupis, Harry W. Shenton, and Michael J. Chajes

Abstract To enhance the maintenance process of the Indian River Inlet Bridge, the Delaware Department of Transportation worked with the Center for Innovative Bridge Engineering (CIBrE) of the University of Delaware (UD) to install a structural health monitoring (SHM) system on the bridge during construction. The SHM system collects data in real time 24/7. For this research, data collected are transformed into 10-minute average values. These average values represent the response of the bridge to slowly changing thermal loads or to constant loads such as dead loads.

This paper presents a method for identifying damage from the structures' strain vs. temperature response. The methodology is evaluated based on both actual response and response simulated using a calibrated finite element model (FEM).

Using data collected over 8 years since the bridge was opened to traffic, a finite element model (FEM) was used to evaluate the ability of the SHM to identify different types and severity of damage. To do this, different levels of severity were simulated, and their effect on the structural response was compared with the observed response, including the variability of that response. Using this approach, the ability to assess various levels of damage has been determined.

Keywords Structural health monitoring (SHM) · Thermal loads · Dead loads · Cable-stayed bridge · Temperature-driven SHM

1 Introduction

In structural health monitoring (SHM), different types of measurements can be used to evaluate the condition of structures under various types of loads. In most cases, truck loads are used as they are easy to measure and apply, and they represent a major load type. These truck loads can be applied during controlled load tests [1] or can be captured from ambient traffic response. In either case, temperature loads are neglected by zeroing the measurements before the passes or removing the effect of slowly changing loads using a moving average. In temperature-driven SHM (TD-SHM), the focus is on the effect of thermal loads on the structure [3]. It has been shown that the strains developed due to thermal loads can be significantly higher than those caused by traffic loads.

2 Background

The Indian River Inlet Bridge (IRIB) is a three-span cable-stayed bridge that was built with an embedded SHM system consisting of more than 120 individual sensors [2]. Since 2012, when the IRIB opened to traffic, the system has operated 24/7, collecting and storing data. Among the collected data are strain and temperature measurements, which have been used in this research. To reduce the effect of traffic loads and ambient noise on the strain measurements, 10-minute averages have been applied to the data.

For the purposes of this research, the focus was on a controlling location of the back span, monitoring the strain measurements captured in the top and bottom of the two edge girders in relation to the measured temperature.

C. Aloupis (✉) · H. W. Shenton · M. J. Chajes
Department of Civil and Environmental Engineering, College of Engineering, University of Delaware, Newark, DE, USA

Z. Mao (ed.), *Model Validation and Uncertainty Quantification, Volume 3*, Conference Proceedings of the Society for Experimental Mechanics Series, https://doi.org/10.1007/978-3-030-77348-9_21

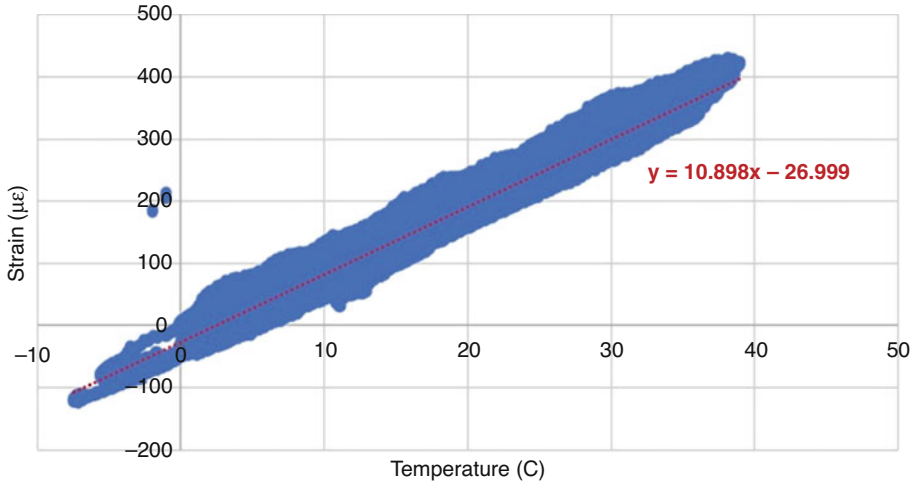

Fig. 1 Example of regression model for strain-temperature relation for a sensor located in the top of east girder in a controlling location for the back span

3 Analysis

Using the 10-minute average data, regression analysis was conducted to define the relationship between the strain and ambient temperature (Fig. 1). The slope and the intercept of the regression line were selected as the parameters to be monitored to identify the behavioral changes of the bridge. To get these two parameters, we first needed to identify the window of time that should be used (e.g., 1, 3, 5, 10 days, etc.) and the nature of the data that should be used (e.g., 24-h data or night-only data). By selecting data that provide more consistent results, smaller changes can be captured. Furthermore, if smaller time windows can be used, earlier alerts of a change are possible.

For all the different sets of data (different time windows and 24 h vs night data), it was observed that both the slope and the intercept followed seasonal patterns. The effect of environmental parameters (e.g., average temperature) on the slope and the intercept was evaluated. Data mining (DM) models that captured these effects were trained. These trained DM models were used to predict the slope and the intercept based on the characteristics of the sample (average/max temperature, season, average/max relative humidity), and these predictions were compared with actual values. The statistical characteristics of the residuals show a significant improvement in the sensitivity of the method.

To evaluate the ability of the method to capture changes in bridge behavior, a finite element model (FEM) of the bridge was used. The model was used to calculate strains developed on the bridge for dead loads and thermal variations. Two baselines were generated for these two different loads to show the healthy condition of the structure. A comparison between the strains due to thermal loads with the measured strains showed that the model was sufficiently accurate. Once the baseline was ready, damage to various bridge elements (cables, girders, and bearings) was simulated using the model. For each damage scenario, the same analyses were conducted for dead and thermal loads. The difference between the baselines and the calculated strains reflects damage to the structure.

Regarding thermal loads, when a change in temperature results in different strains for the damaged and undamaged system, this causes the slope of the regression line to change. Regarding dead load effect, when there is no change in temperature but the strains for the damaged and undamaged system are not the same, this causes the intercept to be affected.

4 Conclusion

In this research, a method for capturing the behavioral changes of the IRIB based on the use of thermal and dead loads was developed. DM models were trained to predict the slope and intercept that a linear regression model should have. These models increased the accuracy of monitoring behavioral changes that affect strains which developed due to dead and thermal loads. When damage was simulated using FEM, it was observed that changes associated with the bridge bearings affect the slope of the regression line, while changes that cause a redistribution of loads (cable or beam damage) affect the intercept. The sensitivity of this method allows one to capture these changes in earlier stages (i.e., smaller changes).

Acknowledgements The authors would like to acknowledge the Delaware Department of Transportation (especially Doug Robb, Craig Stevens, Marx Possible, David Gray, Alastair Probert, Jason Arndt, Craig Kursinski, Raymond Eskaros) and the Federal Highway Administration for the financial support to develop and implement the structural monitoring system.

References

1. Al-Khateeb, H.T., Shenton, H.W., Chajes, M.J., Aloupis, C.: Structural health monitoring of a cable-stayed bridge using regularly conducted diagnostic load tests. Front. Built Environ. **2019**, 5 (2019)
2. Shenton III, H.W., Al-Khateeb, H.T., Chajes, M.J., Wenczel, G.: Indian river inlet bridge (part A): description of the bridge and the structural health monitoring system. Bridg. Struct. **13**, 3–13 (2017)
3. Yarnold, M.T., Moon, F.L.: Temperature-based structural health monitoring baseline for long-span bridges. Eng. Struct. **86**, 157–167 (2015)

Vibration-Based Damage Detection Framework of Large-Scale Structural Systems

O. Markogiannaki, A. Arailopoulos, D. Giagopoulos, and C. Papadimitriou

Abstract The main objective of this work is to present a vibration-based damage estimation framework for structural systems by integrating vibration experimental measurements in a high-fidelity, large-scale, finite element (FE) model. Using the measured responses of a healthy structural system under operational vibrations, a parameterized FE model could be tuned using state-of-the-art FE model updating techniques in order to develop a high-fidelity model of the structural system, representing the healthy reference model. These methods provide much more comprehensive information about the condition of the monitored system than the analysis of raw data. The diagnosed degradation state, along with its identified uncertainties, can be incorporated into robust reliability tools for updating predictions on the residual useful lifetime of structural components and safety against various failure modes, taking into account stochastic models of future loading characteristics. A fault or damage would cause a sudden change in the operational responses of the structure. Incorporating the unhealthy response under measured operational excitations, a series of FE model updating runs of incrementally reparameterized FE models could be automated. The sensitivity of the unhealthy response to the parameter change pertains to the sensitive parts of the FE model, where damage or fault is located. A recursive reparameterization of those sensitive parts, followed by an FE model updating, leads toward both the detection localization and the type and magnitude of the fault or damage. The proposed framework is applied on a small-scale laboratory steel truss bridge.

Keywords FE model update · Transmittance functions · Damage identification

1 Introduction

A fault or damage on structures under operation can cause a sudden change in their response, which gives rise to safety issues and a potential loss of their functionality. Damage can develop due to either sudden extreme load events (such as strong winds, earthquakes) or variable operational loading and environmental effects (e.g., fatigue due to heavy vehicle traffic, corrosion due to environmental conditions). The application of systems for structural health monitoring (SHM) can prevent failures by detecting damage at an early stage before it becomes critical for the safety or functionality of the structure.

A large number of studies on SHM techniques focus on using vibration-based methods to assess the dynamic properties or response changes of structures in order to identify the development of damage. These vibration-based methods are derived from the premise that any physical property changes in a structure will alter its dynamic characteristics, which can in turn be used to identify any damage or deterioration in the structure [1].

One main concern in damage detection techniques has been the selection of appropriate damage indicators. Several techniques consider the variation in modal characteristics such as natural frequencies and mode shapes as damage indicators. For this purpose, the modal assurance criterion (MAC), firstly raised in the late 1970s, has served as an essential indicator [2, 3]. A recent approach [4] is based on a probabilistic treatment of the MAC criterion between the predicted model and the experimental mode shapes applied on reduced-order finite element (FE) modes of the structure. However, the capabilities of modal-based methods may be limited in cases in which local damage does not significantly alter the modal characteristics [5], especially when the level of damage is low. Therefore, different SHM methods have been also developed accounting for

O. Markogiannaki · A. Arailopoulos · D. Giagopoulos (✉)
Department of Mechanical Engineering, University of Western Macedonia, Kozani, Greece
e-mail: dgiagopoulos@uowm.gr

C. Papadimitriou
Department of Mechanical Engineering, University of Thessaly, Volos, Greece

Z. Mao (ed.), *Model Validation and Uncertainty Quantification, Volume 3*, Conference Proceedings of the Society for Experimental Mechanics Series, https://doi.org/10.1007/978-3-030-77348-9_22

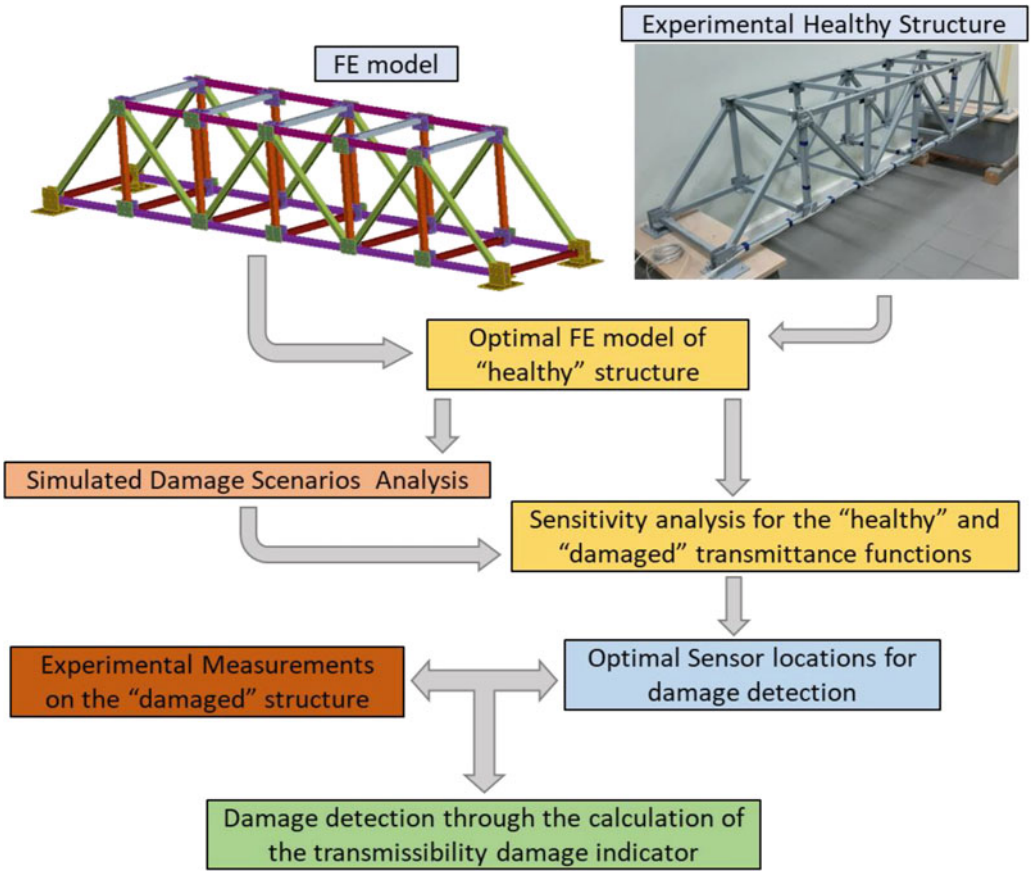

Fig. 1 Flow diagram of the proposed damage identification methodology

response models (frequency response functions (FRFs), operational deflection shapes (ODS), transmissibilities) as damage indicators [6]. A characteristic of such methods is that they depend solely on output measurements. For instance, Maia et al. [7] presented a damage detection method using frequency response models. Fassois and colleagues [8, 9] have proposed the use of functional-model-based methods (FMBMs) for damage detection. Zhan et al. [10] introduced the use of transmittance functions (TFs) in damage detection. Since then, several researchers have worked toward the development of damage indicators based on transmissibility. Chesné and Deraemaeker [11] presented a thorough review on the use of transmittance functions as damage indicators. Poulimenos and Sakellariou [12] introduced recently a novel data-based response-only methodology that is founded on an autoregressive model with an exogenous excitation parametric representation of the transmittance function between vibration measurements at two different locations on the structure. Such methods use data-based models that detect a deviation from the initial health condition based only on undamaged-state data measured on the monitored structure. Although data-based techniques are appealing as they require fewer resources (software, hardware) and engineering knowledge than do physical model-based methods, model-based methods have more potential to address the needs of monitoring systems, from damage detection to damage prediction.

In the present study, a novel approach for damage detection on large-scale structural systems for unknown input excitation is introduced that integrates vibration experimental measurements in a high-fidelity finite element (FE) model and uses transmissibility as an indicator for damage detection. The proposed methodology includes the development of a parameterized FE model. The FE model is optimized using state-of-the-art FE model updating techniques [13–15] based on experimental vibrational measurements on the healthy structure. The optimal model is then subjected to various damage scenarios. A sensitivity analysis is performed for the "healthy" and "damaged" derived transmittance functions to acquire the optimal sensor location for each damage scenario. Finally, experimental measurements can be conducted using appropriate sensor locations to detect damage based on transmissibility as a damage indicator. The flow diagram in Fig. 1 summarizes the proposed approach applied on a laboratory steel truss bridge.

2 Transmittance Function Theoretical Basis

The transmittance function (TF) in accordance with the frequency response function (FRF) (admittance, mobility, inertance) [16–18] is computed by the ratio of the response spectra of two vibration response signals (accelerations, velocities, displacements) measured at two different locations of the structure for a given excitation location and direction regardless of the amplitude and frequency content of the input. Given the definition of the spectral densities, the transmittance function is expressed as the ratio

$$T_{jk}^{r}(\omega) = \frac{S_{jk}^{r}(\omega)}{S_{kk}^{r}(\omega)} = \frac{h_{j}^{r\,*}(\omega)\, h_{k}^{r}(\omega)}{h_{k}^{r\,*}(\omega)\, h_{k}^{r}(\omega)} \tag{1}$$

assuming $h(\omega)$ to be a $n \times 1$ column vector of the $n \times n$ transfer function matrix $H(\omega)$ and $S_{jk}^{r}(\omega)$ is the cross-spectral density (CSD) between the $j - th$ and $k - th$ degrees of freedom (DOFs) of the structural system and $S_{kk}^{r}(\omega)$ is the auto-spectral (power spectral) density (PSD) at the $k - th$ degree of freedom, both for a given input located at the $r - th$ degree of freedom. The above expression clearly denotes the independence of the transmittance function from the excitation, being a nondimensional complex quantity that is easy and simple to compute, defining how the amplitude and phase of the transmitted vibration as a function of frequency is propagated between DOFs j and k of the structural system [10].

3 Transmittance Function Based Damage Detection

The sensitivity of transmittance functions to damage detection is fairly high because the transmitted vibration across any chosen portion of the structure is characterized by a continuous function with peaks and valleys, similarly to the frequency response functions but devoid of the limitation of the distance between the location of the input and the intended response point needed to detect damage [11, 12, 19]. An indicator for damage detection and localization at a single-damaged-case scenario is a scalar value DI_{jk}, which quantifies the discrepancy between healthy and damaged transmittance functions across j and k points for a given frequency band as

$$\mathrm{DI}_{ij}(\omega_1, \omega_2) = \frac{\int_{\omega_1}^{\omega_2} \left| T_{jk}^{h}(\omega) - T_{jk}^{d}(\omega) \right| d\omega}{\int_{\omega_1}^{\omega_2} \left| T_{jk}^{d}(\omega) \right| d\omega} \tag{2}$$

where $|\ |$ denotes amplitude and equivalently the damage indicator with values between $[0, 1]$ for single node-node transmitted signal as at a specific frequency band is

$$\mathrm{DI_m} = \frac{\int_{\omega_1}^{\omega_2} \left| T^{h}(\omega) \right| d\omega}{\int_{\omega_1}^{\omega_2} \left| T^{d}(\omega) \right| d\omega} - 1 \text{ and } \mathrm{DI_p} = \frac{\int_{\omega_1}^{\omega_2} \mathrm{phase}\left(T^{h}(\omega)\right) d\omega}{\int_{\omega_1}^{\omega_2} \mathrm{phase}\left(T^{d}(\omega)\right) d\omega} - 1 \tag{3}$$

for the amplitude and phase difference, respectively.

4 Transmittance Based Finite Element Model Updating Formulation

Derived from the MAC for any measured frequency point, ω_i, a global correlation coefficient may be used [20, 21]:

$$x_{\mathrm{s}}(\omega_i) = \frac{\left| \{T_{\mathrm{X}}(\omega_i)\}^{\mathrm{H}} \{T_{\mathrm{N}}(\omega_i)\} \right|^2}{\left(\{T_{\mathrm{X}}(\omega_i)\}^{\mathrm{H}} \{T_{\mathrm{X}}(\omega_i)\} \right) \left(\{T_{\mathrm{N}}(\omega_i)\}^{\mathrm{H}} \{T_{\mathrm{N}}(\omega_i)\} \right)} \tag{4}$$

where $\{T_{\mathrm{X}}(\omega_i)\}$and $\{T_{\mathrm{N}}(\omega_i)\}$ are the experimental (measured) and the numerical (predicted) transmittance functions at matching excitation – response locations. As the MAC value, $x_{\mathrm{s}}(\omega_i)$ assumes a value between 0 and unity and indicates perfect correlation with $x_{\mathrm{s}}(\omega_i) = 1$. For $x_{\mathrm{s}}(\omega_i) = 0$, no correlation exists [21].

A supplementary correlation coefficient $x_a(\omega_i)$ is used by targeting the discrepancies in amplitude. The amplitude correlation coefficient is defined as:

$$x_a(\omega_i) = \frac{2\left|\{T_X(\omega_i)\}^H \{T_N(\omega_i)\}\right|}{\left(\{T_X(\omega_i)\}^H \{T_X(\omega_i)\}\right) + \left(\{T_N(\omega_i)\}^H \{T_N(\omega_i)\}\right)} \tag{5}$$

where the response vectors are identical to those used for $x_s(\omega_i)$. Thus, two measures of fit are proposed using $x_s(\hat{\omega}_r)$ and $x_a(\hat{\omega}_r)$, which correspond to the identified resonant frequencies of the system:

$$J_1(\underline{\theta}) = \sum_{r=1}^{m}\left[1 - x_s(\hat{\omega}_r, \underline{\theta})^2\right] \text{ and } J_2(\underline{\theta}) = \sum_{r=1}^{m}\left[1 - x_a(\hat{\omega}_r, \underline{\theta})^2\right] \tag{6}$$

Minimizing at global minimum the following single objective traditionally solves the parameter estimation problem:

$$J(\underline{\theta}; \underline{w}) = w_1 J_1(\underline{\theta}) + w_2 J_2(\underline{\theta}) \tag{7}$$

formed by the two objectives $J_i(\underline{\theta})$, using the weighting factors $w_i \geq 0$, $i = 1, 2$, with $w_1 + w_2 = 1$. The objective function $J(\underline{\theta}; \underline{w})$ represents an overall measure of fit between the measured and the model predicted TFs [13, 22–27].

5 Experimental Application and FE Model Updating

In order to examine the applicability of the proposed damage detection and localization methodology, a laboratory-scale steel truss bridge has been constructed. Various experimental tests were conducted where all the necessary elements of the TF matrix required for determining the response of the structure were determined by imposing impulsive loading. The measured frequency range was 0–2048 Hz, which includes the analytical frequency range of interest for the truss, 0–250 Hz. An initial investigation indicated 15 natural frequencies for the truss bridge, in this frequency range. A schematic illustration of the experimental arrangement is presented in Fig. 2. In this figure, the locations and directions of acceleration measurements are presented, applying an impulsive load in various directions and at several locations. Specifically, the red circles present the locations of the five triaxial accelerometers, while the green dots present the preferred locations where impact hummer excitations were imposed.

Measurements from this experimental arrangement led to all combinations of transmittance functions between all measured points, used for the subsequent finite element model update, in order to acquire a high-fidelity optimal FE model of the healthy physical structure, which could be later interrogated in reference to optimal sensor placement for capturing damage. The nominal material parameters of the steel material of the laboratory truss bridge are $E = 210$ GPa for the modulus of elasticity, $\nu = 0.3$ for the Poisson's ratio, and $\rho = 7850\,\text{kgr/m}^3$ for the density.

The developed FE model, along with its parameterization for FE model update, is introduced in order to facilitate the applicability of the updating framework. The parameterized model is consisted of eight (8) parts, as shown in Fig. 3.

All members of the FE model of the truss bridge are modeled with shell elements, whereas all steel plates in connections and supports are modeled with solid elements [28]. The covariance matrix adaptation evolution strategy (CMA-ES) framework [13] is applied at t ±10% from the nominal values as design bounds, in order to update the developed FE model applying the objective function of Eq. (7) using response residuals, which include shape and amplitude correlation coefficients, and considering measured and numerical transmittance functions, including components at all sensor locations and directions. The updated FE model was used to simulate five different damage scenarios where, in each scenario, a single member of the truss was modeled with aluminum material properties, where $E = 69$ GPa is the modulus of elasticity, $\nu = 0.3$ is the Poisson's ratio, and $\rho = 2750\,\text{kgr/m}^3$ is the density introducing damage of approximately 5% based on the healthy and damaged FE models' eigenfrequency differences. After assessing the sensitivity of the TF locations' combination in order to detect a single-damage scenario, the following results are presented.

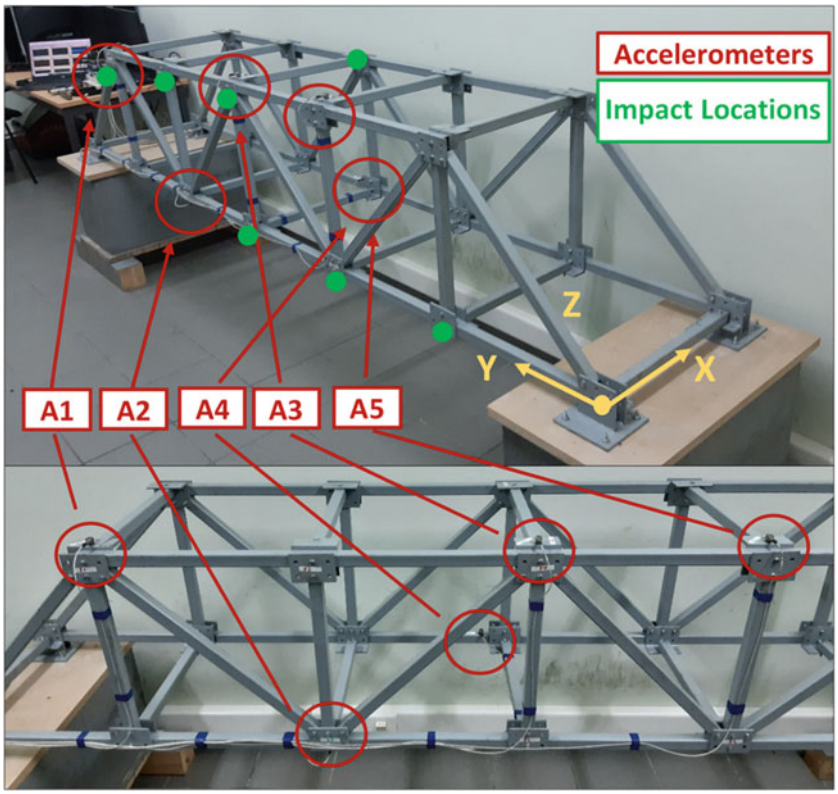

Fig. 2 Experimental setup of a laboratory-scale truss bridge

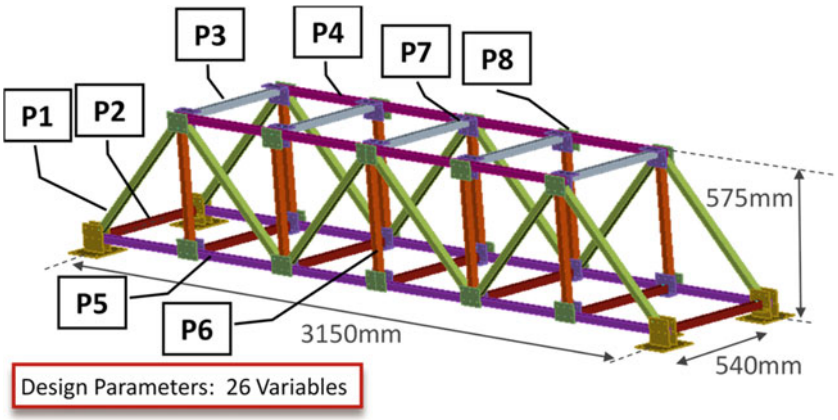

Fig. 3 Parts of the parameterized FE model. Detail of the FE model of the laboratory-scale truss bridge

6 Damage Detection

The following Fig. 4 presents the optimal sensor placement results after a sensitivity analysis in order to detect and localize the damage in an indicative damage scenario, where the middle-lower member of the truss is modeled with aluminum material properties.

During the experimental measurements, triaxial accelerometers were placed at optimal locations, as presented in Fig. 4, and a series of experimental measurements were performed using an impulse hummer exciting the laboratory truss bridge at critical locations to provide clear data for the computation of the equivalent TF matrix.

The following Fig. 5 presents a comparison of the simulated TFs computed by the optimal FE model produced by the updating process depicted by a green continuous line and the respective experimentally measured TFs depicted by a red continuous line. These graphs correspond to an approximate 5% damage of the above indicative damage scenario of the

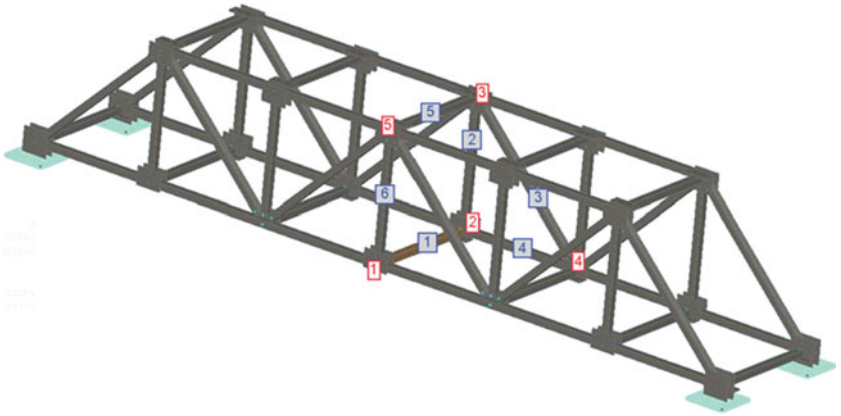

Fig. 4 Measurement locations for TF comparison for damage identification and localization in an indicative damage scenario

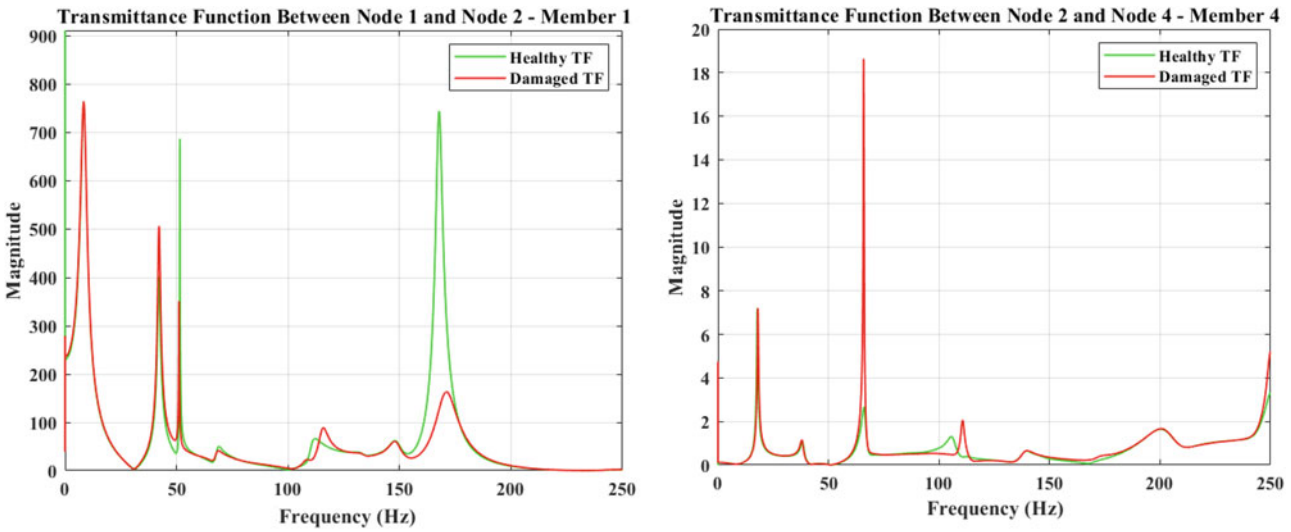

Fig. 5 Healthy optimal FE-model-simulated TFs (green line) against damaged experimentally measured TFs (red line) for 5% damage at element number 1 (material differentiation). Comparison of TFs between members 1 and 4

middle member's material change. Specifically, the left graph presents a comparison between the optimal simulated TFs and the experimental ones in nodes 1 and 2, referring to member number 1, whereas the right graph presents the same comparison between nodes 2 and 4, referring to member number 4. The frequency range is 0–250 Hz, which is the frequency band of interest.

The reason that the two indicative members 1 and 4 were selected to be presented in this comparison is that these two members demonstrate the maximum damage indicator (DI), shown in the bar graph in Fig. 6.

As presented in Fig. 6, the maximum damage indicator between accelerometers 1 and 2 is$DI_1 = 0.175$. This is actually the correct location of the damage as it refers to member 1, which is the one with material differentiation. Additionally, the damage indicator between nodes 2 and 4 is $DI_4 = 0.116$, which is a relatively high value for member 4, which is next to the correct location of the damage. This approach indicated that measuring and comparing the TFs between two adjacent node damage could be conveniently detected and localized, although the damage affects the TFs of the members in the proximity of the actual damage.

7 Conclusion

In this work, an output-only vibration-based methodology for developing a high-fidelity FE model of a laboratory-scale truss bridge, which could be interrogated for damage detection and identification, is presented. A damage detection

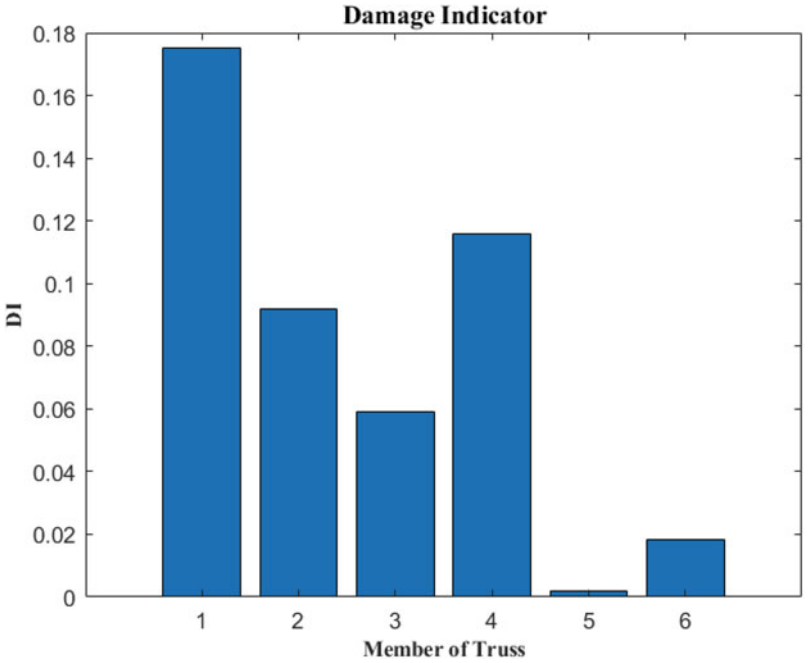

Fig. 6 Damage indicators for 5% damage at element number 1 (material differentiation)

approach having unknown input excitation is introduced that utilizes an optimal high-fidelity finite element (FE) model and transmittance functions as the indicator for damage detection. At first, a parameterized FE model was developed and updated using a state-of-the-art FE modeling evolution strategy based on experimental vibrational measurements on the healthy structure. Various damage scenarios are then simulated, and a sensitivity analysis follows for optimal sensor location placement in order to acquire the most informative transmittance functions for each damage scenario. Experimental measurements are conducted using appropriate sensor locations to detect damage based on an indicative damage scenario of less than 5% damage in the first 15 eigenfrequencies. Results proved the potential of the proposed approach as damage was accurately identified and detected.

Acknowledgments This research is cofinanced by Greece and the European Union (European Social Fund- ESF) through the Operational Programme "Human Resources Development, Education and Lifelong Learning 2014-2020" in the context of the project "Structural Health Monitoring and Damage Detection of Bridges based in vibrational measurements" (MIS 5050131).

References

1. Farahani, R.V., Penumadu, D.: Damage identification of a full-scale five-girder bridge using time-series analysis of vibration data. Eng. Struct. **115**, 129–139 (2016)
2. Allemang, R.J.: The modal assurance criterion (MAC): twenty years of use and abuse. J. Sound Vib. **37**(8), 14–23 (2005)
3. dos Santos, F.L.M., Peeters, B., Van der Auweraer, H., Góes, L.C.S., Desmet, W.: Vibration-based damage detection for a composite helicopter main rotor blade. Case Stud. Mech. Syst. Signal Process. **3**, 22–27 (2016)
4. Argyris, C., Papadimitriou, C., Panetsos, P., Tsopelas, P.: Bayesian model-updating using features of modal data: application to the Metsovo bridge. J. Sens. Actuator Netw. **9**(2), 27 (2020)
5. Azim, M.R., Gül, M.: Damage detection of steel-truss railway bridges using operational vibration data. J. Struct. Eng. **146**(3), 04020008 (2020)
6. Sampaio, R.P.C., Maia, N.M.M., Almeida, R.A.B., Urgueira, A.P.V.: A simple damage detection indicator using operational deflection shapes. Mech. Syst. Signal Process. **72–73**, 629–641 (2016)
7. Maia, N.M.M., Silva, J.M.M., Almas, E.A.M., Sampaio, R.P.C.: Damage detection in structures: from mode shape to frequency response function methods. Mech. Syst. Signal Process. **17**(3), 489–498 (2003)
8. Sakaris, C.S., Sakellariou, J.S., Fassois, S.D.: Random-vibration-based damage detection and precise localization on a lab–scale aircraft stabilizer structure via the Generalized Functional Model Based Method. Struct. Health Monit. **16**(5), 594–610 (2017)
9. Sakellariou, J.S., Fassois, S.D., Sakaris, C.S.: IWSHM 2017: vibration-based damage localization and estimation via the stochastic functional model–based method: an overview. Struct. Health Monit. **17**(6), 1335–1348 (2018)

10. Zhang, H., Schulz, M.J., Naser, A., Ferguson, F., Pai, P.F.: Structural health monitoring using transmittance functions. Mech. Syst. Signal Process. **13**(5), 765–787 (1999)
11. Chesné, S., Deraemaeker, A.: Damage localization using transmissibility functions: a critical review. Mech. Syst. Signal Process. **38**(2), 569–584 (2013)
12. Poulimenos, A.G., Sakellariou, J.S.: A transmittance-based methodology for damage detection under uncertainty: an application to a set of composite beams with manufacturing variability subject to impact damage and varying operating conditions. Struct. Health Monit. **18**(1), 318–333 (2019)
13. Giagopoulos, D., Arailopoulos, A.: Computational framework for model updating of large scale linear and nonlinear finite element models using state of the art evolution strategy. Comput. Struct. **192**, 210–232 (2017)
14. Giagopoulos, D., Arailopoulos, A., Natsiavas, S.: A model-based fatigue damage estimation framework of large-scale structural systems. Struct. Health Monit. **0**(0), 1475921719871953 (2019)
15. Seventekidis, P., Giagopoulos, D., Arailopoulos, A., Markogiannaki, O.: Structural Health Monitoring using deep learning with optimal finite element model generated data. Mech. Syst. Signal Process. **145**, 106972 (2020)
16. Giagopoulos, D., Arailopoulos, A.: Parameter estimation of nonlinear large scale systems through stochastic methods and measurement of its dynamic response. In: 7th European Congress on Computational Methods in Applied Sciences and Engineering, ECCOMAS Congress 2016. National Technical University of Athens, Crete Island, Greece (2016)
17. Arailopoulos, A., Giagopoulos, D.: Finite element model updating techniques of complex assemblies with linear and nonlinear components. In: 34th IMAC, A Conference and Exposition on Structural Dynamics, 2016. Springer New York LLC, Orlando (2016)
18. Giagopoulos, D., Arailopoulos, A.: Finite element model updating of geometrically complex structure through measurement of its dynamic response. In: 1st ECCOMAS Thematic Conference on Uncertainty Quantification in Computational Sciences and Engineering, UNCECOMP 2015. National Technical University of Athens, Crete Island, Greece (2015)
19. Zhang, J., Reynders, E., De Roeck, G., Lombaert, G.: Model updating of periodic structures based on free wave characteristics. J. Sound Vib. **442**, 281–307 (2019)
20. Grafe, H.: Model updating of large structural dynamics models using measured response function. In: Department of Mechanical Engineering. Imperial College, London (1999)
21. Grafe, H.: Review of frequency response function updating methods. 1995, BRITE-URANUS BRE2-CT94-0946
22. Christodoulou, K., Ntotsios, E., Papadimitriou, C., Panetsos, P.: Structural model updating and prediction variability using Pareto optimal models. Comput. Methods Appl. Mech. Eng. **198**(1), 138–149 (2008)
23. Giagopoulos, D., Papadioti, D.-C., Papadimitriou, C., Natsiavas, S.: Bayesian uncertainty quantification and propagation in nonlinear structural dynamics. In: Simmermacher, T., Cogan, S., Moaveni, B., Papadimitriou, C. (eds.) Topics in Model Validation and Uncertainty Quantification, Volume 5: Proceedings of the 31st IMAC, A Conference on Structural Dynamics, 2013, pp. 33–41. Springer New York, New York (2013)
24. Papadimitriou, C., Ntotsios, E., Giagopoulos, D., Natsiavas, S.: Variability of updated finite element models and their predictions consistent with vibration measurements. Struct. Control Health Monit. **19**(5), 630–654 (2012)
25. Ntotsios, E., Papadimitriou, C.: Multi-objective optimization algorithms for finite element model updating. In: International Conference on Noise and Vibration Engineering (ISMA 2008)., pp. 66–80. Katholieke Universiteit Leuven, Leuven (2008)
26. Giagopoulos, D., Arailopoulos, A., Dertimanis, V., Papadimitriou, C., Chatzi, E., Grompanopoulos, K.: Structural health monitoring and fatigue damage estimation using vibration measurements and finite element model updating. Struct. Health Monit. **18**(4), 1475921718790188 (2018)
27. Arailopoulos, A., Giagopoulos, D., Zacharakis, I., Pipili, E.: Integrated reverse engineering strategy for large-scale mechanical systems: application to a steam turbine rotor. Front. Built Environ. **4**(55), 1–6 (2018)
28. BETA CAE Systems, S.A., ANSA & META-Post. 2018, BETA CAE Systems, S.A.: Thessaloniki